Design, Synthesis and Investigations of Liquid Crystalline Organic Semiconductors

A Thesis Submitted in Partial Fulfillment of the
Requirements for the Degree of
Doctor of Philosophy
at
IIT Guwahati
by

Vinod Kumar Vishwakarma

Roll No. 156122010

Department of Chemistry
Indian Institute of Technology Guwahati
Guwahati-781039, Assam
India

August 2022

TH-2983_156122010

"Be less curious about people and more curious about ideas".

Marie Curie

"If you don't fail sometimes, you are not being ambitious enough".

Sundar Pichai

Dedicated to

my beloved parents……

TH-2983_156122010

DECLARATION

I do hereby declare that the research work embodied in this thesis entitled "***Design, Synthesis and Investigations of Liquid Crystalline Organic Semiconductors***" has been carried out by me under the supervision of **Prof. A. S. Achalkumar** in the Department of Chemistry, Indian Institute of Technology Guwahati, Assam - 781039, India.

In keeping with the general practice of reporting scientific observations, due acknowledgements have been made wherever the work described is based on the findings of other investigators.

Vinod Kumar

IIT Guwahati
August, 2022

Vinod Kumar Vishwakarma
Roll No. 156122010

TH-2983_156122010

Dr. A. S. Achalkumar
Professor
Department of Chemistry
Indian Institute of Technology Guwahati
Guwahati – 781039, Assam, India
Phone: +91-361-258-2329
Fax: +91-361-258-2349
E-mail: achalkumar@iitg.ac.in
achalkumar78@gmail.com

CERTIFICATE

This is to certify that the research work presented in this thesis entitled "***Design, Synthesis and Investigations of Liquid Crystalline Organic Semiconductors***" is an authentic record of the results obtained from the research work carried out by **Mr. Vinod Kumar Vishwakarma (Roll No. 156122010)** under my supervision in the Department of Chemistry, Indian Institute of Technology Guwahati, India. This work is original and has not been submitted elsewhere for a degree or award.

IIT Guwahati
August, 2022

Dr. A. S. Achalkumar
Thesis Supervisor

TH-2983_156122010

ACKNOWLEDGEMENTS

The journey towards the completion of my thesis with the outcome of the years of experience, ideas generated in the form of knowledge, was full of hurdles paved way to the fruitful success. Over seven years of my research career I have been supported and assisted by a large number of people, in regards to whom I want to convey my words of heartfelt thanks for their kindness, grace, attention, encouragement, and support.

At the very outset, with the deepest sense of gratitude, I wish to express my sincere thanks to my supervisor, Prof. Ammathnadu S. Achalkumar for his proficient guidance, inspiration, creative and scientific ideas which helped me to explore the domain of my work assembled in this thesis. He has given me an extraordinary amount of freedom to be creative and to work on the problems that have interested me. I have spent countless hours discussing research and ideas in science with him. Without his patience and guidance, I would not have finished this work. Of course, wherever I was standing in the shadow of fear of travel, he helped me to achieve the target by his constant encouragement with his true scientific spirit. It was one of the best choices I have ever made to choose him as my supervisor. Besides my supervisor, I would also like to express my deepest sense of gratitude and heartfelt thanks to my doctoral committee members, Prof. Chandan Kumar Jana, Dr. Krishna Pada Bhabak and Dr. Akshai Kumar A. S. for their periodic evaluation of my work, valuable suggestions, constant support, and encouragement. I would like to express my sincere thanks to Prof. Chandan Mukherjee for providing me his electrochemical workstation for the analysis. I would like to acknowledge Mr. Rajan Singh, Dr. Monica Naorem, Prof. Roy P. Paily for helping in OFET device fabrication and characterization. I also would like to acknowledge Dr. Mangey Ram Nagar, Dr. Deepak Kumar Dubey, Dr. Sujith Sudheendran Swayamprabha and Prof. Jwo-Huei Jou, National Tsing Hua University, Taiwan for OLED device fabrication and characterization. I gratefully acknowledge Dr. Joydip De, Dr. Monika Gupta and Dr. Santanu Kumar Pal, IISER Mohali, Dr. D. S. Shankar Rao and Dr. S. K. Prasad, CeNS, Bangalore, for helping me with X-ray Diffraction analysis.

I would like to acknowledge the Central Instruments Facility, Department of Chemistry, Centre for Nanotechnology and the Department of Electronics and Electrical Engineering IIT Guwahati for providing me with the analytical facilities required during my research. I wish to express my sincere gratitude to the Department of Chemistry and

TH-2983_156122010

the Indian Institute of Technology Guwahati for nurturing our research career and for all the facilities and financial support that was made available to me.

It would have been impossible for me to continue my seven years stay of Ph. D research without the help and support of my batchmates; I am greatly indebted to them. I express my deep sense of gratitude to all my present lab members Dr. Priyanka Kanth, Mr. Paresh Kumar Behera, Mr. Mrinmoy Roy, Mr. Rahul Ahmed, Mr. Nandan Kumar, Ms. Neichoihoi Lhouvum and Mr. Darmendra Adak. I also express my gratitude to my past lab members Dr. Suraj Kumar Pathak, Dr. Subrata Nath, Dr. Balaram Pradhan and Dr. Ravindra Kumar Gupta, Dr. Sachin Kumar Singh, Dr. Hidayath Ulla, Dr. Hemanta Kalita, Dr. Hemant Kumar Singh, late Dr. Nirmalangshu Chakraborthy, Dr. Srikant Turlapati and Mr. Sibasankar Pradhan for their help, scientific conversations and also maintaining a pleasant working environment throughout my Ph.D. tenure.

Thanks to Dr. Babulal Das, Mr. Aniruddha Gogoi, Mr. Basab Bhattacharjee, Mr. Imdadul Islam, Mr. John Sangma Dangou, Mr. Diganta Kumar Hira, Mr. Shyamal Kumar Mondal, Mrs. Abhilasha M. Baruah, Mrs. Lipika Nath, Mr. Tapu Ghosh and Mr. Michael Deka for their support at instrumental laboratory and office-related work during my research.

Of course, I would like to thank almighty to fulfill my PhD carrier with bunch of beloved senior friends and junior friends Dr. Avishek Banik, Dr. Munendra Pal Singh, Dr. Tushar Kanta Sahu, Dr. Biswajit Nayak, Dr. Maimur Hossain, Dr. Subrata Mondal, Dr. Ila Verma, Dr. Amit Raj, Mr. Umesh Chaudhary, Mr. Laxmi Raman Adil, Mr. Debasish Barman and Mr. Bishwanath Mahato for their timely help, support and for the wonderful time we shared during this period.

Finally, my Ph.D. would not have been completed without the eternal love, care, bless, support, patience, non-refundable sacrifices and encouragement of my parents Mr. Shiv Murti and Mrs. Shiv Kumari, my supportive elder brother Mr. Shiv Kumar and younger brothers Anil Kumar, Pawan Kumar, Amit kumar and my lovely wife Mrs. Ruby and sisters Anshu di, Manju di, Savitri di, Aarti, Pooja, Sarita, Ritu, other supportive family members. They encouraged me to pay attention to the world around me and to wonder why and how things work. Of course, everything will go invalid if I forget the blessings of the almighty god without whom nothing will function and I pray to him for his blessings.

Vinod Kumar Vishwakarma

TH-2983_156122010

Some of the findings of this thesis have been communicated / published in international journals as given below:

1. **V. K. Vishwakarma**, S. Nath, M. Gupta, D. K. Dubey, S. S. Swayamprabha, J.-H. Jou, S. K. Pal, A. S. Achalkumar, Room-temperature columnar liquid crystalline materials based on pyrazino [2, 3-g] quinoxaline for bright green organic light-emitting diodes, *ACS Appl. Electron. Mater.*, 2019, **1**, 1959.
2. **V. K. Vishwakarma**, V. Adupa, K. A. Reddy, A. S. Achalkumar, Experimental and theoretical investigations of acid sensing properties of pyrazino [2, 3-g] quinoxaline derivatives, *J. Mol. Struct.*, 2021, **1225**, 129120.
3. **V. K. Vishwakarma,** M. R. Nagar, N. Lhouvum, J.-H., Jou, A. S. Achalkumar, A New Class of Solution Processable Pyrazino[2,3-g]quinoxaline Carbazole Derivative Based on D-A-D Architecture for Achieving High EQE in Yellow and White OLEDs, *Adv. Optical Mater.*, 2022, 2200241.
4. **V. K. Vishwakarma**, M. Roy, R. Singh, R. Paily, D. S. S. Rao, S. K. Prasad**,** A. S. Achalkumar, Liquid Crystalline Naphthalene and Perylene Bisimides with D_2-π_2-A Architecture for High Mobility Organic Field-Effect Transistors (OFETs), manuscript under communication.

Articles that are not included in this thesis:

1. **V. K. Vishwakarma**, A. S., Achalkumar, Structure-Property Relationships of Quinoxaline Based Liquid Crystals, Soft Matter, 2021, **17**, 8221.
2. S. Turlapati, B. N. Sunil, **V. K.**, **Vishwakarma,** A. S., Achalkumar, G. Hegde, Influence of lateral methyl/chloro substituents on the liquid crystalline and photoswitching behavior of bent-core mesogens bearing azobenzene wings: synthesis and characterization. *New J. Chem.*, 2020, **44**, 5731.
3. Vinay S. Sharma, **V. K.**, **Vishwakarma,** Pranav S. Shrivastav, A. S. Achalkumar, Anuj S. Sharma, Priyanka A. Shah, Calixarene functionalized Supramolecular Liquid Crystals and their Diverse Applications, *ACS Omega*, 2022, **7**, 50, 45752–45796.

Papers presented in National/International conferences: (Oral/Poster)

1. **Poster presentation:** "Naphthalimide based metallo-mesogens", **V. K. Vishwakarma** and A. S. Achalkumar, presented at Frontiers in Chemical Sciences (FICS 2016) at Department of Chemistry, IIT Guwahati, India during 8-10 December, **2016**.
2. **Poster presentation:** "1,3,4 thiadiazole bent core mesogens", **V. K. Vishwakarma**, B. Pradhan and A. S. Achalkumar, presented at National Conference in Liquid Crystals (24th NCLC 2017) at Department of Chemical Sciences, IISER Mohali, India during 11-13 October, **2017**.
3. **Poster presentation:** "Columnar liquid crystalline self-assembly of Pyrazino[2,3-g]quinoxaline derivatives: Acidochromism and OLED applications" **V. K.**

TH-2983_156122010

Vishwakarma, D. K. Dubey and A. S. Achalkumar, presented at National Conference in Liquid Crystals (25th NCLC 2018) at Centre of Materials Sciences, University of Allahabad, India during 19-21 December, **2018**.

4. **Oral presentation:** "Room Temperature Columnar Liquid Crystalline Materials based on Pyrazino[2,3-g]quinoxaline for Bright Green OLEDs", **V. K. Vishwakarma**, S. Nath, M. Gupta, D. K. Dubey, S. S. Swayamprabha, J.-H. Jou, S. K. Pal and A. S. Achalkumar, presented at National Conference in Liquid Crystals (26th NCLC 2019) at Department of Applied Sciences, Chitkara University, Punjab, India during 21-23 October, **2019**.
5. **Poster presentation:** "Room Temperature Columnar Self-assembly, Acidochromism and OLED applications of Pyrazino[2,3-g]quinoxaline derivatives" **V. K. Vishwakarma**, and A. S. Achalkumar, presented at *CEMS International Symposium on Supramolecular Chemistry & Functional Materials* at Ito Hall, Hongo Campus, The University of Tokyo, Japan during 08-09 December, **2019**.
6. **Poster presentation:** "Experimental and theoretical investigations of acid sensing properties of Columnar Liquid Crystalline Pyrazino[2,3-g]quinoxaline derivative", **V. K. Vishwakarma**, V. Adupa, K. A. Reddy and A. S. Achalkumar (This paper was adjudged as the 'Best paper presentation' by a research student in 27th National Conference on Liquid Crystals (NCLC 2020) held online mode at Amity University Uttar Pradesh, Noida during 21-23 December **2020** and won '**Deewan Jawahar Nair**' award).
7. **Poster presentation:** "New class of Donor-Acceptor-Donor (D-A-D) based Pyrazino[2,3-g]quinoxaline derivatives" **V. K. Vishwakarma**, and A. S. Achalkumar, presented at the International Webinar on Liquid Crystalline Materials: Chemistry, Physics and Biological Applications (RPLCM-2021) held at Department of Chemistry, Assam University, Silchar, India during 4-5th October, **2021**.
8. **Oral presentation: "**A New Class of Pyrazino[2,3-g]quinoxaline Carbazole Derivatives based on D-A-D Architecture with High Efficiency in Yellow OLEDs", **V. K. Vishwakarma**, N. Lhouvum, M. R. Nagar, J.-H. Jou, and A. S. Achalkumar, presented at Research and Industrial Conclave (RIC)- 2022 at IIT Guwahati, Assam, India during 20-23 January, **2022**.
9. **Oral presentation: "**New Class of Pyrazino[2,3-g]quinoxaline Derivatives Based on Donor-Acceptor-Donor (D-A-D) Architectures", **V. K. Vishwakarma** and A. S. Achalkumar, presented at 28th International Liquid Crystal Conference (ILCC) at NOVA School of Science and Technology, Lisbon, Portugal, during 24th to 29th July **2022**.

TH-2983_156122010

CONTENTS

TH-2983_156122010

TH-2983_156122010

List of abbreviations used in the text

anhyd	anhydrous
bs	broad singlet
Cr	crystal
Col	columnar
d	doublet
DCM	dichloro methane
dd	doublet of a doublet
equiv	equivalents
Et	ethyl
Et_3N	triethyl amine
EtOAc	ethyl acetate
g	gram
h	hour
Hz	hertz
HRMS	high resolution mass spectrometry
I	isotropic
IR	infrared
kJ	kilojoules
J	coupling constant
K	kelvin
LC	liquid crystal
m	multiplet
MHz	megahertz
min	minutes
mmol	milli mole(s)

TH-2983_156122010

n	normal
N	nematic
NMR	Nuclear magnetic resonance
q	quartet
R_f	retention factor
rt	room temperature
s	singlet
t	triplet
THF	tetrahydrofuran
TMS	tetramethyl silane
TLC	thin layer chromatography
UV	ultra violet
XRD	X-ray diffraction

TH-2983_156122010

GENERAL REMARKS

All commercially obtained chemicals were used as received. As required the solvents were dried as per the standard protocols. Silica gel or neutral alumina used as stationery phase for column chromatography. Aluminium sheets coated with silica gel were used for thin layer chromatography (TLC) to monitor the reactions and column purifications. Infrared spectra were measured on a Perkin Elmer IR spectrometer at room temperature by preparing the KBr pellet and also used PerkinElmer Universal ATR Two FT-IR spectrometer without using the KBr pellet. ^{1}H and ^{13}C NMR spectra were recorded using Bruker 400/600 MHz NMR spectrometer. Mass spectrometry was carried out using MALDI-TOF mass spectrometer (Bruker Autoflex Speed MALDI TOF/TOF Mass Spectrometer) or High Resolution Mass Spectrometer. Polarizing optical microscope (POM) (Nikon Eclipse LV100POL) in conjunction with a controllable hot stage (Mettler Toledo FP90 and HCS302-Mk2000) was used for the characterization of mesogens. The phase transitions, associated enthalpy changes were obtained by differential scanning calorimeter (DSC) (Mettler Toledo DSC1) The transition temperatures obtained from calorimetric measurements of the heating and cooling cycles at a rate of 5 °C/min are tabulated. X-ray diffraction (XRD) studies were carried out using image plate and a detector. This setup had Cu Kα ($\lambda = 0.15418$ nm) radiation from a source (GeniX3D, Xenocs and Rigaku, Micromax-007HF) operating at 50 kV and 0.6 mA in conjunction with a multilayer mirror was used to irradiate the sample. Powder and thin-film in glass slides and glass capillaries containing the sample were used for the measurements. The Variable-temperature XRD studies were also carried out with samples filled in Lindemann capillaries. The apparatus essentially involved a high-resolution X-ray powder diffractometer (PANalytical X'Pert PRO) with a high-resolution fast detector PIXCEL. Thermogravimetric analysis (TGA) was accomplished with a thermogravimetric analyzer (Mettler Toledo, model TG/SDTA 851 e and Netzsch, STA449F3A00) under a nitrogen flow at a heating rate of 10 °C/min. Perkin-Elmer Lambda 750/Agilent Cary series, UV/VIS/NIR spectrometer was used to obtain UV-Vis spectra, while Fluoromax-4 fluorescence spectrophotometer and Perkin Elmer LS 50B spectrometer were used to obtain emission spectra in solution state and solid thin film state respectively. Steady State anisotropy experiment was performed on Horiba Scientific Fluoromax spectrofluorometer 4. Time-resolved lifetime measurements were done on time correlated single photon counter from Horiba Jobin Yvon (excitation by 440 nm laser diode). Cyclic Voltammetry

TH-2983_156122010

(CV) studies were carried out using a Versa Stat 3 (Princeton Applied Research) and Metrohm (Autolab PGSTAT204) instruments. Atomic Force microscopy (AFM) images were obtained for the spin-coated films using an Oxford (Cypher) instrument. Field emission scanning electron microscope (FESEM) of Zeiss (model= Sigma-300) instrument operated at 3 kV was used to investigate the surface morphology. The computational studies were performed by using the GaussView 5.0.9 and Avogadro software. The selection of suitable hosts for the fabrication of host-guest OLEDs was carried out by the use of the comprehensive electronic simulation tool SETFOS 4.6.

भारतीय प्रौद्योगिकी संस्थान गुवाहाटी • Indian Institute of Technology Guwahati •

TH-2983_156122010

PREFACE

Liquid crystals (LCs) are unique functional soft materials combining both order and mobility on molecular, supramolecular and macroscopic levels. The shape anisotropic molecules which exhibit this unique behavior are also known as mesogens. They can be organic (forming thermotropic and lyotropic phases), inorganic (metal oxides forming lyotropic phases) or organometallic (metallomesogens) in nature. Conventionally, the anisometric molecules employed to stabilize thermotropic LC phases are either rod-like (calamitic) or disc-like (discotic). Calamitics form the backbone of the well-established flat panel display industry. Discotic LCs also have made notable progress in recent years, both from scientific and application viewpoints and slowly they are finding a foothold in the main stream of organic electronics. It is also known that LC behavior is realizable with molecules differing in their shape from conventional LCs. The general feature of majority of such materials is the molecular structural contrast with in the molecule *i.e.*, these molecules are made up of chemically different molecular parts that are incompatible with each other. Some of the important examples of non-conventional systems are oligomers, polycatenars, bent-core molecules, polyhydroxy amphiphiles, octahedral complexes, star-shaped molecules, rod-coil molecules and dendrimers. In the case of non-conventional LCs, the main driving force for the self-assembly of these molecules to form liquid-crystalline (LC) phases is based on the nano-segregation of chemically or physically different building blocks and the tendency to efficiently fill the space in condensed state.

This thesis entitled *"Design, Synthesis and Investigations of Liquid Crystalline Organic Semiconductors"* have been divided into four chapters. Contents included in this thesis are based on the research output gained from my research programme. Chapter 1 is an introductory chapter to liquid crystals including discotic liquid crystals and their applications in photovoltaic devices, OLEDs, OFETs and sensing applications. Chapter 2 is divided into two parts, Chapter 2a deals with the synthesis and mesomorphic behavior of five new pyrazino[2,3-g]quinoxaline (PQ) derivatives and One of the columnar liquid crystalline materials (**PQ10**) was used in the fabrication of bright green OLEDs. Chapter 2b describes the sensing ability of the pyrazino[2,3-g]quinoxaline derivative (**PQ8**) to volatile trifluoroacetic acid in trace amounts (in parts per billion levels). Chapter 3 explains new design strategies for the synthesis of donor-acceptor-donor (D-A-D) architecture pyrazino[2,3-g]quinoxaline carbazole derivatives with terminal straight and branch alkyl chains. Compound **PQC-12b** was used in OLEDs either as a sole emissive material or as a

TH-2983_156122010

guest in different host materials. Yellow and white organic light-emitting diodes with high external quantum efficiency were achieved. Chapter 4 describes the synthesis of naphthalene and perylene bisimide $D_2\pi_2A$ architecture-based imidazole liquid crystalline derivatives containing ten flexible chains for solution-processable organic field effect transistors (OFETs) device applications. One of both naphthalene and perylene bisimide derivatives (**NI-12** and **PI-12**) were used for the fabrication of OFET devices to measure conductivity.

TH-2983_156122010

Chapter-1

Introduction to Liquid Crystals

TH-2983_156122010

1.1. Introduction to liquid crystals

From the initial days of science, it has been recognized that under appropriate conditions of temperature and pressure, the matter may exist in three possible states, *i.e.* solid, liquid and gas. In the case of crystalline solids, atoms or molecules are fixed in their respective crystal lattices with their positional and orientational order. In the amorphous solid state, the molecules have no long-range orientational order, similar to a frozen liquid state. In the liquid state, the molecules have neither shown positional nor orientational order. They are free to flow and are randomly oriented.

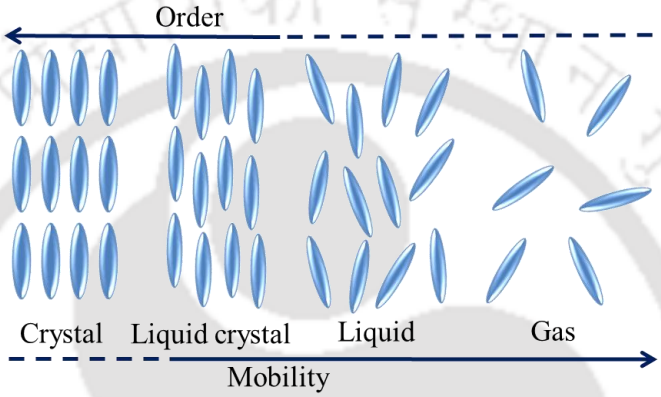

Figure 1.1. Schematic representation of molecular order and mobility in the crystal, liquid crystal, liquid and gas.

Liquid crystals (LC) are a special state of matter that exists between solids and liquids with an intermediate order and mobility (Figure 1.1), this state of matter is also known as 'mesophase' (mesos means "middle") and such molecules that exhibit liquid crystallinity are known as 'mesogens'. In this state, the molecules still have orientational and sometimes positional order, within the mesophase. Liquid-crystalline molecules possess a highly anisotropic shape, which gives rise to the ordering of neighboring molecules in preferred orientations. It is perhaps, convenient to consider a liquid crystal as an ordered liquid, which is, therefore, an anisotropic fluid stabilized by anisotropic dispersion forces resulting from the association of anisotropic molecules. Thus, the liquid crystals/mesogens may be defined as 'orientationally ordered' liquids or 'positionally disordered' crystals.[1] These are the unique soft functional materials having combined properties of both the liquid state (mobility and fluidity) and crystalline state (order, optical birefringence and dielectric anisotropy) on a molecular, supramolecular and macroscopic level. They are extremely sensitive to many external stimuli such as temperature, pressure, light, electric field and magnetic field.[2-9]

TH-2983_156122010

1.2. A brief history of liquid crystals

The field of liquid crystals took birth in the year 1888, when a botanist cum chemist, F. Reinitzer (1857-1927) for the first time accidentally observed the "double melting" behavior of the cholesteryl benzoate (**1.1**) compound.[10] It showed two melting points, one at 145.5 °C, where it first melted to a cloudy liquid and then at 178.5 °C, where it turned to form a clear liquid (Figure 1.2). In the beginning, Reinitzer ascribed this phenomenon to the presence of impurities in the material, but he observed similar behavior upon cooling the clear liquid. This behavior was further examined by the German physicist and well-known crystallographer; Otto Lehmann (1855-1922), who was an expert in polarizing optical microscopy.[11]

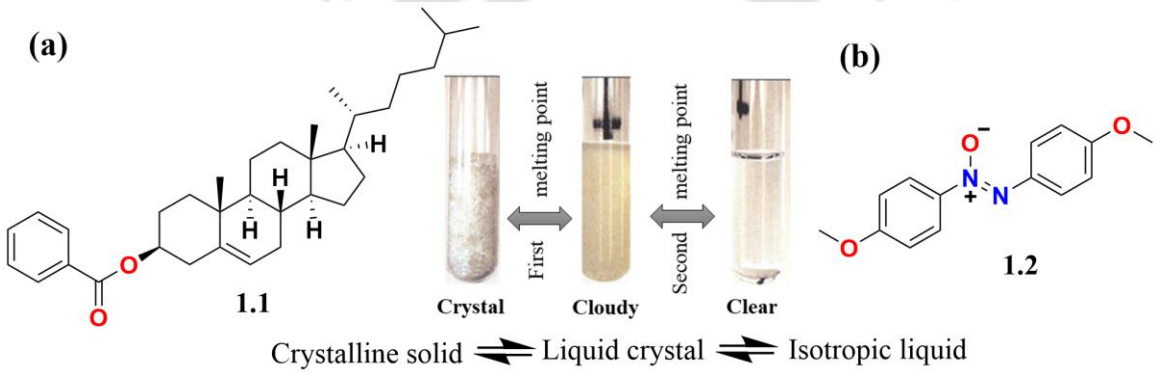

Figure 1.2. (a) Structure of cholesteryl benzoate (**1.1**) and its melting behavior; (b) Structure of para-azoxyanisole (**1.2**).

Within the same year Ludwig Gattermann (1860-1920), an assistant professor at the University of Heidelberg, reported a similar behavior for *p*-azoxyanisole compound (**1.2**) (Figure 1.2b). Gattermann reported a cloudy liquid phase at 116 °C, which disappears at 134 °C. The temperature at which the cloudiness disappeared, is known as the clearing point.[12] Daniel Vorländer (1867-1941) and his co-workers synthesized approx. 1100 LCs and stabilized the structural property relationship of various LCs.[13] He also suggested that the LC phase is mainly exhibited by linear-shaped molecules, which are nowadays known as calamitic LCs.[14] Later, G. W. Gray (1926-2013), who was an emeritus professor of Organic Chemistry at the University of Hull, in 1972 synthesized the well-known family of cyanobiphenyl mesogens, which were the first class of compounds to exhibit a stable nematic phase at room temperature and 4-*n*-pentyl-4′-cynobiphenyl (5CB) was the best among them (Figure 1.3a).[15] From the following general molecular design (Fig.1.3a), several rod-like mesogens were prepared by different research groups in the subsequent years. These rod-like or calamitic mesogens have shown high positive dielectric anisotropy

TH-2983_156122010

and found to be useful in liquid crystal display (LCD) technology.[16]

In 1977, S. Chandrasekhar (1930-2004) and his colleagues accounted that not only calamitic molecules; but also compounds with disc-like (discotic) molecular shapes are capable to exhibit mesophases as shown in Figure 1.3b.[17] Currently more than 3000 discotic liquid crystals (DLCs) are known in the literature.

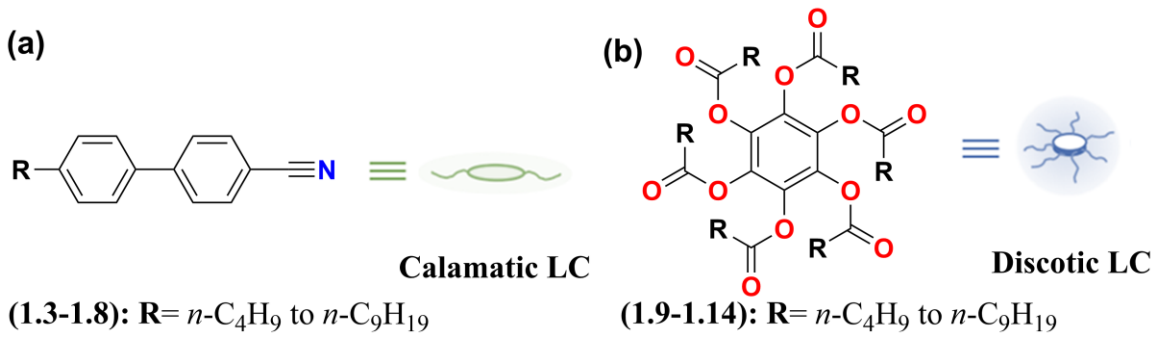

Figure 1.3. Typical examples of conventional LCs (a) Self-assembly of a calamitic (rod-like) LCs 4-alkyl-4'-cyanobiphenyl (**1.3-1.8**) and (b) discotic (disc-like) LCs benzene-hexa-*n*-alkanoates (**1.9-1.14**).

The bent-core (Banana shaped) mesogens were reported by Niori *et al.* in 1996. Typically, their molecular structure can be regarded to have three units; an angular central unit, two linear rigid cores and terminal chains.[18] The discovery of ferroelectricity in non-chiral banana-shaped molecules has led to a very extensive research activity in this field. In the past decades, numerous new mesogenic compounds have been synthesized. It is difficult to imagine a world without liquid crystals; because they are nowadays used in the most diverse applications of our daily life like; TV screens, spatial light modulators, wristwatches, laptops, temperature sensors and many more.

1.3. Classification of liquid crystals

Liquid crystals can be classified in various ways. Firstly, on the basis of the molar mass of the constituent molecules one can categorize these materials into low molar mass (monomeric, dimeric and oligomeric liquid crystals) and high molar mass (main, side and mixed chain polymeric liquid crystals); secondly, depending on how the liquid crystalline phase has been obtained *i.e.* on the type of the external stimuli, either by the change in temperature (thermotropic) or by the action of solvent (lyotropic).

TH-2983_156122010

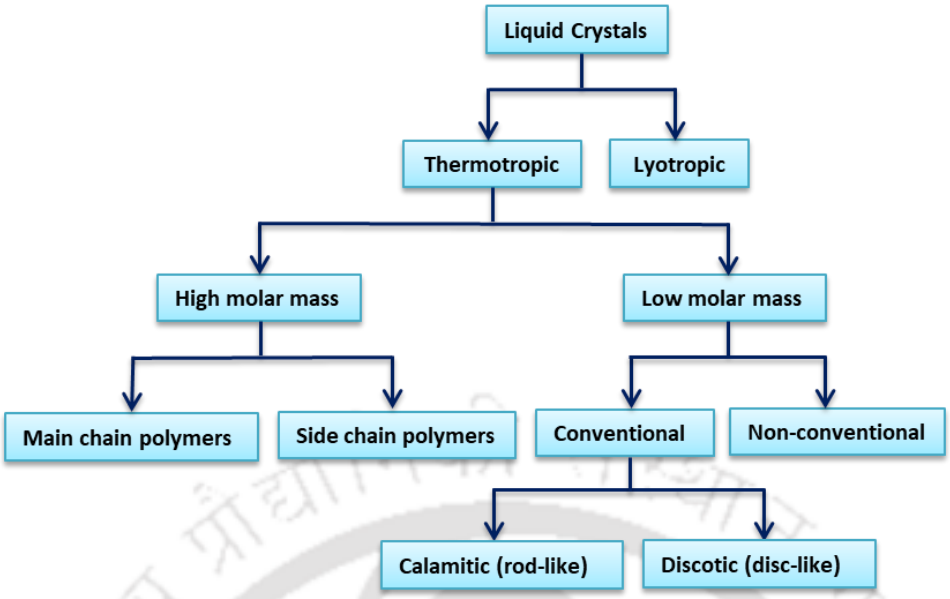

Figure 1.4. Schematic representation of the general classification of liquid crystals.

Generally, a thermotropic LC is made up of two components, usually a rigid core and flexible chain/s connected to this core by different linking groups. However, the LC self-assembly is sensitive even to the type of linking group between these two units. The general template of discotic LCs and various rigid discotic cores (**1.15**-**1.35**) are shown in Figures 1.5 and 1.6 respectively. Depending upon the chemical nature, the constituent molecules can be organic, inorganic or organometallic. Based on the geometrical shape of the core, these LCs can be further classified into conventional LCs and non-conventional LCs. Conventional LCs mainly include calamitic (rod-like) and discotic (disc-like) LCs, while non-conventional LCs include a wide variety of anisotropic molecular designs like oligomeric,[18] phasmidic or polycatenars (dumbbell-shaped or a hybrid structure of a rod and disc-like structure),[19] bananas (bent-cores),[20] star-shaped molecules,[21] dendrimeric,[22] and rod-coil types LCs.[23] The molecular shapes and structures of various non-conventional LCs (**1.36**-**1.41**) are shown in Figures 1.7 and 1.8.

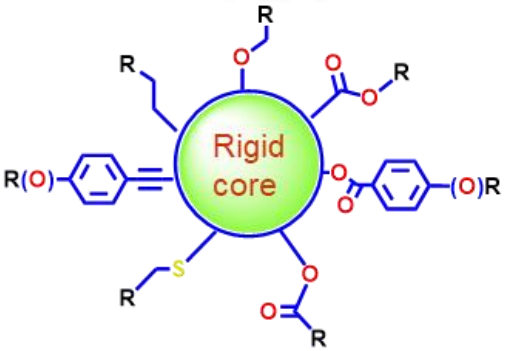

Figure 1.5. General template of discotic liquid crystals.

TH-2983_156122010

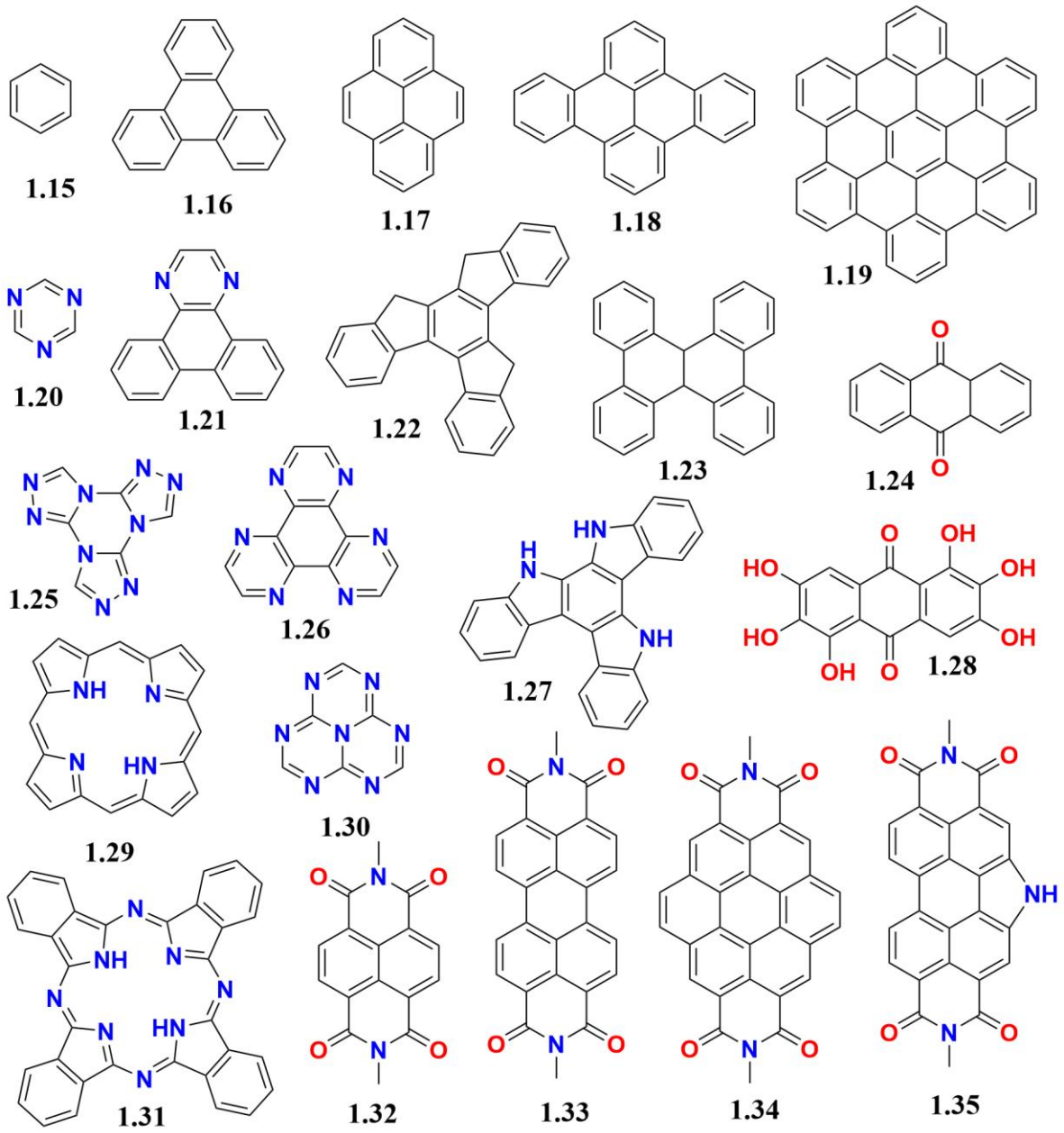

Figure 1.6. Examples of various central cores known for discotic liquid crystals; benzene (**1.15**), triphenylene (**1.16**), pyrene (**1.17**), dibenzonapthacene (**1.18**), hexabenzocoronene (**1.19**) triazine (**1.20**), diazatriphenylene (**1.22**), truxene (**1.22**), dibenzo[g,p]chrysene (**1.23**), anthraquinone (**1.24**), tristriazolotriazine (**1.25**), hexaazatriphenylene (**1.26**), triazatruxene (**1.27**), rufigallol (**1.28**), porphyrin (**1.29**), heptazine (**1.30**), phthalocyanine (**1.31**), naphthalene diimide (**1.32**), perylene diimide (**1.33**), coronene diimide (**1.34**), *N*-annulated-perylene diimide (**1.35**).

TH-2983_156122010

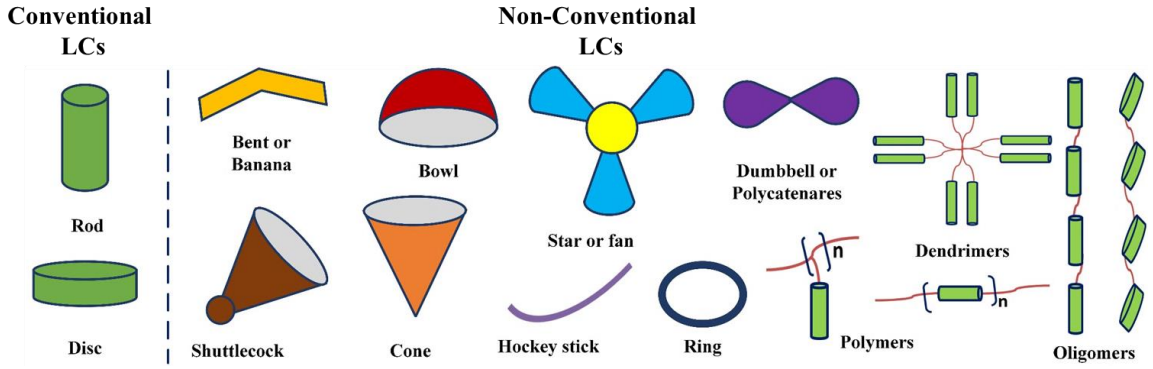

Figure 1.7. Schematic showing the conventional and non-conventional molecular shapes used for the stabilization of LC phases.

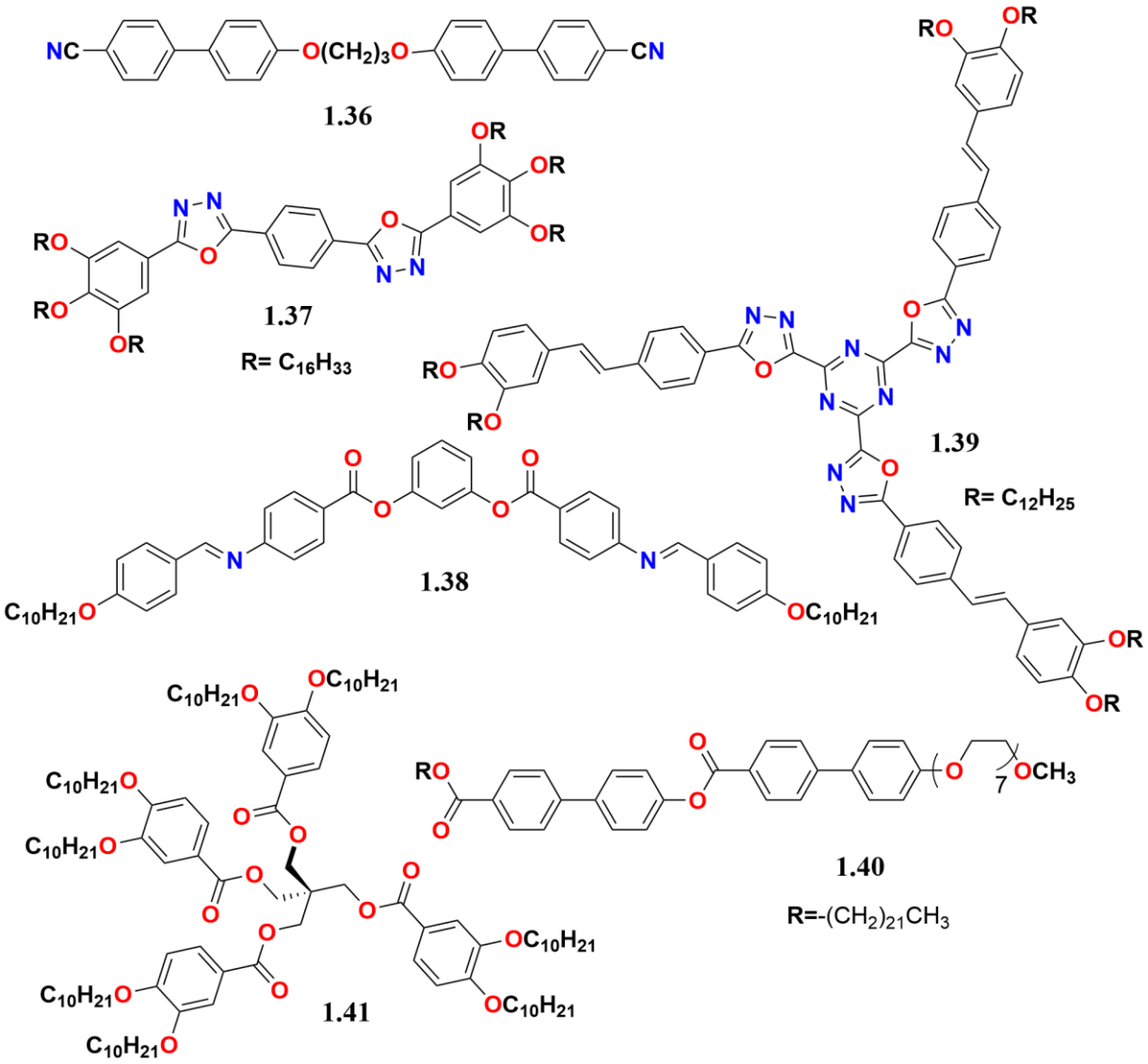

Figure 1.8. Molecular structures of different types of non-conventional LCs (**1.36**-**1.41**).

TH-2983_156122010

1.4. Structures of the liquid crystalline phases

The simplest mesophase where the mesogens are packed with their long-range orientational order and without any positional order is termed nematic (N) LCs, while the mesophase where mesogens are packed with both positional and orientational order is termed smectic (Sm) LCs. Rod-like or calamitic molecules stabilize N and Sm mesophases. There are several subclasses in Sm phases based on the arrangement of molecules in each layer.[24] Smectic LCs, mainly SmA phase has a great potential to be utilized as a charge carrier material due to the layered structure and strong face-to-face π-π interaction. Generally, the disc-like molecules exhibit the nematic phase *i.e.* discotic nematic (N_d), where the individual discs are arranged only with long-range orientational order without any positional order.

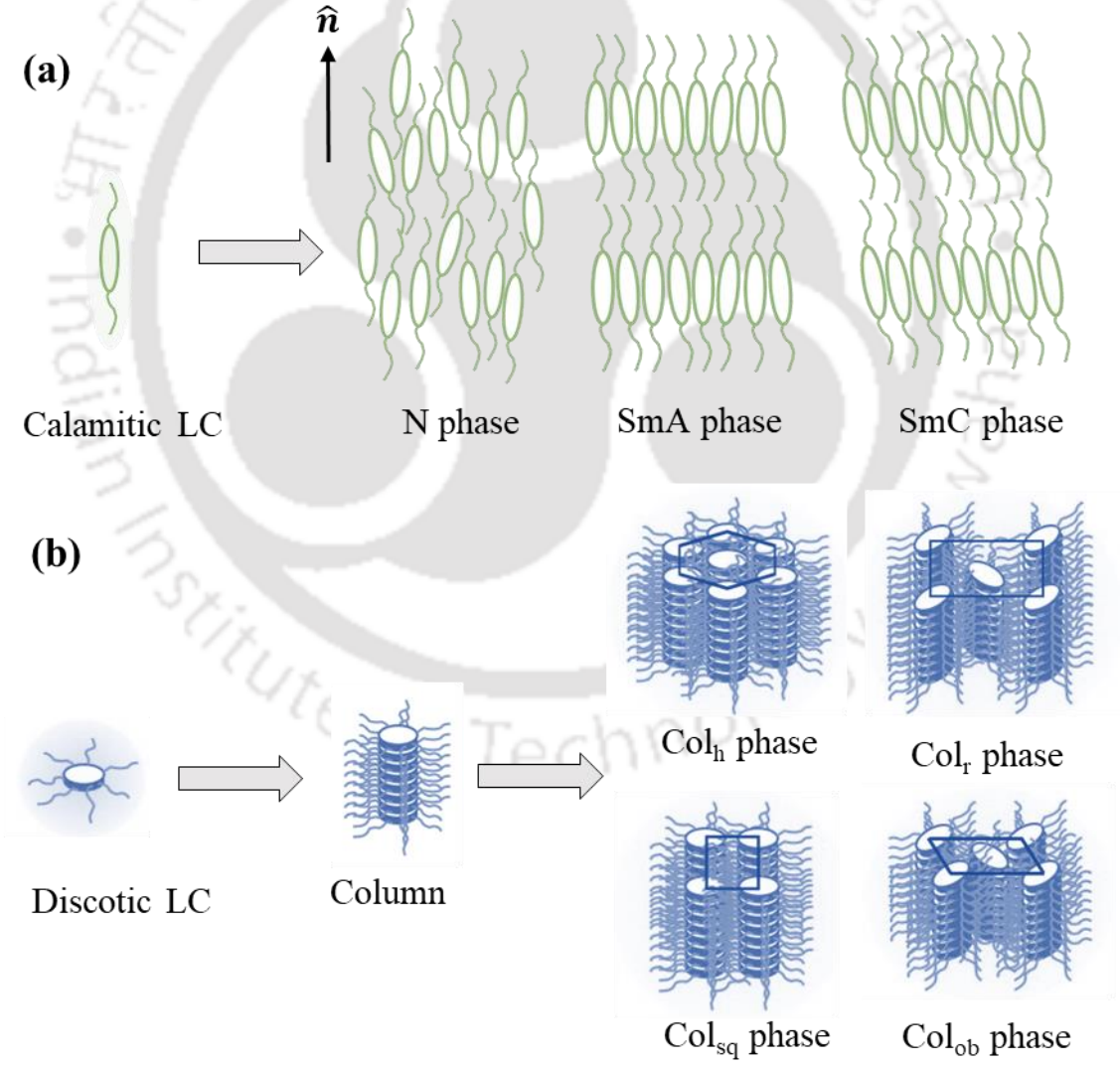

Figure 1.9. Schematic showing the mesophases stabilized by conventional liquid crystals (a) calamitic LC phases; (b) discotic LC phases.

TH-2983_156122010

Similar to the Sm phases of calamitic molecules, discotic molecules also can pack with both orientational and positional order leading to the formation of one-dimensional (1D) columns of indefinite length, which in turn self-organize into different two-dimensional (2D) lattices to form columnar (Col) phases (Figure 1.9). Based on the lattice in which the individual columns are organized they are further classified into columnar hexagonal (Col_h), columnar rectangular (Col_r), columnar oblique (Col_{ob}), columnar square (Col_{sq}), columnar plastic (Col_p), columnar lamellar (Col_L) and helical phase (H phase).[25] Further, based on the arrangement of discs within the column they may be further classified as 'ordered' and 'disordered'. Cubic phases are commonly found in lyotropic LC systems but some discotic phthalocyanine derivatives also exhibit cubic phases.[26] Liquid crystal molecules will self-assemble into different mesophases either by arranging parallel to one another or by the nano-segregation of their incompatible molecular subunits.[24a] The LC self-assembly generally follows the association principle of the condensed soft matter by minimizing the excluded volume and by maximizing the interaction energy. Further secondary interactions like Van der Waals, dipolar, quadrupolar, charge transfer, π-π interaction, metal coordination, ionic and hydrogen bonding also contribute to different extents in promoting the LC self-assembly.

1.5. Identification and characterization of mesophase morphology

There are three essential techniques for the identification and characterization of mesophase morphologies: polarized optical microscopy (POM), differential scanning calorimetry (DSC) and X-ray diffraction (XRD). Utilization of one or more of these three methods of identification and characterization can lead to accurate models of the mesophase morphology and thermal behavior of the materials.

1.5.1. Polarizing optical microscopy

Polarizing optical microscopy (POM) is based on the fact that a liquid crystalline phase is birefringent, which means that when the ray of light passes through the mesophase, it gets split into two rays leading to their interference depending on the polarization of the light as shown in Figure 1.10a. The configuration of a hot-stage equipped polarizing optical microscope is illustrated in Figure 1.10b. POM is the most important technique used to characterize the mesomorphism of a compound. The sample (<1 mg) is placed between a glass slide and cover slip and then placed on a suitably controlled hot stage through which there is an optical path. The hot stage is mounted on the working stage of the microscope.

TH-2983_156122010

The technique makes use of the birefringence of mesophase, wherein the plane polarized light incident on the sample comes through the second polarizer placed at 90° to the first polarizer. The second polarizer is placed between the sample and the objective. Thus, the interference of the two refracted ray's results in the characteristic interference patterns for a particular mesophase (Figure 1.11a-b). This contrasts with the situation where the material is in the isotropic state (in this case liquid) and thus the sample appears black between the cross polarizer. This is due to the isotropic nature of the sample, which will not split the incident light into ordinary ray and extraordinary rays. The light does not pass through the second polarizer and hence appears dark. These textures are diagnostic of a particular mesophase and are best developed when they are obtained on cooling the sample from isotropic state.

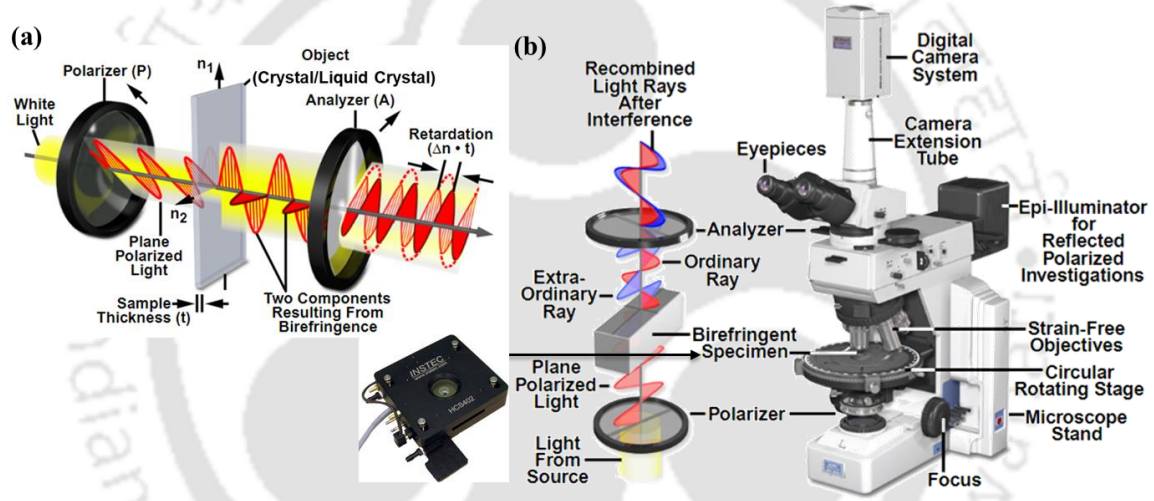

Figure 1.10. (a) Birefringent rays from crystals/liquid crystals between crossed polarizers; (b) the basic configuration of a programmable hot-stage equipped polarizing optical microscope (POM) ©Nikon Corporation.[27]

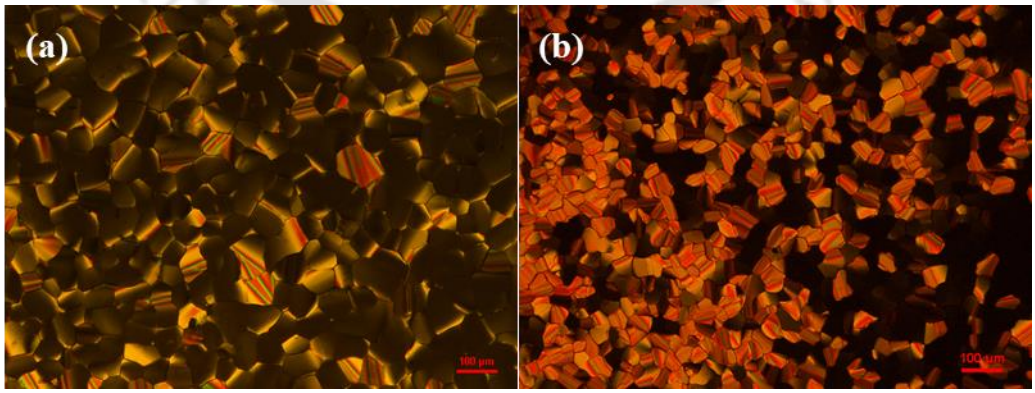

Figure 1.11. Different textures of columnar mesophases (a, b).

TH-2983_156122010

1.5.2. Differential scanning calorimetry

In the DSC experiment, the change in the enthalpy accompanying a phase transition of the sample is recorded as a function of the temperature on both heating and cooling scans conducted at a particular rate. Information about the phase transition may, therefore, be derived from the relative magnitudes of the transition enthalpies, which are obviously much larger for the crystal to mesophase than those found for mesophase-mesophase and mesophase-isotropic liquid transitions. While such information is quite useful, it does not allow making generalizations and the corresponding entropy changes are more useful.

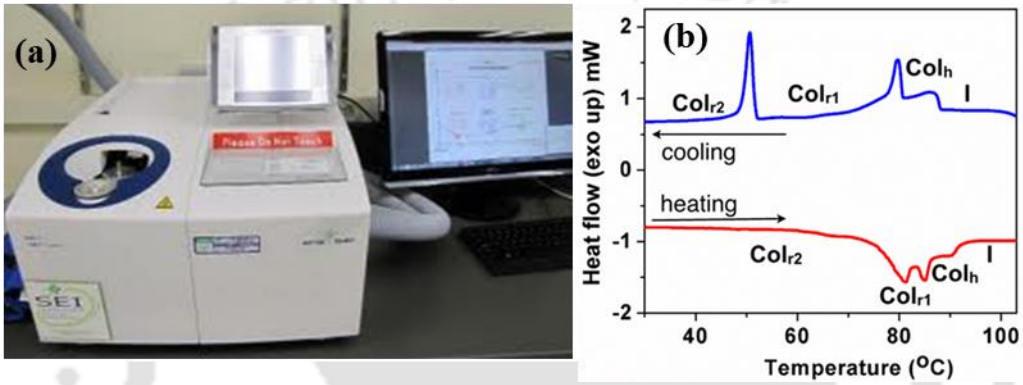

Figure 1.12. (a) Instrument for differential scanning calorimeter (b) DSC curve of a mesogenic compound showing phase (columnar rectangular and hexagonal phases) transitions.

This technique is, therefore, strictly complementary to optical microscopy, as all changes in optical texture do not necessarily correspond to a change in mesophase type, and all phase changes do not always lead to an easily identifiable change in texture. Therefore, DSC traces should always be compared with the results of the optical study to be sure of proper correspondence. DSC instrument and a DSC thermogram of a LC sample are shown in Figure 1.12.

1.5.3. X-ray diffraction analysis

When it comes to structural analysis, X-ray diffractometry is a potent technique. Powder X-ray diffractometry can provide some information about the nature of the phases, but it is impossible to distinguish between reflections caused by inter-columnar and intra-columnar order. As a result, macroscopically orientated samples appropriate for structural examination must be extruded. Wide angle X-ray scattering (WAXS) measurements recorded with the vertical orientation of filaments perpendicular with respect to the incident X-ray beam provide two-dimensional diffractograms with information pertaining to the

TH-2983_156122010

stacking within columns and the 2D packing of those columns, partitioned along the vertical and horizontal directions, respectively. A schematic experimental setup diagram of XRD is shown in Figure 1.13a and the XRD profile is shown in Figure 1.13b. On the top left shows, the peak corresponds to core-core separation and the inset on the top right corresponds to the image pattern.

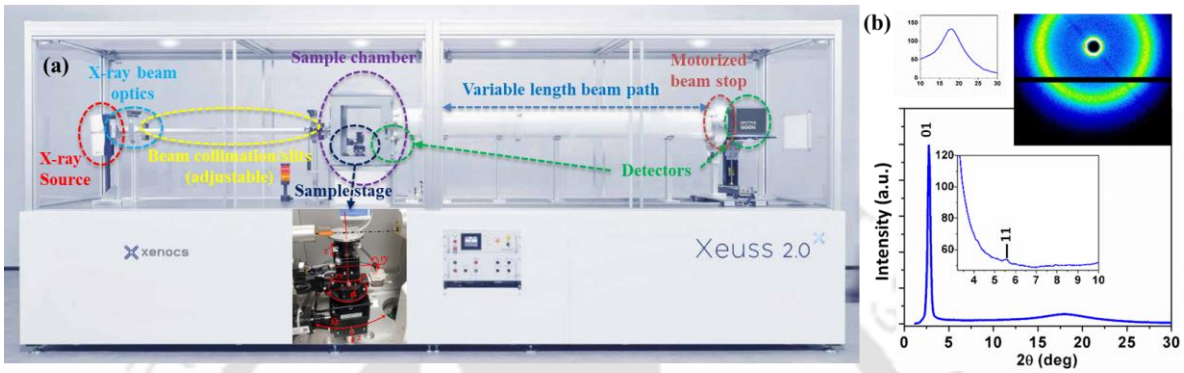

Figure 1.13. (a) A diagram of the experimental setup for SAXS/WAXS Xenocs Xeuss 2.0 instrument reproduced from ©2019-2020 MGML[28]; (b) The XRD plot of a columnar liquid crystalline compound, where the first peak corresponds to the average length of the molecule and second broad peak corresponds to the lateral separation between the molecules (inset on the top left shows the peak corresponding to core-core separation and inset on the top right corresponds to 2D diffraction pattern).

1.5.4. Spectroscopic characterizations

1.5.4.1. UV-visible and fluorescence studies

UV-visible spectroscopy is a non-destructive technique that uses a beam of light that excites the electron in molecules to measure the amount of light absorbed in that compound by providing the absorption spectra. The possible transitions of UV and visible regions of the electronic spectrum are shown in Figure 1.14.[29] The principle of absorption spectroscopy is based on the Beer-Lambert law- $A = \text{Log } I_o / I = \varepsilon c l$; Where I_o = Intensity of the incident light (or the light intensity passing through a reference cell); I = Intensity of light transmitted through the sample solution; ε = molar absorptivity; c = concentration of the solute in mol L^{-1}; l = path length of the sample in cm. Perkin-Elmer Lambda 750/Agilent Cary series, UV/VIS/NIR double beam spectrometers were used to obtain UV-visible spectra in micromolar solution and millimolar solid thin films concentration of the samples.

TH-2983_156122010

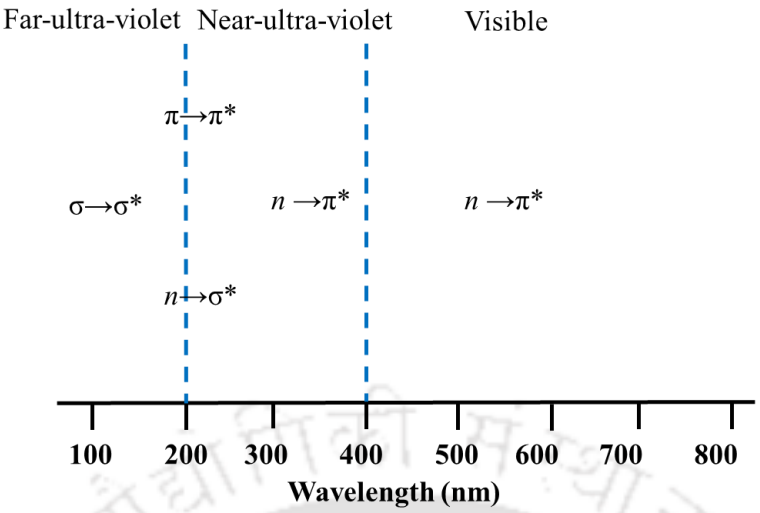

Figure 1.14. The regions of the electronic spectrum and type of possible transitions.

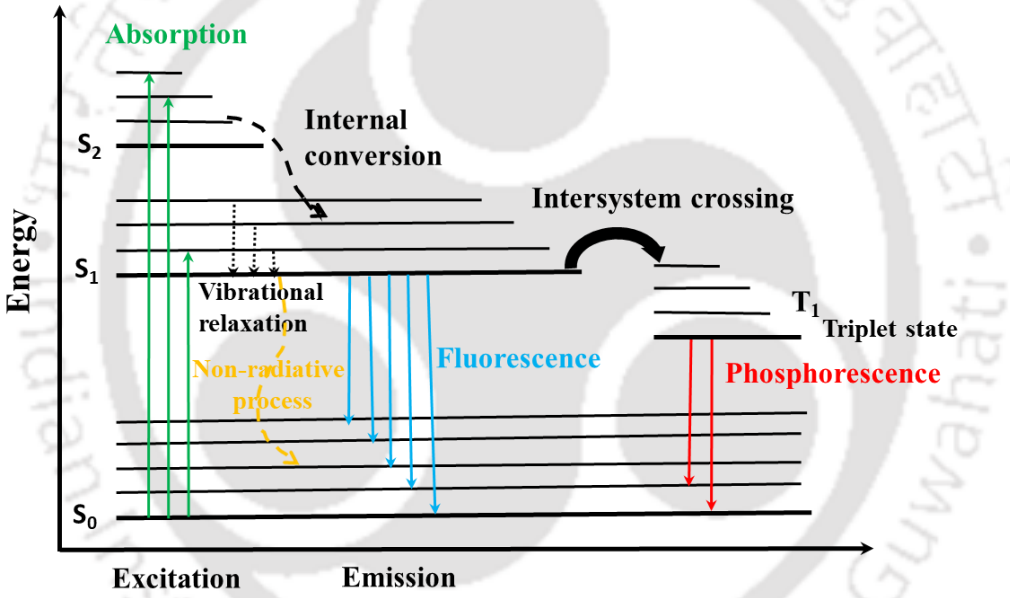

Figure 1.15. Jablonski diagram of fluorescence and phosphorescence.

In fluorescence spectroscopy, electrons upon relaxation from that excited state to the ground state, the molecule releases photons in the form of light through fluorescence emission. Fluorescence is also known as photoluminescence i.e. when light energy, or photons, stimulates the emission of a photon. Chemiluminescence is when chemical energy, stimulates the emission of a photon. Electroluminescence is when electrical energy, stimulates the emission of a photon, such as in some lighting applications. In the case of photoluminescence, light excites an electron to an excited state. The excited state undergoes rapid thermal energy loss to the environment through vibrations, and then a photon is emitted from the lowest-lying singlet

TH-2983_156122010

excited state. This process of photon emission competes with other non-radiative processes including energy transfer and heat loss. Unlike fluorescence, phosphorescence doesn't re-emit the light immediately. Instead, phosphorescence releases light very slowly in the dark due to its spin-forbidden ground transition from a triplet-excited state. When ultraviolet light is shined upon a phosphorescent compound it glows in dark and the compound emits light, creating phosphorescence. The fluorescence and phosphorescence phenomena are shown in the Jablonski diagram Figure 1.15.[30]

1.5.4.2. Relative photoluminescence quantum yield

The fluorescence quantum yield (Q) is a characteristic property of a fluorescent species and is defined as the ratio of photons emitted through fluorescence and the ratio of the photon absorbed by the fluorophore (Equation 1).[31]

$$Q = \frac{\text{Number of photons emitted through fluorescence}}{\text{Number of photons absorbed}} \qquad (1)$$

Q ultimately relates to the efficiency of the pathways leading to the emission of fluorescence (Figure 1.15), providing the probability of the excited state being deactivated by fluorescence rather than by other competing relaxation processes. The absolute method is applicable to both solid and solution phase measurements and the Q can be determined in a single measurement without the need for a reference standard or absorbance data. It is especially useful for samples that absorb and emit in wavelength regions for which there are no reliable quantum yield standards available. The relative comparative method, on the other hand, is the most common way of determining the Q of samples. It relies on the use of well-characterized reference standards, with known Q values and optical properties closely matching the sample of interest. It uses a conventional fluorescence spectrophotometer which detects only a fraction of the light emitted due to a wide range of factors including the refractive index of the solvent, and scattering of light by the sample. Relative values were calculated according to the following equation:

$$Q_S = Q_R \times (m_S / m_R) \times (n_S / n_R)^2$$

Where Q: Quantum yield; m: Slope of the plot of integrated fluorescence intensity *vs* absorbance; n: refractive index. The subscript R refers to the reference fluorophore and

TH-2983_156122010

subscript S refers to the sample under investigation. In order to minimize re-absorption effects, absorbance was kept below 0.15 at the excitation wavelength.[32]

1.5.4.3. Measurement of fluorescence lifetime

Lifetime fluorescence spectroscopy investigates the change in fluorescence over time of a sample when irradiated with UV-visible or near IR light. This decay in fluorescence can be measured over a wide time range: from picoseconds to milliseconds. Fluorescence lifetimes were evaluated utilizing the time-correlated single-photon counting (TCSPC) method in the Edinburgh Instrument Life-Spec II spectrometer. It is a method of using the timing of a pulsed excitation source, like a laser or LED, with the timing of the arrival of single photons on a detector to reconstruct the lifetime decay over many events (repetition of pulses and photons detected).[33] This technique is based on the fact that the probability of detecting a single photon at a time, after an exciting pulse is proportional to the fluorescence intensity at a time. The samples were excited at respective excitation wavelengths keeping the emission wavelength fixed as mentioned earlier using a pulsed diode laser. The fluorescence decays were surveyed by the re-convolution method using the FAST software provided by Edinburgh Instruments.

1.5.5. Surface morphology studies

1.5.5.1. Field emission scanning electron microscope

Field emission scanning electron microscopy (FESEM) is an advanced technology used to capture the microstructure image of the materials. FESEM is typically performed in a high vacuum because gas molecules tend to disturb the electron beam and the emitted secondary and backscattered electrons used for imaging.[34] The morphology of compounds was imaged separately using Gemini 300 FESEM (Carl Zeiss) instrument. Gemini 300 is a high-performance instrument designed for gaining maximum information from the broadest range of samples and high flexibility in imaging and analysis, which can also be future upgradability for any kind of *in situ* application. The uniqueness of this system is imaging at very high resolution (0.8 nm at 15 kV; 1.4 nm at 1 kV), very low to high accelerating voltage (0.02 to 30 kV) and very high magnification range *i.e.* up to 20,00,000x. The samples were prepared by drop-casting (mM) concentration on aluminum-foil wrapped coverslip, then coated with gold (Au) and dried under vacuum before the imaging.

TH-2983_156122010

1.5.5.2. Atomic force microscope

AFM is a high-resolution non-optical imaging technique that operates on the principle of surface sensing using an extremely sharp tip on a micro-machined silicon probe. This tip is used to image a sample by raster scanning across the surface line by line, although the method varies dramatically between distinct operating modes.[35] The compounds were drop-casted on a glass coverslip followed by desiccation prior to acquiring AFM images. Atomic force microscope images are captured with an Oxford Instruments AFM (Cypher S). Cantilevers made of silicon nitride are used having a resonant frequency of ca. 150 to 250 kHz. Images are acquired in non-contact mode. Analysis of the topographic images of the surface is accomplished by using the WSxM v5.0 Develop 6.5 image viewer software.

1.5.6. Cyclic voltammetry

Cyclic voltammetry (CV) is a powerful and popular electrochemical technique commonly employed to investigate the reduction and oxidation processes of molecular species, electronic energy (HOMO-LUMO) levels, which are very important in deciding the energy and electron transfer process as well as the reversibility of a redox process. In the setup of an electrochemical cell, a highly soluble solvent (anhyd dichloromethane); a reference electrode having stable equilibrium potential ($Ag/AgNO_3$), a glassy carbon working electrode, platinum wire as a counter electrode, tetrabutylammonium perchlorate (0.1 M) as a supporting electrolyte were required. A schematic representation of an electrochemical cell and the CV graph is shown in Figure 1.16.[36]

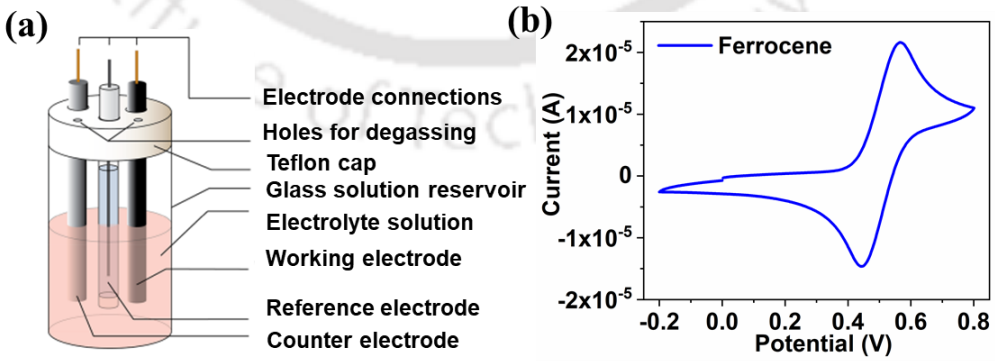

Figure 1.16. Schematic representation of an electrochemical cell (a) reproduced from ref 36. and CV graph (b).

TH-2983_156122010

1.5.7. Theoretical investigations

The density functional theory (DFT) calculations were carried out to obtain the energy-minimized structures, the spatial distribution of HOMO-LUMO levels and to understand the thermally activated delayed fluorescence (TADF) *via* the energy gap between the lowest singlet and lowest triplet states (ΔE_{ST}) and solvatochromism property of the compounds. DFT optimizations of various compounds were accomplished with the exchange-correlation function B3LYP and the basis set 6-31G (d,p) for C, H, N and O atoms incorporating the GaussView 5.0.9 and Avogadro software. The ground state geometry was carried out to optimize by using DFT at B3LYP/6-311G (d,p) level. Time-dependent (TD)-DFT computations were then carried out based on the optimized ground state geometries. In addition to gaseous state, heptane, toluene, chloroform, THF and acetone solvents were also tried using the time-dependent self-consistent field (TD-SCF) method and conductor-like polarizable continuum model (CPCM).[37-39] The corresponding calculations were obtained by the methods of using the GaussView 5.0.9 and Avogadro software.

1.6. Applications of liquid crystals

Numerous potential application of LCs and their technology has become the inseparable part of our daily life *viz.* wristwatches, pocket calculators, computer, laptop and televisions. The LC display industry has grown into a billion-dollar industry due to its ability to have a tunable size, ease of viewing, low power consumption and durability. Col phase offers a one-dimensional pathway for the charge migration where the central aromatic core acts as a conducting unit, while the external peripheral chains act as an insulating mantle (Figure 1.17a). This LC phase is of great importance due to its solution processability, inherent self-assembling and self-healing ability, which in turn enhances the physical properties (optical and conductive) due to the ordered organization. Careful molecular engineering can be employed to tailor these physical properties for enhancing the performance of Col phases as active materials in organic solar cells (OSCs) (Figure 1.17b) (good processability, large absorption coefficient, good charge carrier mobility), as they can be cheaper alternatives in comparison to inorganic counterparts. To meet all these objectives Col phases derived from electron-rich/poor DLCs are the best choice, which mimics the single crystalline organic semiconductors. The “edge on” orientation of the Col

TH-2983_156122010

phases can be translated into the active layers of organic field effect transistors (OFETs) which are the vital components of molecular electronic devices (Figure 1.17c).

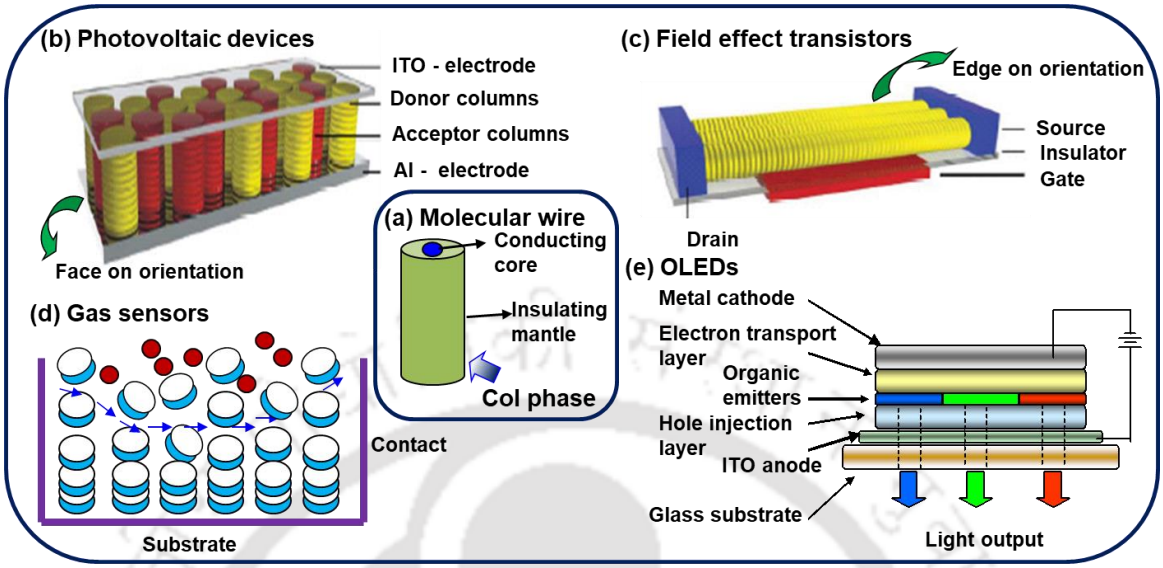

Figure 1.17. Schematic representations of various applications of columnar mesophases (a) molecular wire, (b) photovoltaic devices or solar cells, (c) Field effect transistor, (d) gas sensors and (e) organic light emitting devices (reproduced from ref. 40a with permission from Royal chemical society).

The high mobility for photo-induced charge carriers in the Col phases also makes them worthy of their application in fast and high-resolution xerographic and laser printing as active charge transport layers.[40] Col LCs can be used as a sensitive sensor for both polar and nonpolar molecules because they have a unique conductive surface that can be altered due to the disturbance in the surface (Figure 1.14d).[41]

In recent year's efforts are made to employ Col phases for the construction of organic light emitting diodes (OLEDs) as they can act as good emitting and conductive materials. Col phase with a combination of hole/electron transport and luminescence properties is an ideal material for the fabrication of OLEDs (Figure 1.14e).[42] In an ideal situation, a single-layer device made up of a highly emissive and conductive layer drastically reduces the fabrication cost of large-scale solid state display materials. Researchers are working in this direction to have a solution-processable emissive material with high fluorescence in the aggregated state. However, all the properties cannot be met in a single material. Thus, many a times even after having a solution-processable material with columnar self-assembly with good charge carrier mobility, may not exhibit high electroluminescence. The key reasons why the neat film-based devices displayed poor performances may be the mismatch of hole-injection and electron-injection barriers which

TH-2983_156122010

causes the imbalance of charge carriers in the emissive layer, formation of non-radiative exciton at the hole transport layer and neat-films interface, and concentration quenching due to the aggregation of these compounds in the bulk state.[43-49] Thus to have a working device with the existing dye one need to introduce dopants/host materials to enhance the emission efficiency. In addition, one needs to have a different hole injection layer, electron transport layer, a hole transporting cum electron blocking layer, electron-transporting and hole-blocking layers to have an efficient device.

1.7. Outline of thesis

This thesis describes about simple, short and straightforward synthetic pathways, various characterization and applications of new LC/non-LC organic materials, with their potential applications in acid sensing, optoelectronic devices mainly OLEDs and conductivity applications. Their structure-property relationship was also studied with respect to liquid crystallinity. Few molecules exhibited room temperature discotic columnar LC behavior and were investigated for the abovesaid applications. A brief overview of the chapters is given below:

Chapter 1, the present chapter gives a general introduction to liquid crystals and their various applications.

Chapter 2a addresses the synthesis and characterization of five new pyrazino[2,3-g]quinoxaline (PQ) derivatives which are substituted with eight peripheral flexible tails of varying lengths based on the central pyrazino[2,3-g]quinoxaline central core. The out-of-plane conformation of the phenyl rings made the self-assembly very sensitive to minute variations in the molecular structure. The compounds with very short/branched peripheral chains did not stabilize any liquid crystalline phase, while the medium to long chain homologs exhibited columnar phases. All the compounds exhibited a high molar extinction coefficient and bright greenish yellow emission behavior in solution and solid state. Solvent-dependent aggregation behavior was noticed and they could form long fibers of several micrometers in length. One of the columnar liquid crystalline materials (**PQ10**) was used in the fabrication of OLEDs either as single emissive material or as a dopant at low concentrations in different host materials. Higher efficiency and bright green emission were perceived in the host-guest OLED, with CBP host, at 3 wt % concentration.

Chapter 2b describes the sensing ability of the pyrazino[2,3-g]quinoxaline derivative to volatile trifluoroacetic acid in trace amounts (in parts per billion levels). The

TH-2983_156122010

reversible detection of acid-sensing behavior was visually perceivable in both solution as well as in the drop-casted film on a TLC paper-based strip. Density functional theory studies were carried out to elucidate the mechanism of the sensing behavior.

Chapter 3 explains new design strategies for the synthesis of donor-acceptor-donor pyrazino[2,3-g]quinoxaline carbazole derivatives with straight chain (**PQC-12n)** and branched alkyl (**PQC-12b**) peripheral chains. The electron-donating carbazole moieties that have been placed in the periphery showed a strong electron-donating ability, high molar extinction coefficients and lower band-gap, bright emission behavior in solution and solid-state, along with positive solvatochromism. The non-planar conformation of the carbazole rings with respect to the central pyrazino[2,3-g]quinoxaline unit made the molecules stack one above the other in columns. However, the nonplanar conformation also helped to minimize unfavorable fluorescence quenching in the solid state. These materials have good potential for applications in organic optoelectronic devices. Compound **PQC-12b** was used in OLEDs either as a sole emissive material or as a guest in different host materials. Yellow and white organic light-emitting diodes with high external quantum efficiency were fabricated.

Chapter 4 describes a new donor-π-acceptor-π-donor (D-π-A-π-D) architecture with the detailed synthesis of naphthalene and perylene-based imidazole derivatives containing ten flexible chains for solution processable optoelectronic device (OFETs) applications. These compounds showed a wide range of columnar LC behavior, which was characterized by POM, DSC and detailed XRD studies. These materials showed a very high molar extinction coefficient and low band gap as understood from photophysical studies which were confirmed by cyclic voltammetry and DFT analysis. Both naphthalene and perylene bisimide derivatives (**NI-12** and **PI-12**) were utilized for the fabrication of OFET devices to measure conductivity.

1.8. References

1. B. Wunderlich and J. Grebowicz, *Adv. Polym. Sci*., 1984, **2**, 60/61, 1-59.
2. D. Demus, J. Goodby, G. W. Gray, H. W. Spiess and V. Vill, *Wiley-VCH*, Weinheim, 1998, Vol 1-3.
3. B. Bahadur, *World Scientific*, Singapore, 1990, Vol 1-3.
4. S. Chandrasekhar, *Cambridge University Press*, Cambridge 1992.
5. P. J. Collings and M. Hird, *Taylor & Francis Ltd.*, London, 1997.
6. P. J. Collings and S. J. Patel, *Oxford University Press*, Oxford, 1997.

TH-2983_156122010

7. H., Kelker and W. Hatz, *VCH, Deerfield Beach*, FL, 1980.
8. P. J. Collings, *Princeton University Press*, 1990.
9. P. G. De Gennes and J. Prost, 2nd ed., *Oxford University Press*, New York, 1993.
10. F. Reintzer, *Monatshefte für Chemie.*, 1988, **9**, 421-441.
11. (a) O. Lehman and *Z. Krist.*, 1890, **18**, 464-467; (b) O. Lehmann, *Z. Phys. Chem.*, 1889, **4**, 462-472.
12. L. Gattermann, *Ber. Dtsch. Chem. Ges.*, 1890, **23**, 1218-1228.
13. D. Vorländer, *Kristallinisch-flussige substanzen, Stuttgart*, Enke, 1905.
14. D. Vorländer, *Ber Dtsch Chem Ges.* 1907, **40**, 1970-1972.
15. G. W. Gray, K. J. Harrison, J. A. Nash, and E. P. Raynes, *Electron. Lett.*, 1973 **9,** 616.
16. V. Vill, *Liquid Crystals*, 1998, **24**, 21-24.
17. S. Chandrasekhar, B. K. Sadashiva and K. A. Suresh, *Pramana*, 1977**, 9**, 471-480.
18. (a) H. Kelker and B. Scheurle, *Angew. Chem.*, 1969, **81**, 903-904; (b) C. T. Imrie and G. R. Luckhurst, in *Handbook of liquid crystals, Vol-2B*, Eds., D. Demus, p. 801; (c) C. T. Imrie and P. A. Henderson, *Curr. Opin. Colloid Interface Sci*., 2002, **7**, 298-311; (d) C. T. Imrie in *Structure and Bonding - Liquid crystals, II*, Ed: D. M. P. Mingos, Springer-Verlag, 1999, p.149; (e) N. Tamaoki, *Adv. Mater*., 2001, **13**, 1135-1147; (f) C. V. Yelamaggad, G. Shanker, U. S. Hiremath, and S. K. Prasad, *J. Mater. Chem.*, 2008, **18**, 2927-2949; (g) A. S. Achalkumar, U. S. Hiremath, D. S. Shankar Rao and C. V. Yelamaggad, *Liq. Cryst.*, 2011, **38**, 1563-1589; (h) E. Allard, F. Oswald, B. Donnio, D. Guillon, J.U. Delgado, F. Langa and R. Deschenaux, *Org. Lett*., 2005, **7**, 383 and the references cited there; (i) C. V. Yelamaggad, S. A. Nagamani, U. S. Hiremath, D. S. S. Rao and S. K. Prasad *Liq. Cryst*., 2002, **29**, 231; (j) C. T. Imrie, F. E. Karasz and G. S. Attard, *Macromolecules*, 1993, **26**, 545; (k) C. T. Imrie, P. A. Henderson and J. M. Seddon, *J. Mater. Chem.*, 2004, **14**, 2486-2488.
19. (a) J. Tang, R. Huang, H. Gao, X. Cheng, M. Prehm, and C. Tschierske, *RSC Adv.*, 2012, **2**, 2842-2847; (b) X. Yang, H. Dai, Q. He, J. Tang, X. Cheng, M. Prehm, and C. Tschierske, *Liq. Cryst.*, 2013, **40**, 8, 1028-1034; (c) J. Malthete, A. M. Levulut and N. H. Tinh, *J. Phys. Lett.*, 1985, **46**, 875-880; (d) J. Malthete, H. T. Nguyen and C. Destrade, *Liq. Cryst.*, 1993, **13**, 171-187; (e) H.-T. Nguyen, C. Destrade and J. Malthete, *Adv. Mater.*, 1997, **9**, 375–388; (f) K. E. Rowe and D. W. Bruce, *J. Mater. Chem.*, 1998, **8**, 331-341; (g) B. P. Hoag and D. L. Gin, *Adv. Mater.*, 1998, **10**, 1546-1551; (h) T. Yasuda, K. Kishimoto and T. Kato, *Chem. Commun.*, 2006, **32**, 3399-3401; (i) J. Seo, S. Kim, S. H. Gihm, C. R. Park and S. Y. Park, *J. Mater. Chem.*, 2007, **17**, 5052-5057; (j) S.-J. Yoon, J. H. Kim, K. S. Kim, J. W. Chung, B. Heinrich, F. Mathevet, P. Kim, B. Donnio, A.-J. Attias, D. Kim and S. Y. Park, *Adv. Funct. Mater.*, 2012, **22**, 61-69; (k) V. N. Kozhevnikov, B. Donnio and D. W. Bruce, *Angew. Chem. Int. Ed.*, 2008, **47**, 6286-6289; (l) C. Alstermark, M. Eriksson, M. Nilsson, C. Destrade and H. T. Nguyen, *Liq Cryst.*, 1990, **8**, 75-80; (m) D. Fazio, C. Mongin, B. Donnio, Y. Galerne D. Guillon and D.W. Bruce. *J. Mater. Chem.*, 2001, **11**, 2852-2863; (n) D. M. Huck, H. L. Nguyen, P. N. Horton, M. B. Hursthouse, D. Guillon, B. Donnio and D. W. Bruce, *Polyhedron*, 2006, **25**, 307-324; (o) A. I. Smirnova and D. W. Bruce, *J. Mater. Chem.*,

TH-2983_156122010

2006, **16**, 4299-4306; (p) E. Gorecka, D. Pociecha, J. Mieczkowski, J. Matraszek, B. Donnio and D. Guillon, *J. Am. Chem. Soc.*, 2004, **126**, 15946-15947; (q) C. Tschierske, *Angew. Chem. Int. Ed.*, 2000, **39**, 2454-2458; (r) E. Gorecka, D. Pociecha, J. Matraszek, J. Mieczkowski, Y. Shimbo, Y. Takanishi and H. Takezoe, *Phys. Rev. E.*, 2006, **73**, 31704-31708; (s) J. Barbera, E. Cavero, M. Lehmann, J. L. Serrano, T. Sierra and J. T. Vazquez, *J. Am. Chem. Soc.*, 2003, **125**, 4527-4533; (t) D. Pucci, *Liq Cryst.*, 2011, **38**, 1451-1465; (u) K. Han and B.-K. Cho, *Soft Matter*, 2014, **10**, 7588-7594; (v) C. V. Yelamaggad, G. Shanker, R. V. R. Rao, D. S. S. Rao, S. K. Prasad, and V. V. S. Babu, *Chem. Eur. J.*, 2008, **14**, 10462-10471.

20. (a) T. Niori, T. Sekine, J. Watanabe, T. Furukawa and H. Takezoe, *J. Mater. Chem.*, 1996, **6**, 1231-1233; (b) R. A. Reddy and C. Tschierske, *J. Mater. Chem.*, 2006, **16**, 907-961; (c) H. Takezoe and Y. Takanishi, *Jpn. J. of App. Phys.*, 2006, **45**, No. 2A, 597-625; (d) G. Pelzi, S. Diele and W. Weissflog, *Adv. Mater.*, 1999, **11**, 707-724; (e) M. B. Ros, J. L. Serrano, M. R. de la Fuente and C. L. Folcia, *J. Mater. Chem.*, 2005, **15**, 5093-5098; (f) C. Tschierske and G. Dantlgraber, *Pramana*, 2003, **61**, 455; (g) J. Etxebarria and M. B. Ros, *J. Mater. Chem.*, 2008, **18**, 2919-2926; (h) M. Lehmann, J. Seltmann, A. A. Auer, E. Prochnow and U. Benedikt, *J. Mater. Chem.*, 2009, **19**, 1978-1988; (i) M. Lehmann and J. Seltmann, *Beilstein J. Org. Chem.*, 2009, **5**, 73 (1-9); (j) T. Niori, T. Sekine, J. Watanabe, T. Furukawa and H. Takezoe, *Mol. Cryst. Liq. Cryst.*, 1997, **301**, 337-342; (k) T. Sekine, Y. Takanishi, T. Niori, J. Watanabe and T. Takezoe, *J. Mater. Chem.*, 1997, **7**, 1307-1309; (l) Y. Matsunaga and S. Miyamoto, *Mol. Cryst. Liq. Cryst.*, 1993, **237**, 311-317; (m) R. Cai and E. Samulski, *Liq. Cryst.*, 1991, **9**, 617-634.
21. (a) A. Pegenau, P. Goring and C. Tschierske, *Chem. Commun.*, 1996, **22**, 2563-2564; (b) M. Lehmann, R. I. Gearba, M. H. J. Koch, and D. A. Ivanov, *Chem. Mater.*, 2004, **16**, 374-376; (c) M. Lehmann and M. Jahr, *Chem. Mater.*, 2008, **20**, 5453-5456; (d) H. Detert, M. Lehmann and H. Meier, *Materials*, 2010, **3**, 3218–3330; (e) M. Lehmann, *Chem. Eur. J.*, 2009, **15**, 3638–3651; (f) S. Varghese, N. S. S. Kumar, A. Krishna, D. S. S. Rao, S. K. Prasad and S. Das, *Adv. Funct. Mater.*, 2009, **19**, 2064-2073.
22. (a) J. H. Cameron, A. Facher, G. Lattermann and S. Diele, *Adv. Mater.*, 1997, **9**, 398-403; (b) A. Pegenau, T. Hegmann, C. Tschierske and S. Diele, *Chem. Eur. J.*, 1999, **5**, 1643-1660; (c) S. I. Stupp, M. Keser and G. N. Tew, *Polymer*, 1998, **39**, 4505-4508; (d) H. Meier, M. Lehmann, and U. Kolb, *Chem. Eur. J.*, 2000, **6**, 2462-2469; (e) V. Percec, A. E. Dulcey, V. S. K. Balagurusamy, Y. Miura, J. Smidrkal, M. Peterca, S. Nummelin, U. Edlund, S. D. Hudson, P. A. Heiney, H. Duan, S. N. Magonov, and S. A. Vinogradov, *Nature*, 2004, **430**, 764-768; (f) M. Lehmann, C. Köhn, H. Meier, S. Renker and A. Oehlhof, *J. Mater. Chem.*, 2006, **16**, 441-451; (g) B. M. Rosen, C. J. Wilson, D. A. Wilson, M. Peterca, M. R. Imam, and V. Percec, *Chem Rev.*, 2009, **109**, 6275-6540; (h) B. Donnio, *Inorganica Chimica Acta*, 2014, **409**, 53-67; (i) D. J. Pesak and J. S. Moore, *Angew. Chem. Int. Ed.*, 1997, **36**, 1636-1639.
23. M. Lee, D. -W. Lee and B. -K. Cho, *J. Am. Chem. Soc.*, 1998, **120**, 13258-13259.

TH-2983_156122010

24. (a) C. Tschierske, *Angew. Chem. Int. Ed.*, 2013, **52**, 8828-8878; (b) Goodby, Mandle, Davis, Zhong and Cowling, *Liq. Cryst.*, 2015, **42**, 593–622.
25. (a) T. Wöhrle, I. Wurzbach, J. Kirres, A. Kostidou, N. Kapernaum, J. Litterscheidt, J. C. Haenle, P. Staffeld, A. Baro, F. Giesselmann and S. Laschat, *Chem. Rev.*, 2016, **116**, 1139–1241. (b) R. K. Gupta and A. A. Sudhakar, *Langmuir*, 2019, **35**, 2455–2479.
26. S. Kumar, *CRS Press*, Taylor & Francis Group: Boca Raton, FL, 2011.
27. (a) P. C. D. Robinson and M. W. Davidson, Nikon, Florida, USA., 2000-2013; (b) D. B. Murphy, K. R. Spring and M. W. Davidson, Nikon, Florida, USA, 2000-2013; (c) D. B. Murphy, K. R. Spring T. J. Fellers and M. W. Davidson, Nikon, Florida, USA, 2000-2013.
28. https://mgml.eu/laboratories/instruments/xeuss#prettyPhoto©2019-2020 MGML.
29. C. N. Banwell, *McGraw-Hill*, New York, 1972.
30. T. Schweizer, K. Heiko T. Koch. *Automotive and Engine Technology*, 2021, **6**, 275-287.
31. P. Atkins, J. De Paula and J. Keeler, *Oxford University Press*, Oxford, 2018.
32. S. Dhami, A. J. de Mello, G. Rumbles, S. M. Bishop, D. Phillips and A. Beeby, *Photochem. Photobiol.*, 1995, **61**, 341.
33. (a) M. Y. Berezin and S. Achilefu, *Chemical reviews*, 2010, 110, 2641-2684; (b) N. Boens, M. Ameloot, and B. Valeur, *Standardization and Quality Assurance in Fluorescence Measurements I:* Springer Series on Fluorescence, 2008, 215-232.
34. R. P. Jaya, *New Materials in Civil Engineering*, Butterworth-Heinemann, 2020, 493-527.
35. https://afm.oxinst.com/outreach/how-does-an-afm-microscope-work.
36. N. Elgrishi, K. J. Rountree, B. D. McCarthy, E. S. Rountree, T. T. Eisenhart, and J. L. Dempsey, *Journal of chemical education*, 2018, **95**, 197-206.
37. M. J. Frisch, G. W. Trucks, H. B. Schlegel, G. E. Scuseria, M. A. Robb, J. R. Cheeseman, G. Scalmani, V. Barone, G. A. Petersson, H. Nakatsuji, X. Li, M. Caricato, A. V. Marenich, J. Bloino, B. G. Janesko, R. Gomperts, B. Mennucci, H. P. Hratchian, J. V. Ortiz, A. F. Izmaylov, J. L. Sonnenberg, D. Williams-Young, F. Ding, F. Lip-parini, F. Egidi, J. Goings, B. Peng, A. Petrone, T. Henderson, D. Ranasinghe, V. G. Zakrzewski, J. Gao, N. Rega, G. Zheng, W. Liang, M. Hada, M. Ehara, K. Toyota, R. Fukuda, J. Hasegawa, M. Ishida, T. Nakajima, Y. Honda, O. Kitao, H. Nakai, T. Vreven, K. Throssell, J. A. Montgomery Jr., J. E. Peralta, F. Ogliaro, M. J. Bearpark, J. J. Heyd, E. N. Brothers, K. N. Kudin, V. N. Staroverov, T. A. Keith, R. Kobayashi, J. Normand, K. Raghavachari, A. P. Rendell, J. C. Burant, S. S. Iyengar, J. Tomasi, M. Cossi, J. M. Millam, M. Klene, C. Adamo, R. Cammi, J. W. Ochterski, R. L. Martin, K. Morokuma, O. Farkas, J. B. Foresman, D. J. Fox, *Gaussian~16 Revision C.01*, Gaussian Inc., Wallingford CT, 2016.
38. J. Tomasi, B. Mennucci and E. Cance, *Theochem*, 1999, **464**, 211.
39. A. D. Becke, *J Chem Phys* 1993, **98**, 5648-5652.
40. (a) C. D. Simpson, J. Wu, M. D. Watson and K. Mullen, *J. Mater. Chem.*, 2004, **14**, 494-504; (b) S. Laschat, A. Baro, N. Steinke, F. Giesselmann, C. Hägele, G. Scalia, R.

TH-2983_156122010

Judele, E. Kapatsina, S. Sauer, A. Schreivogel and M. Tosoni, *Angew. Chem.Int. Ed.*, 2007, **46**, 4832-4887.

41. N. Boden, R. Bissel, J. Clements and B. Movaghar, *Curr. Sci.*, 1996, **71**, 599-601.
42. T. Christ, B. Glusen, A. Greiner, A. Kettner, R. Sander, V. Stumpflen, V. Tsukruk and J. H. Wendorff, *Adv. Mater*.,1997, **9**, 48-52.
43. D. Thakur, M. R. Nagar, A. Tomar, D. k. Dubey, S. Kumar, S. S. Swayamprabha, S. Banik, J. H. Jou, and S. Ghosh, *ACS Appl. Electron. Mater.*, 2021, **3**, 2317−2332.
44. Anupriya, K. R. J. Thomas, M. R. Nagar and J. H. Jou, *Opt. Mater.*, 2022, **124**, 112017.
45. A. Sharma, K. R. J. Thomas, M. R. Nagar and J. H. Jou, *Mater. Adv.*, 2021, **2**, 6326-6338.
46. J. Eccher, G. C. Faria, H. Bock, H. Von Seggern and I. H. Bechtold, *ACS Appl. Mater. Interfaces*, 2013, **5**, 11935-11943.
47. R. K. Gupta, D. Das, M. Gupta, S. K. Pal, P. K. Iyer and A. A. Sudhakar, *J. Mater. Chem. C*, 2017, **5**, 1767-1781.
48. I. Bala, N. Singh, R. A. K. Yadav, J. De, S. P. Gupta, D. P. Singh, D. K. Dubey, J. H. Jou, R. Douali and S. K. Pal, *J. Mater. Chem. C*, 2020, **8**, 12485-12494.
49. C. Keum, D. Becker, E. Archer, H. Bock, H. Kitzerow, M. C. Gather and C. Murawsk, *Adv. Optical Mater.*, 2020, **8**, 2000414.

TH-2983_156122010

Chapter-2a

Columnar liquid crystals based on pyrazino[2,3-g]quinoxaline derivatives and their application in organic light-emitting diodes

TH-2983_156122010

2.1. Introduction

In organic electronics, especially in organic photovoltaics the search for low band gap materials is addressed by two approaches, the first one is by having a donor-acceptor (D-A) system and the second one is by having a planarized system via the quinoidization of a conjugated system.[1] In the first approach, there is a mixing of energy levels of donor and acceptor moieties, while the second one occurs due to the dearomatization of the conjugated structure *via* quinoid formation, but with the incorporation of an aromatic system with higher resonance stabilization energy.[2] Pyrazino[2,3-g]quinoxaline (PQ) as shown in Figure 2.1, is one such heteroaromatic core that makes a good acceptor material for the construction of low band gap materials. This is due to its strong electron-withdrawing ability, and also due to the higher quinoid structure at 5 and 10 positions. The strong π-π interactions make these molecules crystalline in nature, which may promote exciton migration and high charge carrier mobility. Judicial structural modification of PQ molecules may lead to a change in their self-assembly, photophysical behavior and may provide promising materials.[3] Utilization of π-conjugated materials as one-dimensional waveguides, require good fluorescence, proper crystal dimensions, and smooth crystal surface. However, π-conjugated molecules prefer to stack cofacially, leading to enhanced intermolecular π-π interactions. This often leads to a luminescence quenching as in the case of H-aggregates.[4-10] In the case of J-aggregates, where the molecules are arranged with slip-stacked arrangements, exhibit high fluorescence but cannot be used as waveguides due to their significant self-absorption and because of their relatively small Stokes shift.[4] Considering the inherent fluorescence and self-assembling behavior, PQ derivatives can be considered for such applications, provided they self-assemble in a preferred manner. When the PQ core is connected with peripheral phenyl groups, it reduces the crystalline packing due to the non-planarity of the conjugated structure. This molecular design may prevent the aggregation caused quenching (ACQ) due to the weakened intermolecular π-π interactions within the stacks. The presence of flexible alkyl chains in the peripheral rings might lead to further tunability of the self-assembly and the emission behavior in the aggregated state. All these presumptions were considered to explore the structure-property relationships of these relatively new liquid crystalline materials.

TH-2983_156122010

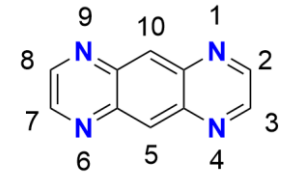

Pyrazino[2,3-g]quinoxaline

Figure 2.1. General molecular structure of pyrazino[2,3-g]quinoxaline (PQ) with the possible positions for substitutions.

In 2010, Chen and Pei designed and synthesized pyrazino[2,3-g]quinoxaline derivatives in their quest to achieve high-efficiency active waveguide fibers (Figure 2.2). They studied effects of the molecular geometry and symmetry on their optical properties and crystal dimensions. Liquid crystalline behaviors were investigated by a combined application of optical spectroscopy, microscopy, single crystal analysis, and 1D- and 2D-WAXD techniques. At a single molecular level, the geometrical difference of steric hindrance between a 5-member aromatic ring and a 6-member aromatic ring leads to different extent of conjugation.

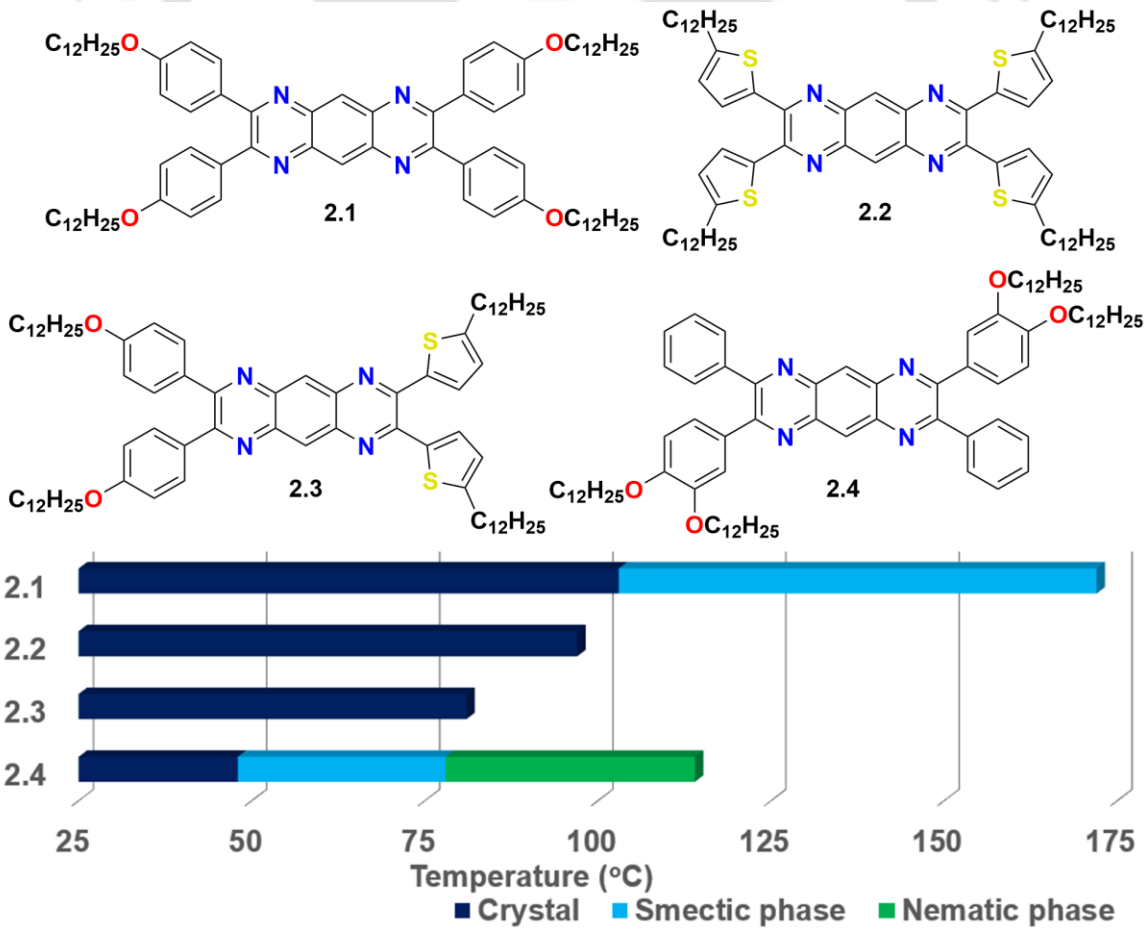

Figure 2.2. Molecular structures and bar graphs showing the phase behavior of PQ derivatives (**2.1-2.4**)[11]

TH-2983_156122010

The absence of a symmetrical centre in the molecule was found to be more unfavorable to the growth of fiber than the absence of mirror planes; because in this series the alkyl chains tend to arrange parallelly, which affects the long-range self-assembly of the non-planar aromatic core. Compound **2.1** exhibited layered phases (either SmA or SmC) and compound **2.4** exhibited an addition nematic phase above 78 ^{o}C, while compounds **2.2** and **2.3** were non-liquid crystalline (Figure 2.2). The LC behaviors of **2.1** and **2.4** further confirm the role with which the alkyl chains play in molecular packing: (1) they provide the nanophase segregation force; (2) their positions strongly influence the molecular anisotropy and the strength of intermolecular interactions. The crystalline fibrous aggregates of **2.1** and **2.2** behaved as low-loss active waveguide fibers. This proved the success of their strategy of combining the nonplanar aromatic core to increase the intra-columnar distance of molecular stacks (4.5 Å) and the alkyl a chain as structural group to promote self-assembly.[11] Su and Grimsdale in 2011 synthesized and characterized a series of PQ molecules with a systematic change in the substituents and observed a series of complex conjugation effects from the arms and substituents at the quinoidal positions, which explains the electronic properties of the PQ molecules.[3] Yang and Schröder in 2017, developed PQ containing ligands with eight carboxylic acid groups that were also utilized in the preparation of metal-organic frameworks (MOFs), which showed high adsorption efficiencies for methane.[12]

It was envisaged that with an appropriate molecular design, PQ derivatives may self-assemble to form Col phases. To achieve that they should be designed with a general discotic design template, where a central planar core is connected with several peripheral flexible chains. Columnar (Col) phases formed by the stacking of disk-like mesogens one above the other are often termed ‘molecular wires’ and have the potential to be utilized as active layers in organic electronic devices. In the case of Col phases, the central unit (usually aromatic) acts as a conducting core, while the peripheral sheath of flexible chains acts as an insulating mantle. The Col self-assembly brings an anisotropy to the physical properties like charge carrier mobility, where the charge migration along the column is higher than that across the column. As it was mentioned earlier, for different applications in various devices one need to control the self-assembly of these columnar aggregates.[13] For example, for the application in organic solar cells, field effect transistors or light emitting diodes the intracolumnar order should be very high as it will facilitate the exciton migration or charge carrier mobility along the columns.[14] In this chapter, different PQ derivatives were synthesized which showed self-assembly to form Col phases. Their

TH-2983_156122010

thermal and photophysical behavior were investigated and their utility as emissive layers in organic light emitting diodes was explored.

2.2. Result and discussion

2.2.1. Synthesis and molecular structural characterization

The target PQ derivatives were prepared, following a straightforward synthetic scheme starting from veratrole (Scheme 2.1). Two equivalents of veratrole were reacted with oxalyl chloride in presence of anhydrous $AlCl_3$ by Friedel-Craft's acylation to obtain the corresponding benzil derivative **1**.[15]

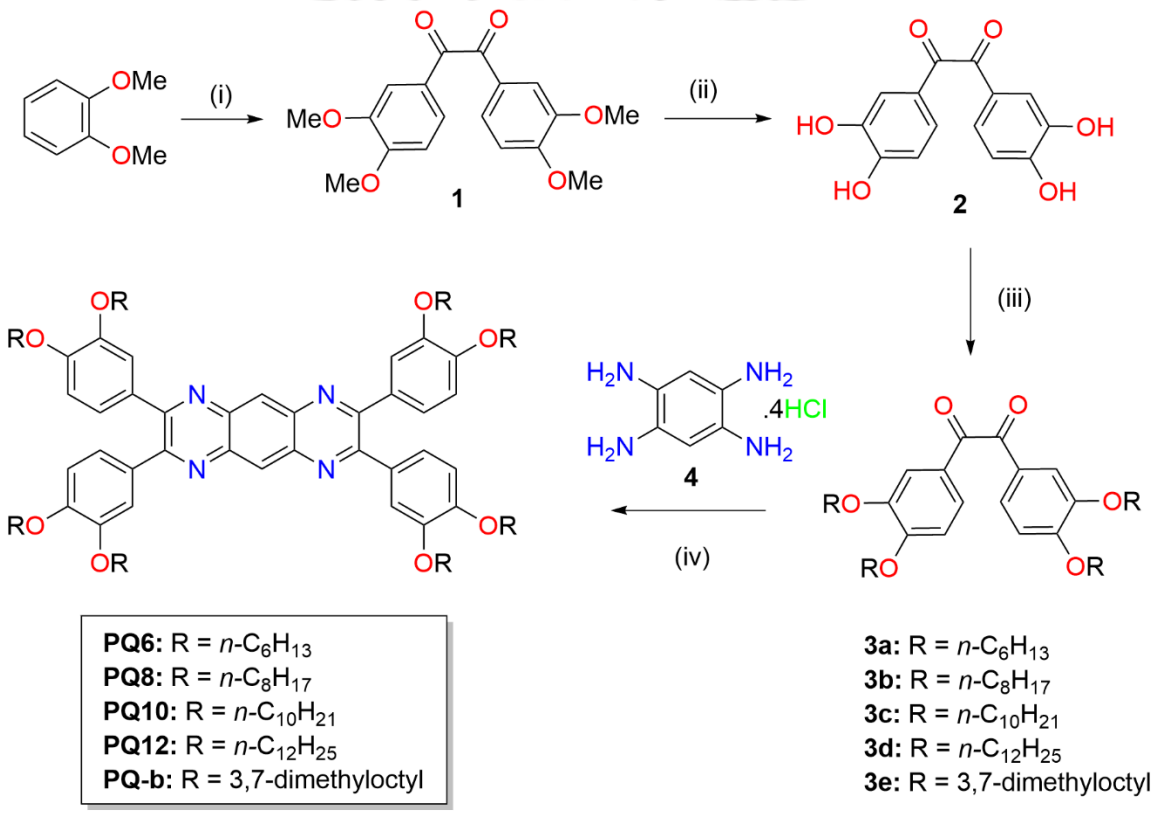

Scheme 2.1. Synthesis of PQ derivatives; Reagents and conditions: (i) 1,2-Dichloroethane, oxalyl chloride, anhydrous $AlCl_3$, 0 °C (30 min.), rt (17 h), 57%; (ii) 47% HBr, glacial acetic acid, reflux, 16 h, 80%; (iii) anhydrous K_2CO_3, 1-Bromoalkane, anhydrous DMF, 80 °C, 17 h, 85-90%; (iv) Methanol: acetic acid (1:3), 120 °C, triethylamine, 12 h, 75-85%.

This benzil derivative was demethylated on refluxing in presence of hydrobromic acid to obtain the tetrahydroxy derivative **2**.[15] This compound was alkylated under Williamson's ether synthesis protocol, in the presence of anhydrous K_2CO_3 to obtain the tetraalkylated derivatives (**3a-e**). These tetraalkylated 1,2-diketones were condensed with 1,2,4,5-tetraaminobenzene tetrahydrochloride to get the target PQ derivatives (**PQ6-12** and **PQ-b**).[16] Structural characterization and purity of all the compounds were investigated and confirmed by various analytical techniques i.e. (^{1}H, ^{13}C NMR, IR spectroscopy,

TH-2983_156122010

HRMS/MALDI-TOF mass spectrometry), which were discussed in the experimental section of this chapter. One of the final PQ derivatives (**PQ-10**) was utilized in the OLED device fabrication, ^{1}H and ^{13}C NMR spectra, which are shown in Figure 2.3.

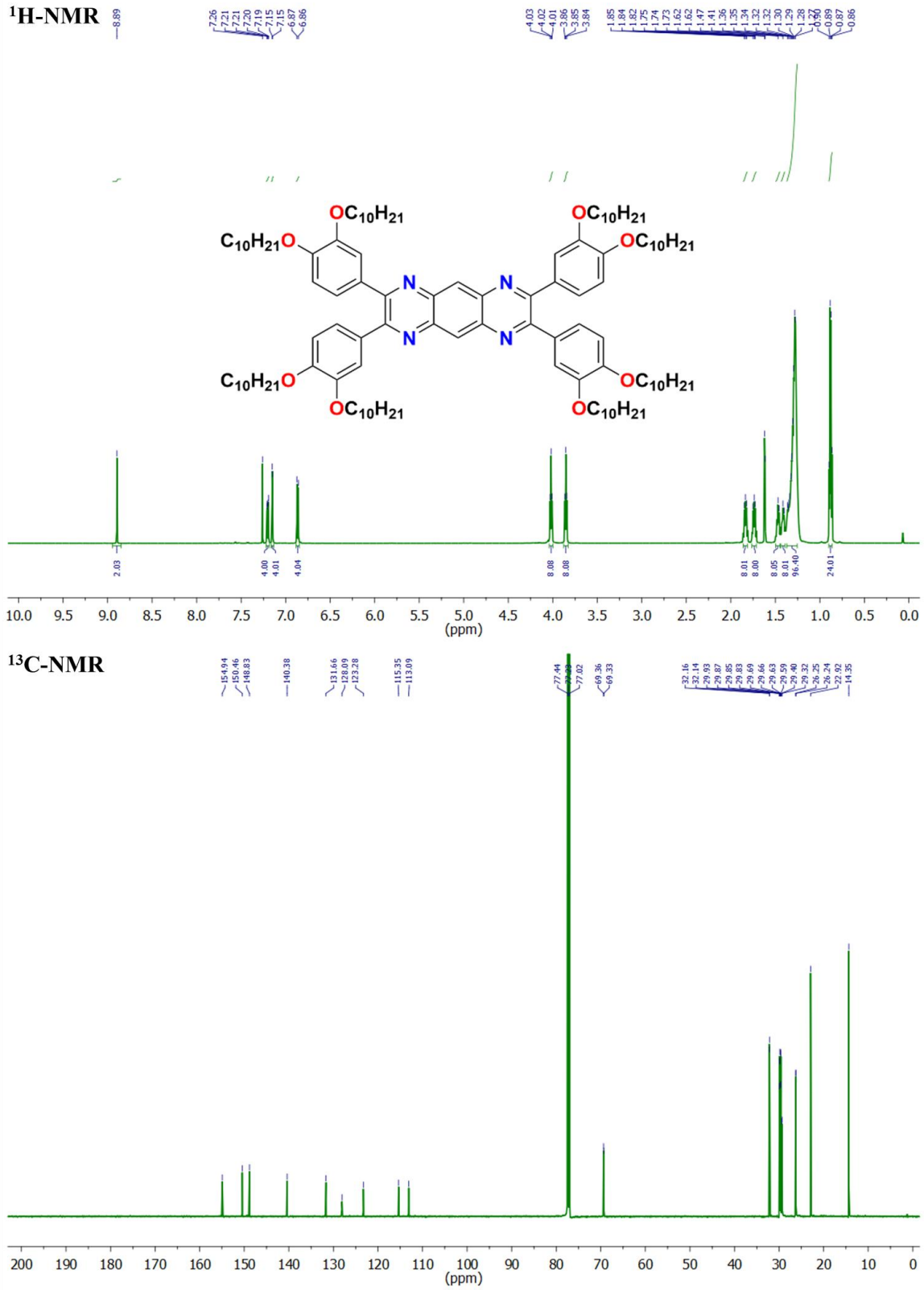

Figure 2.3. ^{1}H NMR (600 MHz) and ^{13}C NMR (150 MHz) spectra of compound **PQ-10** in $CDCl_3$.

TH-2983_156122010

2.2.2. Thermal behavior

The preliminary evidence for the liquid crystallinity was the conversion of the crystalline sample to a shearable birefringent fluid on heating, which was confirmed with the help of polarizing optical microscopy (POM) with a programmable hot stage. The phase transition temperatures and associated enthalpy changes were determined with the help of differential scanning calorimetry (DSC). The transition temperatures observed in DSC traces were in concurrence with the POM observations. All the mesophases observed were finally confirmed by the powder X-ray diffraction (PXRD) studies carried out at different temperatures. The summary of the thermal behavior of all the target molecules obtained by these complementary studies is presented in Table 2.1 and schematically represented in Figure 2.4.

Table 2.1. Phase transition temperatures[a] (°C) and corresponding enthalpies (kJ mol^{-1}) of the **PQ** derivatives

Entry	Phase sequence	
	Heating	**Cooling**
PQ6	Cr 93.5 (8.9) I[b]	-
PQ8	Col_{ob} 90 (6.3) Col_h 99.3 (1.9) I	I 96.2 (4.4) Col_h 80 (6.9) Col_{ob}[c]
PQ10	Col_{r3} 79.3 (1.3) Col_{r2} 88.5 (3.3) Col_{r1} 94.4 (0.3) I	I 91.3 (2) Col_{r1} 82.2 (3.8) Col_{r2} 43 (2.3) Col_{r3}[c]
PQ12	Col_{r2} 81.1 (1.1) Col_{r1} 85.2 (0.5) Col_h 90.4 (0.1) I	I 87.1 (0.7) Col_h 79.5 (2.5) Col_{r1} 50.7 (2.6) Col_{r2}[c]
PQ-b	Viscous liquid	-

[a]Peak temperatures in the DSC thermograms obtained during the first cooling and second heating cycles at 5 °C min^{-1}; [b]The isotropic liquid freezes after a long time; [c]mesophase freezes in a glassy state (Cr = crystal; Col_h = Columnar hexagonal; Col_{ob} = Columnar oblique; Col_r = Columnar rectangular; I = Isotropic liquid.)

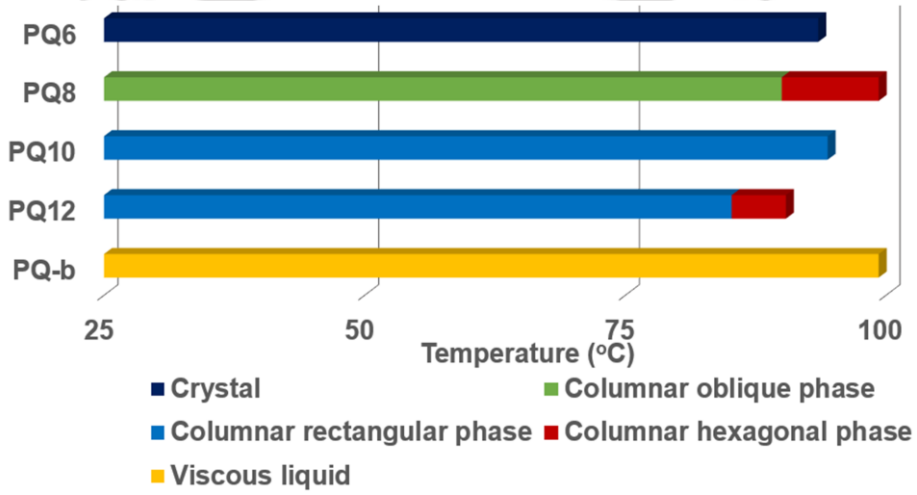

Figure 2.4. Bar graph representing the thermal behavior of PQ derivatives (based on second heating scan).

TH-2983_156122010

PQ6 with eight *n*-hexyloxy chains turned to crystalline, indicates the flexibility provided by these chains are not enough to stabilize liquid crystalline self-assembly (Figure 2.4 and 2.6a). Photomicrographs of compound **PQ6** at 25 ^{o}C and after cooling for a day from the isotropic state are shown in Figure 2.5a-b. It is interesting to note that planar discotic like hexaalkoxytriphenylenes exhibit mesomorphism with six *n*-hexyloxy chains.[17]

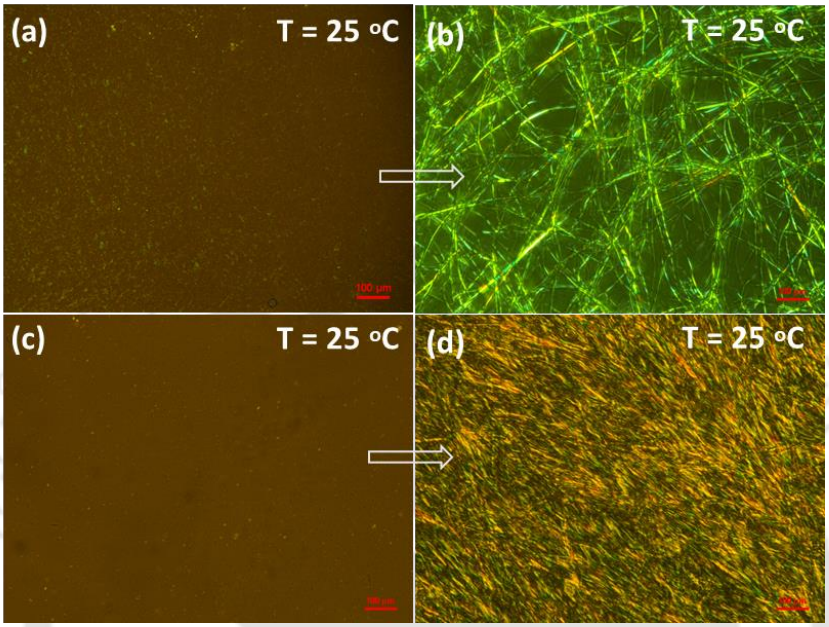

Figure 2.5. Photomicrograph of compound **PQ6** (a, b) and **PQ-b** (c, d) at 25 ^{o}C taken after cooling (a, c) and a day after cooling (b, d) from the isotropic state (scale bar corresponds to 100 μm).

Higher homologues **PQ8**, **PQ10** and **PQ12** stabilize Col phases over a thermal range of 9-12 degrees in the heating cycle. It was surprising to see that the PQ derivative with eight 3,7-dimethyloctyloxy chains (**PQ-b**) turned to be viscous liquid (Figure 2.4). However, a slow crystallization was observed after keeping for a day as shown in Figure 2.5c-d. It was expected that this compound would have an extended mesophase range in comparison to **PQ8** and **PQ10** with *n*-octyloxy and *n*-decyloxy chains. But considering the non-planar structure of these molecules, even the increased steric hindrance of the branched chains destabilizes the liquid crystalline nature of these samples. It was to be noted that in the case of planar disc-like molecules, such branched chains will lead to a reduction in the melting point and thus an increase in the mesophase range.[17] The smaller mesophase ranges of the PQ derivatives in comparison to other polycyclic planar discotic molecules may be due to the out of plane conformation of the peripheral aromatic rings. As an example for this series, the mesomorphic behavior of compound **PQ8** was discussed in detail.

TH-2983_156122010

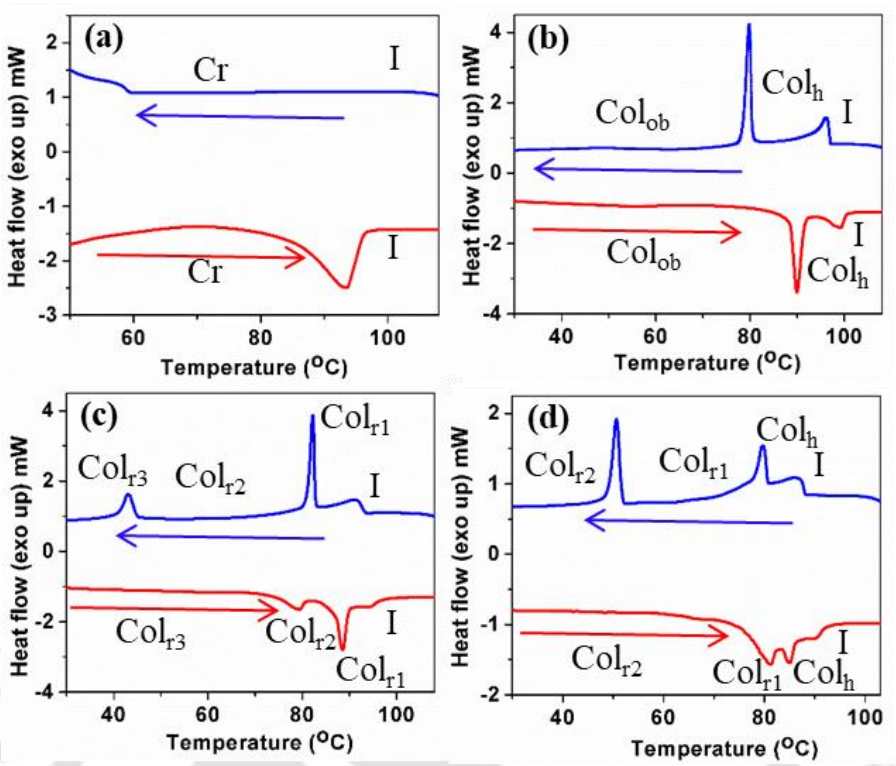

Figure 2.6. DSC scans obtained from compounds **PQ6** (a), **PQ8** (b), **PQ10** (c) and **PQ12** (d) in the first cooling (in blue cycle) and second heating (in red cycle) scans at 5 °C min^{-1}.

The crystalline sample of derivatives **PQ8** on heating under the POM showed a crystal to LC phase transition at around 90 °C, which later clears at ≈ 100 °C. On cooling this isotropic liquid at a rate of 5°C min^{-1}, a bright mosaic texture was observed which is characteristic of the columnar hexagonal (Col$_h$) phase. Further cooling leads to a transition at 80 °C, (ΔH = 6.9 kJ mol^{-1}) accompanying a textural change as seen in Figures 2.7a-c. This texture remains unchanged without any crystallization even at room temperature (RT) as seen in the DSC scans Figures 2.6b. Second heating shows a Col-Col phase transition. The high temperature and low temperature mesophases were analyzed by XRD studies. The XRD profile obtained at 87 °C (Figure 2.7d), showed one strong peak along with two peaks of low intensity in the low angle region. These peaks correspond to *d*-spacings of 30.12 Å, 17.20 Å and 14.94 Å, which can be assigned to 10, 11 and 20 reflections of a hexagonal lattice, as they fit with a ratio of 1: 0.57: 0.5 (Table 2.2). Along with these peaks, two diffused reflections were observed in the wide angle. The first one corresponds to the packing of flexible chains, while the second diffused reflection corresponds to the stacking of the discotic cores within the column. The core-core stacking distance was found to be 3.47 Å. Thus the mesophase can be assigned to a Col$_h$ phase (Figure 2.8a). The lattice parameter '*a*', which is the side of a hexagonal unit cell, was found

TH-2983_156122010

to be 34.8 Å. This value was found to be 30% less than the calculated molecular diameter (D = 37.9 Å), suggesting the interdigitation of the flexible alkyl chains from the neighboring molecules. XRD profile obtained at 60 °C (Figure 2.7e), showed a similar profile but increased reflections at the low angle. The d-spacings of 31.16 Å, 22.76 Å, 18.22 Å, 15.75 Å, 14.13 Å, 12.01 Å, 11.33 Å, 9.73 Å, 8.98 Å and 7.85 Å can be assigned to 02, 11, 10, 04, 25, -12, 22, 21, -14, -15 reflections of an oblique lattice (γ = 40.5°) with the cell parameters a = 28.1 Å, b = 96.0 Å and c = 3.49 Å (Figure 2.8b). A similar XRD pattern was found even at room temperature confirming the oblique nature of the Col phase, without undergoing crystallization (Table 2.2 and Figure 2.7f).

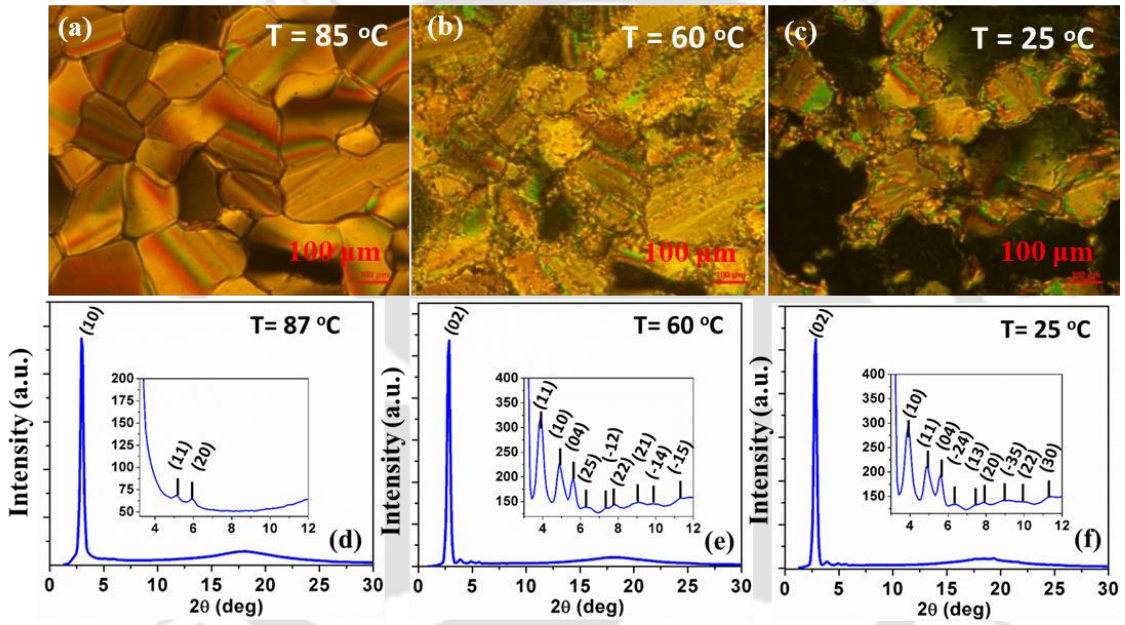

Figure 2.7. POM images obtained for the Col_h phase **PQ8** at 85 °C (a); for the Col_{ob} phase at 60 °C (b) and for the Col_{ob} phase at 25 °C (c) on cooling from the isotropic state. The XRD profiles of compound **PQ8** depicting the intensity against the 2θ obtained for the Col_h phase at 87 °C (d); Col_{ob} phase at 60 °C (e) and Col_{ob} phase at 25 °C (f) (Inset shows the expanded portion of the small angle region).

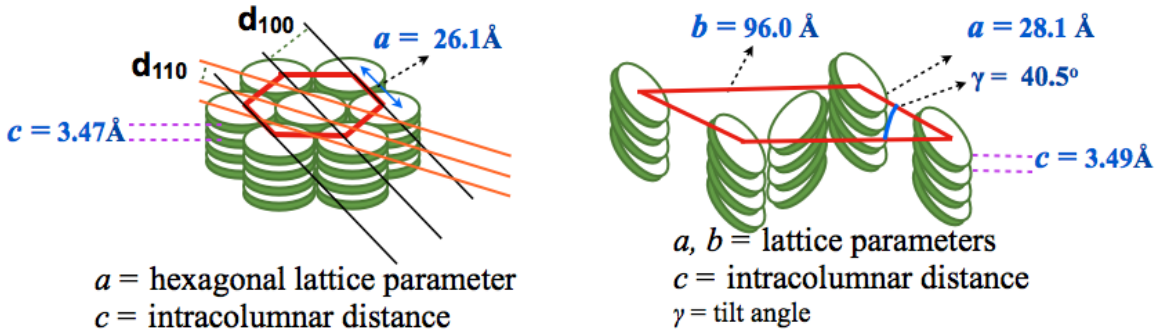

Figure 2.8. The models of columnar packing for the Col_h phase at 87 °C (a) and Col_{ob} phase at 60 °C (b) of the compound **PQ8**.

TH-2983_156122010

Table 2.2. Results of the (*hk*) indexation of the XRD profiles of the compound **PQ8** at a given temperature (*T*) of the mesophases[a]

Compounds (D/Å)	Phase (T/°C)	d_{obs} (Å)	d_{cal} (Å)	Miller indices *hk*	Lattice parameters (Å)
PQ8 (37.9)	Col_h (87)	30.12 17.20 14.94 4.93 (h_a) 3.47 (h_c)	30.12 17.39 15.06	10 11 20	a = 34.8 c = 3.47
	Col_{ob} (60)	31.16 22.76 18.22 15.75 14.13 12.01 11.33 9.73 8.98 7.85 4.85 (h_a) 3.49 (h_c)	31.16 22.76 18.22 15.58 14.01 12.20 11.38 10.19 8.95 7.87	02 11 10 04 25 -12 22 21 -14 -15	a = 28.1 b = 96.0 c = 3.49 γ = 40.5°
	Col_{ob} (25)	31.18 22.82 18.21 15.73 13.95 11.92 11.27 9.83 9.06 7.82 4.81 4.59 4.14 (h_a) 3.49 (h_c)	31.18 22.82 18.21 15.59 14.02 12.17 11.41 9.48 9.11 7.61 4.82 4.56	02 10 11 04 -24 13 20 -35 22 30 43 50	a = 28.4 b = 77.7 c = 3.49 γ = 53.4°

[a] The diameter (D) of the disk (estimated from Chem 3D Pro 8.0 molecular model software from Cambridge Soft). d_{obs}: spacing observed; d_{cal}: spacing calculated (deduced from the lattice parameters; a for Col_h phase; a and b for Col_{ob} phase; c is the height of the unit cell). The spacings marked h_a and h_c correspond to diffuse reflections in the wide-angle region arising from correlations between the alkyl chains and core regions, respectively.

Higher homologue **PQ10**, with eight *n*-decyloxy chains on heating exhibited a crystal-LC phase transition at ≈79 °C (ΔH = 0.3 kJ mol^{-1}) before clearing to isotropic liquid at ≈ 94 °C (Figures 2.6c). On cooling from the isotropic phase, a transition to a colorful mosaic texture was noticed. On further cooling, a transition with an enthalpy change of 3.8 kJ mol^{-1} was noticed at ≈82 °C. This change was accompanied with a variation in the brightness/color of the texture (Figure 2.9a-c). Further cooling exhibited a transition at ≈ 43 °C (ΔH = 2.3 kJ mol^{-1}), but the texture remained almost the same without any shearability. Similar behavior was observed in the case of **PQ12**, which exhibited three different phases as per the DSC scans

TH-2983_156122010

(Figures 2.6d), but with a little variation in the optical texture (Figure 2.10a-c). However, from the XRD studies it was found that **PQ10** exhibited transitions between three columnar rectangular (Col_r) phases, while compound **PQ12** exhibited a high temperature Col_h phase and two low temperature Col_r phases as shown in Table 2.3, (Figure 2.9d-f and 2.10d-f).

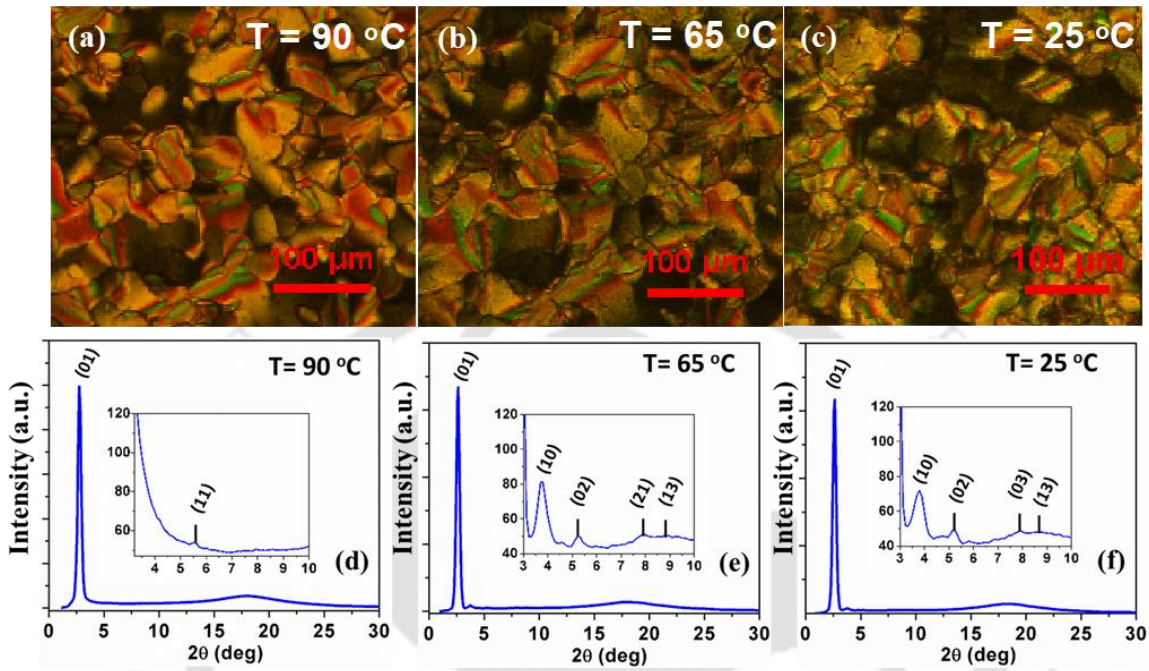

Figure 2.9. The POM images of compound **PQ10** obtained for the Col_r phase at 90 °C (a); at 65 °C (b) and at 25 °C (c); The XRD profiles at 90 °C (d); at 65 °C (e) and at 25 °C (f).

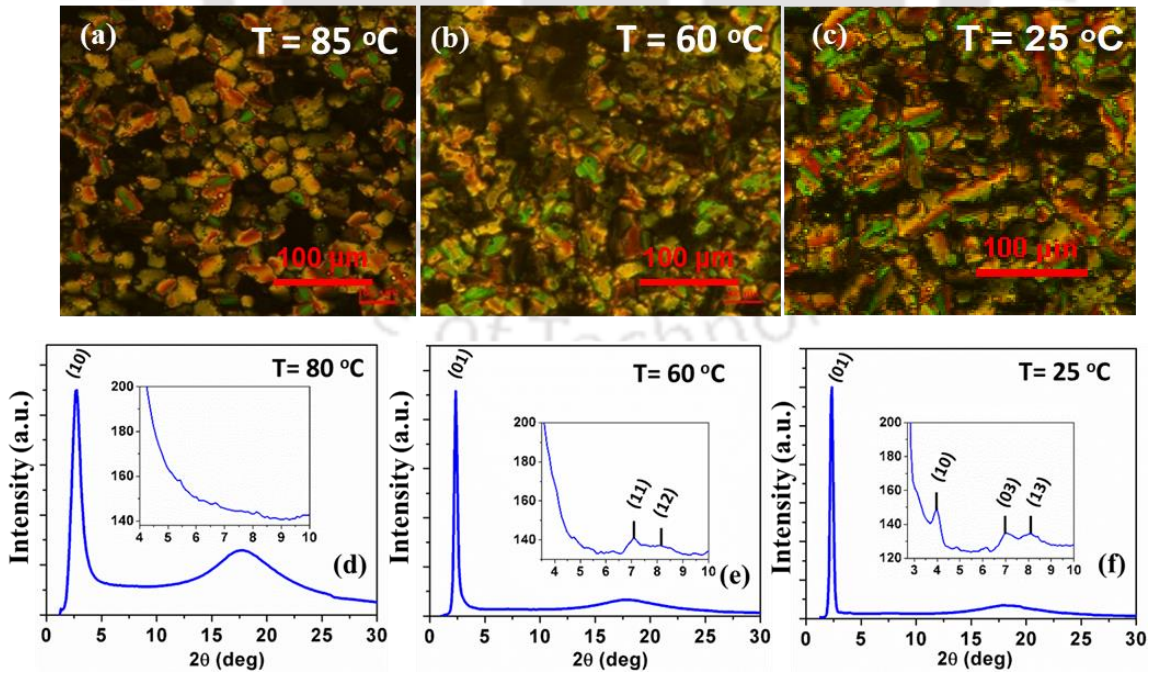

Figure 2.10. POM images obtained for the Col_h phase **PQ12** at 85 °C (a); for the Col_r phase at 60 °C (b) and at 25 °C (c); The XRD profiles of compound **PQ12** at 80 °C (d); at 60 °C (e) and at 25 °C (f).

TH-2983_156122010

Table 2.3. Results of the (*hk*) indexation of the XRD profiles of the compound **PQ10** and **PQ12** at a given temperature (*T*) of the mesophases[a]

Compounds (D/Å)	Phase (T/°C)	d_{obs} (Å)	d_{cal} (Å)	Miller indices *hk*	Lattice parameters (Å)
PQ10 (37.9)	Col_{r1} (90)	32.24 16.00 4.95 (h_a) 3.49 (h_c)	32.24 16.00	01 11	a = 18.4 b = 32.2 c = 3.49
	Col_{r2} (65)	33.43 23.66 16.86 11.16 10.05 4.88 (h_a) 3.53 (h_c)	33.43 23.66 16.72 11.15 10.08	01 10 02 21 13	a = 23.7 b = 33.4 c = 3.53
	Col_{r3} (25)	33.40 23.36 16.99 11.21 10.11 4.14 (h_a) 3.49 (h_c)	33.40 23.36 16.70 11.13 10.05	01 10 02 03 13	a = 23.4 b = 33.4 c = 3.49
PQ12 (37.9)	Col_h (80)	32.28 4.94 (h_a) 3.48 (h_c)	32.28	10	a = 37.3 c = 3.48
	Col_{r1} (60)	37.52 12.49 10.97 4.92 (h_a) 3.47 (h_c)	37.52 12.49 10.82	01 11 12	a = 13.3 b = 37.5 c = 3.47
	Col_{r2} (25)	37.53 22.15 12.65 10.97 4.85 (h_a) 4.60 3.75 3.47 (h_c)	37.53 21.67 12.51 10.83 4.81 4.59	01 10 03 13 44 45	a = 22.2 b = 37.5 c = 3.47

[a] The diameter (D) of the disk (estimated from Chem 3D Pro 8.0 molecular model software from Cambridge Soft). d_{obs}: spacing observed; d_{cal}: spacing calculated (deduced from the lattice parameters; a for Col_h phase; a and b for Col_r phase; c is the height of the unit cell). The spacings marked h_a and h_c correspond to diffuse reflections in the wide-angle region arising from correlations between the alkyl chains and core regions, respectively.

Ichihara *et al*. observed the stabilization of long range Col_r phases in the case of metal containing phthalocyanines which are connected to eight 3,4-dialkoxyphenyl groups, while the ring closure reaction between the phenyl groups lead to the stabilization of columnar tetragonal (Col_{tet}) phase.[18] Similarly, in the case of PQ derivatives, it is assumed that the phenyl groups are unable to freely rotate in the bulk state as they are not in the same plane of the central core. Their out of plane orientation prevents the cores from attaining the homeotropic alignment, as well as

TH-2983_156122010

the tendency to exhibit Col_h or Col_{tet} phases. From the TGA studies, it was found that these compounds (**PQ6-PQ12** and **PQ-b**) were stable at least up to 230 °C and the TGA plot were shown in Figure 2.11.

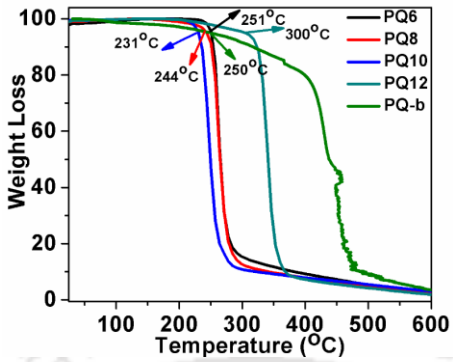

Figure 2.11. TGA plots of compounds **PQ6-PQ12** and **PQ-b** (heating rate of 10 °C min^{-1}, Nitrogen atmosphere).

2.2.3. Photophysical properties

The investigation of the photophysical properties of all the PQ compounds in solution and in solid thin films were shown in Table 2.4 and Figure 2.12a-b. The absorption spectra of the PQ derivatives in micromolar solutions exhibited a structure less broad absorption band centered at 470 nm as shown in Figure 2.13a. Similarly, the emission spectra of these compounds showed (Figure 2.13b) an emission maximum centered around 539-544 nm with a large Stokes shift in the range of 2724 cm^{-1} to 2894 cm^{-1}. These compounds exhibited high molar extinction coefficients in the range of 11513-16873 $Lmol^{-1}cm^{-1}$. The optical band gap of these compounds calculated from their absorption onset was found to be 2.38 eV.

Table 2.4. Photophysical properties of PQ derivatives

	Solution state[a]						Thin film state[f]		
	Abs.	ε	Emission[b]	Stokes shift	$\Delta E^{c}_{g,\,opt}$	Quantum yield[d]	Abs.	Emission[e]	Stokes shift
PQ6	470	12490	543	2860	2.38	0.23	435, 456, 482	557	3976
PQ8	470	16873	544	2894	2.38	0.23	436, 456, 483	543	3514
PQ10	470	13738	540	2758	2.38	0.23	434, 456, 483	538	3342
PQ12	470	11513	539	2724	2.38	0.24	434, 456, 483	534	3203
PQ-b	470	15740	541	2792	2.38	0.24	461, 480	544	3310

[a] micromolar solutions in $CHCl_3$; [b] λ_{ex} = 470 nm; [c] calculated from the red edge of the absorption band; [d]relative quantum yields of these compounds calculated with respect to a solution of fluorescein in a 0.1 M NaOH solution as the standard (Q_f = 0.79); [e] λ_{ex} = 456 nm .[f]Thin films were obtained by the spin coating of millimolar solution of compounds in toluene on quartz plate.

TH-2983_156122010

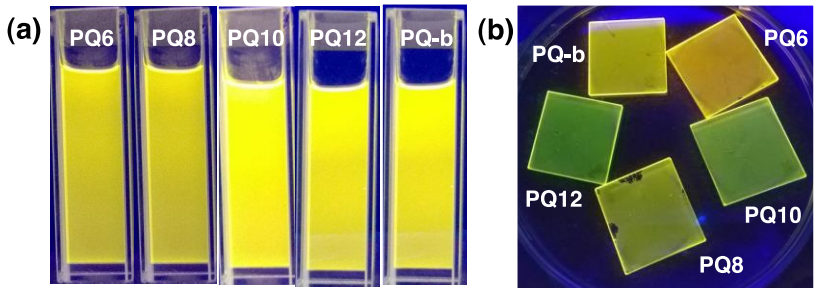

Figure 2.12. Photographs of micromolar solutions of compounds **PQ6-PQ12** and **PQ-b** in chloroform (a) and spin-coated thin films on quartz plates (b) under UV light of long wavelength (λ = 365 nm).

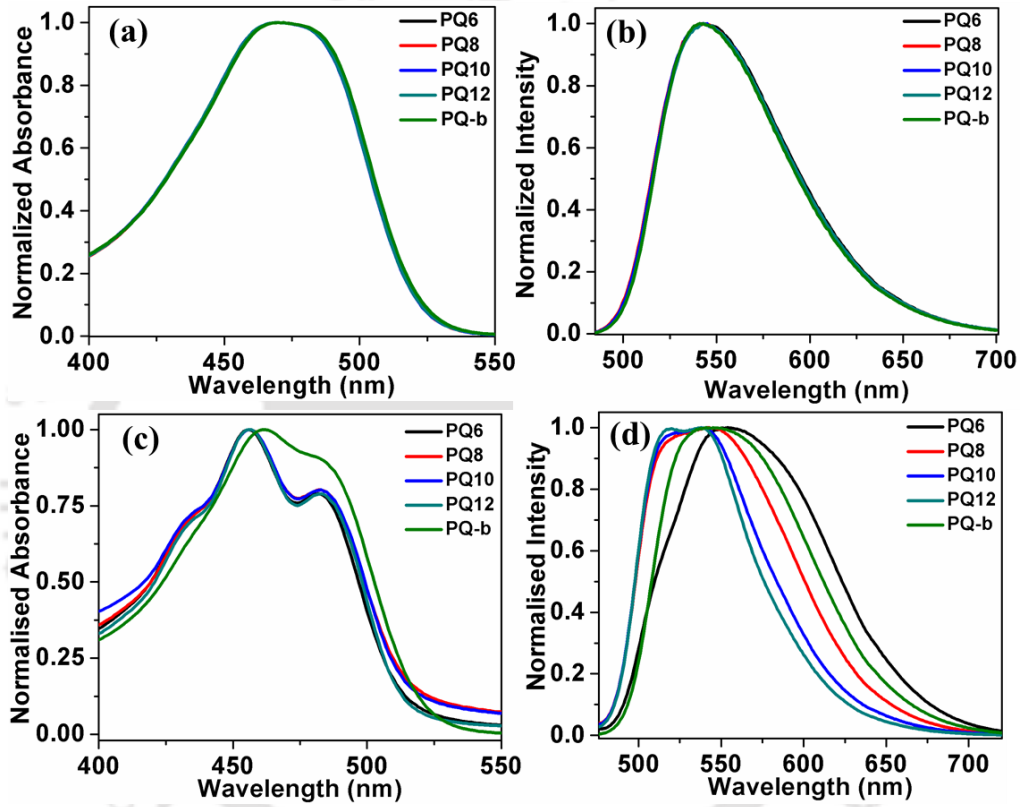

Figure 2.13. Overlay of absorption of compounds **PQ6-PQ12** and **PQ-b** (a) and emission spectra (b) in micromolar chloroform solutions; absorption (c) and emission spectra (d) of compounds in the thin film state obtained by spin coating on quartz plates.

The absorption spectra of the representative compound **PQ8** in micromolar solution on increasing the concentration led to a red-shifted absorption band. Emission spectra showed an increase in the intensity in the beginning with the increase in concentration, but at higher concentrations, the aggregation caused quenching (ACQ) of luminescence was noticed along with a red-shift in the emission (Figure 2.14). The red-shifted absorption along with the aggregation suggests the formation of J-aggregates.[19-21] The initial increase in the emission intensity may be due to the excimer emission, where the excited state life-time remains in the range of nanoseconds. It was confirmed that the aggregation leads to

TH-2983_156122010

aggregation caused quenching (ACQ) of luminescence by the mixed solvent method, where chloroform was chosen as a good solvent, while methanol was chosen as a poor solvent. The addition of methanol to chloroform solution with the maintenance of the concentration led to the aggregation of **PQ8**. Red-shifted absorption band and ACQ with a red shift in the emission was noticed, as seen in the case of concentration dependent experiments (Figure 2.15). Dynamic Light Scattering (DLS) studies have shown that in the case of chloroform solutions aggregates are not noticed, while the addition of methanol leads to the formation of aggregates of ≈ 370 nm size (Figure 2.16). Field emission scanning electron microscopy (FESEM) images also confirmed the formation of fibrous aggregates with the addition of methanol (Figure 2.17).

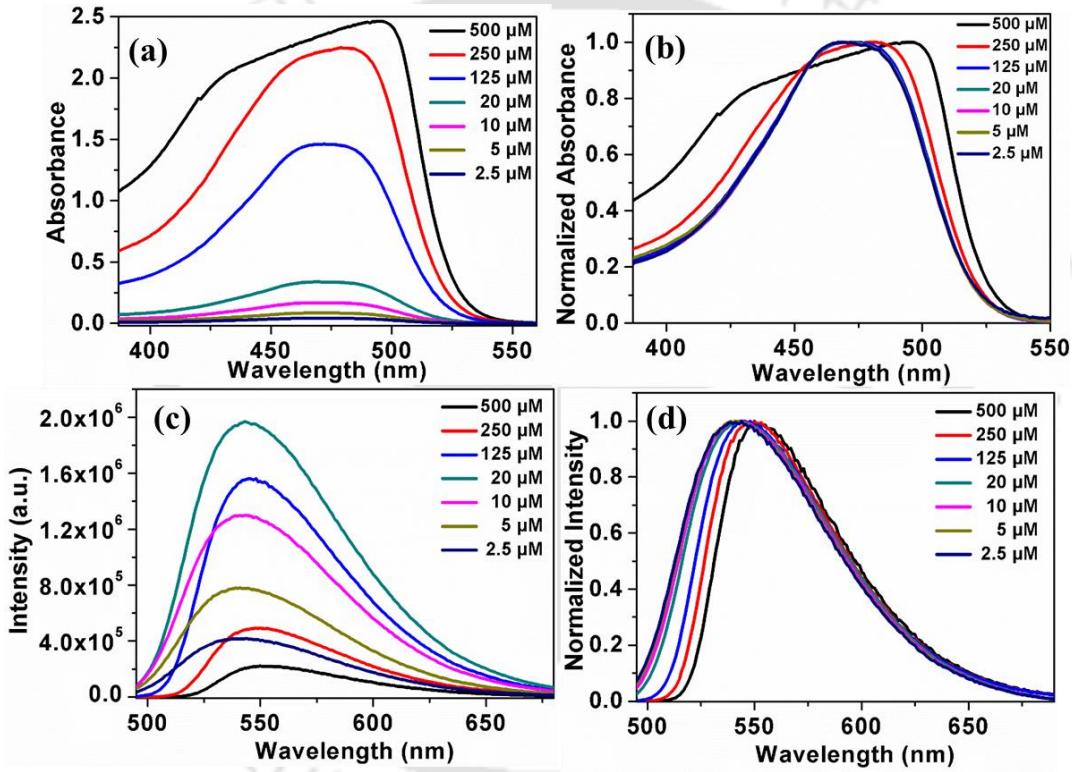

Figure 2.14. Overlay of absorption spectra of compound **PQ8** (a); normalized version of the same (b); overlay of emission spectra (c) and normalized version of the same (d) in chloroform solutions with varying concentrations.

The thin films were prepared by the spin coating on quartz plate with a 2mM solution in toluene. Interestingly, the absorption spectra of the thin films were well structured in comparison to solution spectra (Figure 2.13c) and exhibited a blue shift in comparison to the solutions by 14 nm, while the emission spectra (Figure 2.13d) remained almost the same in the range of 534-557 nm. Blue-shifted absorption in the aggregated state corresponds to the formation of H-aggregates.[19-21] The Stokes shift also showed an increase in comparison to solutions, varying in the range of 3203-3976 cm^{-1}. The absorption and

TH-2983_156122010

emission spectra of the films were obtained after annealing them at 10 ^{o}C below the clearing points for 10 minutes. The overlay of these spectra did not show much difference, even though a small decrease in the emission intensity is noted due to the closer packing of the molecules leading to ACQ (Figure 2.18a-f).

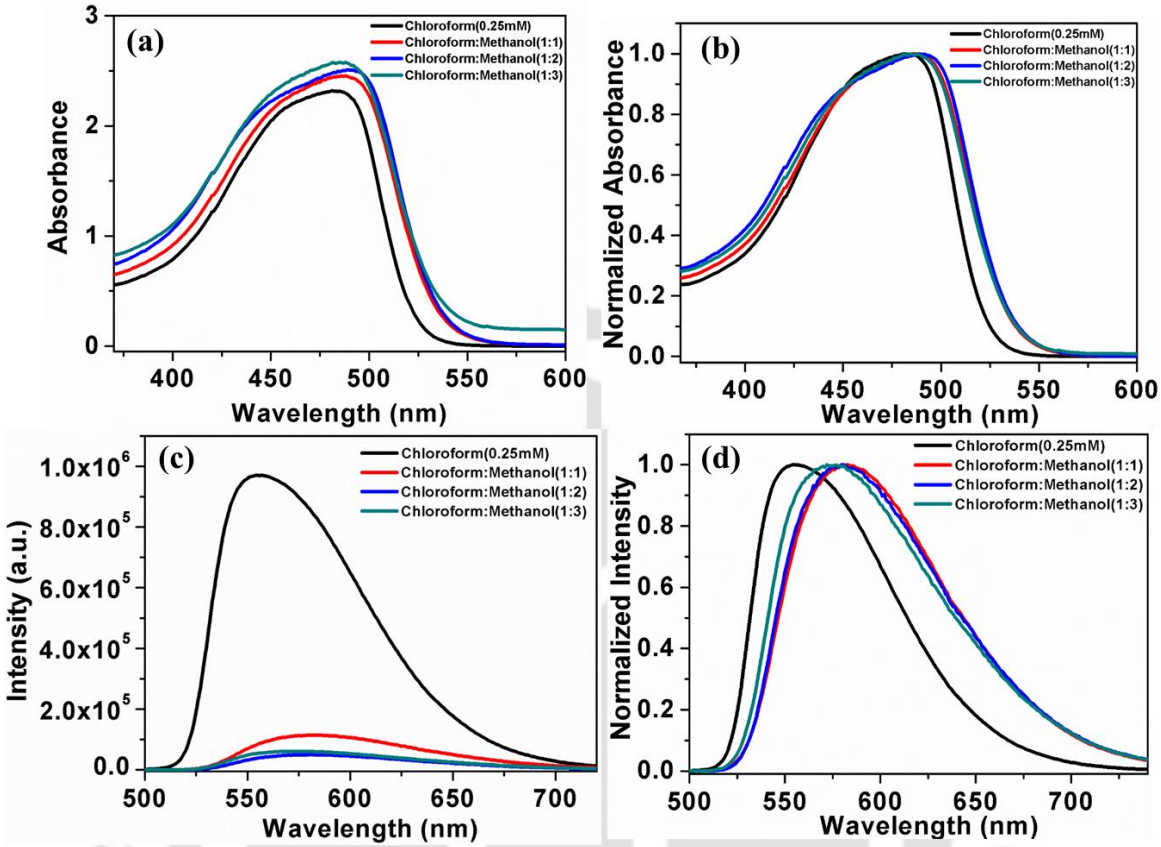

Figure 2.15. Overlay of absorption spectra of compound **PQ8**(a); normalized version of the same (b); overlay of emission spectra (c) and normalized version of the same (d) in chloroform and chloroform:methanol solutions with varying concentrations.

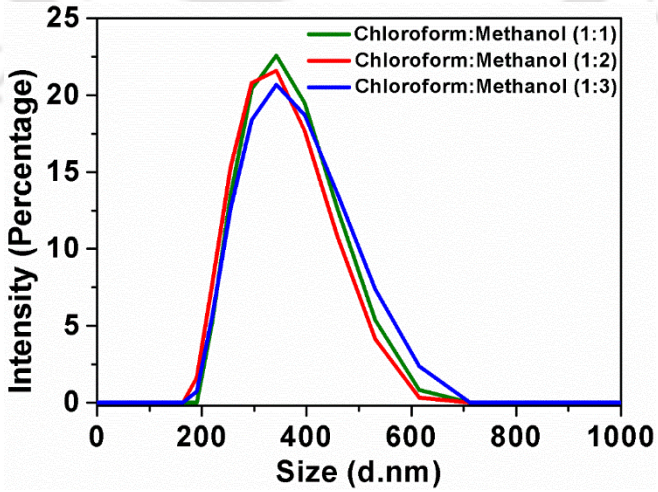

Figure 2.16. DLS profiles of 0.25 mM solutions of compound **PQ8**, with varying chloroform-methanol ratios.

TH-2983_156122010

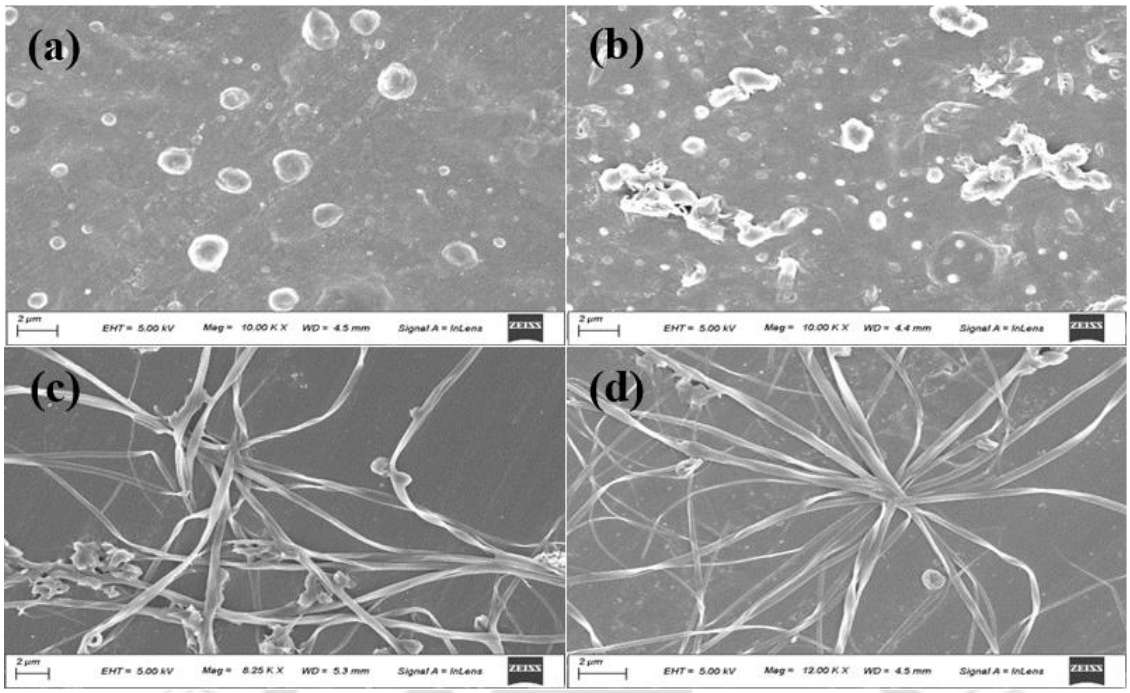

Figure 2.17. FESEM images obtained for the thin films obtained by drop-casting the solutions of **PQ8**, (a) obtained from 0.25 mM chloroform solution; (b) obtained from chloroform-methanol (1:1, 0.25 mM) solution; (c) obtained from chloroform-methanol (1:2, 0.25 mM) solution; (d) obtained from chloroform-methanol (1:3, 0.25 mM) solution.

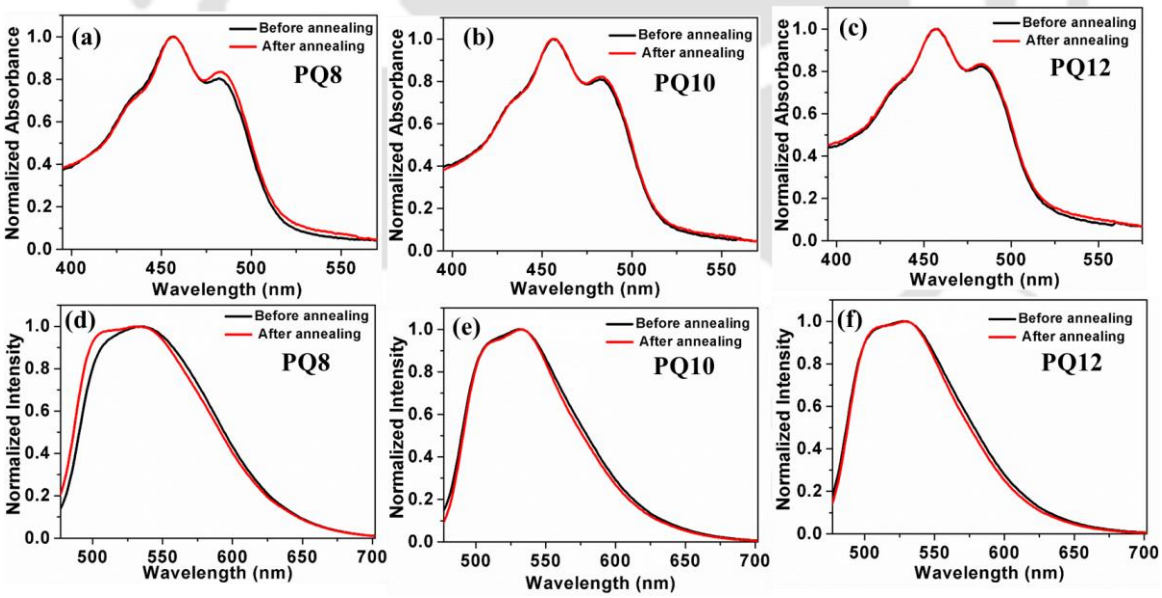

Figure 2.18. Overlay of normalized absorption spectra (upper row) and fluorescence spectra (lower row) of thin films obtained for compounds **PQ8, PQ10** and **PQ12** (before annealing: black trace, after annealing: red trace).

Visually the emission of these solutions was found to be perceivable as yellowish, while in the thin film state, they exhibited a yellowish-green emission as shown in Figure 2.12a-b. Overlay of emission spectra of micromolar solutions over that of thin films showed a decrease in the intensity suggesting an aggregation-induced quenching of luminescence,

TH-2983_156122010

which is characteristic of H-aggregates, where the molecules are stacked with a head-to-head overlap, that was also corroborated by the blue-shifted absorption spectra of the thin films.[19-21] The time-resolved photoluminescence studies of these films exhibited two excited species but with shorter lifetimes suggesting the ACQ (Table 2.5 and Figure 2.19a, b).

Table 2.5. Data obtained from the time-resolved photoluminescence experiments of compounds **PQ6-PQ12 & PQ-b**.

Solution[a]		**Thin film**[b]	
Entry	Fraction (Life time)	Entry	Fraction (Life time)
PQ6	100% (2.18 ns)	**PQ6**	62.30% (0.34 ns); 37.70% (1.99 ns)
PQ8	100% (2.19 ns)	**PQ8**	35.62% (0.79 ns); 64.38% (1.92 ns)
PQ10	100% (2.20 ns)	**PQ10**	32.21% (0.60 ns); 67.79% (1.47 ns)
PQ12	100% (2.20 ns)	**PQ12**	76.20% (1.68 ns); 23.86% (1.81 ns)
PQ-b	100% (2.21 ns)	**PQ-b**	62.91% (0.51 ns); 37.09% (1.56 ns)
[a]Concentration: 5 μM solution in chloroform; [b]Concentration of solution used for spin coating: 2 mM in toluene			

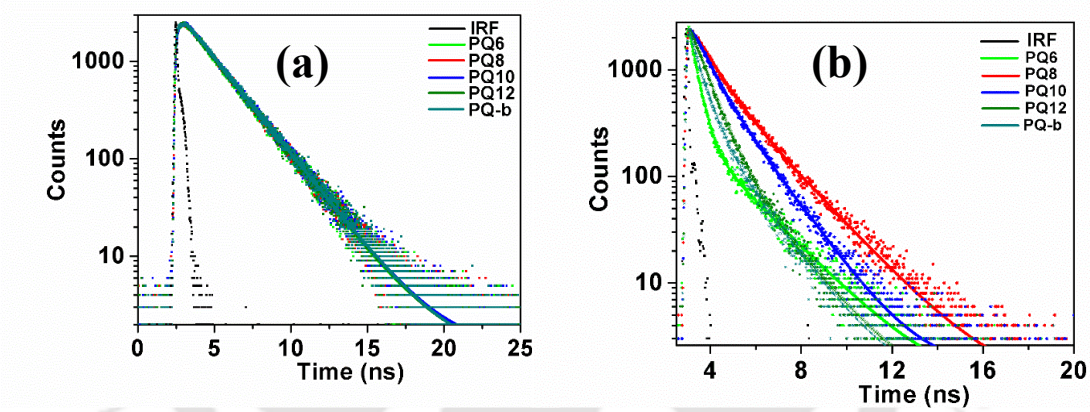

Figure 2.19. Fluorescence decay plots of compounds **PQ6-PQ12** & **PQ-b** in micromolar solution in chloroform (a) and for the spin-coated thin film on quartz plate using a 2mM solution in toluene (b) (IRF: Instrument response function).

Relative quantum yields of compounds **PQ6-PQ12** & **PQ-b** were measured with respect to fluorescein (Q_f = 0.79 in 0.1M NaOH) in chloroform solution as the standard and were found to be around 0.24 (Table 2.6 and Figure 2.20). Relative values were calculated according to the following equation: $Q_S = Q_R \times (m_S / m_R) \times (n_S / n_R)^2$

Where Q: Quantum yield; m: Slope of the plot of integrated fluorescence intensity *vs* absorbance; n_S: refractive index (1.4459 for Chloroform).

The subscript R refers to the reference fluorophore (fluorescein) and subscript S refers to the sample under investigation. In order to minimize re-absorption effects, absorbance was kept below 0.15 at the excitation wavelength of 470 nm.

TH-2983_156122010

The quantum yield of fluorescein is 0.79. A simplified equation for the calculation after substituting the appropriate values is given below and the values obtained are given in the table below.

$Q_S = 0.79 \times (m_S / m_R) \times (1.4459/1.333)^2$

$= 0.79 \times (m_S / m_R) \times 1.1766$

Table 2.6. Relative quantum yields of PQ derivatives

Entry	m_S	m_R	Q_s[a,b,c]
PQ6	7.41679×10^8	2.99056×10^9	0.23
PQ8	7.28837×10^8	2.99056×10^9	0.23
PQ10	7.36019×10^8	2.99056×10^9	0.23
PQ12	7.59768×10^8	2.99056×10^9	0.24
PQ-b	7.71774×10^8	2.99056×10^9	0.24

[a] Measured in Chloroform.
[b]Excited at absorption maxima.
[c]Fluorescein (Q_f = 0.79) in Chloroform.

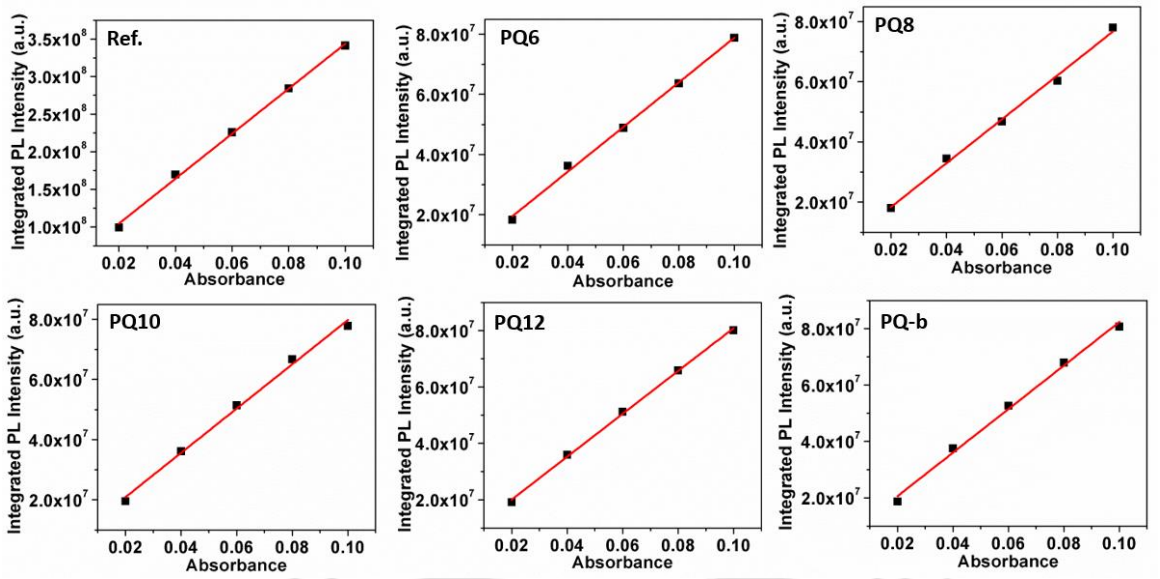

Figure 2.20. Plots of integrated photoluminescence intensity vs absorbance of (**Ref.**) Fluorescein (0.1M NaOH solution) excited at 470 nm; integrated photoluminescence intensity vs absorbance of compounds **PQ6-PQ12** and **PQ-b** (in chloroform solution) excited at 470 nm.

2.2.4. Electrochemical properties and DFT studies

Cyclic voltammetry (CV) studies of **PQ6-PQ12** were carried out to comprehend the electronic energy levels, which are very important in deciding the energy and electron transfer process as well as the reversibility of a redox process. CV studies were carried out in anhydrous dichloromethane solutions in millimolar concentration (Table 2.7 and Figure 2.21). All the compounds exhibited an

TH-2983_156122010

irreversible oxidation potential at ~1.33 to 1.36 V. From this value, the HOMO level was calculated and found to be ~-5.65 to -5.68 eV. LUMO levels were calculated by subtracting the HOMO energy values from the optical band gap (2.38 eV) which was obtained from the absorption onset values. LUMO levels were found to be around -3.27 to -3.30 eV.

Table 2.7. Electrochemical properties of PQ derivatives in solution[a,b]

Compounds	λ_{max} (nm)	λ_{onset} (nm)	E_{1oxd}[e]	E_{HOMO}[c,f]	E_{LUMO}[c,g]	$\Delta E_{g,opt}$[c,d]
PQ6	470	521	1.33	-5.65	-3.27	2.38
PQ8	470	520	1.34	-5.66	-3.28	2.38
PQ10	470	520	1.36	-5.68	-3.30	2.38
PQ12	470	521	1.35	-5.67	-3.29	2.38

[a] Dichloromethane solutions. [b] Experimental conditions: Ag/AgCl as reference electrode, glassy carbon working electrode, platinum wire counter electrode, TBAP (0.1M) as a supporting electrolyte, room temperature. [c] Electron volts (eV). [d] Optical band gap determined from the red edge of the longest wavelength in the UV-visible absorption spectra [$E_{g(eV)}=1240/\lambda_{onset}(nm)$]. [e] in volts(V). [f] Estimated from the formula by using E_{HOMO}= -(4.8-$E_{1/2,Fc/Fc+}$+$E_{oxd,onset}$) eV. [g] Estimated from the formula $E_{LUMO}=E_{HOMO}+E_{g,opt}$ eV; $E_{1/2,\ Fc/Fc+}$ = 0.48.

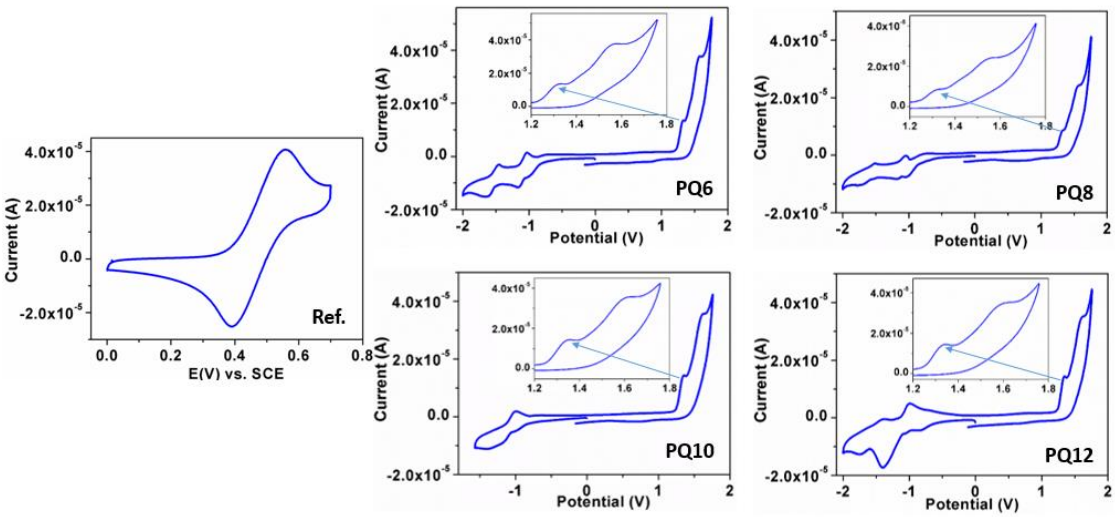

Figure 2.21. Cyclic voltammograms of (**Ref.**) ferrocene and compounds **PQ6-PQ12** in DCM solution of tetra-*n*-butylammonium perchlorate (TBAP) (0.1 M) at a scanning rate 0.1 mV s^{-1}; the half-wave potential of Fc/Fc+ was found to be 0.48 V relative to Ag/Ag+ reference electrode and first oxidation peaks shown by arrow (inset).

From the DFT simulations, it was observed that the cyclized molecules assume a planar shape in comparison to the uncyclized PQ derivatives. Thus, the cyclized version may show enhanced mesophase stabilization (Figure 2.22a-d). Another important observation is the steady decrease of the clearing points among the LC PQ derivatives starting from **PQ8** to **PQ12**. Usually, with the increase in molecular weight, the clearing point is supposed to increase, due to the enhanced van der Waals interactions. But in the

TH-2983_156122010

case of PQ derivatives the core is not planar (Figure 2.22a, c). Thus the increase in the chain length results in the decrease of core-core interactions and the individual disks are dislodged at lower temperature in the case of **PQ12** in comparison to **PQ10** or **PQ8** (Table 2.1 and Figure 2.4).

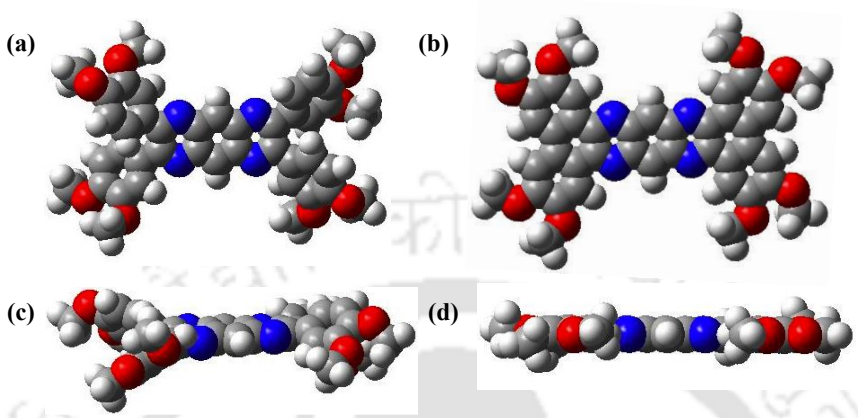

Figure 2.22. Optimized geometry of PQ derivative (chain length is limited to methyl for clarity purpose) (a) top view; (c) side view (note the out of plane orientation of the outer phenyl rings); cyclized version (b) top view and (d) side view (note the planar structure due to cyclization) DFT calculations are performed at B3LYP/6-31G(dp) level.

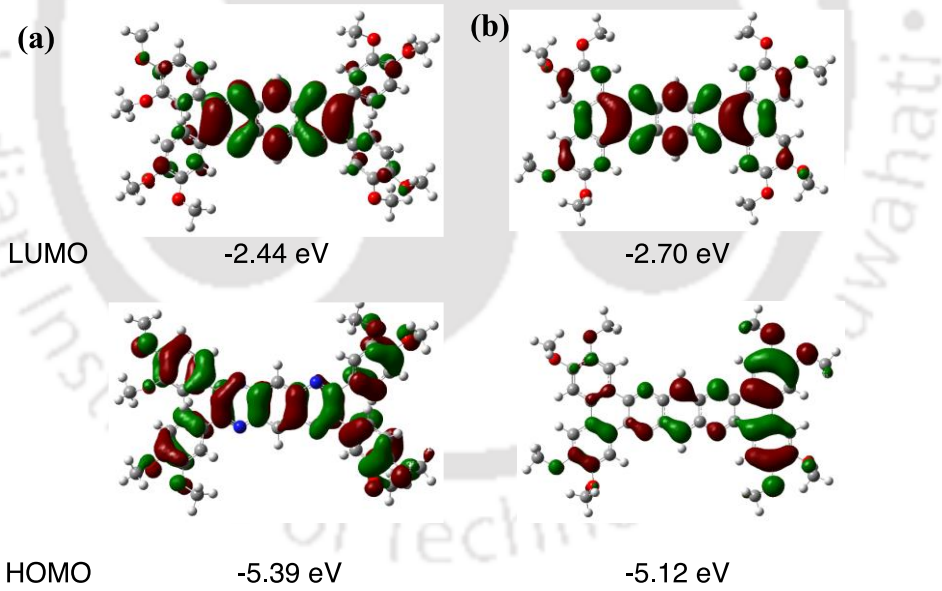

Figure 2.23. HOMO and LUMO levels of PQ derivative (chain length is limited to methyl for clarity purpose) (a); and that of the cyclized version (b) (DFT calculations are performed at B3LYP/6-31G(dp) level).

The DFT calculations were carried out to obtain the energy-minimized structures and the HOMO-LUMO levels (Figure 2.23a, b). It was also curious to know the effect of cyclization on the energy levels of frontier molecular orbitals. The planar molecular structure has been shown to reduce the LUMO level and increase

TH-2983_156122010

the HOMO level, with an overall lowering of band gap from 2.95 eV to 2.42 eV in comparison to the PQ derivative. Another major difference noted was the distribution of HOMO energy levels. In the case of the PQ derivative, the HOMO energy level was distributed throughout the aromatic structure, while such uniform distribution was not seen in the case of cyclized derivative (Figure 2.23b). In the case of LUMO energy levels, the distribution was found to be the same in both cases. In comparison to the energy levels obtained from electrochemistry, the DFT calculations showed an increased LUMO value but a lowered HOMO value. The difference between the two LUMO values calculated (by DFT and cyclic voltammetry) was found to be higher in comparison to the difference in HOMO values. The values of HOMO and LUMO energy levels of PQ derivatives obtained from DFT calculations were in line with the earlier reports.[3]

2.2.5. Electroluminescence studies

To evaluate the potential of **PQ10** as a fluorescent green light-emitting material, a series of OLED devices were fabricated. Figure 2.24a shows the device structures of all the studied OLEDs and their corresponding energy levels diagram. Initially, a non-doped OLED device was fabricated with the following device structure ITO (125 nm)/PEDOT: PSS (35 nm)/PQ (20 nm)/TPBi (35 nm)/LiF (1 nm)/Al (100 nm) and obtained key EL performances are listed in Table 2.8 The designed device was composed of an indium tin oxide (ITO) anode layer (125 nm), followed by a poly(3,4-ethylene-dioxythiophene)-poly(styrenesulfonate) (PEDOT:PSS) hole injection layer (HIL) (35 nm), a single emissive layer (EML) (20 nm) with the synthesized green emitter (**PQ10**) via spin-coating, a 35 nm 1,3,5-tris(N-phenylbenzimidazol-2-yl)benzene (TPBi) electron transporting and hole blocking layer (ETL), a 1 nm lithium fluoride (LiF) layer, and a 100 nm aluminum (Al) cathode layer. The non-doped OLED device showed poor EL performance with broad and red-shifted EL spectra (Figure 2.24b) when compared to PL recorded in micromolar chloroform solution (Figure 2.13b) and on the thin film state obtained by spin coating on quartz plates (Figure 2.13d). The resultant device exhibited a PE of 0.2 lm W^{-1}, a CE of 0.3 cd A^{-1}, an EQE of 0.2% at 100 cd m^{-2} with CIE coordinates of (0.39, 0.48) (Figure 2.25). The poor performance of the non-doped devices may be attributed to the unbalanced charge transport, which results in charge leakage at the interface of electrodes without recombining inside the emitting layer. Hence, to

TH-2983_156122010

improve the EL performance of the **PQ10**, and employed them as dopant emitters in the 4,4'-bis(*N*-carbazolyl)-1,1'-biphenyl (CBP) host matrix with different weight ratios (1 and 7.5 wt%) in the same device structure. Figure 2.24b shows the effect of doping concentrations of the dye **PQ10** on the CBP host containing OLED devices. Besides the CBP host, for comparison, two other hosts, 2,7-bis(carbazol-9-yl)-9,9-ditolylfluorene (Spiro-2CBP) and 4,4',4''-tris(*N*-carbazolyl)triphenylamine (TCTA), were also studied herein. All the fabricated doped OLED devices show green emissions with a major peak centered at 532 nm. Furthermore, as the doping concentration of green emitter decreases from 7.5 to 1 wt%, EL spectra of the fabricated OLED device shifted towards a lower wavelength. The reason for this blue-shift may be attributed to the effective emitter dispersion. The employed host can be utilized to disperse the dopant to prevent the red-shift caused by emitter aggregation. Figure 2.24c shows the electroluminescent (EL) spectra of the best performing OLED device. Figure 2.24d shows the effect of three different molecular hosts on the EL spectra of the composing OLEDs. It is also notable that in all the reported devices no emission corresponding to the host in the deep-blue region can be observed, indicating an efficient host-to-guest energy transfer that has occurred and these three molecular materials prove to be good hosts for the synthesized green emitter.

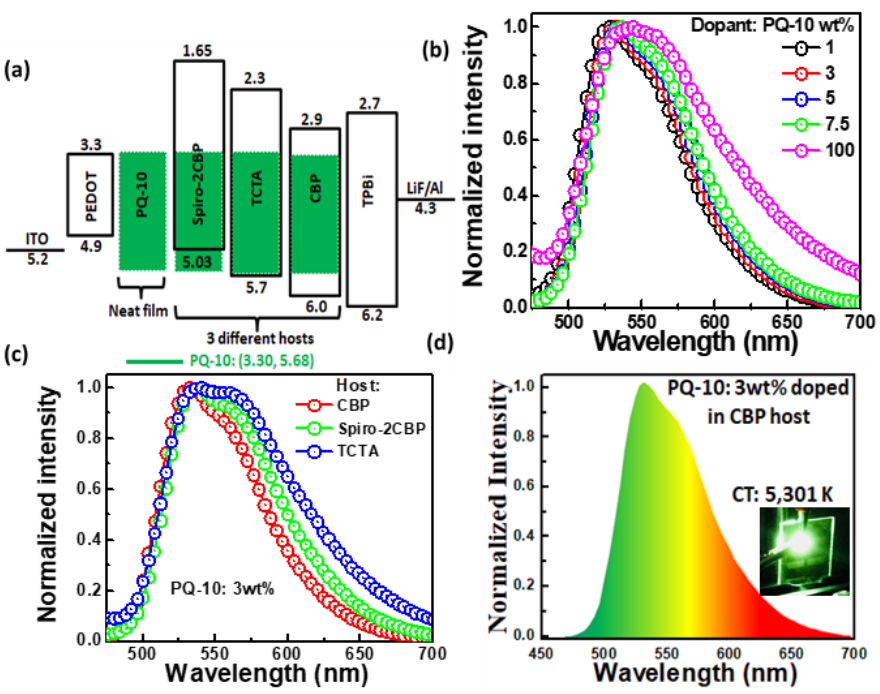

Figure 2.24. (a) Schematic energy-level diagram of the solution-processed green OLEDs (The three different hosts studied were CBP, Spiro-2CBP and TCTA); (b) Doping concentration and (c) host effects on the electroluminescence (EL) spectra of the devices

TH-2983_156122010

containing the green emitter, **PQ10**; (d) EL spectra of the best performing device a 100 cd/m^2 with the OLED device image (inset).

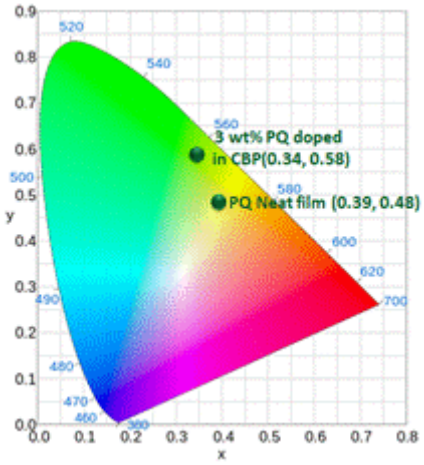

Figure. 2.25. Chromaticity diagram of the device prepared from PQ10 neat film and for the device prepared from the film of 3 wt% PQ in CBP host.

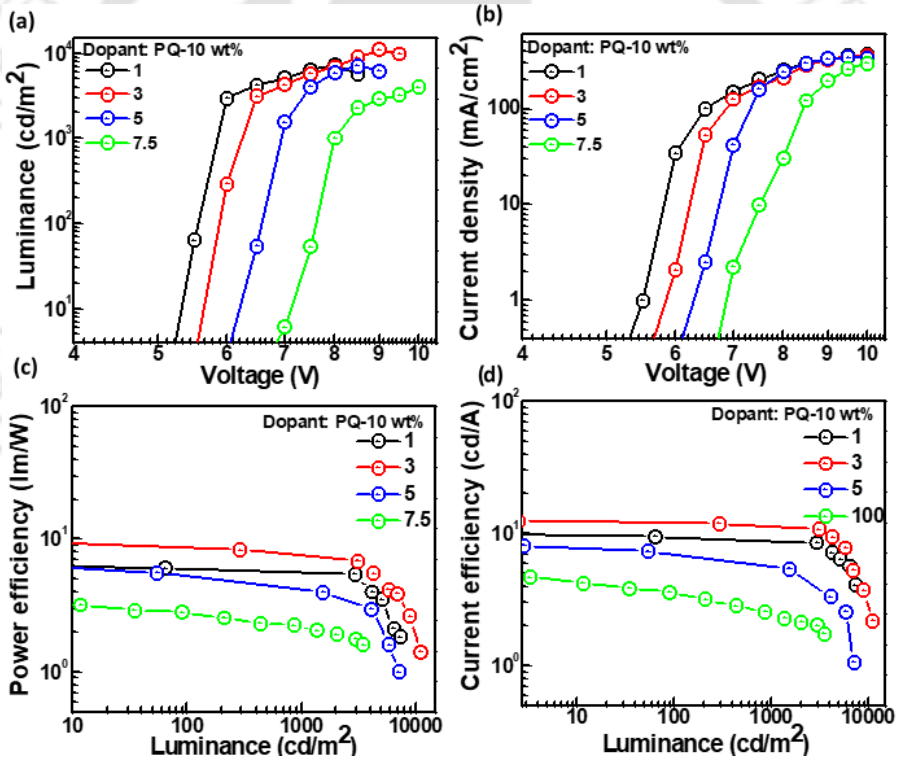

Figure 2.26. Doping concentration effects on the (a) luminance, (b) current density, (c) power efficiency, and (d) current efficiency results of the solution-processed **PQ10** containing green OLED devices.

Table 2.8 displays the sound effects of doping concentrations of the green emitter and employed different molecular host materials on the electroluminescent features of the studied solution processed green OLED devices. The doping concentration of the dye **PQ10** strongly affects the device performance, as shown in

TH-2983_156122010

Figure 2.26. For example, by consuming bipolar CBP as the main matrix, the power efficiency (PE) at 100 cd m^{-2} is increased from 6.0 to 9.3 lm W^{-1} as the doping concentration is augmented from 1 wt% to 3 wt%. One can also note that as the concentration of the dye further increases to 5 and 7.5 wt%, the power efficiency starts to drop, plausibly may be endorsed to triplet–triplet annihilation as well as concentration-quenching. Furthermore, the self-aggregation of the emitter at high concentration also may be reason beyond this efficiency decrement. The different employed molecular host materials also display very different properties on the device performance, as shown in (Figure 2.27). Moreover, very little effect was observed in the resultant EL emission. For example, the resulting PE at 100 cd m^{-2} is 2.3 lm W^{-1} as the TCTA host is employed, and it has increased to 4.3 and 9.3 lm W^{-1} as the host is altered to Spiro-2CBP and CBP, individually.

Table 2.8. Key electroluminescent data of all the fabricated OLED devices consisting of PQ10 as a fluorescent green emitter via cost-effective solution process.

Host	Turn on voltage (V_{on})[a]	Dopant (wt%)	PE_{100}/CE_{100}/ EQE_{100} (lm W^{-1}/ cd A^{-1}/ %)	PE_{1000}/ CE_{1000}/ EQE_{1000} (lm W^{-1}/ cd A^{-1}/ %)	$PE_{max}/CE_{max}/EQE_{max}$ (lm W^{-1}/ cd A^{-1}/ %)[b]	CT(K) (100/1000 cd m^{-2})	CIE_{xy}[c] coordinates	Max. Lum. (cd m^{-2})
-	8.1	100	0.2/0.3/0.2	-/-/-	0.2/0.4/0.2	-/-	(0.39, 0.48)	480
CBP	5.1	1	6/9.5/3.8	5.8/9.2/3.2	6.9/10.0/4.1	5,519/5,603	(0.32, 0.56)	7,296
	5.5	3	9.3/12.3/5.4	7.9/11.7/4.8	9.7/12.4/5.8	5,031/5,136	(0.34, 0.58)	11,052
	6.1	5	5.5/7.3/3.2	4.6/6.1/2.8	6.4/8.0/3.6	4,844/4,978	(0.36, 0.60)	7,140
	7.0	7.5	2.8/3.6/1.9	2.2/2.5/1.4	3.3/4.3/2.1	4,700/4,870	(0.38, 0.60)	3,488
Spiro-2CBP	5.2	3	4.4/8.2/3.1	3.7/6.9/5.3	5.6/9.3/2.9	4,606/4,700	(0.38, 0.54)	6,838
TCTA	3.4	3	2.3/3.2/1.6	1.5/2.8/1.2	3.1/3.4/1.5	4,270/4,571	(0.40, 0.54)	3,260

TH-2983_156122010

It's also worth mentioning that for the same doping concentration, *i.e.* 3 wt%, resulting external quantum efficiency (EQE) is 1.6% when consuming the TCTA as a host, and rises to 3.1 or 5.4% as the host is altered to Spiro-2CBP, or CBP, respectively. The reasons why the bipolar CBP host consisting device shows better efficacy as compared with other counterparts may be four folds, *i.e.*, (1) a low energy trap between the consecutive ETL and emissive layers to facilitate the injection of the electron,[22-23] (2) an effective and complete host-to-guest energy transfer, which was also confirmed by resulting EL spectra,[24-25] (3) the capability of electron-hole pair to generate on both matrix (host) and filler (guest),[26] and (4) an effective hole-confining function because of deeper HOMO level of employed ETL materials.[27-28]

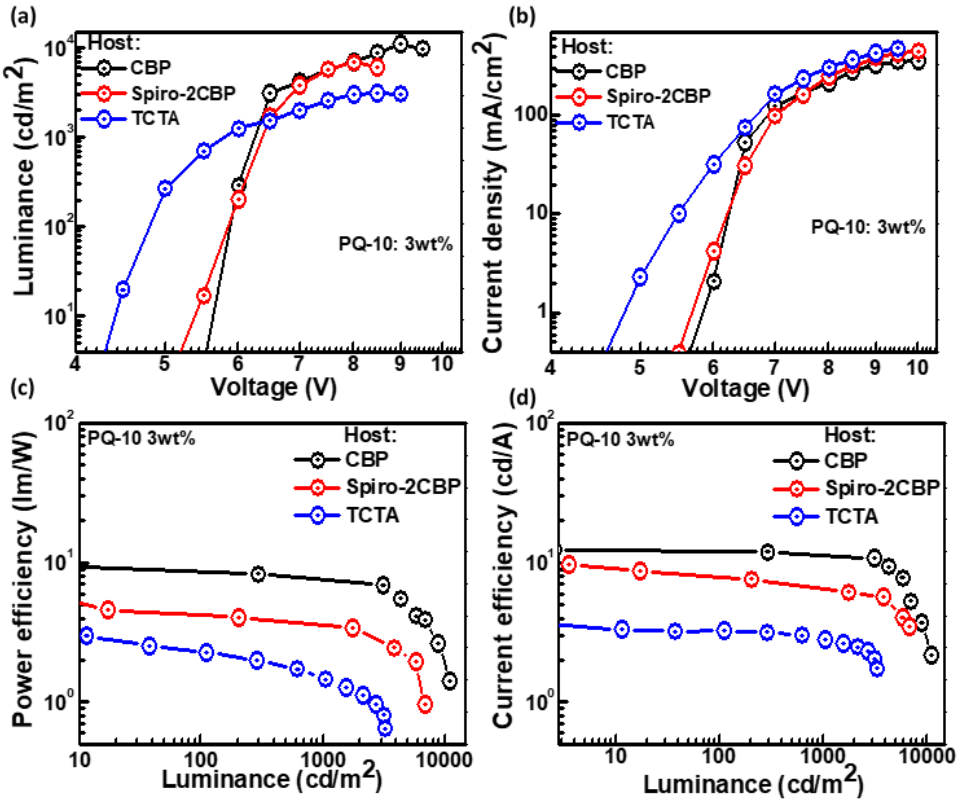

Figure 2.27. Host effects on the (a) luminance, (b) current density, (c) power efficiency, and (d) current efficiency results of the solution-processed **PQ10** containing green OLED devices.

Furthermore, the synthesized green emitter possesses a sufficient low LUMO level, which favors the injection of the minority carriers, *i.e.* electrons, which may also lead to a well-adjusted injection of carriers and facilitate the generation of the excitons in the guest. Nevertheless, it is thought that a noteworthy device performance can only be recognized if a satisfactory amount of excitons are spawned on the employed host. Low energy barrier from both the consecutive charge

TH-2983_156122010

transporting layer in order to improve the number of excitons into the desired recombination zone and balanced charge carrier distribution are the key factors to enable the aforementioned postulates. In the designed device architecture, the CBP host has a supreme electron injection pathway, *i.e.*, it shows a -0.2 eV electron trap rather than a barrier, when compared with other two counterparts, Spiro-2CBP and TCTA, that have the electron injection barrier of 1.05 to 0.4 eV, respectively. Moreover, the electron-trapping character would accordingly enable the injection of electrons, foremost to a well-adjusted carrier injection on the host. Additionally, the CBP host displays relatively higher hole and electron mobilities than the TCTA and the Spiro-2CBP counterparts,[29-31] which lead to a more effective carrier recombination in the emissive zone, hence a higher efficacy and EQE was observed.

The absolute PL quantum efficiency (PLQY) of the emissive layers was measured in the form of a film under nitrogen atmosphere using an integrating sphere.[32] The PLQY value of the neat film of **PQ10** prepared on glass substrate is 80±2%, which is increased to 92±2%, 90±2% and 84±2% as the 3 wt% of **PQ10** doped in CBP, Spiro-2CBP and TCTA host respectively. These results indicate that judicious host selection could boost PLQY values, which favor the generation of exciton in the recombination, hence enhanced device performance, especially when compared with non-doped device.

The standard method to fabricate OLEDs is a vacuum thermal deposition, but this method is expensive and leads to the inefficient usage of materials. In this regard, solution process to fabricate OLED devices is attracting considerable attention owing to its superb features such as low-cost, roll-to-roll fabrication, large area manufacturing and simple device structures. However, this technique is facing problems with availability of solution processable small molecules with high quantum efficiency and purity. Considering the molecular structure of **PQ10**, it provides an improved solubility in common green solvent, making it highly solution processable. In addition, its excellent photophysical properties, appropriate molecular orbital energy level, self-healing ability from defects due to the fluidic columnar self-assembly makes this class of molecules promising for the fabrication of solution processable OLEDs. One of the best-optimized OLED device displayed an EQE higher than that theoretical limit of fluorescent molecules, *i.e.* 5%. Since the efficiency of the OLED device depends on efficient charge transport from the hole transport layer and electron transparent layer into an emitter layer. Within the emitter layer, charge migrates via hopping process from orbital of one molecule to another. In this regard, materials having

TH-2983_156122010

columnar self-assembly are advantageous to enhance the device performance due to the higher charge carrier mobility (advantageous for hopping process in emitter layer), caused by the long-range order of columnar structure. Though the **PQ10** as a single emitting layer did not show appreciable efficiency, further improvements in the molecular structure to improve the charge recombination in addition to columnar self-assembly may enhance its applicability.

2.3. Conclusion

In conclusion, a series of PQ derivatives were synthesized and characterized that self-assemble to form 1D columns of indefinite length with many of the derivatives stabilizing the room temperature columnar phase. The length of the peripheral tails was varied in order to understand its effect on photophysical and thermal behavior. All the PQ derivatives typically exhibit lower isotropic temperatures (< 100 ^{o}C), which is mainly due to the out of plane conformation of the phenyl rings of PQ derivatives. DFT calculations showed that cyclized derivatives may show planar shape and lower band gap in comparison to PQ derivatives. This is due to the decreased LUMO and increased HOMO energy levels upon cyclization. PQ derivatives with shorter peripheral flexible chains (**PQ6**) and with branched flexible chains (**PQ-b**) turned to be non-liquid crystalline. The molecular structure of PQ derivatives makes them sensitive even to a small change in the nature of peripheral tails in stabilizing the liquid crystallinity. These compounds exhibited columnar phases of rectangular, oblique or hexagonal lattice. Only the PQ derivatives with medium to longer flexible chains exhibited the columnar phase. All the compounds exhibited high absorption coefficient and large Stokes shift. These compounds emitted in the yellow region with a good quantum yield. However, the **PQ10** compound for OLED device exhibited a high solid state PLQY value, which further increased on doping to different host materials. One of the best-optimized OLED device displayed an EQE higher than that theoretical limit of fluorescent molecules, *i.e.* 5%. All these qualities make these materials promising towards their application as solid-state light emissive display materials. Further improvements in the molecular structure to improve the charge recombination in addition to columnar self-assembly may improve their applicability in OLEDs. Further synthetic tuning to unravel the structure-property relationships will be undertaken in future.

TH-2983_156122010

2.4. Experimental section

In this section the detailed synthesis procedure and the molecular structural characterization data have been presented for the intermediates and target compounds mentioned in the scheme.

Synthesis of 3,3´,4,4´-tetramethoxy benzil (1)[15]

To a 250 ml two neck dried round-bottom flask (RB) under argon containing solution of veratrole (36.189 mmol, 1.0 equiv.) in 1,2-dichloroethane (40 mL), was added oxalyl chloride (21.71 mmol, 0.6 equiv.) by syringe at 0 ^{o}C. The reaction mixture was kept at 0 ^{o}C for 10 min, and then anhyd. $AlCl_3$ (18.10 mmol, 0.5 equiv.) was added. After 30 min at 0 ^{o}C, the reaction mixture was allowed to reach room temperature and stayed for overnight. The reaction mixture was then poured into 100 mL HCl (1M) solution. The organic layer was then extracted twice with dichloromethane (DCM) and dried with anhydrous sodium sulfate and concentrated. This crude product was purified in column chromatography with silica gel and eluted with 50-70% DCM-hexane to get the pure product. Removal of solvent yielded a yellow solid.

1: *Rf* = 0.39 (70% DCM-Hexane); Pale yellowish solid, yield: 57%; IR (KBr pellet) ν_{max} in cm^{-1} 3016, 2967, 2932, 2851, 1658, 1593, 1585, 1515, 1450, 1417, 1352, 1269, 1230, 1141, 1013, 871, 790, 726, 639, 580, 432; ^{1}H NMR (600 MHz, $CDCl_3$, 299 K): 7.60-7.60 (d, J = 1.80 Hz, 2H, H_{Ar}), 7.49-7.47 (dd, J_1 = 8.40 Hz, J_2 = 1.80 Hz, 2H, H_{Ar}), 6.89-6.88 (d, J = 8.40 Hz, 2H, H_{Ar}), 3.96 (s, 6H, 2 × -OCH_3), 3.96 (s, 6H, 2 × -OCH_3); ^{13}C NMR (150 MHz, $CDCl_3$, 298.1K): 193.52, 154.78, 149.49, 126.41, 126.35, 110.26, 110.18, 56.24, 56.08; HRMS (+ESI mode) exact mass calculated for $C_{18}H_{18}O_6$ ($M+H^+$): 331.1176, found: 331.1283.

Synthesis of 3,3´,4,4´-tetrahydroxy benzil (2)[18]

Compound **1** (6.00 g, 18.1 mmol), 47% hydrobromic acid (50 mL) and glacial acetic acid (50 mL) were taken in 250 ml RB flask and refluxed for 16 h. After cooling to room temperature, the reaction mixture was extracted with ether and neutralized with 50 mL NaOH (1M) solution. The organic layer was dried with anhydrous sodium sulfate and concentrated. The crude product was recrystallized with water, which yielded a greenish solid.

TH-2983_156122010

2: Pale greenish solid, yield: 80%; IR (KBr pellet) ν_{max} in cm^{-1} 3393, 1649, 1590, 1526, 1442, 1402, 1293, 1193, 1169, 1115, 985, 881, 812, 745, 631, 569; HRMS (+ESI mode) exact mass calculated for $C_{14}H_{10}O_6$ ($M+Na^+$): 297.0369, found: 297.0456.

Synthesis of 3,3´,4,4´-tetrakis(alkyloxy)benzil (3a, 3b, 3c, 3d & 3e)[18]

Into a 100 mL RB flask, anhydrous K_2CO_3 (8.8 equiv.), compound **2** (1.0 equiv.), appropriate 1-bromoalkanes (4.4 equiv.), catalytic amount of KI and anhydrous *N*,*N*-dimethylformamide (40 mL) were placed and the reaction mixture was stirred at 80 °C under nitrogen atmosphere for 17 h. The reaction mixture was extracted with ethyl acetate and washed with water and dried over anhydrous sodium sulfate. Then solvent is evaporated. The crude product was purified by column chromatography on silica gel. Eluting with 2-5% ethyl acetate-hexane mixture and evaporation provided the product in 85-90% yield.

3a: R_f = 0.5 (5% EtOAc-Hexane); White solid, yield: 85%; IR (KBr pellet) ν_{max} in cm^{-1} 2952, 2925, 2858, 2869, 1663, 1595, 1585, 1513, 1465, 1432, 1306, 1264, 1147, 1072, 1043, 994, 758, 711, 653; ^{1}H NMR (600 MHz, $CDCl_3$, 299 K): 7.57-7.56 (d, J = 1.80 Hz, 2H, H_{Ar}), 7.44-7.42 (dd, J_1 = 8.40 Hz, J_2 = 1.80 Hz, 2H, H_{Ar}), 6.85-6.84 (d, J = 8.40 Hz, 2H, H_{Ar}), 4.07-4.04 (m, 8H, 4 × -OCH_2), 1.86-1.81 (m, 8H, 4 × -OCH_2-CH_2), 1.49-1.44 (m, 8H, alkyl chain), 1.37-1.32 (m, 16H, alkyl chain), 0.92-0.89 (m, 12H, 4 × -CH_3); ^{13}C NMR (150 MHz, $CDCl_3$, 298.1K): 194.04, 155.19, 149.50, 126.39, 126.34, 112.45, 111.78, 69.43, 69.32, 31.75, 31.70, 29.23, 29.09, 25.85, 25.79, 22.80, 22.77, 14.22, 14.19; HRMS (+ESI mode) exact mass calculated for $C_{38}H_{58}O_6$ ($M+H^+$): 611.4306, found: 611.4483.

3b: R_f = 0.52 (5% EtOAc-Hexane); White solid, yield: 86%; IR (KBr pellet) ν_{max} in cm^{-1} 2952, 2923, 2852, 1664, 1595, 1513, 1465, 1431, 1390, 1264, 1146, 1066, 1015, 961, 812, 758, 711, 653; ^{1}H NMR (600 MHz, $CDCl_3$, 299 K): 7.56-7.56 (d, J = 2.40 Hz, 2H, H_{Ar}), 7.43-7.41 (dd, J_1 = 8.40 Hz, J_2 = 1.80 Hz, 2H, H_{Ar}), 6.85-6.83 (d, J = 9.00 Hz, 2H, H_{Ar}), 4.06-4.04 (m, 8H, 4 × -OCH_2), 1.86-1.81 (m, 8H, 4 × -OCH_2-CH_2), 1.49-1.43 (m, 8H, alkyl chain), 1.38-1.33 (m, 8H, alkyl chain), 1.32-1.25 (m, 24H, alkyl chain), 0.90-0.86 (m, 12H, 4× -CH_3); ^{13}C NMR (150 MHz, $CDCl_3$, 298.1K): 194.06, 155.15, 149.46, 126.38, 126.33, 112.31, 111.70, 69.41, 69.31, 32.03, 32.00, 29.56, 29.51, 29.49, 29.45, 29.26, 29.11, 26.19, 26.12, 22.90, 22.88, 14.35, 14.33; HRMS (+ESI mode) exact mass calculated for $C_{46}H_{74}O_6$ ($M+H^+$): 723.5558, found: 723.5816.

TH-2983_156122010

3c: R_f = 0.55 (5% EtOAc-Hexane); White solid, yield: 88%; IR (KBr pellet) ν_{max} in cm^{-1} 2952, 2922, 2850, 1664, 1594, 1512, 1466, 1431, 1390, 1264, 1147, 1071, 1021, 984, 811, 756, 712, 654; ^{1}H NMR (600 MHz, $CDCl_3$, 299 K): 7.56-7.56 (d, J = 1.2 Hz, 2H, H_{Ar}), 7.43-7.41 (dd, J_1 = 8.40 Hz, J_2 = 1.80 Hz, 2H, H_{Ar}), 6.85-6.83 (d, J = 8.40 Hz, 2H, H_{Ar}), 4.06-4.04 (m, 8H, 4 × -OCH_2), 1.86-1.81 (m, 8H, 4 × -OCH_2-CH_2), 1.49-1.43 (m, 8H, alkyl chain), 1.35-1.33 (m, 8H, alkyl chain), 1.30-1.27 (m, 40H, alkyl chain), 0.89-0.86 (m, 12H, 4 × -CH_3); ^{13}C NMR (150 MHz, $CDCl_3$, 298.1K): 193.86, 154.94, 149.26, 126.18, 126.13, 112.11, 111.50, 69.20, 69.10, 31.93, 31.91, 29.63, 29.59, 29.56, 29.40, 29.37, 29.34, 29.05, 28.90, 25.98, 25.91, 22.71, 22.69, 14.14, 14.13; HRMS (+ESI mode) exact mass calculated for $C_{54}H_{90}O_6$ ($M+H^+$): 835.6810, found: 835.7074.

3d: R_f = 0.58 (5% EtOAc-Hexane); White solid, yield: 90%; IR (KBr pellet) ν_{max} in cm^{-1} 2951, 2921, 2850, 1664, 1594, 1513, 1466, 1431, 1391, 1265, 1146, 1073, 875, 756, 715, 654; ^{1}H NMR (600 MHz, $CDCl_3$, 299 K): 7.57-7.56 (d, J = 1.80 Hz, 2H, H_{Ar}), 7.43-7.41 (dd, J_1 = 8.40 Hz, J_2 = 1.80 Hz, 2H, H_{Ar}), 6.85-6.83 (d, J = 8.40 Hz, 2H, H_{Ar}), 4.06-4.04 (m, 8H, 4 × -OCH_2), 1.86-1.81 (m, 8H, 4 × -OCH_2-CH_2), 1.49-1.43 (m, 8H, alkyl chain), 1.38-1.33 (m, 8H, alkyl chain), 1.28-1.25 (m, 56H, alkyl chain), 0.89-0.86 (m, 12H, 4 × -CH_3); ^{13}C NMR (150 MHz, $CDCl_3$, 298.1K): 193.85, 154.94, 149.26, 126.18, 126.13, 112.11, 111.49, 69.20, 69.10, 31.94, 31.93, 29.72, 29.69, 29.68, 29.66, 29.64, 29.61, 29.60, 29.41, 29.39, 29.38, 29.35, 28.90, 25.99, 25.92, 22.71, 14.15; MALDI-TOF exact mass calculated for $C_{62}H_{106}O_6$ ($M+Na^+$): 969.7881, found: 970.0880.

3e: R_f = 0.61 (5% EtOAc-Hexane); Colorless viscous liquid, yield: 85%; IR (KBr pellet) ν_{max} in cm^{-1} 2954, 2927, 2870, 1661, 1592, 1512, 1466, 1430, 1384, 1266, 1139, 1046, 1014, 876, 725, 641; ^{1}H NMR (600 MHz, $CDCl_3$, 299 K): 7.58-7.58 (d, J = 1.80 Hz, 2H, H_{Ar}), 7.44-7.42 (dd, J_1 = 8.40 Hz, J_2 = 1.80 Hz, 2H, H_{Ar}), 6.86-6.84 (d, J = 8.40 Hz, 2H, H_{Ar}), 4.12-4.05 (m, 8H, 4 × -OCH_2), 1.90-1.87 (m, 4H, alkyl chain), 1.70-1.62 (m, 8H, alkyl chain), 1.54-1.50 (m, 4H, alkyl chain), 1.34-1.25 (m, 12H, alkyl chain), 1.18-1.12 (m, 12H, alkyl chain), 0.95-0.93 (t, J = 6.60 Hz, 12H, 4 × -CH_3), 0.88-0.83 (m, 24H, 8 × -CH_3); ^{13}C NMR (150 MHz, $CDCl_3$, 298.1K): 193.80, 154.88, 149.25, 126.17, 126.11, 111.88, 111.36, 67.50, 67.49, 67.45, 39.20, 39.17, 37.29, 37.26, 37.25, 37.22, 35.96, 35.94, 35.76, 35.74, 29.91, 29.89, 29.86, 29.84, 27.96, 27.94, 24.70, 24.70, 24.67, 22.69, 22.67, 22.59, 22.58, 19.68, 19.62; HRMS (+ESI mode) exact mass calculated for $C_{54}H_{90}O_6$ ($M+H^+$): 835.6810, found: 835.7052.

TH-2983_156122010

Synthesis of 2,3,7,8-tetrakis(3,4-bis(alkyloxy)phenyl)pyrazino[2,3-g]quinoxaline (PQ6, PQ8, PQ10, PQ12 & PQ-b)[33]

Compounds **3a, 3b, 3c, 3d & 3e** (2.1 equiv.) and benzene-1,2,3,4-tetraamine tetrahydrochloride (1.0 equiv.) were transferred into a 50 mL two neck RB flask with 4 mL methanol and 12 mL acetic acid (1:3) under argon atmosphere, which was heated to 100 ^{o}C. After addition of 1.0 mL of triethylamine further refluxed at 130 ^{o}C for 12 h. and concentrated the reaction mixture. The crude product was purified by column chromatography on neutral alumina with 2-5% ethyl acetate-hexane, to yield a yellow solid.

PQ6: R_f = 0.54 (10% EtOAc-Hexane); Yellowish solid, yield: 77%; IR (KBr pellet) ν_{max} in cm^{-1} 2928, 2859, 1635, 1600, 1518, 1473, 1459, 1419, 1399, 1342, 1259, 1192, 1138, 1123, 1060, 1041, 1023, 927, 877, 802, 727, 624; ^{1}H NMR (600 MHz, $CDCl_3$, 299 K): 8.89 (s, 2H, H_{Ar}), 7.20-7.19 (dd, J_1 = 8.10 Hz, J_2 = 1.80 Hz, 4H, H_{Ar}), 7.16-7.15 (d, J = 1.80 Hz, 4H, H_{Ar}), 6.87-6.86 (d, J = 8.40 Hz, 4H, H_{Ar}), 4.03-4.01 (t, 8H, J = 6.60 Hz, 4 × -OCH_2), 3.87-3.85 (t, J = 6.60 Hz, 8H, 4 × -OCH_2), 1.86-1.81 (m, 8H, 4 × -OCH_2-CH_2), 1.76-1.72 (m, 8H, 4 × -OCH_2-CH_2), 1.50-1.45 (m, 8H, alkyl chain), 1.45-1.40 (m, 8H, alkyl chain), 1.37-1.31 (m, 32H, alkyl chain), 0.92-0.89 (m, 24H, 8 × -CH_3); ^{13}C NMR (150 MHz, $CDCl_3$, 298.1K): 154.72, 150.32, 148.69, 140.20, 131.53, 127.90, 123.10, 115.25, 112.97, 77.23, 77.02, 76.81, 69.19, 69.16, 53.44, 31.62, 31.57, 29.71, 29.17, 29.12, 29.09, 25.69, 22.65, 22.63, 14.05; MALDI-TOF exact mass calculated for $C_{82}H_{118}N_4O_8$ ($M+H^+$): 1287.9023, found: 1287.9160. Elemental analysis calculated (%) for $C_{82}H_{118}N_4O_8$: C, 76.48; H, 9.24; N, 4.35. Found: C, 76.16; H, 8.93; N, 4.18.

PQ8: R_f = 0.57 (10% EtOAc-Hexane); Yellowish solid, yield: 79%; IR (KBr pellet) ν_{max} in cm^{-1} 2923, 2854, 1599, 1518, 1468, 1419, 1341, 1261, 1218, 1192, 1138, 1123, 1071, 1023, 998, 878, 804, 722, 624; ^{1}H NMR (600 MHz, $CDCl_3$, 299 K): 8.89 (s, 2H, H_{Ar}), 7.21-7.19 (dd, J_1 = 8.40 Hz, J_2 = 1.80 Hz, 4H, H_{Ar}), 7.15-7.15 (d, J = 1.80 Hz, 4H, H_{Ar}), 6.87-6.86 (d, J = 8.40 Hz, 4H, H_{Ar}), 4.03-4.01 (t, J = 6.60 Hz, 8H, 4 × -OCH_2), 3.87-3.84 (t, J = 6.60 Hz, 8H, 4 × -OCH_2), 1.86-1.81 (m, 8H, 4 × -OCH_2-CH_2), 1.76-1.72 (m, 8H, 4 × -OCH_2-CH_2), 1.50-1.45 (m, 8H, alkyl chain), 1.43-1.39 (m, 8H, alkyl chain), 1.37-1.25 (m, 64H, alkyl chain), 0.90-0.87 (m, 24H, 8 × -CH_3); ^{13}C NMR (150 MHz, $CDCl_3$, 298.1K): 154.74, 150.26, 148.62, 140.17, 131.44, 127.86, 123.08, 115.13, 112.87, 77.23, 77.02, 76.81, 69.15, 69.12, 31.86, 31.84, 29.71, 29.42, 29.39, 29.36, 29.30, 29.18, 29.11, 26.03, 26.02, 22.71, 22.69, 14.14; MALDI-TOF exact mass calculated for $C_{98}H_{150}N_4O_8$ ($M+H^+$):

TH-2983_156122010

1512.1527, found: 1512.1430. Elemental analysis calculated (%) for $C_{98}H_{150}N_4O_8$: C, 77.83; H, 10.00; N, 3.70. Found: C, 78.05; H, 9.86; N, 3.55.

PQ10: R_f = 0.60 (10% EtOAc-Hexane); Yellowish solid, yield: 80%; IR (KBr pellet) ν_{max} in cm^{-1} 2921, 2852, 1599, 1551, 1517, 1470, 1404, 1343, 1259, 1192, 1138, 1019, 878, 803, 721, 625; ^{1}H NMR (600 MHz, $CDCl_3$, 299 K): 8.89 (s, 2H, H_{Ar}), 7.21-7.19 (dd, J_1 = 8.40 Hz, J_2 = 1.80 Hz, 4H, H_{Ar}), 7.15-7.15(d, J = 2.40 Hz, 4H, H_{Ar}), 6.87-6.86 (d, J = 8.40 Hz, 4H, H_{Ar}), 4.03-4.01 (t, J = 6.60 Hz, 8H, 4 × -OCH_2), 3.86-3.84 (t, J = 6.60 Hz, 8H, 4 × -OCH_2), 1.86-1.81 (m, 8H, 4 × -OCH_2-CH_2), 1.76-1.71 (m, 8H, 4 × -OCH_2-CH_2), 1.49-1.44 (m, 8H, alkyl chain), 1.43-1.39 (m, 8H, alkyl chain), 1.37-1.27 (m, 96H, alkyl chain), 0.90-0.86 (m, 24H, 8 × -CH_3); ^{13}C NMR (150 MHz, $CDCl_3$, 298.1K): 154.94, 150.46, 148.83, 140.38, 131.66, 128.09, 123.28, 115.35, 113.09, 77.44, 77.23, 77.02, 69.36, 69.33, 32.16, 32.14, 29.93, 29.87, 29.85, 29.83, 29.69, 29.66, 29.63, 29.59, 29.40, 29.32, 26.25, 26.24, 22.92, 14.35; MALDI-TOF exact mass calculated for $C_{114}H_{182}N_4O_8$ ($M+H^+$): 1736.4031, found: 1736.4310. Elemental analysis calculated (%) for $C_{114}H_{182}N_4O_8$: C, 78.84; H, 10.56; N, 3.23. Found: C, 78.74; H, 10.51; N, 3.18.

PQ12: R_f = 0.63 (10% EtOAc-Hexane); Yellowish solid, yield: 85%; IR (KBr pellet) ν_{max} in cm^{-1} 2920, 2852, 1600, 1517, 1469, 1420, 1402, 1343, 1259, 1193, 1139, 1022, 878, 804, 720, 624; ^{1}H NMR (600 MHz, $CDCl_3$, 299 K): 8.89 (s, 2H, H_{Ar}), 7.21-7.19 (dd, J_1 = 8.40 Hz, J_2 = 1.80 Hz, 4H, H_{Ar}), 7.15-7.14 (d, J = 2.40 Hz, 4H, H_{Ar}), 6.87-6.86 (d, J = 8.40 Hz, 4H, H_{Ar}), 4.03-4.01 (t, J = 6.60 Hz, 8H, 4 × -OCH_2), 3.86-3.84 (t, J = 6.60 Hz, 8H, 4 × -OCH_2), 1.86-1.81 (m, 8H, 4 × -OCH_2-CH_2), 1.76-1.71 (m, 8H, 4 × -OCH_2-CH_2), 1.49-1.44 (m, 8H, alkyl chain), 1.42-1.39 (m, 8H, alkyl chain), 1.36-1.26 (m, 128H, alkyl chain), 0.89-0.86 (m, 24H, 8 × -CH_3); ^{13}C NMR (150 MHz, $CDCl_3$, 298.1K): 154.94, 150.47, 148.83, 140.39, 131.67, 128.10, 123.28, 115.37, 113.11, 69.36, 69.34, 32.16, 30.00, 29.95, 29.93, 29.91, 29.89, 29.70, 29.67, 29.63, 29.61, 29.41, 29.33, 26.26, 22.93, 14.36; MALDI-TOF exact mass calculated for $C_{130}H_{214}N_4O_8$ ($M+H^+$): 1960.6535, found: 1960.5680. Elemental analysis calculated (%) for $C_{130}H_{214}N_4O_8$: C, 79.62; H, 11.00; N, 2.86. Found: C, 79.78; H, 11.20; N, 2.64.

PQ-b: R_f = 0.69 (10% EtOAc-Hexane); Yellowish waxy liquid, yield: 75%; IR (KBr pellet) ν_{max} in cm^{-1} 2955, 2926, 2869, 1600, 1515, 1466, 1425, 1384, 1340, 1261, 1215, 1138, 1138, 1048, 1017, 933, 877, 810, 657, 623; ^{1}H NMR (600 MHz, $CDCl_3$, 299 K): 8.91 (s, 2H, H_{Ar}), 7.23-7.21 (d, J = 8.40 Hz, 4H, H_{Ar}), 7.18 (s, 4H, H_{Ar}), 6.88-6.87 (d, J = 8.4 Hz,

TH-2983_156122010

4H, H_{Ar}), 4.09-4.02 (m, 8H, 4 × -OCH_2), 3.93-3.86 (m, 8H, 4 × -OCH_2), 1.91-1.87 (m, 4H, 2 × -OCH_2-CH_2), 1.85-1.80 (m, 4H, 2 × -OCH_2-CH_2), 1.70-1.62 (m, 12H, alkyl chain), 1.58-1.50 (m, 12H, alkyl chain), 1.38-1.25 (m, 24H, alkyl chain), 1.19-1.15 (m, 24H, alkyl chain), 0.97-0.95 (d, J = 6.60 Hz, 12H, 4 × -CH_3), 0.92-0.91 (d, J = 6.60 Hz, 12H, 4 × -CH_3), 0.89-0.86 (m, 48H, 16 × -CH_3); ^{13}C NMR (150 MHz, $CDCl_3$, 298.1K): 154.72, 150.23, 148.60, 140.17, 131.39, 127.85, 123.00, 114.90, 112.64, 67.41, 39.23, 37.37, 37.35, 36.07, 36.05, 36.00, 35.99, 29.94, 29.68, 29.64, 27.98, 27.97, 24.75, 24.71, 22.71, 22.61, 19.69, 19.58; MALDI-TOF exact mass calculated for $C_{114}H_{182}N_4O_8$ ($M+H^+$): 1736.4031, found: 1737.7730. Elemental analysis calculated (%) for $C_{114}H_{182}N_4O_8$: C, 78.84; H, 10.56; N, 3.23. Found: C, 78.65; H, 10.76; N, 3.15.

2.5. References

1. J. Roncali, *Macromol. Rapid Commun.*, 2007, **28**, 1761-1775.
2. A. Ajayaghosh, *Chem. Soc. Rev.*, 2003, **32**, 181-191.
3. T. L. Tam, F. Zhou, H. Li, J. C. Y. Pang, Y. M. Lam, S. G. Mhaisalkar, H. Su and A. C. Grimsdale, *J. Mater. Chem.*, 2011, **21**, 17798-17804.
4. K. Takazawa, Y. Kitahama, Y. Kimura and G. Kido, *Nano Lett.*, 2005, **5**, 1293-1296.
5. K. Takazawa, *J. Phys. Chem. C*, 2007, **111**, 8671-8676.
6. A. N. Lebedenko, G. Y. Guralchuk, A. V. Sorokin, S. L. Yefimova and Y. V. Malyukin, *J. Phys. Chem. B*, 2006, **110**, 17772-17775.
7. Y. S. Zhao, J. Xu, A. Peng, H. Fu, Y. Ma, L. Jiang and J. Yao, *Angew. Chem., Int. Ed*. 2008, **47**, 7301-7305.
8. Y. S. Zhao, A. Peng, H. Fu, Y. Ma and J. Yao, *Adv. Mater.*, 2008, **20**, 1661-1665.
9. Q. Liao, H. Fu, and J. Yao, *Adv. Mater.*, 2009, **21**, 4153-4157.
10. Y. Che, X. Yang, K. Balakrishnan, J. Zuo and L. Zang, *Chem. Mater.*, 2009, **21**, 2930-2934.
11. X. Wang, Y. Zhou, T. Lei, N. Hu, E.-Q. Chen and J. Pei, *Chem. Mater.*, 2010, **22**, 3735-3745.
12. F. Moreau, D. I. Kolokolov, A. G. Stepanov, T. L. Easun, A. Dailly, W. Lewis, A. J. Blake, H. Nowell, M. J. Lennox, E. Besley, S. Yang and M. Schröder, *Proc. Natl. Acad. Sci. U.S.A.*, 2017, **114**, 123056-123061.
13. T. Wöhrle, I. Wurzbach, J. Kirres, A. Kostidou, N. Kapernaum, J. Litterscheidt, J. C. Haenle, P. Staffeld, A. Baro, F. Giesselmann and S. Laschat, *Chem Rev.*, 2016, **116**, 1139-1241.
14. R. K. Gupta and A. S. Achalkumar, *Langmuir*. 2018, **35**, 2455-2479.
15. T. T. Bui, O. Thiebaut, E. Grelet, M. F. Achard, B. G. D. Bonnevel and K. I. M. C. Ching, *Eur. J. Inorg. Chem.*, 2011**, *17*, *2663-2676.***
16. I. Hisaki, N. Q. E. Affendy and N. Tohnai, *Cryst Eng Comm*., 2017, **19**, 4892-4898.

TH-2983_156122010

17. R. K. Gupta, D. Das, M. Gupta, S. K. Pal, P. K. Iyer, A. S. Achalkumar, *J. Mater. Chem. C*, 2017, **5**, 1767-1781.
18. M. Ichihara, M. Miida, B. Mohr and K. Ohta, *J. Porphyrins Phthalocyanines*, 2006, **10**, 1145-1155.
19. M. Kasha, H. R. Rawls, and M. A. EL-Bayoumi, *Pure Appl. Chem.*, 1965, **11**, 371.
20. F. C. Spano, *Acc. Chem. Res.*, 2010, **43**, 429-439.
21. S. K. Pathak, S. Nath, R. K. Gupta, D. S. S. Rao, S. K. Prasad and A. S. Achalkumar, *J. Mater. Chem. C*, 2015, **3**, 8166-8182.
22. M. Gross, D. C. Muller, H. G. Nothofer, U. Scherf, D. Neher, C. Brauchle and K. Meerholz, *Nature*., 2000, **405**, 661-665.
23. H. Yanagi, M. Kikuchi, K. B. Kim, H. Hiramatsu, T. Kamiya, M. Hirano and H. Hosono, *Org. Electron.*, 2008, **9**, 890-894.
24. S. J. Yeh, M. F. Wu, C. T. Chen, Y. H. Song, Y. Chi, M. H. Ho, S. F. Hsu and C. H. Chen, *Adv. Mater.*, 2005, **17**, 285-289.
25. J. H. Jou, M. F. Hsu, W. B. Wang, C. L. Chin, Y. C. Chung, C. T. Chen, J. J. Shyue, S. M. Shen, M. H. Wu, W. C. Chang, C. P. Liu, S. Z. Chen and H. Y. Chen, *Chem. Mater.*, 2009, **21**, 2565-2567.
26. J. H. Jou, Y. M. Yang, S. Z. Chen, J. R. Tseng, S. H. Peng, C. Y. Hsieh, Y. X. Lin, C. L. Chin, J. J. Syue, S. S. Sun, C. T. Chen, C. W. Wang, C. C. Chen, S. H. Lai and F. C. Tung, *Adv. Optical Mater.*, 2013, **1**, 657-667.
27. V. I. Adamovich, S. R. Cordero, P. I. Djurovich, A. Tamayo, M. E. Thompson, B. W. D'Andrade and S. R. Forrest, *Org. Electron.*, 2003, **4**, 77-87.
28. Q. Zhang, T. Komino, S. Huang, S. Matsunami, K. Goushi and C. Adachi, *Adv. Funct. Mater.*, 2012, **22**, 2327-2336.
29. J. W. Kang, S. H. Lee, H. D. Park, W. I. Jeong, K. M. Yoo, Y. S. Park and J. J. Kim, *Appl. Phys. Lett.*, 2007, **90**, 223508.
30. M. Lehnhardt, S. Hamwi, M. Hoping, J. Reinker, T. Riedl, W. Kowalsky, *Appl. Phys. Lett.*, 2010, **96**, 193301.
31. J. H. Jou, W. B. Wang, S. Z. Chen, J. J. Shyue, M. F. Hsu, C. W. Lin, S. M. Shen, C. J. Wang, C. P. Liu, C. T. Chen, M. F. Wu and S. W. Liu, *J. Mater. Chem.*, 2010, **20**, 8411-8416.
32. J. C. De Mello, H. F. Wittmann, R. H. Friend, *Adv. Mater.* 1997, **9**, 230-232.
33. W. Liu, X. Luo, Y. Bao, Y. P. Liu, G. H. Ning, I. Abdelwahab, L. Li, C. T. Nai, Z. G. Hu, D. Zhao, B. Liu, S. Y. Quek and K. P. Loh, *Nature Chemistry*, 2017, **9**, 563-570.

TH-2983_156122010

Chapter-2b

Application of pyrazino[2,3-g]quinoxaline derivative in the sensing of volatile organic acid

TH-2983_156122010

2.6. Introduction

In recent years, fluorescent materials are gaining the interest of the scientific community due to their potential applications in cell imaging,[1a-b] sensing[2a-b] and optical storage devices[3], *etc*. The quinoxaline, as well as pyrazino[2,3-g]quinoxaline derivatives are well-known fluorescent materials that have potential in the construction of organic electronic devices like organic photovoltaics (OPVs)[4a-c], organic field effect transistors (OFETs)[5] and organic light-emitting diodes (OLEDs).[6a-b] This is due to the low band gap between the frontier molecular orbitals (HOMO-LUMO) which is arising due to their planar quinoid structure.[7] The pyrazino[2,3-g]quinoxaline (PQ) is a fused three-ring system where a central benzene ring is crammed between two symmetrical pyrazine rings, which leads to a planar π-conjugated system and the presence of hetero-atoms like nitrogen make the system electron deficient.[8] The lone pairs on the sp^2 nitrogen can accept a proton from any acids. The inherent push-pull nature of such molecules makes them fluorescent, reduces the band gap and also makes them ideal platforms to build fluorescent chemosensors. The detection of volatile acid is very significant from the viewpoint of the environment as well as industry.[9] It is important if such sensors are capable to show reversibility in their response to such analytes making them reusable.[10] Gupta *et al.* synthesized a series of V-shaped molecules based on quinoxaline derivatives (**2.5**), which exhibited fluorescence 'turn-on' response to trifluoroacetic acid (TFA) with reversibility on basification.[9] The other moieties like imidazole (**2.6**),[11] cyanostilbene (**2.7**),[12] acylhydrazone (**2.8**),[2a] benzilmonohydrazone (**2.9** and **2.10**),[13a-b] benzoxazole (**2.11**),[14] benzothiazole (**2.12**),[14-15] benzothiadiazole (**2.13**),[15] dimethylamine substituted bisbenzocoumarin (**2.14**),[16] 4H-pyran derivatives (**2.15**),[17] vinylidene-naphthofurans (**2.16**),[18] pyridine (**2.17**), 1,3-diazine (**2.18**), 1,4-diazine (**2.19**), 1,2-diazine (**2.20**) and phthalazine (**2.21**),[19] pyrimidinyl (**2.22**) [20] and pyridine (**2.23** and **2.24**)[21,22] based molecules have been reported in the literature for acid detection (Figure 2.28). This was the motivation to explore the acidochromic property in the pyrazino[2,3-g]quinoxaline derivatives. To the best of our knowledge, this is the first report on pyrazino[2,3-g]quinoxaline derivative, which exhibited sensitivity to volatile acid like TFA in parts per billion (ppb) level. The molecular structure of the pyrazino[2,3-g]quinoxaline derivative utilized in the present study is shown in Figure 2.29. Considering the presence of sp^2-hybridized nitrogens in the molecular structure and inherent fluorescence of this molecule, it was envisaged that this molecule could be utilized as a sensor for the detection of acids in trace amounts. The

TH-2983_156122010

presence of eight long aliphatic chains may increase the electron-donating nature to the central electron deficient core, in addition to providing solubility in common organic solvents.

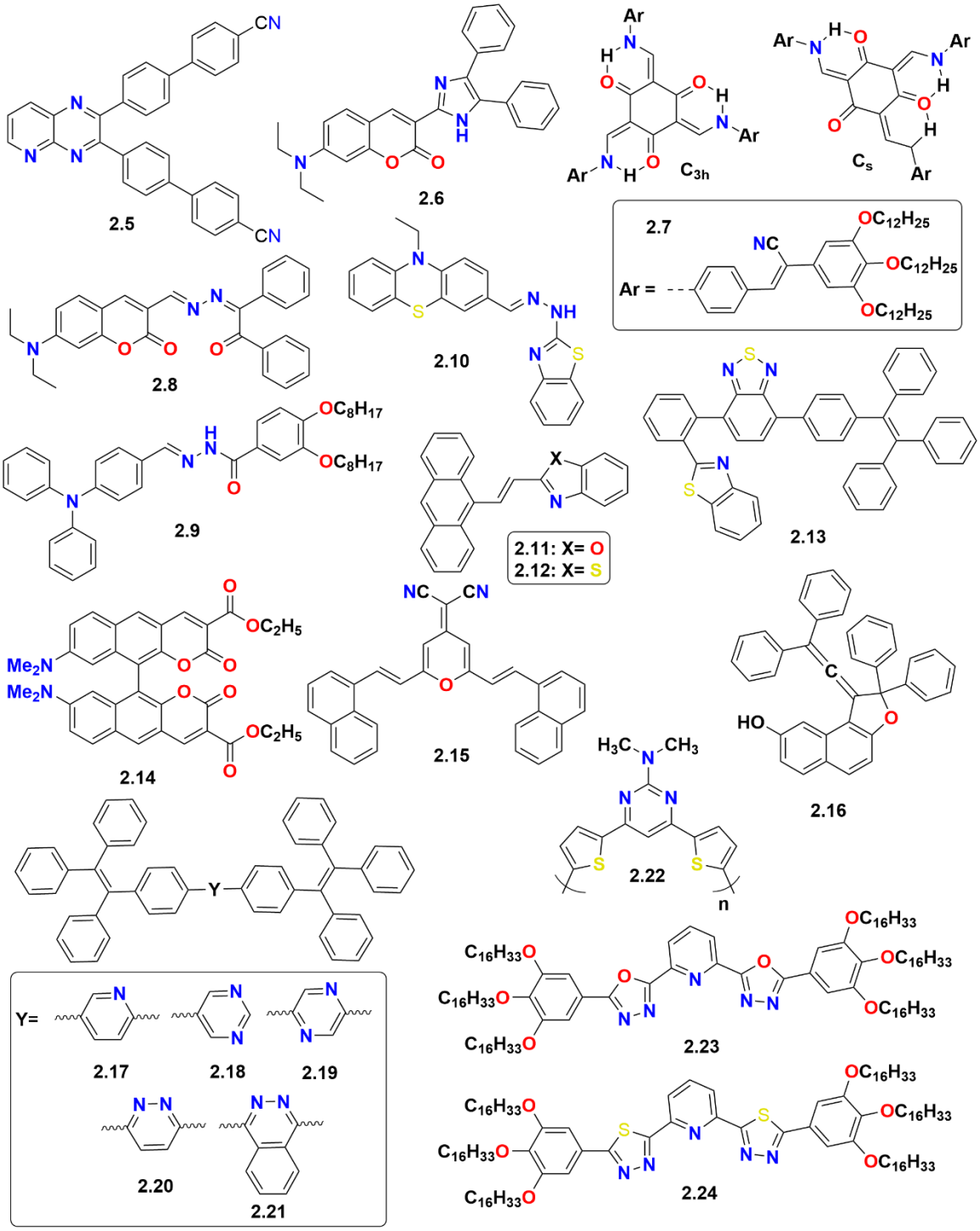

Figure 2.28. The various TFA acid sensing molecular probes were reported in the literature.

TH-2983_156122010

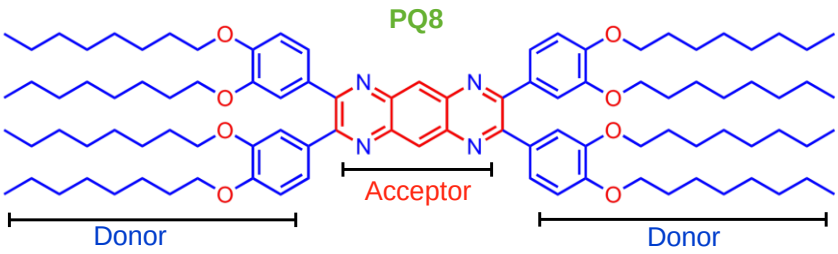

Figure 2.29. The molecular structure of pyrazino[2,3-g]quinoxaline derivative (**PQ8**) which is used in sensing.

2.7. Results and discussion

2.7.1. Experimental (Materials and instrumentation)

The reagents and materials for synthesis and other characterization were purchased either from local suppliers or from Sigma-Aldrich or Alfa Aesar and used as received. Synthesis of **PQ8** was carried out in chapter 2a. Perkin-Elmer Lambda 750, UV/VIS/NIR spectrometer was used to obtain UV-Vis spectra, while Fluoromax-4 fluorescence spectrophotometer and Perkin Elmer LS 50B spectrometer were used to obtain emission spectra in solution state and solid thin film state respectively. ^{1}H NMR titration was recorded using Bruker 600 MHz NMR spectrometer and the chemical shifts are reported in ppm relative to TMS as an internal standard. Time-resolved lifetime measurements were done on a time-correlated single photon counter from the Horiba Jobin Yvon spectrophotometer.

2.7.2. Acidochromic properties

The compound **PQ8** was highly soluble in chloroform. The micromolar chloroform solution of compound **PQ8** exhibited a single absorption maximum centered at 470 nm with a high extinction coefficient (ε = 16873 $Lmol^{-1}cm^{-1}$) and an emission maximum centered at 544 nm along with a good Stokes shift (2894 cm^{-1}) as shown in Figure 2.30. A volatile acid *i.e.* trifluoroacetic acid (TFA) was chosen as an analyte for such testing (Figure 2.31a-b). To a micromolar solution of **PQ8** in chloroform, a micromolar solution of TFA was added in small amounts. The absorption and emission spectra were obtained after each addition. The absorption spectra showed a red shift with the addition of TFA, but emission spectra showed a quenching of intensity with a slight blue shift as shown in Figures 2.32a-d and 2.33a-d. This could be due to an alteration in the polarization of the ground and excited states, which in turn alters the energy gap between the excited and ground states.

TH-2983_156122010

The blue-shifted emission suggests the decreased intramolecular charge transfer (ICT)[10] which occurs between the peripheral dioctyloxyphenyl donors and the protonated pyrazinoquinoxaline acceptor. The protonation normally leads to an increased electron accepting ability of the pyrazinoquinoxaline moiety due to the positively charged nitrogen. However, the positive charge is also compensated by the trifluoroacetate counteranion. The emission intensity of the solution was reduced with the gradual addition of TFA, but the fluorescence quenching was found to be drastic (Figure 2.32b). Neutralization of this solution with the gradual addition of triethylamine (TEA) reverted the absorption and emission maxima to their original position (Figure 2.32a-d). In the case of emission, the intensity was recovered to the original by the addition of TEA (Figure 2.32d). The emission quenching on exposure to TFA and the recovery of emission on exposure to TEA was visually perceivable both in solution in daylight as well as under UV light of long wavelength (λ = 365 nm).

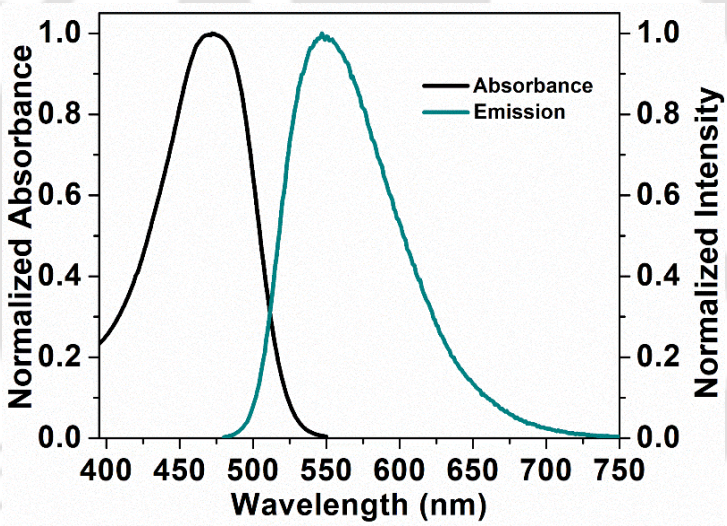

Figure 2.30. Normalized absorption (λ_{max}= 470 nm) and emission spectrum (λ_{max}= 544 nm) of compound **PQ8** in micromolar chloroform solution.

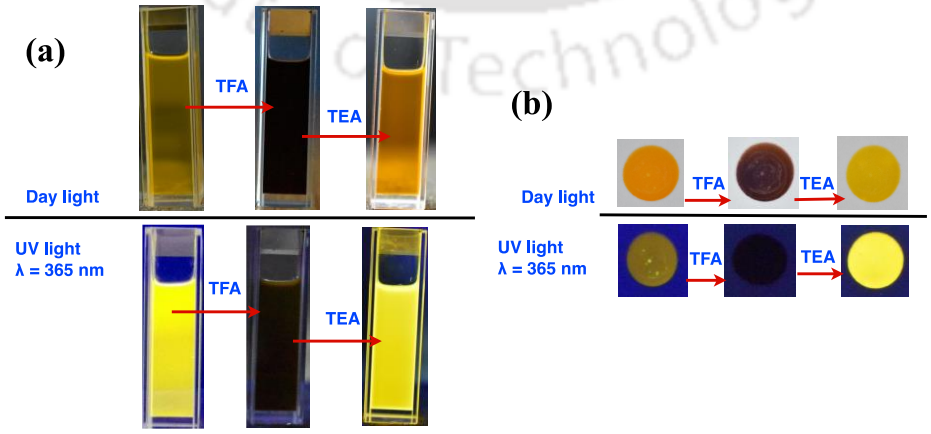

Figure 2.31. Photographs showing the response of the solution of compound **PQ8** to TFA and TEA (a); drop casted film on a TLC plate (b), as seen under daylight and UV light (λ = 365 nm).

TH-2983_156122010

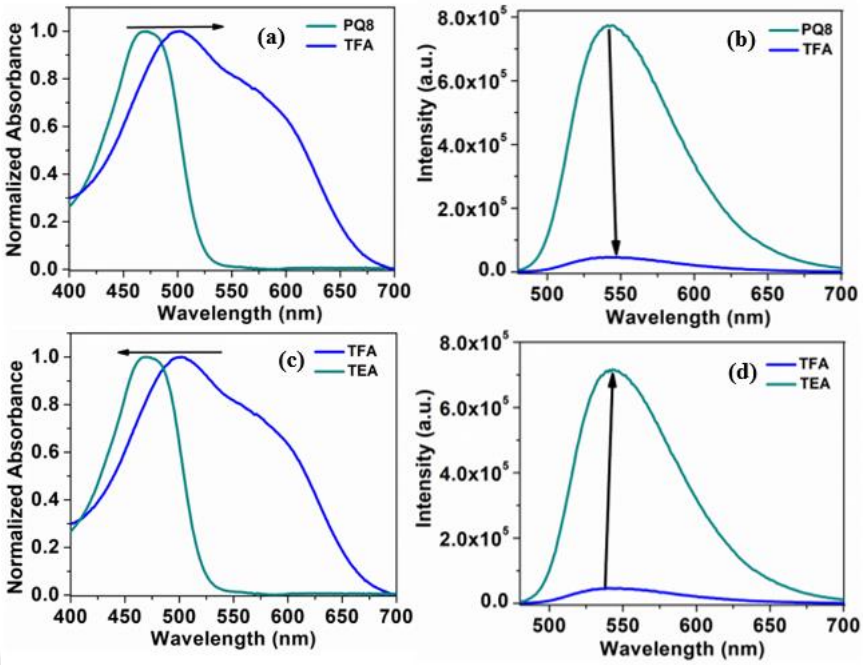

Figure 2.32. Normalized absorption spectrum of compound **PQ8** on exposure to TFA (a); emission spectrum of compound **PQ8** on exposure to TFA (b); recovery of the original absorption of compound **PQ8** on neutralization with TEA (c) and recovery of original emission of compound **PQ8** by neutralization with TEA (d).

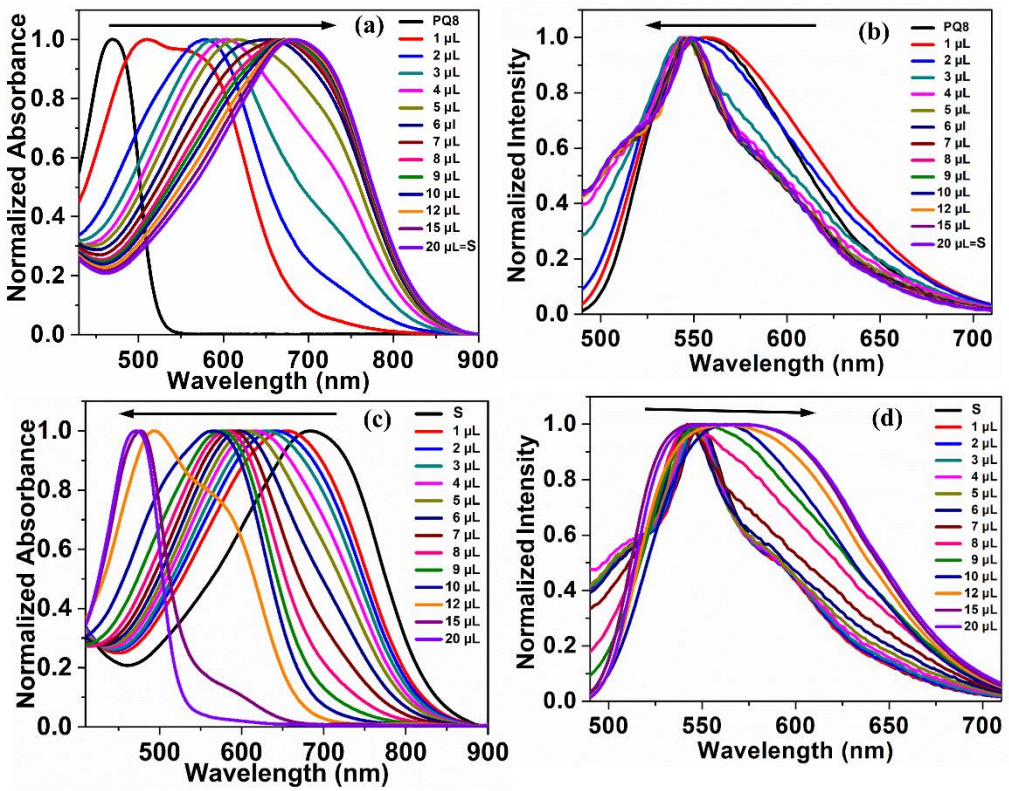

Figure 2.33. The normalized absorption spectrum of compound **PQ8** on successive addition of TFA (1 µL to 20 µL) (a); normalized emission spectrum of compound **PQ8** on successive addition of TFA (1 µL to 20 µL) (b); normalized absorption spectrum of solution **S** (**PQ8**+20µL TFA) on successive addition of TEA (c); normalized emission spectrum of solution **S** (**PQ8**+20µL TFA) on successive addition of TEA (d).

TH-2983_156122010

The same color change was noted for the thin films on quartz plates prepared by spin coating. The red-shift with a reduction in the absorbance of this compound in solution with the addition of TFA confirmed the formation of a new species (Figure 2.32). The time-resolved photoluminescence studies were also carried out to understand the nature of the excited state species. For example, the micromolar solution of compound **PQ8** in chloroform exhibited a monoexponential decay curve with a lifetime of 2.2 ns. The addition of TFA also showed a species with a decreased lifetime of 1.9 ns, while the neutralization with one equivalent TEA (with respect to TFA) produced the species with a lifetime of 2.2 ns, which is in agreement with the absorption and emission spectra (Figures 2.32 and 2.34 and Table 2.9).

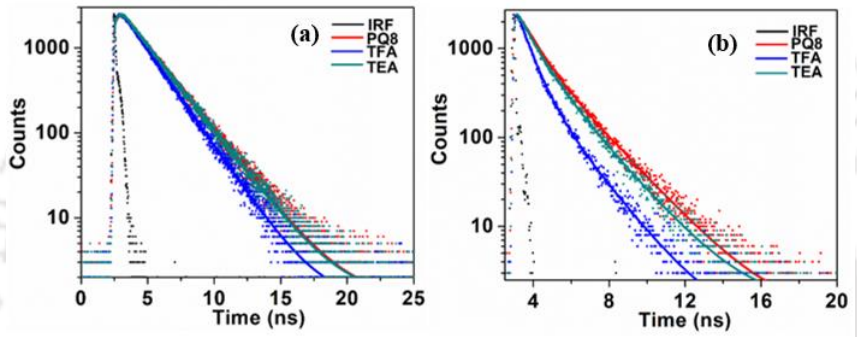

Figure 2.34. Fluorescence decay plots of compound **PQ8** micromolar solution in chloroform, on the addition of TFA and TEA (a); fluorescence decay plots of compound **PQ8** in the thin film state (b) (obtained by spin coating of a 2 mM solution of compound **PQ8** in toluene on quartz plate using a 2 mM solution in toluene) on exposure to TFA and TEA.

Table 2.9. Data obtained from the time-resolved photoluminescence experiments.

Solution[a]		Thin film[b]	
Entry	Fraction (Lifetime)	Entry	Fraction (Lifetime)
PQ8	100 % (2.19 ns)	**PQ8**	35.62 % (0.79 ns); 64.38 % (1.92 ns)
TFA	100 % (1.92 ns)	**TFA**	58.73 % (0.63 ns); 41.26 % (1.65 ns)
TEA	100 % (2.15 ns)	**TEA**	40.38 % (0.84 ns); 59.62 % (1.85 ns)
[a]Concentration: 5 μM solution in chloroform; [b]Concentration of solution used for spin coating: 2 mM in toluene.			

For calculating the detection limit, different samples of **PQ8** (5 μM) each containing TFA solution (0.00 μM, 3.25 μM, 6.50 μM, 9.75 μM and 13.00 μM) in 2 mL $CHCl_3$ were prepared separately and the fluorescence spectrum was then recorded for each sample by exciting at 470 nm. The detection limit plot for TFA was obtained by plotting changes in the fluorescence intensity *vs*. the concentration of TFA. The curve demonstrates a linear relationship and the correlation coefficient (R) via linear regression analysis was calculated to be 0.99. The limit of detection (LOD) was then calculated using the equation $3\sigma/K$, where

TH-2983_156122010

σ signifies the standard deviation for the intensity of **PQ8** in the absence of TFA and K denotes the slope of the equation.

$LOD = 3 \times \sigma / K$

$LOD = 3 \times 25018.75 / 3.3857 \times 10^4$

$= 2.22$ μM or 252.77 ppb

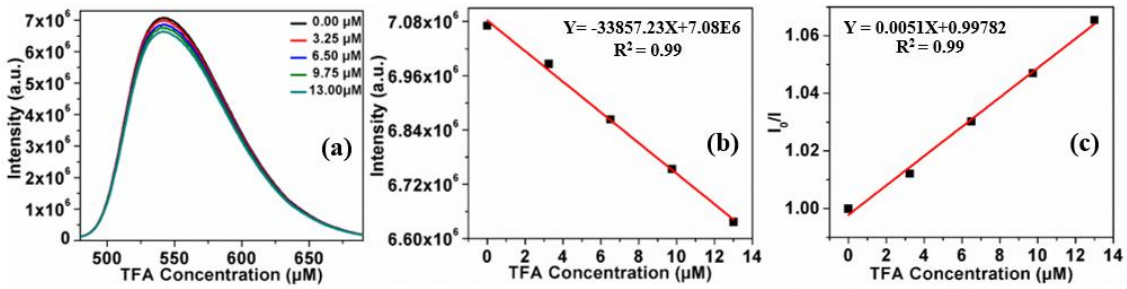

Figure 2.35. Fluorescence response of compound **PQ8** (5 μM) in chloroform on incremental addition of TFA solution (a); Plot showing the variation of fluorescence intensity of compound **PQ8** (5 μM) in chloroform on the addition of TFA (b); Stern-Volmer plot obtained for the same (c).

The sensitivity of the compound **PQ8** in response to TFA was measured and found to be 252.8 ppb (parts per billion) (Figure 2.35). The drastic quenching of the fluorescence on the addition of TFA can be explained as follows. An overlay of the absorption spectrum of protonated **PQ8** and emission spectrum of **PQ8** shows that the absorption band of protonated form shows a complete overlapping on the emission band of the neutral **PQ8**. This leads to an intermolecular Förster resonance energy transfer (FRET), where the protonated form behaves as an energy acceptor while the neutral form acts as an energy donor, thus resulting in the "turn-off" or quenching of the fluorescence of the **PQ8** (Figure 2.36).[10]

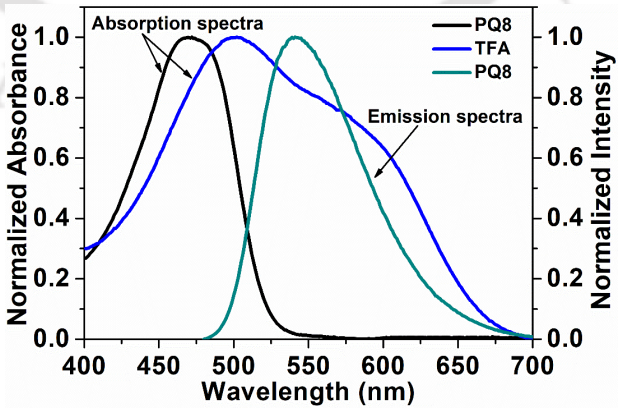

Figure 2.36. An overlay of the absorption and emission spectra of compound **PQ8** (5 μM) in chloroform, the emission spectrum of partially protonated **PQ8**.

Compound **PQ8** also exhibited quenching of fluorescence in response to other organic acids like methanesulfonic acid (MSA), trifluoroacetic acid (TFA), cyanoacetic

TH-2983_156122010

acid (CAA), bromoacetic acid (BAA), formic acid (FA) and acetic acid (AA) although no much change in the absorbance was noticed. The minor change in the intensity of the emission with other organic acids is due to the variation in the pKa values of these acids (Figure 2.37 (i) and (ii)). Similarly, various metal salts of Li^{+}, Mn^{2+}, Fe^{2+}, Co^{2+}, Cr^{3+}, Fe^{3+} and Eu^{3+} were utilized to test the sensing efficiency of compound **PQ8**. Among the positively charged metal ions, the trivalent cations (Cr^{3+}, Fe^{2+}, Fe^{3+} and Eu^{3+}) exhibited a major decrease in the absorption and photoluminescence intensity (Figure 2.37 (iii) and (iv)). It was observed that quenching of **PQ8** emission is not selective to TFA with respect to other acids and metal ions.

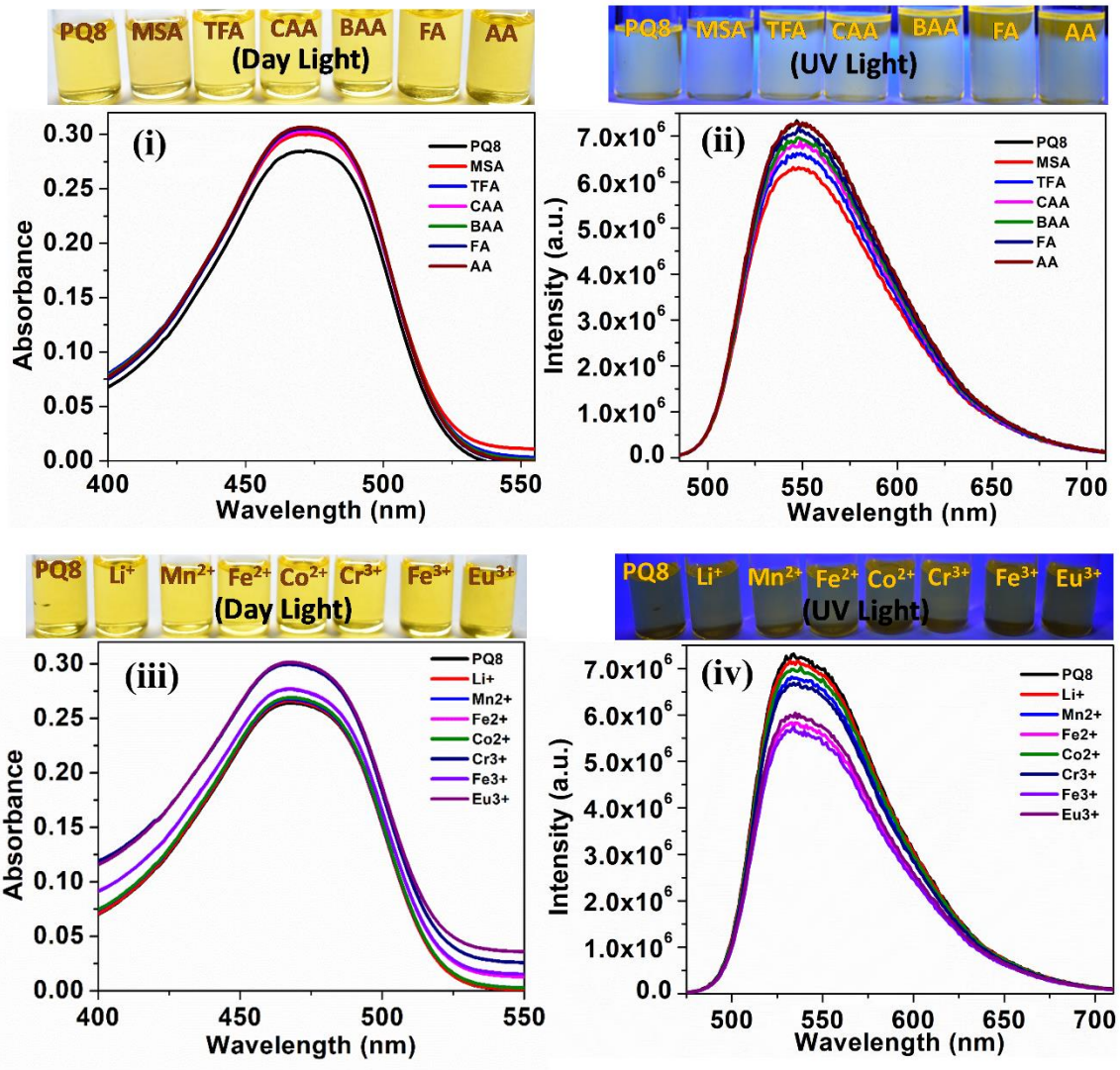

Figure 2.37. Absorption spectrum of compound **PQ8** (5 µM) on addition of various organic acids 4 equiv. (20 µM) in chloroform solutions (i); emission spectrum of compound **PQ8** (5 µM) on addition of various organic acids 4 equiv. (20 µM) in chloroform solutions (ii); Absorption spectrum of compound **PQ8** (5 µM) on addition of various metal ions 4 equiv. (20 µM) in THF solutions (iii); emission spectrum of compound **PQ8** (5 µM) on addition of metal ions 4 equiv. (20 µM) in THF solutions (iv).

TH-2983_156122010

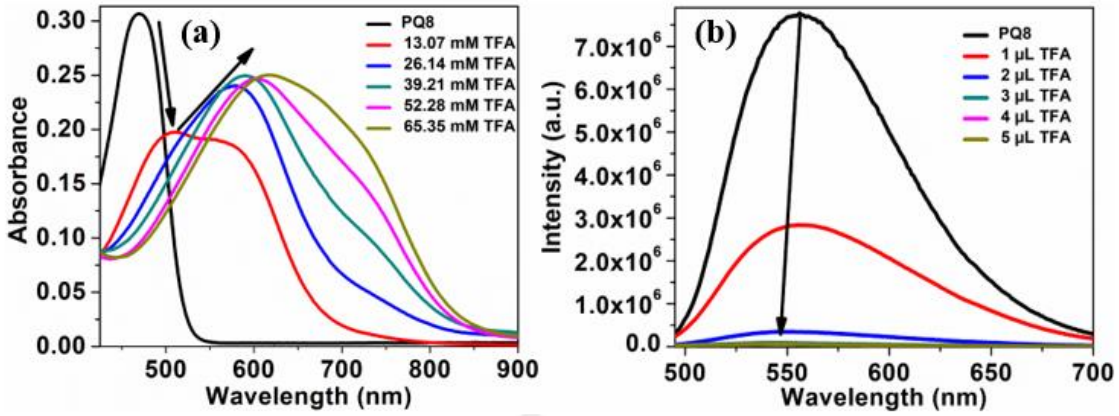

Figure 2.38. Absorption spectrum of compound **PQ8** (5 µM) on successive addition of TFA (1 µL to 5 µL) in chloroform solutions (a); emission spectrum of compound **PQ8** on successive addition of TFA (1 µL to 5 µL) in chloroform solutions (b) [1 µL TFA=13.07 mM concentration].

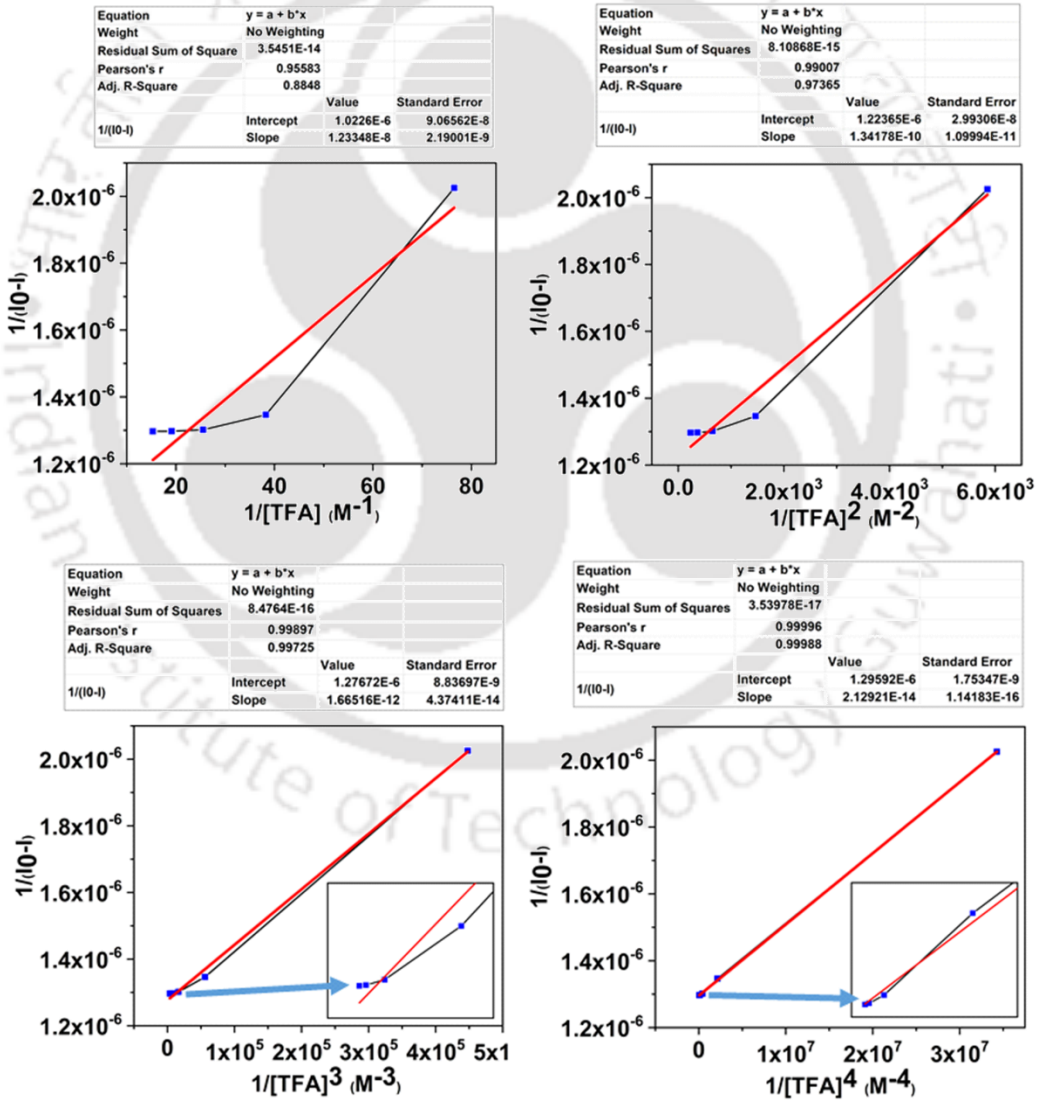

Figure 2.39. Benesi-Hildebrand plot[1-4] of **PQ8** derivative in presence of TFA to understand the stoichiometry of acid and sensor molecules (1/ $[TFA]^n$ Where [TFA] is TFA concentration (n=1, 2, 3 and 4) Here n= no. of TFA bind to **PQ8** and I_0 is PL intensity in absence of TFA and I is PL intensity in presence of TFA).

TH-2983_156122010

In order to understand the stoichiometry of the complexation, the emission data of Figure 2.38 were utilized and drawn the Benesi-Hildebrand plots[23-26] (as shown in Figure 2.39), and found that the stoichiometric ratio of acid (TFA) and sensor molecules (**PQ8**) was in 1:4 ratios.

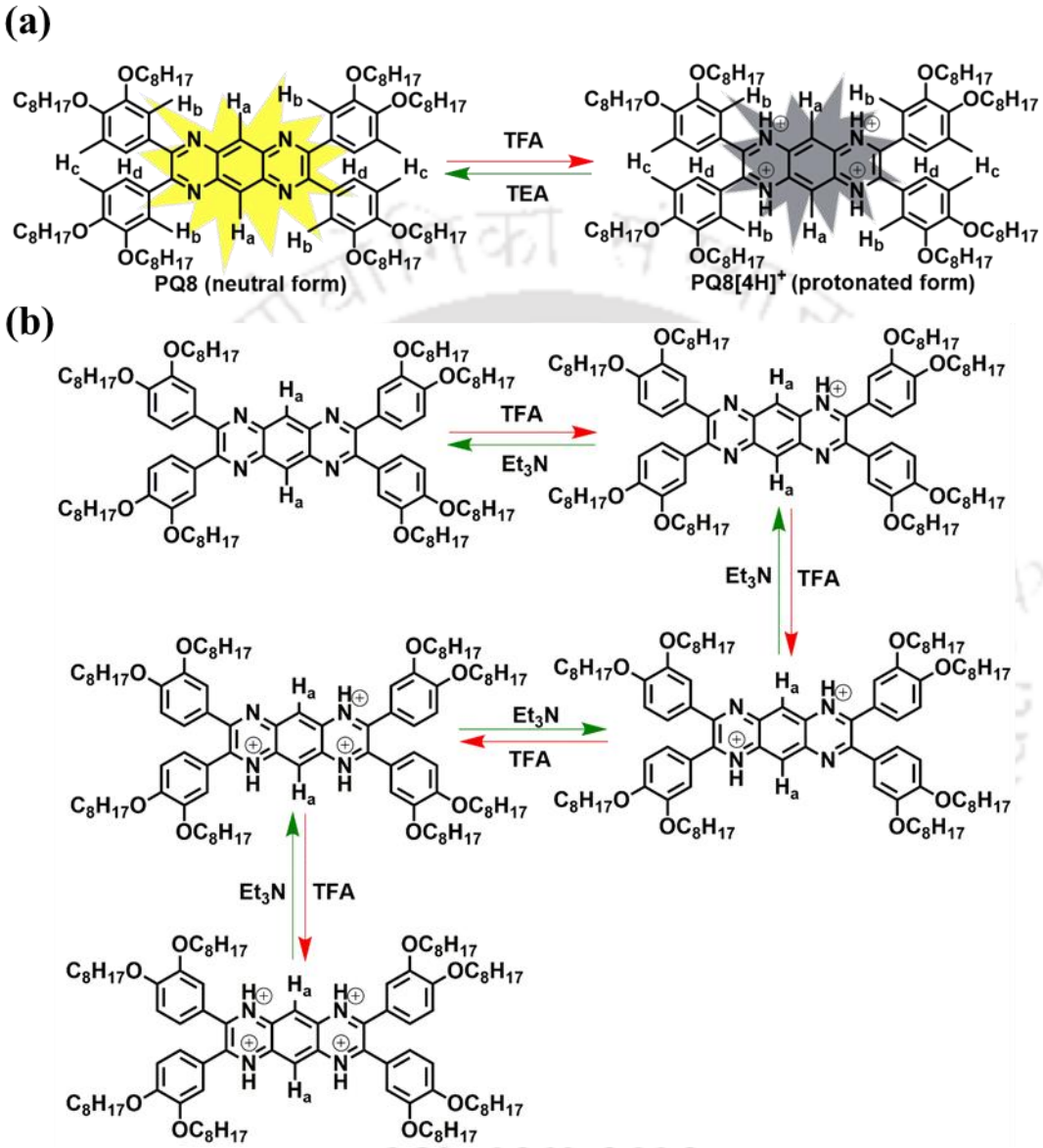

Figure 2.40. (a) Schematic illustration of the response of **PQ8** with on addition of TFA and then TEA; (b) Possible ways of protonation and deprotonation in **PQ8** on treating with TFA and neutralization with TEA.

Similar stoichiometric ratios of 1:2 and 1:3 behaviors were observed with sensor molecules containing two or three nitrogen.[9] Thus it is expected that **PQ8** could form a protonated complex with 1:4 stoichiometric ratios as it contains four nitrogen atoms in its molecular structure (Figure 2.40a, b). From the ^{1}H NMR spectra, it was envisioned that the protonation of the compounds led to a downfield shift of the protons on the central ring. Interestingly, the neutralization with the

TH-2983_156122010

triethylamine leads to a recovery of the signals to their original position (Figure 2.41). This corroborated the binding interactions between **PQ8** and TFA, as well as the reversibility of the addition of TEA.

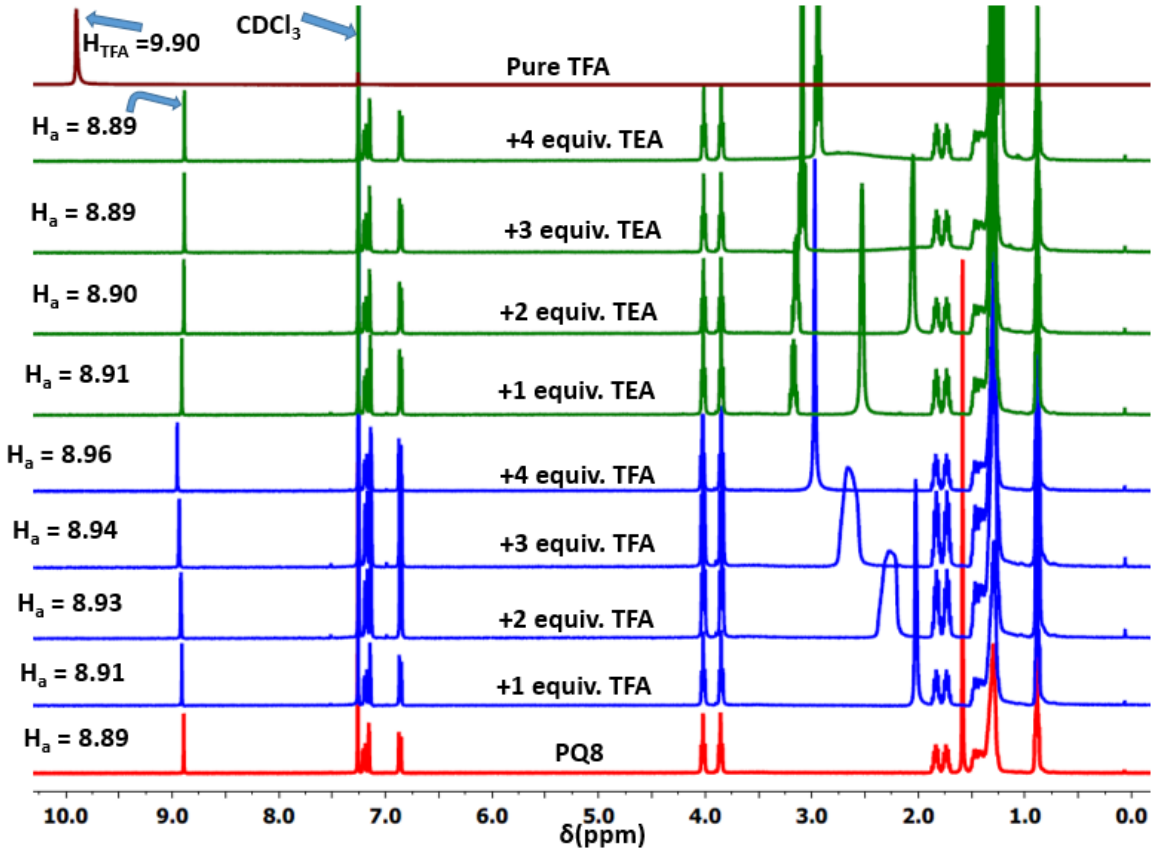

Figure 2.41. ^{1}H NMR spectra of **PQ8** (2mM) (red trace); **PQ8** on addition of TFA (blue trace) and **PQ8**-TFA mixture after neutralizing with TEA (green trace).

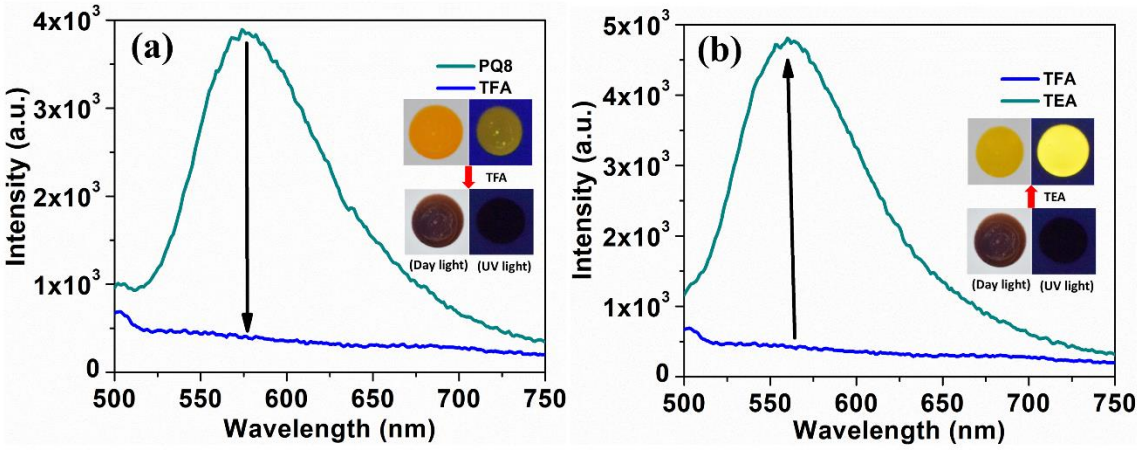

Figure 2.42. The emission spectrum of compound **PQ8** in TLC plate on exposure to TFA vapors (a) and recovery of emission of compound **PQ8** by neutralization with TEA vapors (b) (obtained by 2 mM chloroform solution of compound **PQ8** on TLC plate).

For testing its applicability of **PQ8**, a prototype handheld device, which was prepared by drop casted the solution on a preloaded silica gel thin layer chromatography

TH-2983_156122010

(TLC) plate and allowed the solvent to evaporate. The film formed on exposure to TFA and TEA vapors exhibited a similar response to that in solution and could be reused a number of times. The emission spectra also confirmed that on exposure of TFA to the **PQ8** and then with TEA with a drastic drop and recovery of the intensity (Figure 2.42).

As discussed earlier even in the thin film (spin-coated on quartz plate) state as well, the compound **PQ8** exhibited a similar response, which was illustrated by a change in the lifetime of the excited species (Table 2.9). It should be noted that in comparison to the previously reported quinoxaline derivative, which showed an increase in the emission intensity in response to acid, the present compound showed a quenching of fluorescence.[9]

2.7.3. Density Functional Theory (DFT) studies

DFT studies were performed at the level of B3LYP/6-31+G(d) using Gaussian 16[27] to understand the sensing mechanism of **PQ8**. Graphical outputs of the computational results were generated with the Gaussview version 6.11.[28] Initially **PQ8** and TFA were optimized separately in the absence of the solvent. The optimized structure has been used as the starting point for further calculation which includes protonation and solvating in chloroform (dielectric constant $\varepsilon = 4.7113$) using the polarizable continuum model (PCM). The structures were confirmed to be minima by vibrational frequency analyses (Figure 2.43). The distance between protonated hydrogen of **PQ8** and oxygen of the deprotonated TFA was found to be 1.6 Å after optimization. The HOMO-LUMO energy gap between the highest occupied molecular orbital (HOMO) and the lowest unoccupied molecular orbital (LUMO) was calculated to study the kinetic stability of the molecules.[29] From Figure 2.45, It was noticed that the energy gap for protonated **PQ8** (2.072 eV) is less than that of **PQ8**+TFA (2.379 eV) which suggests that the complex formed is chemically stable. Finally, UV-vis spectra calculations are done for the complex and **PQ8** in the presence of chloroform and compared to the experimental UV-vis spectra. A similar approach was followed for testing chemo-sensors theoretically in the past.[30–33] The theoretical absorption maximum of the **PQ8** was found to be 398 nm with an oscillator strength of 1.4, which was red-shifted to 467 nm with an oscillator strength of 1.33 on the addition of TFA (Figure 2.44). The red shifting of absorption maximum was consistent with the experimental observation, where the addition of TFA led to red-shift with the tail extending to 700 nm (Figure 2.36).

TH-2983_156122010

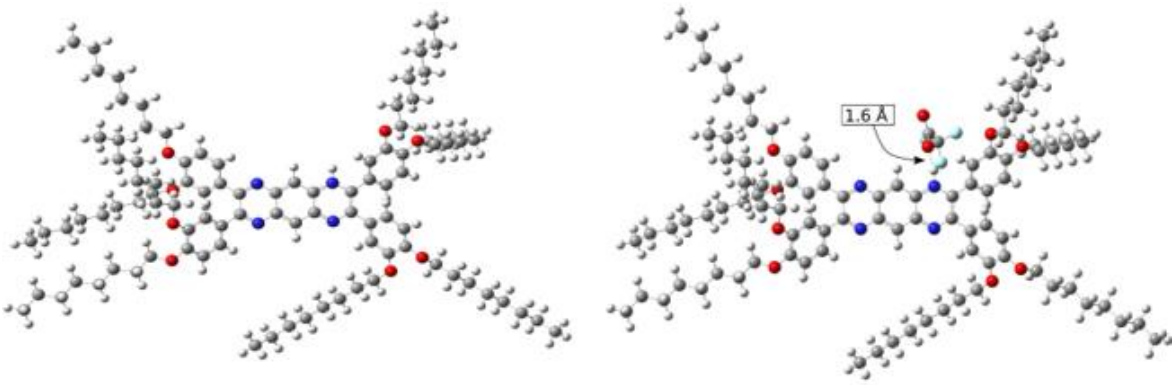

Figure 2.43. (a) Energy minimized structure of protonated PQ8, (b) Energy minimized structure of the complex formed between PQ8 and TFA.

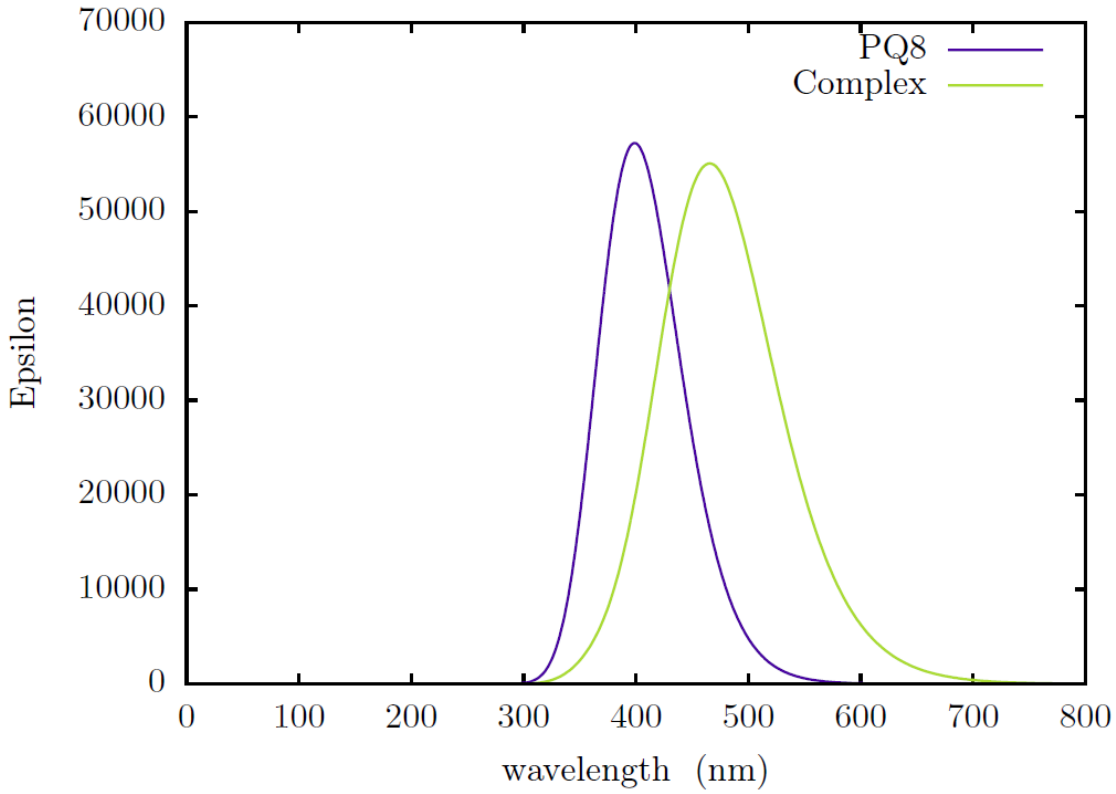

Figure 2.44. Theoretical UV-vis spectra of compound **PQ8** and its protonated complex in chloroform, calculated at TD-B3LYP/6-31+G(d).

The chemical stability of the complex can also be confirmed by calculating the $E_{interaction}$ as $E_{interaction} = E_{complex} - \{E_{PQ8} + E_{TFA}\}$. If $E_{interaction}$ is negative, it is imperative that the complex is stable. Based on the values given in Figure 2.44 and from the above expression, the value of $E_{interaction}$ was found to be −0.17 hartree or −446.335 kJ.mol^{-1}. Thus the protonation of the nitrogen of **PQ8** is responsible for the fluorescence quenching, and thus the detection of TFA.

TH-2983_156122010

Compound name	HOMO	LUMO	Energy (hartree)
TFA	 -6.30 ev	 0.31 ev	-526.20
PQ8	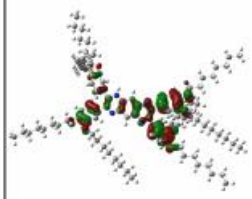 -6.39 ev	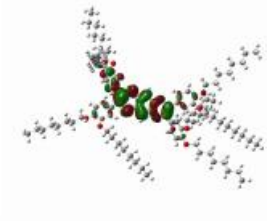 -4.32 ev	-4643.78
complex	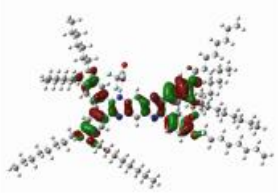 -6.03 ev	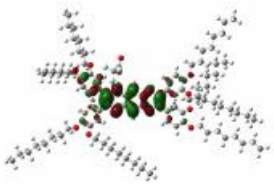 -3.65 ev	-5170.15

1 hartree = 2625.50 kJ.mol^{-1}

Figure 2.45. HOMO and LUMO of deprotonated TFA and protonated **PQ8** and complex of both solvated in chloroform.

2.8. Conclusion

In conclusion, a pyrazino[2,3-g]quinoxaline derivative was designed and synthesized, which can be utilized for the naked-eye detection of volatile acids like trifluoroacetic acid in trace amounts (in parts per billion levels), both in solution and drop casted TLC paper-based strip by fluorescence quenching. When treated with an equivalent amount of base (TEA) the compound retains its original fluorescence. This was confirmed with the help of several complementary studies like UV-visible spectroscopy, fluorescence spectroscopy, time-resolved photoluminescence and ^{1}H-NMR spectroscopy. DFT studies elucidated that the interaction between the protonated pyrazino[2,3-g]quinoxaline derivative and deprotonated TFA leads to the formation of a stable complex. The intermolecular fluorescence resonance energy transfer that occurs from the **PQ8** to the protonated **PQ8** leads to the quenching of fluorescence. Thus the **PQ8** seems to be a promising candidate for the detection of acid at very low levels and this has the potential to be utilized in other areas like bio-imaging as well.

TH-2983_156122010

2.9. References

1. (a) J. Qi, C. Chen, X. Y. Zhang, X. L. Hu, S. L. Ji, R. T. K. Kwok, J. W. Y. Lam, D. Ding and B. Z. Tang, *Nat. Commun*. 2018, **9**, 1848. (b) M. N. Noolvi, H. M. Patel, V. Bhardwaj and A. Chauhan, *Eur. J. Med. Chem*, 2011, **46**, 2327−2346.
2. (a) T. Zhang, F. Chen, C. Zhang, X. Che, W. Li, B. Bai, H. Wang and M. Li, *ACS Omega*, 2020, **5**, 5675−5683. (b) S. Nath, S. K. Pathak, B. Pradhan, R. K. Gupta, K. A. Reddy, G. Krishnamoorthy and A. S. Achalkumar, *New J. Chem.*, 2018, **42**, 5382−5394.
3. C. C. Corredor, Z. L. Huang and K. D. Belfield, *Adv. Mater.* 2006, **18**, 2910–2914.
4. (a) X. Liu, T. Liu, C. Duan, J. Wang, S. Pang, W. Xiong, Y. Sun, F. Huang and Y. Cao, *J. Mater. Chem. A*, 2017, **5**, 1713–1723. (b) L. P. Zhang, K. J. Jiang, G. Li, Q. Q. Zhang and L. M. Yang, *J. Mater. Chem. A*, 2014, **2**, 14852–14857. (c) Q. Peng, X. Liu, Y. Qin, J. Xu, M. Lia and M. Dai, *J. Mater. Chem*., 2011, **21**, 7714–7722.
5. J. Quinn, C. Guo, L. Ko, B. Sun, Y. He and Y. Li, *RSC Adv.*, 2016, **6**, 22043–22051.
6. (a) G. Bernardo, M. A. Esteves, A. M. Guerreiro, B. Gigante and J. Morgado, *Optical Materials*, 2008, **31**, 320–327. (b) J. F. Wang, Y. Kawabe, Shaheen, M. M. Morrell, G. E. Jabbour, P. A. Lee, J. Anderson, N. R. Armstrong, B. Kippelen and E. A. Mash, *Adv. Mater.* 1998, **10**, 230–233.
7. T. L. Tam, F. Zhou, H. Li, J. C. Y. Pang, Y. M. Lam, S. G. Mhaisalkar, H. Su and A. C. Grimsdale, *J. Mater. Chem.* 2011, **21**, 17798−17804.
8. L. P. Zhang, X. Li, T. Liu, L. Kang, X. Huang and Y. Zhao, *Chem. Commun*. 2020, DOI: 10.1039/d0cc02285c.
9. S. Gupta and M. D. Milton, *Dyes and Pigments*, 2019, **165**, 474–487.
10. Y. Fu and N. S. Finney, *RSC Adv*. 2018, **8**, 29051–29061.
11. A. A. Bhagwat, K. C. Avhad, D. S. Patil and N. Sekar, *Photochem. Photobiol.*, 2019, **95**, 740–754.
12. R. K. Gupta, S. K. Pathak, J. De, S. K. Pal and A. S. Achalkumar, *J. Mater. Chem. C*, 2018, **6**, 1844−1852.
13. (a) B. Aydiner, *Turk J Chem.*, 2019, **43**, 1086−1097. (b) T. Sachdeva, S. Bishnoi and M. D. Milton, *Chemistry Select*, 2017, **2**, 11307–11313.
14. K. C. Naeem, A. Subhakumari, S. Varughesec and V. C. Nair, *J. Mater. Chem. C*, 2015, **3**, 10225–10231.
15. A. Ekbote, S. M. Mobin and R. Misra, *J. Mater. Chem. C*, 2018, **6**, 10888–10901.
16. S. Chen, W. Liu, Z. Ge, W. Zhang, K. P. Wang and Z. Q. Hu, *CrystEngComm*, 2018, **20**, 5432–5441.
17. Y. Zhou, Y. Liu, Y. Guo, M. Liu, J. Chen, X. Huang, W. Gao, J. Ding, Y. Cheng and H. Wu, *Dyes and Pigments*, 2017, **141**, 428–440.
18. C. M. Sousa, J. Berthet, S. Delbaere and P. J. Coelho, *Dyes and Pigments*, 2017, **137**, 593–600.
19. R. Tang, X. Wang, W. Zhang, X. Zhuang, S. Bi, W. Zhang and F. Zhang, *J. Mater. Chem. C*, 2016, **4**, 7640–7648.
20. X. Mamtimin, A. Aikebaierjiang, M. Alifujiang, T. Tuerxun, Z. Kurban, W. F. Sun and I. Nurulla, *J Polym Res*, 2011, **18**, 105–109.

TH-2983_156122010

21. B. Pradhan, M. Gupta, S. K. Pal and A. S. Achalkumar, *J. Mater. Chem. C*, 2016, **4**, 9669-9673.
22. B. Pradhan, R. K. Gupta, S. K. Pathak, J. De, S. K. Pal and A. S. Achalkumar, *New J. Chem*. 2018, **42**, 3781-3798.
23. S. Goswami, D. Sen, N. K. Das, H. K Fun and C. K. Quah, *Chem. Commun.*, 2011, **47**, 9101–9103.
24. F. Yan, M. Wang, D. Cao, N. Yang, B. Ma, and L. Chen, *Journal of Spectroscopy*, 2012, **2013**, Article ID 878234.
25. S. K. Ghatak, D. Dey, S. Sen and K. Sen, *Analyst*, 2013, **138**, 2308–2314.
26. E. Jabeen, N. K. Janjua, S. Ahmed, I. Murtaza, T. Ali, N. Masood, A. S. Rizvi, G. Murtaza, *Journal of Molecular Structure*, 2017, **1150**, 459-468.
27. M. J. Frisch, G. W. Trucks, H. B. Schlegel, G. E. Scuseria, M. A. Robb, J. R. Cheeseman, G. Scalmani, V. Barone, G. A. Petersson, H. Nakatsuji, X. Li, M. Caricato, A. V. Marenich, J. Bloino, B. G. Janesko, R. Gomperts, B. Mennucci, H. P. Hratchian, J. V. Ortiz, A. F. Izmaylov, J. L. Sonnenberg, D. Williams-Young, F. Ding, F. Lipparini, F. Egidi, J. Goings, B. Peng, A. Petrone, T. Henderson, D. Ranasinghe, V. G. Zakrzewski, J. Gao, N. Rega, G. Zheng, W. Liang, M. Hada, M. Ehara, K. Toyota, R. Fukuda, J. Hasegawa, M. Ishida, T. Nakajima, Y. Honda, O. Kitao, H. Nakai, T. Vreven, K. Throssell, J. A. Montgomery, Jr., J. E. Peralta, F. Ogliaro, M. J. Bearpark, J. J. Heyd, E. N. Brothers, K. N. Kudin, V. N. Staroverov, T. A. Keith, R. Kobayashi, J. Normand, K. Raghavachari, A. P. Rendell, J. C. Burant, S. S. Iyengar, J. Tomasi, M. Cossi, J. M. Millam, M. Klene, C. Adamo, R. Cammi, J. W. Ochterski, R. L. Martin, K. Morokuma, O. Farkas, J. B. Foresman, and D. J. Fox. Gaussian~16 Revision C.01. 2016. Gaussian Inc. Wallingford CT.
28. R. Dennington, T. A. Keith and J. M. Millam, Gaussview Version 6, 2019, Semichem Inc. Shawnee Mission KS.
29. L.P. Ding, F. H. Zhang, Y. S. Zhu, C. Lu, X. Y. Kuang, J. Lv and P. Shao, *Scientific Reports*, 2015, **5**, 15951.
30. N. Iqbal, S. A. Ali, I. Munir, S. Khan, K. Ayub, M. A. Rashida, M. Islam, Z. Shafiq, R. Ludwig, and A. Hameed, *RSC advances*, 2018, **8**, 1993–2003.
31. I. O. Isaac, I. Munir, M. A. Rashida, S. A. Ali, Z. Shafiq, M. Islam, R. Ludwig, K. Ayub, K. M. Khan, and A. Hameed, *Royal Society open science*, 2018, **5**, 180646.
32. M. Ishtiaq, I. Munir, M. A. Rashida, K. Ayub, J. Iqbal, R. Ludwig, K. M. Khan, S. A. Ali, A. Hameed, *RSC advances*, 2016, **6**, 64009–64018.
33. M. Islam, A. Hameed, K. Ayub, M. M. Naseer, J. Hussain, R. D. Alharthy, A. Asari, R. Ludwig, M. A. Rashida, and Z. Shafiq, *Chemistry Select*, 2018, **3**, 7633–7642.

TH-2983_156122010

Chapter-3

Pyrazino[2,3-g]quinoxaline carbazole derivatives based on D-A-D architecture for organic light-emitting diodes

TH-2983_156122010

3.1. Introduction

Carbazole-based materials have been investigated for their excellent fluorescence, hole transport behavior, excellent photoconductivity, and electron-donating nature with a deep HOMO level. Carbazole-containing polymers were used as organic light-emitting diodes,[1–3] photovoltaic cells,[4,5] and thin-film transistors.[6,7] They have also found application in electrochromic devices as they can form relatively stable cations on the application of voltage.[8,9] Carbazole-based compounds also found application in the synthesis of several thermally activated delayed fluorescence (TADF) materials, which are capable of enhancing the emission efficiency of present-day OLEDs by harvesting the excitons in a triplet state.[10,11] However, the realization of such beneficial materials requires the proper combination of carbazoles with suitable acceptor units with a twisted structure with a reduced energy gap between the singlet and triplet states. Carbazoles are also utilized as donor units in donor-acceptor (D-A) compounds with a high potential for synthetic tunability, ambipolar charge transport, and light-emitting materials with high emission efficiency.[12–15] A wide variety of carbazole derivatives are used in fluorescent and phosphorescent OLEDs due to their suitable energy levels, good charge transport behavior, and high triplet energies as host materials.[16–21] Being an inexpensive, stable starting material with the ease of functionalization by *N*-alkylation and core modification, carbazole provides enormous opportunities for structural modifications to realize functional materials.[22] Quinoxaline derivatives also have been used in organic electronic devices like organic solar cells,[23,24] OLEDs,[25] and OFETs.[26] They have also found application in the construction of supramolecular self-assembling materials,[27] sensors[28] and also as acceptor units in the building of donor-acceptor (D-A) systems with low energy gaps.[29]

Chen and Pei developed tetrasubstituted pyrazino[2,3-g]quinoxaline derivatives with thiophene and phenyl rings, which leads to varying extent of conjugation to achieve high-efficiency active waveguide fibers.[30] Su and Grimsdale further extended the conjugation and introduced substituents at the quinoidal positions to study the electronic properties of the pyrazino[2,3-g]quinoxaline derivatives.[31] A water-soluble pyrazino[2,3-g]quinoxaline based photosensitizer reported by Zhao *et al.*, which exhibits both a high fluorescence quantum yield and singlet oxygen quantum yield, with potential as a novel photosensitizer for both one-photon excitation and two-photon excitation photodynamic therapy applications.[32] Hisaki *et al.* demonstrated X-shaped tetracarboxylic acid derivatives with pyrazinoquinoxaline cores that stabilize hydrogen-bonded rhombic network

TH-2983_156122010

(RhomNet) sheets with one-dimensional (1D) inclusion channels.[33] Yang and Schröder developed pyrazino[2,3-g]quinoxaline derivatives bearing eight carboxylic acid groups which were also utilized in the preparation of metal-organic frameworks (MOFs), with high adsorption efficiencies for methane.[34] Mastalerz and Bauerle *et al.* were synthesized a new class of pyrazino[2,3-g]quinoxaline core-functionalized π-conjugated dendrimers based on an electron-accepting core. These compounds showed broad absorption bands over 300-700 nm and have reduced HOMO-LUMO gaps of 1.7-1.9 eV. Incorporation of these compounds in bulk heterojunction solar cells as electron-donating material along with $PC_{61}BM$ as electron acceptor gave power conversion efficiencies of up to 1.3% for the second-generation dendrimer.[35] Sun and Huang *et al.* developed three perylenediimide (PDI) acceptors by functionalizing the bay-positions of PDI with benzil, 2,3-diphenylquinoxaline and 2,3,7,8-tetraphenylpyrazino[2,3-g]quinoxaline as linkers, respectively, which exhibited good photovoltaic properties as n-type conductors.[23]

A series of pyrazino[2,3-g]quinoxaline based molecules with eight peripheral alkyloxy chains of varying length was discussed in chapter 2a and one of the ambient Col LC materials was utilized in the host-guest OLED configuration with CBP host, at 3 wt% concentration there was a display of external quantum efficiency (EQE) of 5.8%, which was much higher than the theoretical limit of fluorescent molecules, i.e., 5%. Rybak *et al.* reported quinoxaline derivatives with semiflexible cores stabilizing columnar mesomorphism.[36] All the abovesaid works inspired to combine carbazole units with pyrazino[2,3-g]quinoxaline central core.

Organic light-emitting diodes (OLEDs) are recently gaining much interest with an increasing foothold in the multibillion-dollar display industry. However, there is a need to overcome major challenges like color purity, compound stability, and the limitation of external quantum efficiency (EQE). The EQE is bound by the theoretical limit of the formation of 25% singlet excitons which are utilized in the emission process. Thus EQE of traditional fluorescence OLEDs is proportionate to the fluorescence efficiency of the molecule. Thus there is a great demand for materials that have near unity fluorescence quantum yield. Another approach to improve EQE is to harvest the remaining 75% triplet excitons through phosphorescence or through thermally activated delayed fluorescence (TADF) as shown in Figure 3.1. Phosphorescence usually requires an organic host and a transition metal-based guest. However, this requires appropriate HOMO-LUMO levels of guest and host, charge carrier transport properties, and high triplet energy. TADF process is based on the reverse intersystem crossing (RISC) from triplet to singlet state. This occurs

TH-2983_156122010

if the energy gap between the singlet and triplet states (ΔE_{ST}) falls below the available thermal energy, which will help to improve the theoretical EQE to around 30%.[13] However, the thin films of TADF emitters alone exhibit reduced performance due to the triplet quenching process. Thus, using a host-guest system is preferred to improve the device performance. The host matrix helps in the minimization of unfavorable triplet quenching and triplet-triplet annihilation and also modulates the ΔE_{ST} of the TADF emitter. The introduction of diluting side groups around the emissive cores with the dendrimeric or polymeric design leads to the dispersion of fluorescent core in such intramolecular host and reduces the crystallinity and phase separation, further leading to enhanced device stability. Further, such modification also helps in the modulation of ΔE_{ST} and also the solution processability of the material.

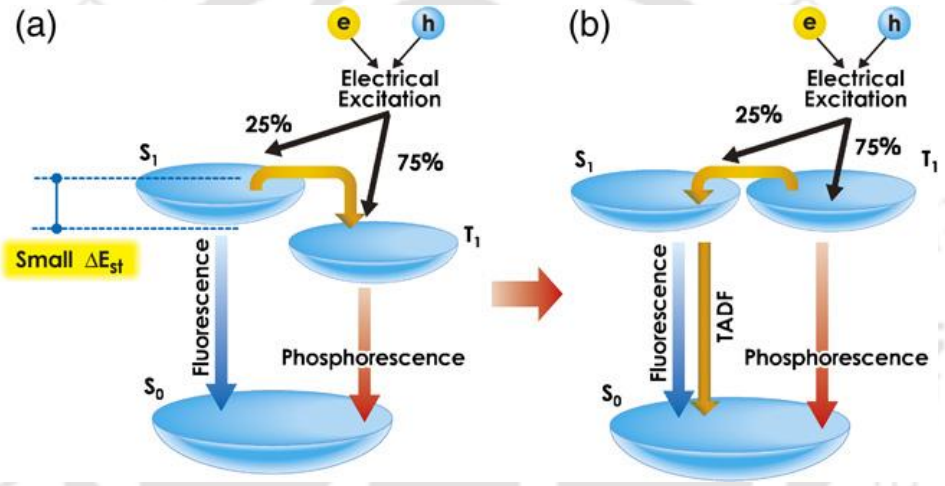

Figure 3.1. Generation process of singlet and triplet excitons upon electrical excitation. (a) Conventional fluorescent and phosphorescent materials. (b) For TADF materials, the S_1 and T_1 levels are close to each other and reverse energy transfer occurs with a high efficiency, enabling highly efficient EL from the S_1 level. (Figure reproduced from reference 11 copyright © 2014, The Japan Society of Applied Physics.)

Considering all the points mentioned above, pyrazinoquinoxaline derivatives were designed and synthesized. It contains four carbazole units bearing flexible alkyl chains leading to a twisted D-A-D molecular structure (Figure 3.2). Further, the self-assembly, photophysical, electrochemical properties, along with the fabrication of multilayer OLEDs both as a single component or as a guest in the host matrix, were studied in detail. The OLED fabricated with compound (**PQC-12b**) alone exhibited very low efficiency, while doping into a bipolar host matrix increased the EQE to 8.0%. Further, the device performance was improved (EQE = 15.3%) with the introduction of a TADF emitter to harvest the triplet excitons, resulting in high color purity. The introduction of a phosphorescent blue emitter to this yellowish-green emitter led to the technologically

TH-2983_156122010

important white OLED (WOLED) with an EQE of 12.0% coupled with high brightness. The impressive efficiencies, device lifetime, and stability of compound **PQC-12b** make it a highly promising material for the fabrication of cost-effective solid-state displays and commercial lighting applications.

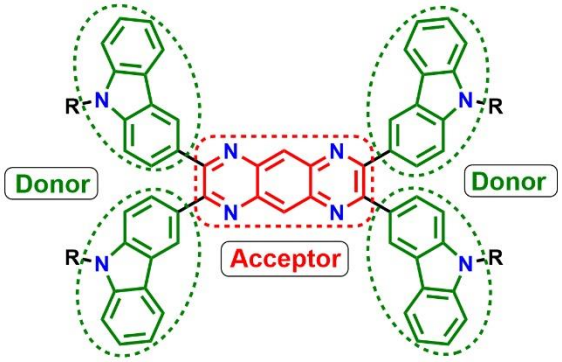

Figure 3.2. Schematic structural representation of the pyrazino[2,3-g]quinoxaline carbazole (PQC) derivative with their donor and acceptor moieties along with flexible alkyl chains (R).

3.2. Result and discussion

3.2.1. Synthesis and molecular structural characterization

The target PQC derivatives were prepared from the following simple, short and straightforward synthetic pathway (Scheme 3.1). In the first step, *N*-alkylation of carbazole (**1n** and **1b)** was carried out via the nucleophilic substitution reaction with normal/branched alkyl bromide in the presence of a strong base (KOH). In the second step, two equivalents of *N*-alkylated carbazole were reacted with oxalyl chloride in the presence of anhydrous $AlCl_3$ by Friedel-Craft's acylation to obtain the corresponding *N*-alkylated carbazole 1,2-diketone derivatives (**2n** and **2b)**. Finally, the corresponding diketones were condensed with 1,2,4,5-tetraaminobenzene tetrahydrochloride to get the target PQC derivatives.

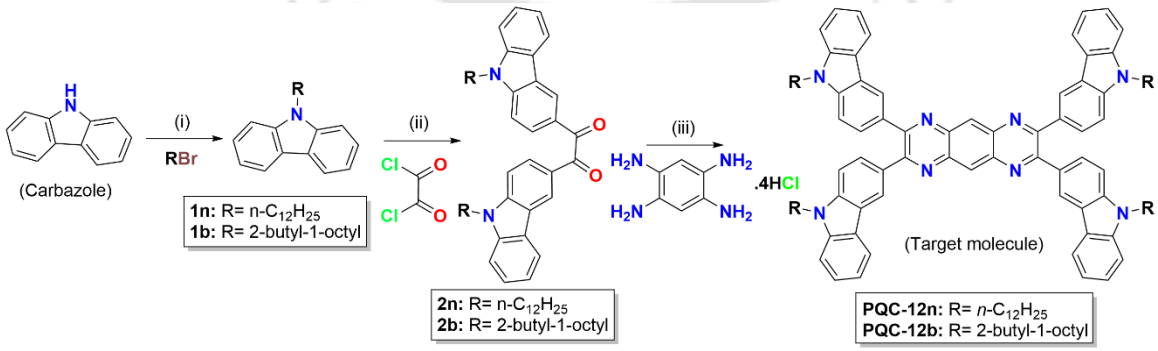

Scheme 3.1. Reagents and conditions: (i) R-Br, KOH, DMSO, 24 h, rt, 85-90%; (ii) 1,2-Dichloroethane, oxalyl chloride, anhydrous $AlCl_3$, 0 °C (30 min.), rt (17 h), 40-45%; (iii) Methanol: acetic acid (1:3), 130 °C, triethylamine, 12 h, 75-80%.

TH-2983_156122010

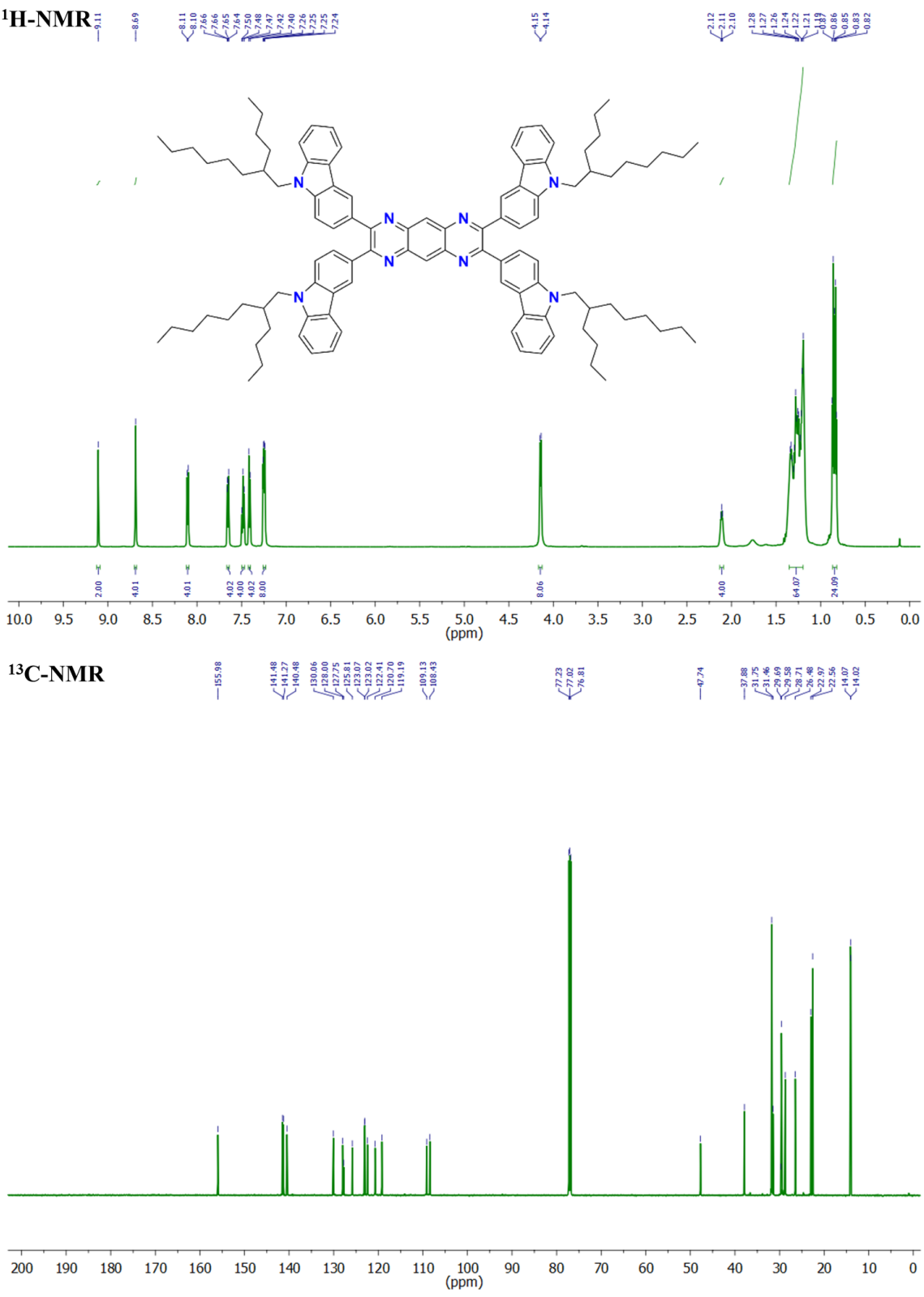

Figure 3.3. ^{1}H NMR (600 MHz) and ^{13}C NMR (150 MHz) spectra of compound **PQC-12b** in $CDCl_3$.

Structural elucidation and purity of all the compounds were investigated and confirmed by various analytical techniques i.e. (^{1}H, ^{13}C NMR, IR spectroscopy, HRMS/MALDI-TOF mass spectrometry), which were discussed in the experimental

TH-2983_156122010

section of this chapter. One of the final carbazole PQ derivative's (**PQC-12b**) ^{1}H and ^{13}C NMR spectra were shown in Figure 3.3.

3.2.2. Thermal behavior

The thermal behavior of both (**PQC-12n** and **PQC-12b**) compounds was studied with various techniques like polarizing optical microscopy (POM) along with a programmable hot stage, differential scanning calorimetry (DSC), and thermo-gravimetric analysis (TGA). POM studies of the **PQC-12n** compound did not show any characteristic birefringence and optical textures in the heating and cooling process. In contrast, compound **PQC-12b** on cooling from the isotropic state shows crystallization texture, which was non-sharable and started from 160 ^{o}C and persists till room temperature (Figure 3.4). DSC studies confirmed the crystal-crystal (Cr-Cr) transition and a crystal-isotropic transition (Cr-I) on heating in both compounds. But on cooling, both the compounds did not show any isotropic-crystal (I-Cr) transition, while a very small peak was observed around 25 ^{o}C. The **PQC-12n** compound was found to be glassy in nature, while the **PQC-12b** compound shows crystalline nature in the POM observation. **PQC-12n** exhibited a lower clearing temperature than its branched-chain counterpart (Figure 3.5 and Table 3.1).

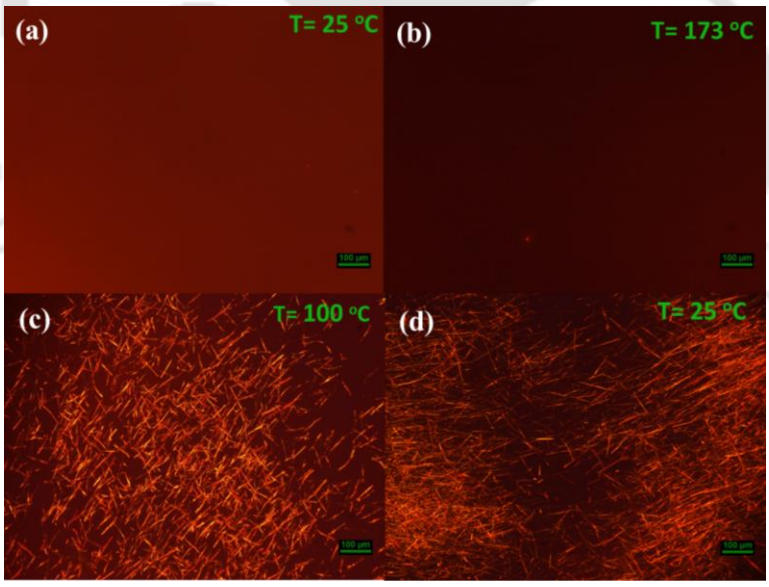

Figure 3.4. Photomicrograph of compounds **PQC-12n** (a) at 25 ^{o}C; **PQC-12b** (b) at 173 ^{o}C, (c) at 100 ^{o}C and (d) at 25 ^{o}C on cooling from the isotropic melting.

TH-2983_156122010

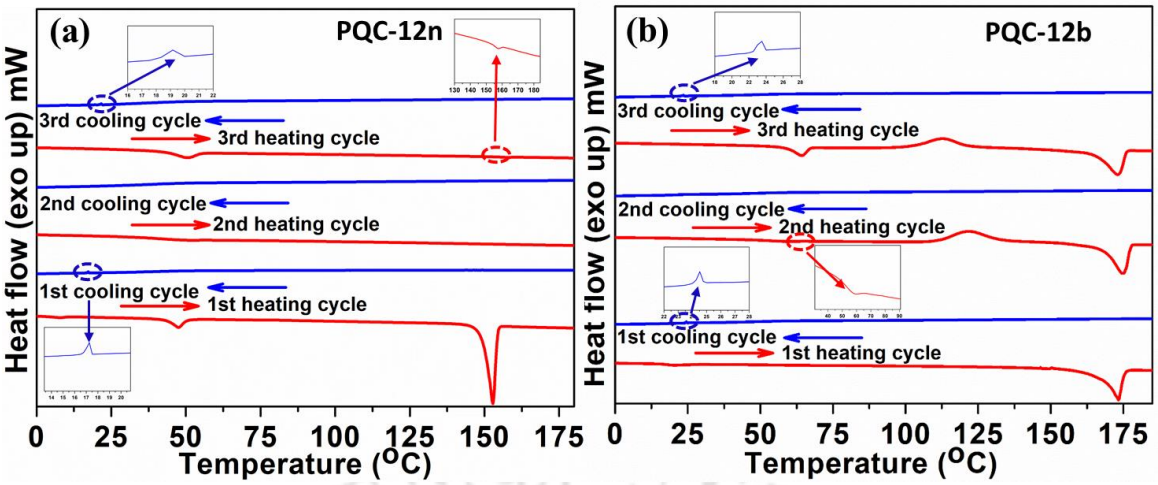

Figure 3.5. (a) DSC traces obtained for compound **PQC-12n**; (b) **PQC-12b** in the first, second and third heating and cooling scans at a rate of 5 °C min^{-1} under the Nitrogen gas atmosphere. The third scan was done after a week to observe the small transition peaks, which was not seen in the second scan.

TGA studies revealed that the compounds are stable at least up to 248 °C (Figure 3.6). Further, XRD studies of the powder sample revealed the crystalline nature. The drop casted thin film of these compounds was studied by XRD studies. Both the compounds behaved differently, *i.e.*, the **PQC-12b** shows more crystalline nature compared to **PQC-12n**. The **PQC-12n** exhibited a peak with a *d*-spacing of 21.02 Å along with a diffused peak at a wide-angle region. However, **PQC-12b** showed a sharp peak at the low angle region with a *d*-spacing of 21.12 Å and multiple peaks in the mid and wide-angle region Figure 3.7.

Table 3.1. Phase transition temperatures[a] (°C) and corresponding enthalpies (kJ mol^{-1}) of the **PQC-12n** and **PQC-12b** derivatives

Entry	Phase sequence					
	1st Heating	2nd Heating	3rd Heating[b]	1st Cooling	2nd Cooling	3rd Cooling[b]
PQC-12n	Cr_{r1} 47.5 (4.97) C_{r2} 153.3 (43.53) I	-	Cr_{r1} 50.4 (5.26) C_{r2} 157.9 (0.08) I	I 16.7[c] C_r	G	I 19.2[c] C_r
PQC-12b	C_{r1} 20.5[c] C_{r2} 173.5 (34.5) I	Cr_{r1} 59.7[c] C_{r2} 121.5 (22.4) C_{r3} 174.5 (31.0) I	Cr_{r1} 65.15 (7.7) Cr_{r2} 115.9 (17.9) C_{r3} 174.5 (32.0) I	I 24.5[c] C_r	G	I 23.5[c] C_r

[a]Peak temperatures in the DSC thermograms obtained during the heating and cooling cycles at 5 °C min^{-1}; [b] 3rd cycle was performed after a few days to observe slow crystallization peaks (Cr = crystal; G=glassy state; I = isotropic liquid.); (c) very small change in enthalpies observed in DSC thermograms.

TH-2983_156122010

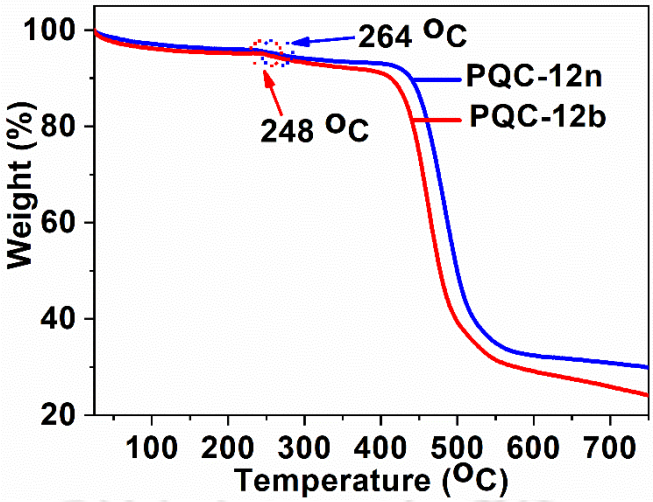

Figure 3.6. TGA thermograms of **PQC-12n** and **PQC-12b** at a scan rate of 10 °C min^{-1} under the nitrogen gas atmosphere.

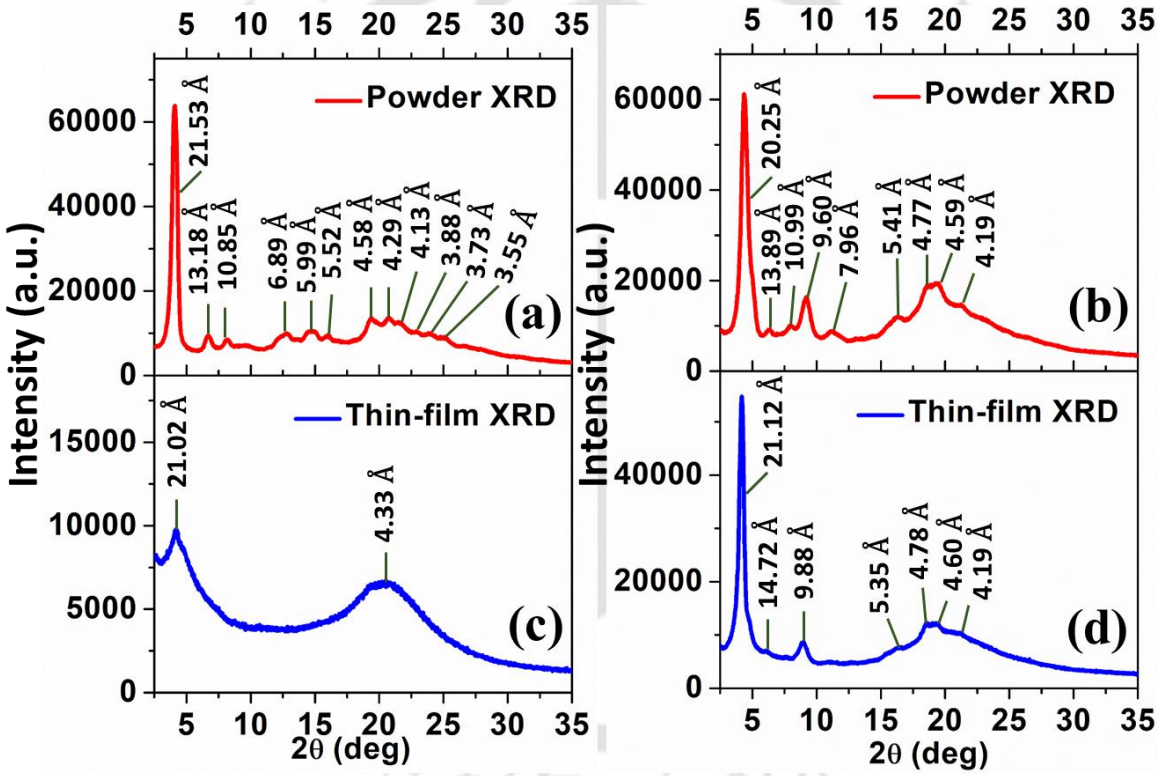

Figure 3.7. PXRD (a and b) and TXRD pattern (c and d) of compounds **PQC-12n** and **PQC-12b** (with their corresponding *d*-spacing value) in their powder and thin film-state, prepared by a thermal evaporation technique on the glass substrates at RT. (Here the hkl values were not shown in the XRD graph as these compounds didn't shown liquid crystalline behaviour.)

3.2.3. Photophysical properties

The photophysical properties of both PQC derivatives were studied in solution and solid thin films (Figure 3.8). The absorption spectra of PQC derivatives in micromolar solution were observed at 486/487 nm and 506 nm (λ_{max}). The PL emission spectra of both compounds showed an emission maximum at 546 nm with large Stokes shifts (1448 cm^{-1})

TH-2983_156122010

and very high molar extinction coefficients in the range of 57127-63033 $Lmol^{-1}cm^{-1}$. (Table 3.2 and Figure 3.9)

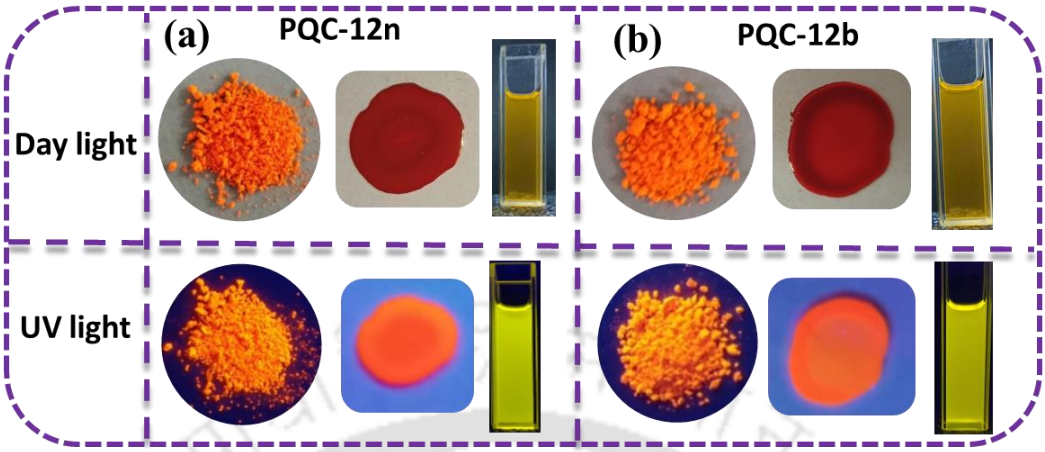

Figure 3.8. Photographs of compounds **PQC-12n** (a) and **PQC-12b** (b) powder, thin-film and in THF solution were taken under daylight and UV light.

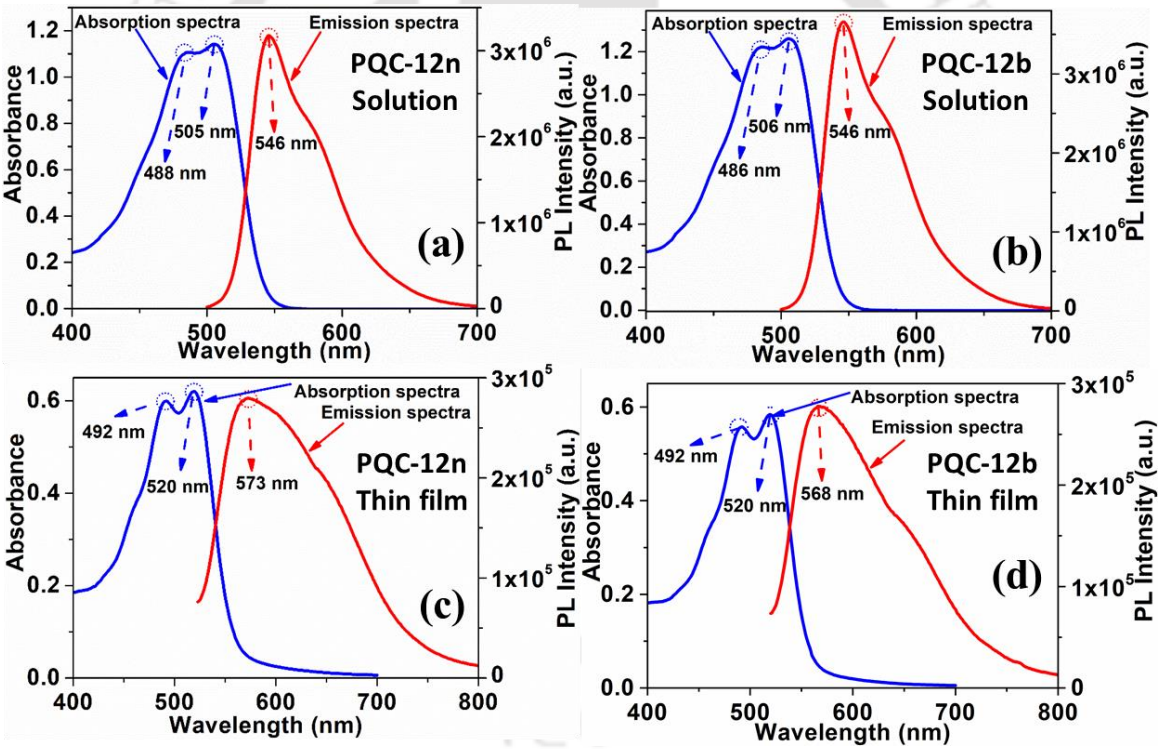

Figure 3.9. An overlay of the absorption and emission spectra of compound **PQC-12n** and **PQC-12b** in THF solution and thin-film state.

The thin films of these compounds were prepared by the spin coating of the millimolar solutions of the compounds in toluene solvent over quartz plates. The absorption spectra of the thin films showed a red shift in comparison to the solutions by 14 nm, while the emission spectra also showed a red shift in similar ways by 22-27 nm. The Stokes shift also had shown a slight increase compared to solutions, varying in the range of 1625-1779 cm^{-1} (Table 3.2). Visually the emission of these solutions was found to be perceivable as

TH-2983_156122010

yellowish (in case of THF solvents), while in the thin film state, they exhibited an orange emission, under UV light of long-wavelength (λ_{max} = 365 nm) as shown in Figure 3.8. Overlay of emission spectra of micromolar solutions over thin films showed a decrease in the intensity suggesting an aggregation-induced luminescence quenching.

Table 3.2. Photophysical properties of PQC derivatives

	Solution state[a]						Thin film state[f]		
	Absorption (nm)	ε ($Lmol^{-1}cm^{-1}$)	Emission[b] (nm)	Stokes shift (cm^{-1})	$\Delta E^{c}_{g,opt}$ (eV)	Quantum yield[d]	Absorption (nm)	Emission[e] (nm)	Stokes shift (cm^{-1})
PQC-12n	486, 506	57127	546	1448	2.28	0.72	492, 520	573	1779
PQC-12b	487, 506	63033	546	1448	2.28	0.74	492, 520	568	1625

[a] micromolar solutions in THF; [b] λ_{ex} = 506 nm; [c] calculated from the red edge of the absorption band; [d]relative quantum yields of these compounds calculated with respect to a solution of rhodamine in a ethanol solution as the standard (Q_f = 0.95); [e] λ_{ex} = 520 nm .[f]Thin films were obtained by the spin coating of millimolar solution of compounds in toluene on quartz plate.

The surface morphology of the thin film was investigated with the help of atomic force microscopy (AFM) and showed that the surface roughness is very small (RMS roughness ≈ 2.4 nm), highlighting the good film-forming ability (Figure 3.10) for **PQC-12b** compound.

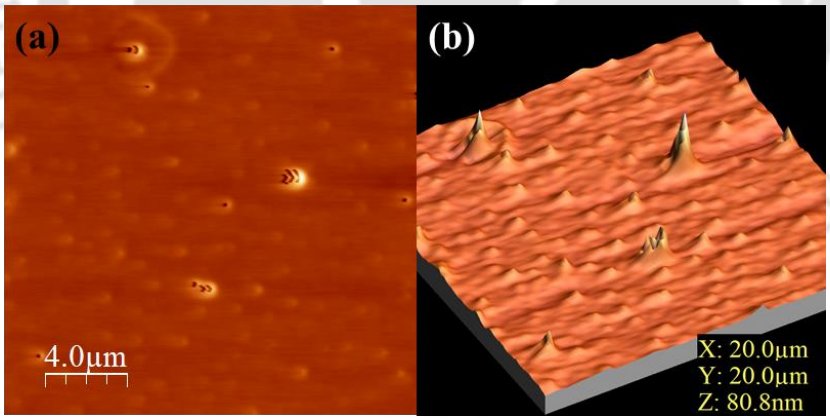

Figure 3.10. AFM image of the spin-coated thin film on quartz substrate using a millimolar **PQC-12b** solution in toluene.

Time-resolved photoluminescence studies in solution showed the presence of one excited species and in thin films, two excited species with shorter lifetimes were observed for both compounds **PQC-12n** and **PQC-12b**, suggesting the ACQ in solid state (Table 3.3 and Figure 3.11).

TH-2983_156122010

Table 3.3. Data obtained from the time-resolved photoluminescence experiments of compounds **PQC-12n** and **PQC-12b** derivatives.

	Solution[a]	**Thin film**[b]
Entry	Fraction (Life time)	Fraction (Life time)
PQC-12n	100% (2.27 ns)	61.13% (0.23 ns); 38.87% (1.97 ns)
PQC-12b	100% (2.29 ns)	84.27% (0.49 ns); 15.73% (1.71 ns)
[a]Concentration: 20 μM solution in THF; [b]Concentration of solution used for spin coating: 20 mM in toluene		

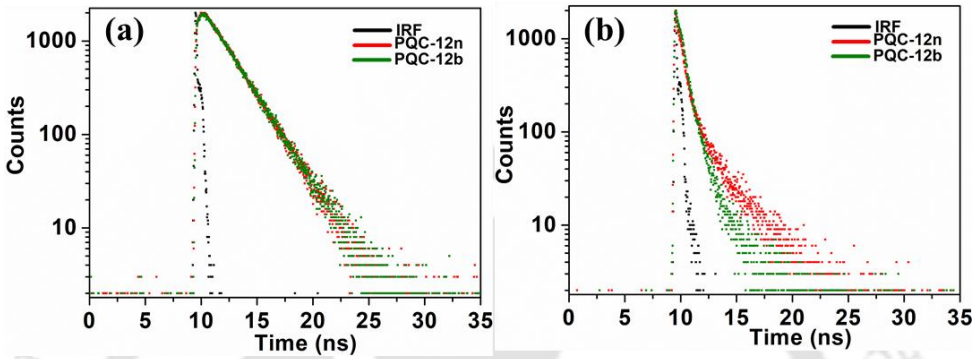

Figure 3.11. Fluorescence decay plots of compounds **PQC-12n** & **PQC-12b** in micromolar solution in THF (a) and for the spin-coated thin film on quartz plate using a millimolar solution in toluene (b) (IRF: Instrument response function).

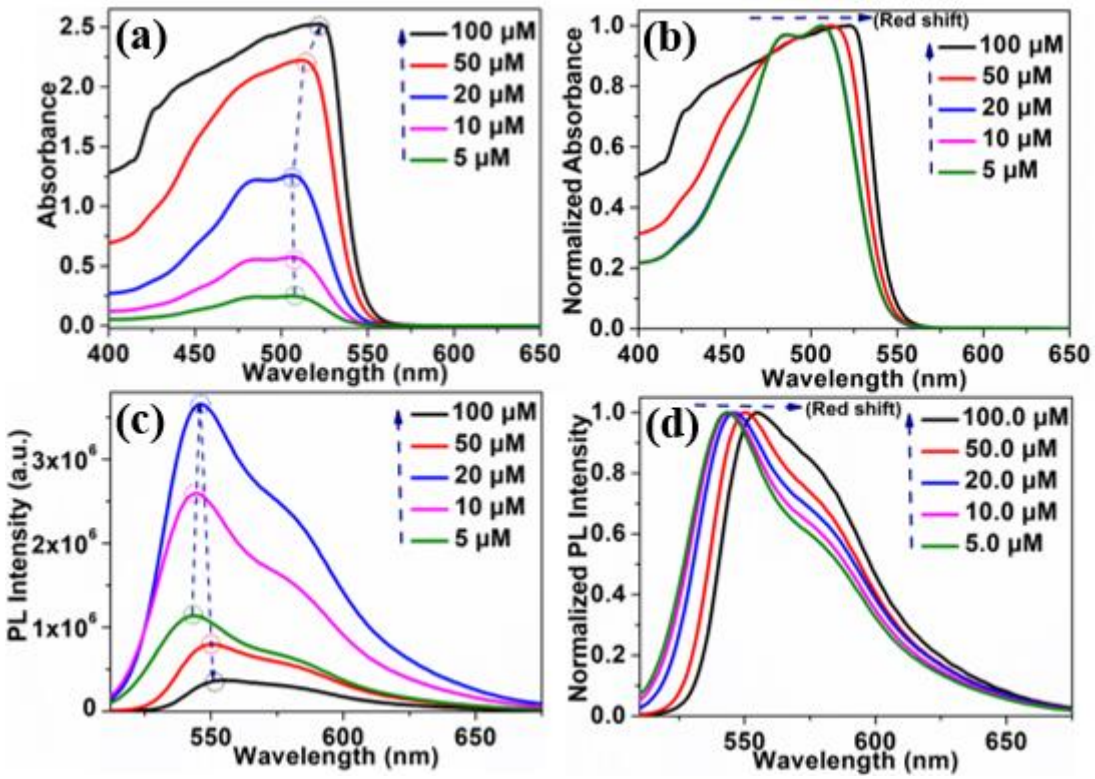

Figure 3.12. Compound **PQC-12b** showing the aggregation behavior (red-shift) in higher concentration in UV and PL study; (a) Overlay of absorption spectra; (b) normalized version of the

TH-2983_156122010

same; (c) overlay of emission spectra and (d) normalized version of the same with varying concentrations of compound **PQC-12b** in THF solution.

Table 3.4. Absorption and emission of compound **PQC-12b** in different concentrations

PQC-12b (in THF)		
Concentration	Absorption (nm)	Emission (nm)
100 µM	521	555
50 µM	509	550
20 µM	486, 506	546
10 µM	485, 506	544
5 µM	485, 506	543

The absorption spectra of the representative compound **PQC-12b** in micromolar solution on increasing the concentration led to a red-shifted absorption band (Table 3.4 and Figure 3.12). Emission spectra showed an increase in the intensity at the beginning with the increase in concentration, but at higher concentration, the aggregation caused quenching (ACQ) of luminescence were noticed along with a red-shift in the emission. The red-shifted absorption along with the aggregation suggests the formation of J-aggregates. The optical band-gap of both PQC compounds calculated from their absorption onset was found to be 2.28 eV. The initial rise in the emission intensity could be due to the excimer emission, with the excited-state lifetime of a few nanoseconds.

Photophysical studies of the compound **PQC-12b** in the aggregated state were carried out in THF-water mixtures at fixed concentrations of the compound **PQC-12b** but by varying the ratio of THF and water (Figure 3.13). The PL intensity at 546 nm (f_w= 0%) is quenched on the addition of water (f_w = 10% to f_w = 40%) with redshift of ~17 nm). At f_w = 50%, the emission spectra were blue-shifted (~5 nm, 558 nm) with an increase in the PL intensity and showed maximum emission at f_w = 60%, as shown in Figure 3.13. Further

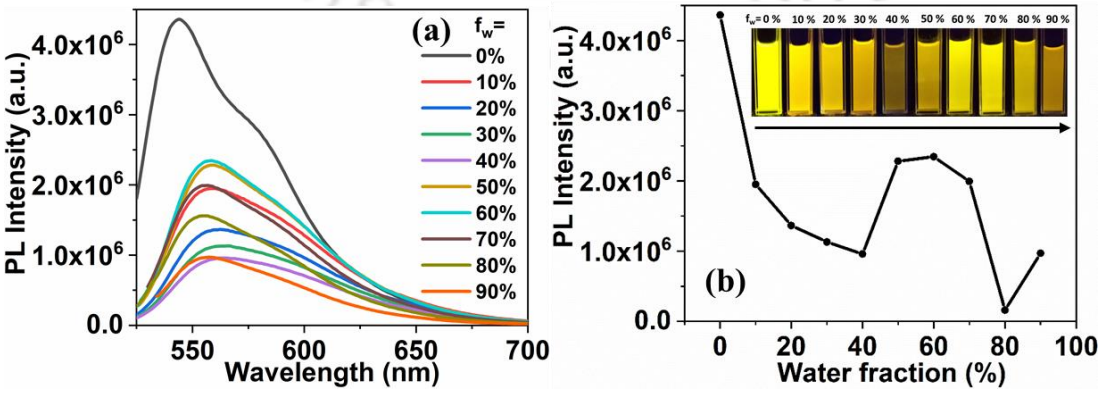

TH-2983_156122010

Figure 3.13. PL spectra of **PQC-12b** (1×10^{-5} M) in Water/THF mixtures with different water fractions (a); Changes in PL peak intensity with water fraction; (b) (inset: photographs of compound **PQC-12b** under UV-light in THF-water upon increasing water fraction from $f_w = 0$ to 90%).

increase in the amount of water leads to a blue-shifted emission (~3 nm) with the concurrent decrease in the PL intensity (at $f_w = 80\%$). The decrease in the PL intensity on increasing the amount of water ($f_w > 90\%$) may be the outcome of precipitation (Figure 3.13).

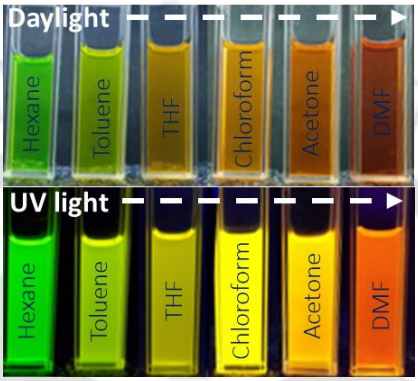

Figure 3.14. Photographs of **PQC-12b** taken in different solvents: Hexane, Toluene, THF, Chloroform, Acetone and DMF in micromolar concentration (arrow indicates the lower to higher polarity order) under daylight and UV light.

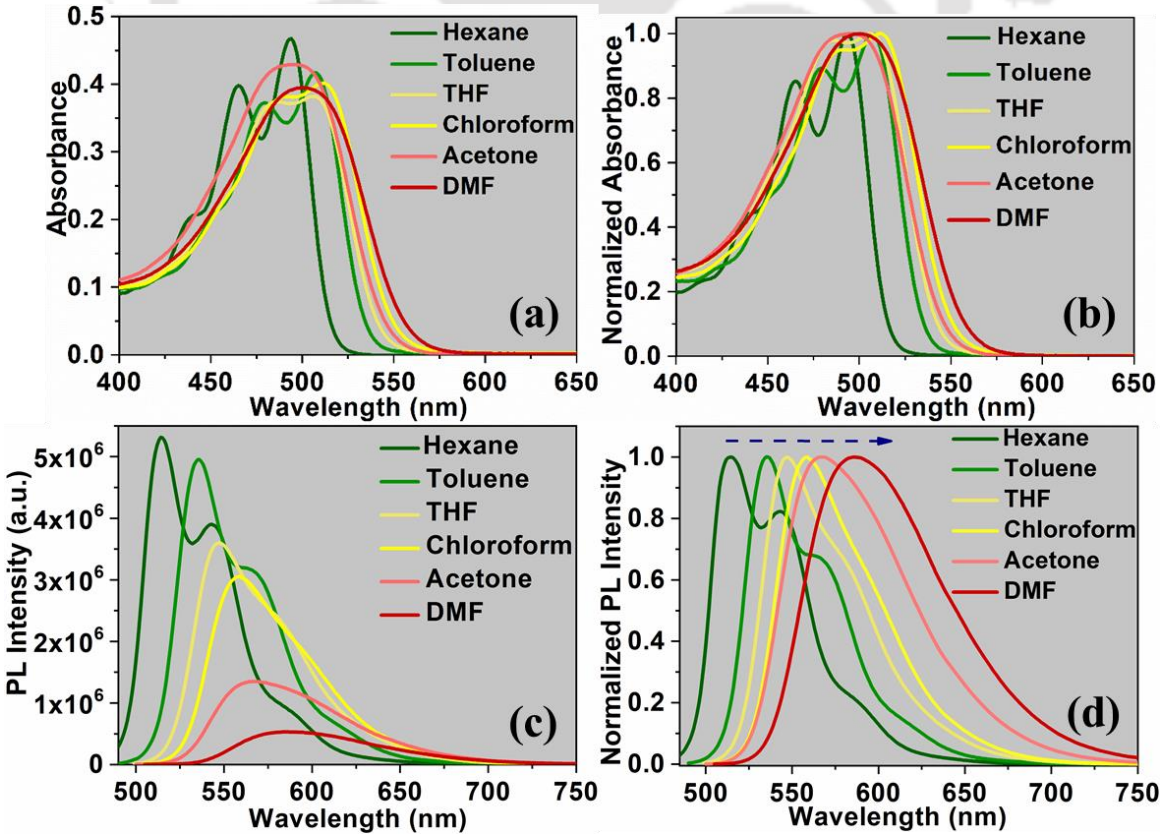

TH-2983_156122010

Figure 3.15. Solvatochromism study of compound **PQC-12b**. PL spectra showing the decreases in intensity and red-shifts with an increase in the solvent polarity; (a) Overlay of absorption spectra; (b) normalized version of the same; (c) overlay of PL spectra and (d) normalized version of the same.

Table: 3.5. Absorption and emission of compound **PQC-12b** (20 μM) in different solvents

PQC-12b		
Solvents	**Absorption (nm)**	**Emission (nm)**
Hexane	465, 494	515, 543
Toluene	480, 506	535, 558
THF	487, 506	546
Chloroform	490, 511	558
Acetone	496	567
DMF	500	586

The red-shifted absorption band and ACQ with a red-shift in the emission were noticed, as seen in the example of solvent-dependent experiments. The compound exhibited a positive solvatochromism, where red-shifted emission spectra were observed with the increase in the solvent polarity, which confirmed the polar nature of the excited state (Table 3.5, Figure 3.14 and 3.15). This solvatochromism behavior was in line with the DFT studies which was further discussed in the DFT section.

Relative quantum yields of compounds **PQC-12n** and **PQC-12b** were measured with respect to rhodamine 6G (Q_f = 0.95) in ethanol solution as the standard. Absolute values were calculated according to the following equation: $Q_S = Q_R \times (m_S / m_R) \times (n_S / n_R)^2$ Where, Q: Quantum yield; m: Slope of the plot of integrated fluorescence intensity *vs* absorbance; n: refractive index (1.407 for THF and 1.361 for ethanol). The subscript R refers to the reference fluorophore (rhodamine 6G) and subscript S refers to the sample under investigation. In order to minimize re-absorption effects, absorbance was kept below 0.15 at the excitation wavelength of 506 nm. The quantum yield of rhodamine 6G is 0.95. A simplified equation for the calculation after substituting the appropriate values is given below and values obtained are given in the table below.

$Q_S = 0.95 \times (m_S / m_R) \times (1.407/1.361)^2$

$= 0.95 \times (m_S / m_R) \times 1.06919$

The relative quantum yields calculated with respect to a solution of rhodamine 6G in ethanol solution as the standard (Q_f = 0.95) were found to be around 0.72 and 0.74 (Table 3.6, Figure 3.16).

TH-2983_156122010

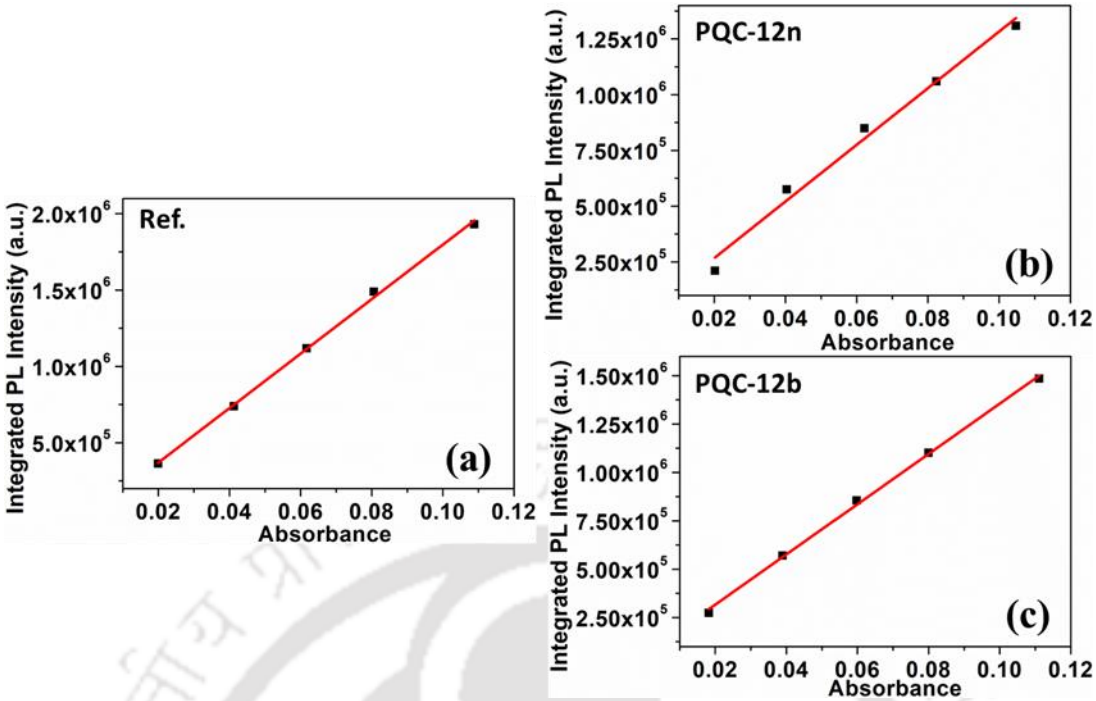

Figure 3.16. Plots of integrated photoluminescence intensity vs absorbance of **Ref.** (Rhodamine 6G) in ethanol solution excited at 506 nm (a); integrated photoluminescence intensity vs absorbance of compounds **PQC-12n** (b) and **PQC-12b** (c) in THF solution excited at 506 nm.

Table 3.6. Relative quantum yields of PQC derivatives

Compounds	m_S	m_R	$Q_s^{a,b,c}$
PQC-12n	1.26937×10^7	1.78472×10^7	0.72
PQC-12b	1.29836×10^7	1.78472×10^7	0.74
[a] Measured in THF; [b]Excited at absorption maxima; [c]Rhodamine (Q_f = 0.95) in ethanol.			

3.2.4. Electrochemical properties and DFT studies

Cyclic voltammetry (CV) studies of **PQC-12n** and **PQ-12b** were carried out to comprehend the electronic energy levels, which are very important in deciding the energy and electron transfer process as well as the reversibility of a redox process. CV studies were carried out in anhydrous dichloromethane solutions in millimolar concentration (Table 3.7 and Figure 3.17). All the compounds exhibited an irreversible oxidation potential at ~ 1.13 V. From this value, the HOMO level was calculated and found to be ~ -5.42 eV. LUMO levels were calculated by subtracting the HOMO energy values from the optical band gap (2.28 eV) which was obtained from the absorption onset values. LUMO levels were found to be around -3.14 eV.

TH-2983_156122010

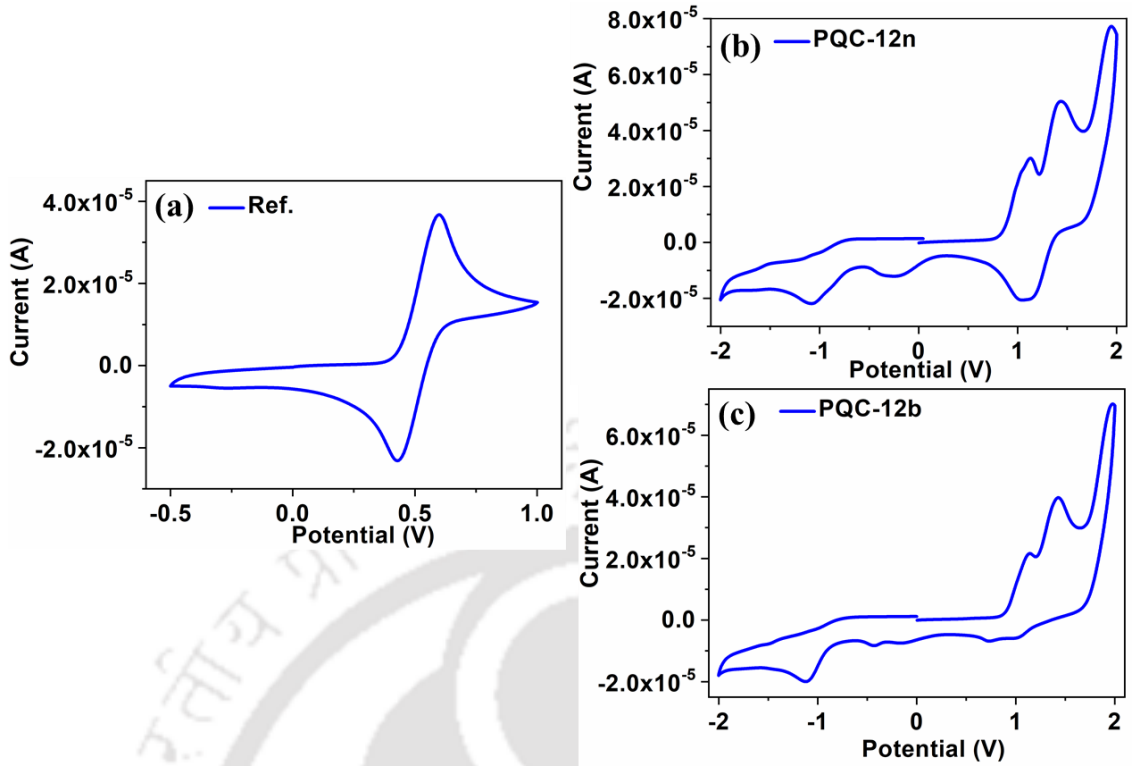

Figure 3.17. Cyclic voltammetry of (**Ref.**) ferrocene (a); cyclic voltammetry (CV) plots of compounds **PQC-12n** (b) and **PQC-12b** (c) in DCM solution of tetra-n-butylammonium perchlorate (TBAP) (0.1 M) at a scanning rate 100 mV s^{-1} and 20 mV s^{-1} respectively; the half wave potential of Fc/Fc^{+} was found to be 0.51 V relative to Ag/Ag^{+} reference electrode.

Table 3.7. Electrochemical properties of **PQC-12n** and **PQC-12b** derivatives in solution[a,b]

Compounds	E_{1oxd}[c]	E_{2oxd}[c]	E_{HOMO}[c,e]	E_{LUMO}[c,f]	$\Delta E_{g,opt}$[d,g]
PQC-12n	1.13	1.43	-5.42	-3.14	2.28
PQC-12b	1.13	1.43	-5.42	-3.14	2.28

[a]Dichloromethane solutions; [b]experimental conditions: $Ag/AgNO_3$ as reference electrode, glassy carbon working electrode, platinum wire counter electrode, TBAP (0.1M) as a supporting electrolyte, room temperature; [c]in volts (V); [d]in eV; [e]estimated from the formula by using E_{HOMO}= -(4.8-$E_{1/2,Fc/Fc+}$+$E_{oxd,onset}$) eV; [f]estimated from the formula E_{HOMO}=E_{LUMO}-$E_{g,opt}$ eV; [g]calculated from the red edge of the absorption band; $E_{1/2,\ Fc/Fc+}$ = 0.51.

The DFT calculations were carried out to obtain the energy-minimized structures, the spatial distribution of HOMO-LUMO levels (Figure 3.18a-b) and to understand the thermally activated delayed fluorescence (TADF) *via* the energy gap between the lowest singlet and lowest triplet states (ΔE_{ST}) and solvatochromism property of the PQC derivatives (Table 3.8). The optimized structure of compound **PQC-12n** and **PQC-12b** reveals that the carbazole moiety is twisted with respect to the central pyrazino[2,3-

TH-2983_156122010

g]quinoxaline unit. The dihedral angles between donor and acceptor units were found to be 46.8º, 46.9º, 136.4º and 139.7º in **PQC-12n** and similarly 46.7º, 46.7º, 136.2º and 139.9º respectively, in **PQC-12b** as shown in Figure 3.19a-b. The HOMO distribution is mainly localized on the cabarzole moiety with very limited spread over PQ unit. The LUMO is mainly localized on the pyrazino[2,3-g]quinoxaline (**PQ**) part, resulting in a small overlap between the HOMO and the LUMO. In comparison to the energy levels obtained from electrochemistry, the TD-DFT calculations showed an increased LUMO value but a lowered HOMO value. The difference between the two LUMO values calculated (by DFT and cyclic voltammetry) was found to be higher in comparison to the difference in HOMO values. The values of HOMO and LUMO energy levels of compounds **PQC-12n** and **PQC-12b** obtained from DFT calculations were comparable with the results obtained in earlier chapter. The 3D molecular electrostatic potential (MEP) contour map of the optimized structure of compound **PQC-12b** shown in Figure 3.19c-d (In the mapped electrostatic potential surface, the red and blue colors correspond to the negative and positive electrostatic potential, respectively, whereas the green color corresponds to the zero electrostatic potential). The molecular diameter of the optimized structures was found to be around 46.86 Å and 38.2 Å (Figure 3.19e-f).

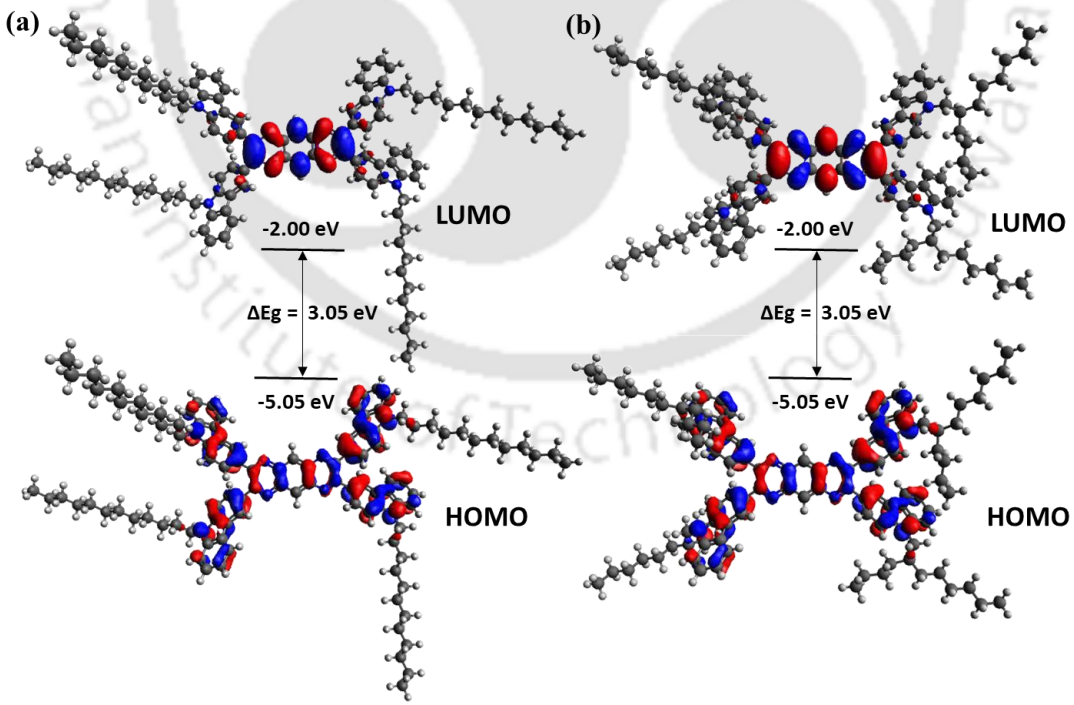

Figure 3.18. (a) HOMO and LUMO levels of **PQC-12n** and **PQC-12b** (DFT calculations were performed at B3LYP/6-31G (d, p) level).

TH-2983_156122010

Table 3.8. Theoretical TD-DFT calculations of **PQC-12n** and **PQC-12b** derivatives

(TD-DFT analysis)					
Compound (phase/Solvents)	**Absorption (nm)**	**ΔE_{ST}**	**HOMO**	**LUMO**	**ΔE_g**
PQC-12n (Gas phase)	470	0.52	-5.05	-2.00	3.05
PQC-12b (Gas phase)	471	0.51	-5.05	-2.00	3.05
PQC-12b (Heptane)	487	0.42	-5.18	-2.19	2.99
PQC-12b (Toluene)	491	0.40	-5.20	-2.24	2.96
PQC-12b (Chloroform)	499	0.36	-5.27	-2.34	2.93
PQC-12b (THF)	502	0.34	-5.30	-2.39	2.91
PQC-12b (Acetone)	505	0.33	-5.33	-2.44	2.89

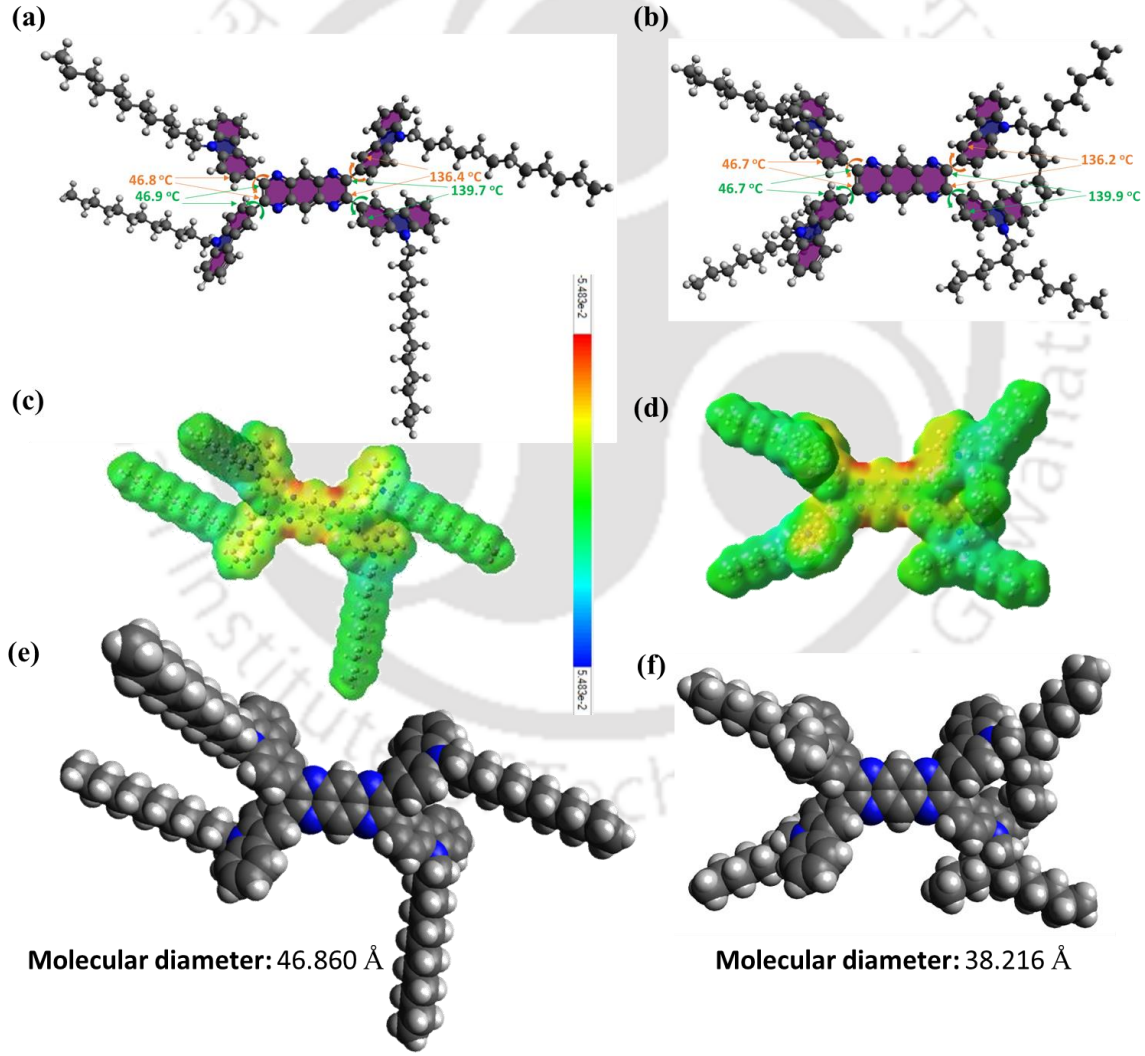

Figure 3.19. The optimized conformations and dihedral angles of the **PQC-12n** (a) and **PQC-12b** (b); 3D molecular electrostatic potential (MEP) contour map of optimized structure **PQC-12n** (c) and **PQC-12b** (d); the molecular diameter of the optimized conformations **PQC-12n** (e) and **PQC-12b** (f); carried out by TD-DFT analysis at the B3LYP/6-31G (d, p).

TH-2983_156122010

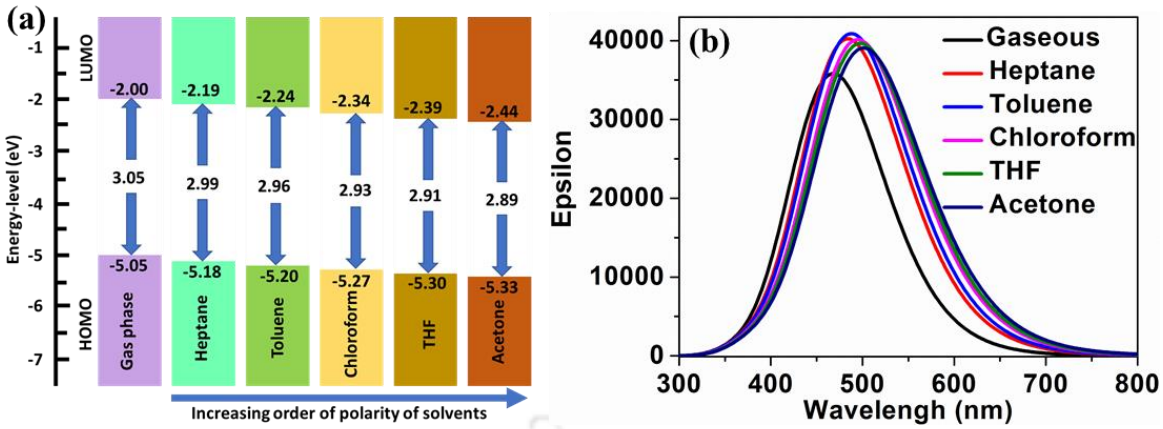

Figure 3.20. Schematic diagram showing the HOMO-LUMO levels, energy band-gap (a); and UV spectra (b) were performed of compound **PQC-12b** in gaseous phase, heptane, toluene, chloroform, THF and acetone solvents. (TD-DFT studies were calculated at B3LYP/6-31G (d, p), cpcm level).

DFT studies were also used to understand the solvatochromism behavior. Absorption and emission spectra of compound **PQC-12b** were obtained in solvents of varying polarity (from hexane to DMF). No significant change in the peak maxima and the shape of the absorption band was noticed on varying the solvent polarity. This was in line with the DFT studies (Figure 3.20b). The steady state emission spectra of compound **PQC-12b** exhibited solvatochromic fluorescence on varying the polarity of solvents. A red-shifted absorption band and ACQ with a red-shifted emission were noticed in these solvent-dependent experiments. The overlay of the normalized emission spectra shows a red-shift on moving from non-polar to polar solvents (green to orange emission) (Table 3.5, Figure 3.14 and Figure 3.15). This phenomenon is generally called positive solvatochromism, which indicates that increasing the solvent polarity induces the dipolar stabilization of the excited state (Table 3.8). The substantial solvatochromic shifts observed in the fluorescence spectra in comparison to insignificant changes in the absorption spectra propose an excited state with a stronger intramolecular charge transfer (ICT) character and larger dipole moments relative to the ground state. The large Stokes shift and spectral broadening also indicates a highly polarized ICT state.[37]

Solvent-dependent TD-DFT studies suggest that both ΔE_{ST} and the band-gap decrease on increasing solvent polarities (Table 3.8 and Figure 3.20a). The decrease in ΔE_{ST} was observed by increasing the polarities from non-polar to polar solvents. This is mainly due to stabilization of the singlet excited (S_1) state while the change in the energy level of the lowest triplet excited state (T_1) is minimum, leading to a reduction in the energy gap between S_1 and T_1. Thus the ΔE_{ST} value has changed from 0.51 eV to 0.32 eV, on moving from non-polar to polar solvents. The stabilization of S_1 state was further confirmed by the

TH-2983_156122010

increase in Stokes shift in PL spectra of **PQC-12b** with the increase in the solvent polarity (Table 3.5, Figure 3.14 and Figure 3.15).[38-39]

3.2.5. Electroluminescence studies

3.2.5.1. Device fabrication and characterization

To explore the electroluminescent properties of one of the emitter materials **PQC-12b**, the organic light-emitting diodes (OLEDs) were fabricated on glass substrates, which have indium tin oxide (ITO) as an anode. **PQC-12b** based devices were fabricated with the solution process. The device structures were exhibited following device configurations: ITO/ PEDOT: PSS/ **PQC-12b**/ TPBi/LiF/Al and ITO/ PEDOT: PSS/ CBP:1, 3, 5, 7.5, 10.0, and 12.5 wt% **PQC-12b**/TPBi/LiF/Al for non-doped and doped devices, respectively. The device structure for triplet-exciton harvesting, consisted of ITO/ PEDOT: PSS/ CBP:10.0 wt% **PQC-12b**: 3, 6, 9, 12.5, and 15 wt% 4CzIPN/ TPBi/LiF/Al. The warm white OLED devices were fabricated with the following device configuration: ITO/ PEDOT: PSS/ CBP:20.0 wt% FIrpic: 3, 5, 7.5, and 10 wt% **PQC-12b**/ TPBi/ LiF/Al. Initially, ITO coated glass substrates were washed with soap solution, rinsed in deionized water for 2 min, cleaned with acetone at 50 ^{o}C for 30 min, and isopropyl alcohol at 60 ^{o}C for 40 min. A Water-bath-tub sonicator was used to carry out this washing procedure. To remove impurities and residual solvents, substrates were exposed to the ultraviolet-ozone (UVO) light for 15-20 min. After UVO treatment, these substrates were loaded into the glovebox, which was purged with nitrogen. PEDOT: PSS was spin-coated at 4,000 rpm for 20 s to form a hole-injection layer followed by annealing at 130 ^{o}C for 15 minutes. The guests PQC-12b, 4CzIPN, FIrpic, and host (CBP) were separately dispersed in tetrahydrofuran (THF) solvent at 40 °C till 50 min in a water-bath-tub sonicator. Formerly, the desired emissive layer solutions were prepared by filtering and mixing them in the desired ratio. Then, emissive layers of neat and doped **PQC-12b** were spin-coated onto the different PEDOT: PSS thin layers at 2,700 rpm for 20 s. Subsequently, samples were loaded into a thermal evaporator chamber purged with helium and nitrogen to deposit consequent layers. After that, an electron transport layer TPBi, an electron injection layer LiF and a cathode Al were prepared successively via the thermal evaporation method at a base pressure of 4.0×10^{-6} Torr. Then, the mini vacuum chamber was used to keep the device after the fabrication. During the testing process, the devices were measured one by one at room temperature conditions. To measure the electroluminescence (EL) spectrum, luminance,

TH-2983_156122010

and the CIE coordinates, a photo research (PR-655) spectrometer was utilized. A computer mounted voltmeter (Keithley 2400) and spectrophotometer CS-100 Minolta was used to measure current density-voltage-luminance (J-V-L) characteristics of the fabricated devices.

3.2.5.2. Host selection and simulation studies

The proper selection of promising host materials is difficult for solution-processable OLEDs. The appropriate host must have superior photophysical and electrical properties for achieving highly-efficient OLEDs. First, a suitable host should have greater singlet and triplet energy as compared with dopants, confining excitons into emissive layer and efficient energy transfer from host-to-guest. Second, these materials should exhibit appropriate HOMO and LUMO levels that can be matched with a dopant, which helps to improve the host-to-guest energy transfer. Moreover, well-matched HOMO LUMO energy levels of the host with charge-transporting layers provide low turn-on voltages. Third, suitable host materials should have electron and hole transportability, which enhances the injection and transport of charge carriers into the emissive layer. Last but not least, the host materials should be soluble in common organic solvents and exhibit good thermal stability, which improves the uniformity and smoothness of thin films, these thin-films help to reduce the heat generation and density of unwanted traps. On the basis of the above-mentioned properties, the commercially available host materials were collected. Their chemical structures are shown in Figure 3.21a. Their energy levels are shown in Figure 3.21b. The key properties of utilized host materials are tabulated in Table 3.9.

Table 3.9. Summarized properties of host materials.

Host	HOMO (-eV)	LUMO (-eV)	Triplet energy (eV)	Bandgap (eV)	Reference
CBP	6.0	2.9	2.49	3.1	40
mCBP	6.0	2.3	2.8	3.7	41
TCTA	5.7	2.3	2.76	3.4	42
BCzPh	5.8	2.3	2.74	3.5	43
α-NPD	5.5	2.4	2.29	3.1	44
TAPC	5.5	2.0	2.87	3.5	44
NPB	5.5	2.4	2.3	3.1	45
m-MTDATA	5.1	2.0	2.7	3.1	46
PVK	5.8	2.2	2.50	3.6	47

TH-2983_156122010

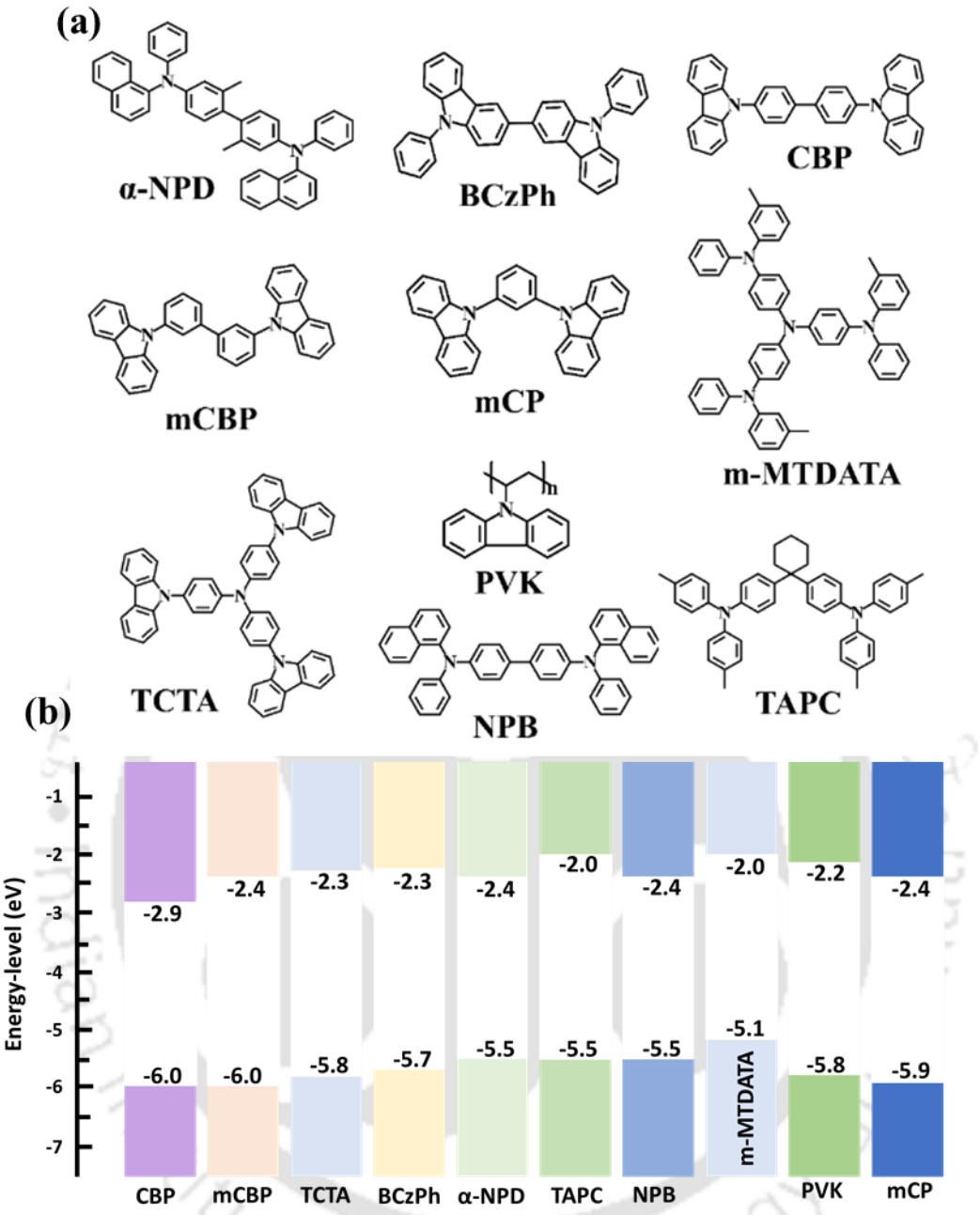

Figure 3.21. (a) Chemical structures of host materials. (b) Schematic diagram of energy levels of host materials.

Amongst, five different materials were used as a host in the simulation of yellow fluorescent OLEDs with a comprehensive electronic simulation tool SETFOS 4.6. Figure 3.22a-c demonstrates the electronic simulation outcomes, which show that the exciton generation within the emissive layer and interfaces of the emissive layer and charge transport layers greatly affect the device performance. Figure 3.21a shows the effects of hosts on the recombination rate profile in each active layer of fluorescent OLED. Two peaks were found at the interface of the emissive layer and charge-transporting layers,

TH-2983_156122010

which may be attributed to the cascade alignment of the molecular orbitals. It is observed that mCBP, TCTA, BCzPh, and α-NPD based devices exhibit a higher recombination rate in ETL and at the EML/ETL interface as compared to CBP-based devices. It was also observed that α-NPD based device possesses a reduced recombination rate in EML and increased recombination rate in the ETL layer, which may comprise the device performance.

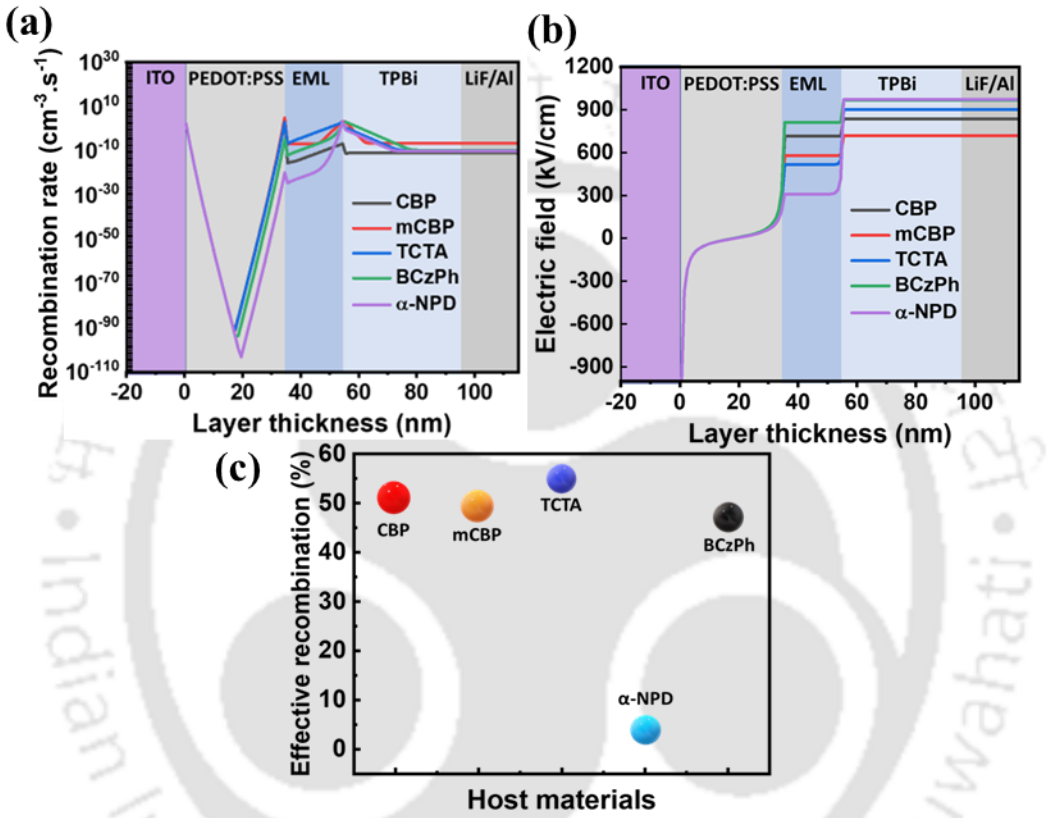

Figure 3.22. Simulation results such as the effect of host materials (a) on the recombination rate and (b) electric field profile in each active layer of OLED having device configuration of ITO/PEDOT: PSS/EML/TPBi/LiF/Al. (c) Effects of host materials on effective recombination in the emissive layer. Effective recombination rate is the ratio of the recombination rate in EML and total recombination rate.

Figure 3.22b demonstrates the effect of hosts on the electric field profile in each active layer of OLED. During device operation, an intrinsically generated electric field exhibits negative effects on the recombination rate of the emissive zone. Simulation results display that the α-NPD based device shows lower electric-field in EML and higher electric-field in ETL as compared to other hosts. This electric field profile distribution can be demonstrated by the following reasons: (i) HOMO and LUMO energy-level band offsets, (ii) charge injection into emissive layer, (iii) accumulation of charge carriers at the interfaces between the EML and charge transporting layers, and (iv) influence of contact

TH-2983_156122010

materials.[48–55] Figure 3.22c shows the effects of host materials on effective recombination in the emissive layer. As observed from the results, CBP, mCBP, TCTA, and BCzPh based devices display almost the same effective recombination rate (R_{eff}) in the EML. The R_{eff} for CBP, mCBP, TCTA, and BCzPh based devices are 51, 49, 55, and 47%, higher than that of α-NPD based devices. Hence, better device performance can be predicted with suitable hosts materials.

3.2.5.3. Doped and non-doped devices

To investigate the potential of **PQC-12b** as a fluorescent yellowish green light-emitting material, initially, Organic light-emitting diodes (LEDs) were fabricated with simplified device configurations: ITO (125 nm)/PEDOT:PSS (35 nm)/**PQC-12b** (20 nm)/TPBi (35 nm)/LiF (1 nm)/Al (100 nm) for non-doped OLEDs and ITO (125 nm)/PEDOT: PSS (35 nm)/ CBP: x wt% **PQC-12b** (20 nm)/TPBi (35 nm)/LiF (1 nm)/Al (100 nm) for doped OLEDs, where x = 1, 3, 5, 7.5, 10 and 12.5% were utilized to optimize the device performance. In order to improve the performance of OLEDs, The fabrication of OLEDs was done by doping **PQC-12b** into different hosts with simplified device configuration: ITO (125 nm)/PEDOT: PSS (35 nm)/ Hosts: 10 wt% **PQC-12b** (20 nm)/TPBi (35 nm)/LiF (1 nm)/Al (100 nm), where hosts were N,N'-bis(naphthalen-1-yl)-N,N'-bis(phenyl)-2,2'-dimethylbenzidine (α-NPD), 9,9'-Diphenyl-9H,9'H-3,3'-bicarbazole (BCzPh), tris(4-carbazoyl-9-ylphenyl)amine (TCTA), 3,3′-Di(9H-carbazol-9-yl)-1,1′-biphenyl (mCBP), and 4,4′-bis(9-carbazolyl)-1,1′-biphenyl (CBP). In this study, indium tin oxide (ITO) and aluminium (Al) were employed as anode and cathode. Poly(3,4-ethylenedioxythiophene)-poly(styrenesulfonate) (PEDOT: PSS) and lithium fluoride (LiF) acted as hole-injection layer and electron-injection layer, respectively and 2,2',2''-(1,3,5-Benzinetriyl)-tris(1-phenyl-1-H-benzimidazole) (TPBi) was incorporated as electron transport layer.

The energy-level diagram of the fabricated OLEDs consisting of **PQC-12b** as an emitter and other functional materials is shown in Figure 3.23(a). Before fabrication of OLEDs, the cleaning process of ITO coated glass substrates were carried-out with soap solution, deionized water, acetone, alcohol, and ultra-violet treatment for optimized time and temperature. Formerly, PEDOT: PSS was spin-coated to form a 35 nm hole-injection layer, and the emitter/host-guest mixed solution was spin-coated to deposit a 20 nm emissive layer. From the perspective of good efficiencies, thermally evaporated TPBi, LiF,

TH-2983_156122010

and Al to deposit 40, 1, and 100 nm layers, respectively, by a thermal evaporator under a high vacuum, *i.e.*, 10^{-6} Torr.

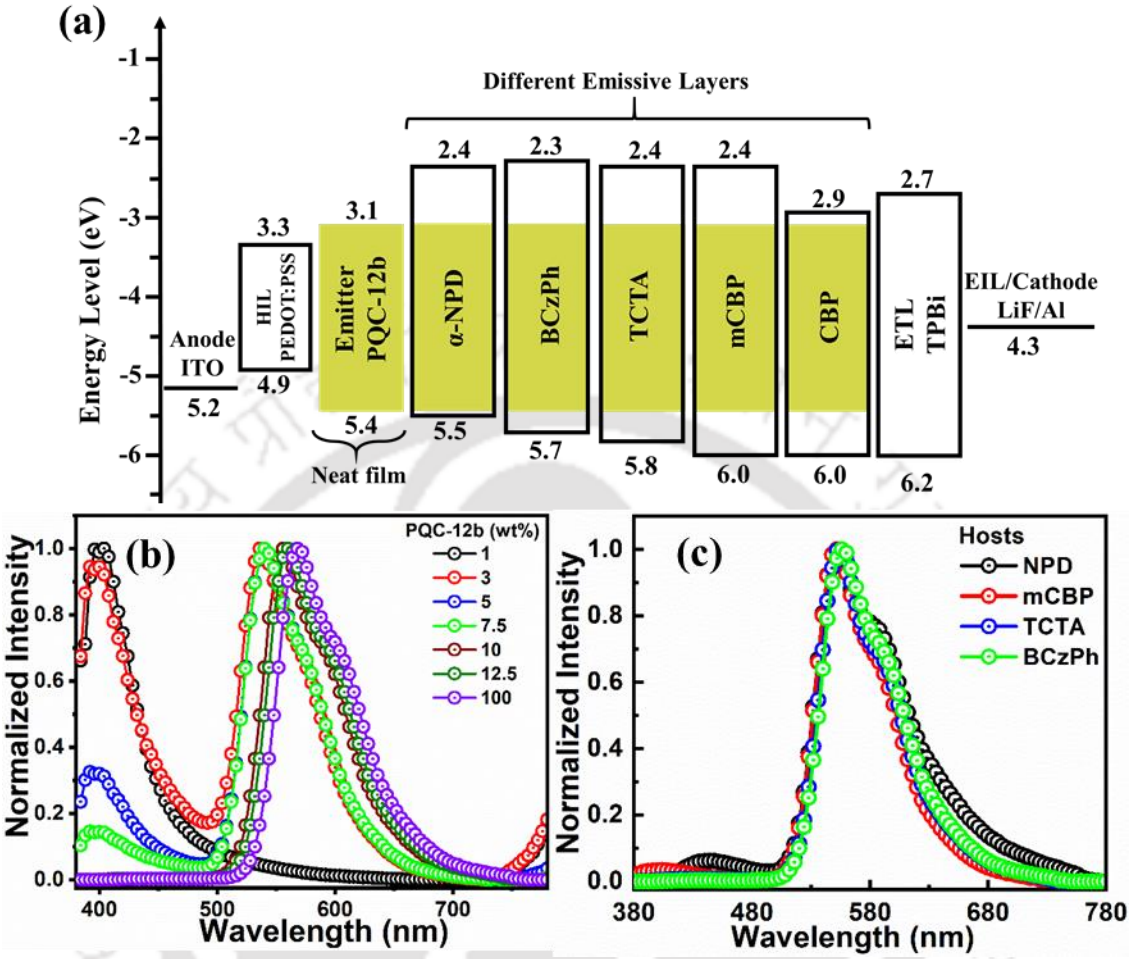

Figure 3.23. (a) Energy-level diagram of the solution-processed yellowish-green OLEDs. The five different investigated hosts were α-NPD, BCzPh, TCTA, mCBP, and CBP. Effects on the electroluminescence (EL) spectra of the devices with (b) different doping concentrations in CBP and (c) other hosts containing 10 wt% **PQC-12b** green emitter.

Initially, the non-doped OLED was fabricated and investigated. This non-doped OLED displayed poor performance with broad and red-shifted electroluminescent (EL) spectra, as shown in Figure 3.23(b). Its respective electroluminescence performance is summarized in Table 3.10. The non-doped OLED with **PQC-12b** exhibited a maximum power efficacy (PE_{max}) of 0.4 lm W^{-1}, a maximum current efficacy (CE_{max}) of 0.8 cd A^{-1}, and maximum external quantum efficiency (EQE_{max}) of 0.1%, having a maximum luminance (L_{max}) of 232 cd m^{-2} with CIE coordinates of (0.37, 0.55). This unsatisfactory performance of non-doped OLED may be attributed to leakage of charge carriers, mismatched hole and electron injections, and exciton quenching by emitters aggregation, which imbalance the charge carriers into the emissive layer.[56,57] Furthermore, the EL

TH-2983_156122010

performance of fluorescent OLEDs may be improved with a suitable host matrix for emitters and efficiency-effective architectures. [58–61] Hence, EL performance of **PQC-12b** fluorescent emitter-based OLEDs was further improved through optimization of **PQC-12b** concentration doped into bipolar CBP host matrix. 1, 3, 5, 7.5, 10, and 12.5 wt% dopants were employed and fabricated the OLEDs with the same device configurations. The effect of the doping concentration of **PQC-12b** on EL spectra is shown in Figure 3.23b. The EL spectrum was found to exhibit one extra emission peak at a short wavelength for 1-7.5 wt% dopant concentrations. With the increase of **PQC-12b** concentration, unwanted emission peak at short wavelength 400 nm started decreasing, while that at 540 nm could be observed with red-shifted emission. The EL spectra seemingly correspond to the yellowish-green emission of **PQC-12b**, with the existence of emission from the host CBP material, indicating inefficient energy transfer from the host to guest **PQC-12b** and also insufficient charge-carrier recombination in the emissive layer. As the dopant concentration increases, the host transfers energy to the guest effectively, which reduces the emission peak at a short wavelength.

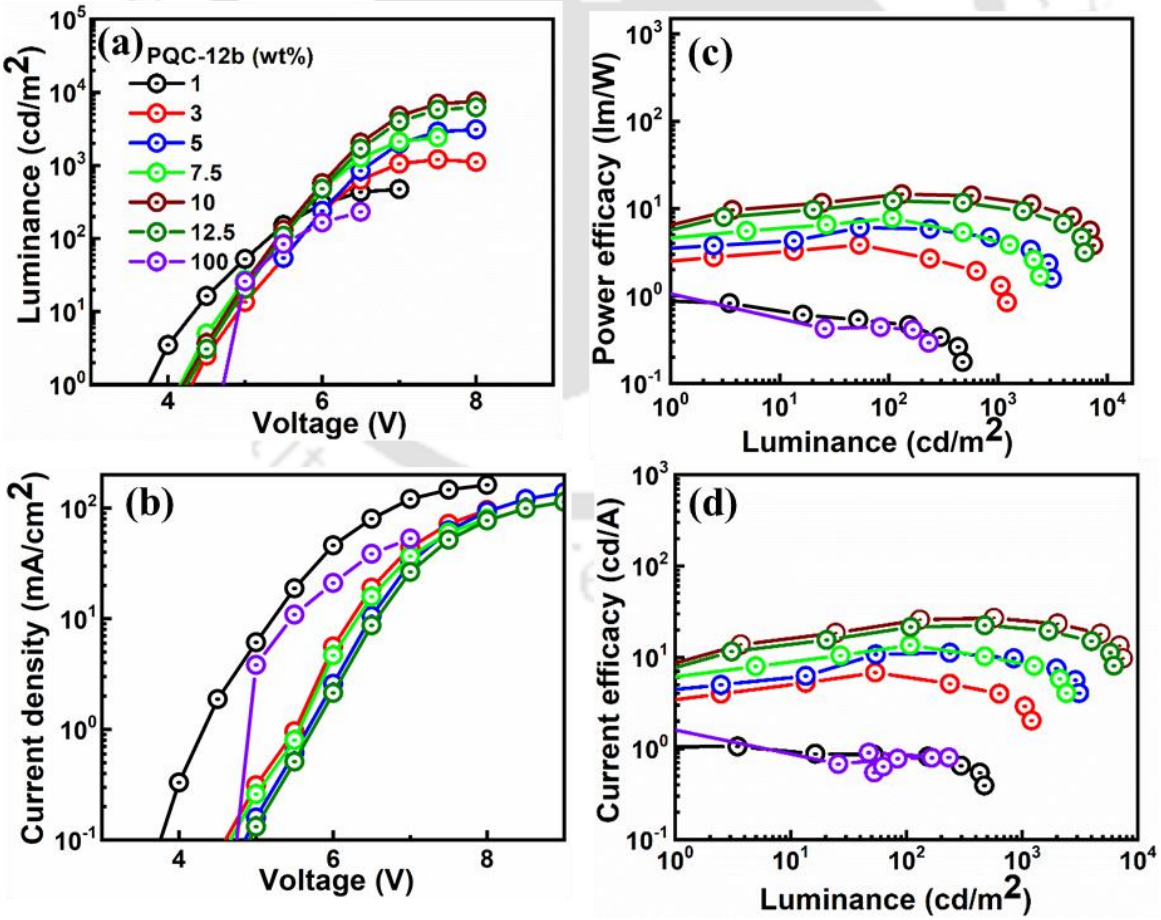

Figure 3.24. The dopant concentration effects on the (a) luminance, (b) current density, (c) power efficacy, and (d) current efficacy of the solution-processed **PQC-12b** containing OLEDs.

TH-2983_156122010

In order to find a suitable host for **PQC-12b** emitter, the four other hosts, *i.e.*, α-NPD, BCzPh, TCTA and mCBP were employed. The effect of these host materials on the EL spectra of fabricated OLEDs is shown in Figure 3.23c. Greatly, EL spectra did not exhibit emission peaks from the particular host materials, confirming an efficient energy transfer from host-to-guest and effective charge-carrier recombination in the emissive zone. The EL spectra of OLEDs were found to be almost identical to the corresponding solid-state PL of the **PQC-12b**, indicating the appropriate dispersion of the **PQC-12b** into the host materials. It also evidences that all incorporated host materials are effective hosts for **PQC-12b**.

Table 3.10. Summarized electroluminescent properties of OLEDs consisting of **PQC-12b** as an emitter with different hosts, i.e., CBP, α-NPD, TCTA, mCBP, and BCzPh and different concentrations of **PQC-12b**.

Hosts	**Dopant Conc. (wt%)**	**Turn-on Voltage (V)**	**Power efficacy (lm W^{-1})**	**Current efficacy (cd A^{-1})**	**EQE (%)**	**CIE @100, 1,000 cd m^{-2}**	**L_{max} (cd m^{-2})**
			@ 100 cd m^{-2} /1,000 cd m^{-2}/ maximum values				
CBP	1	3.1	0.5/ - / 0.5	0.8/ - / 0.8	0.1/ - / 0.1	(0.17, 0.09)/ -	474
	3	3.7	3.6/ 1.4/ 3.8	6.4/ 3.0/ 6.6	2.7/ 1.7/ 2.8	(0.30, 0.41)/ (0.28, 0.35)	1,210
	5	3.8	6.0/ 4.5/ 6.0	10.8/ 9.4/ 10.8	3.1/ 2.9/ 3.1	(0.37, 0.55)/ (0.36, 0.52)	3,110
	7.5	4.0	7.6/ 4.4/ 7.7	13.2/ 8.7/ 13.5	5.6/ 4.8/ 5.7	(0.38, 0.41)/ (0.28, 0.35)	2,420
	10	3.1	13.7/ 13.2/ 14.1	23.6/ 25.8/ 26.8	6.7/ 8.0/ 8.0	(0.37, 0.55)/ (0.36, 0.52)	7,464
	12.5	3.8	11.9/ 10.7/ 12.1	20.8/ 21.1/ 22.2	5.9/ 6.5/ 6.6	(0.39, 0.55)/ (0.36, 0.52)	6,220
	100	4.5	0.4/ - / 0.4	0.8/ - / 0.8	0.1/ - / 0.1	(0.37, 0.55)/ -	232
α-NPD	10	3.3	3.2/ 2.1/ 5.3	4.5/ 4.0/ 5.1	1.5/ 1.4/ 1.8	(0.44, 0.5)/ (0.41, 0.46)	5,794
TCTA		4.0	6.3/ 3.9/ 11.6	10.1/ 8.2/ 13.0	2.9/ 2.4/ 3.8	(0.46, 0.53)/ (0.44, 0.52)	5,116
mCBP		5.2	6.1/ 4.8/ 6.2	12.2/ 11.7/ 12.2	3.4/ 3.4/ 3.4	(0.44, 0.54)/ (0.43, 0.53)	5,118
BCzPh		3.5	9.3/ 5.4/ 18.5	12.3/ 9.7/ 17.8	3.6/ 2.9/ 5.4	(0.46, 0.53)/ (0.45, 0.52)	9,734

TH-2983_156122010

Table 3.10 shows the summarized EL properties of OLEDs consisting of **PQC-12b** as an emitter with different concentrations of **PQC-12b**. As observed from Table 3.10 and Figure 3.24a-d, the doping concentration of **PQC-12b** significantly influences the OLEDs performance. Figure 3.24a illustrates the effects of doping concentration on luminance-voltage characteristics of OLEDs. The luminance is increased as the applied voltage varies from 0 to 8 V and luminance start dropping after 8 V. The luminance was enhanced on increasing the doping concentration from 1 to 10 wt% in the CBP host matrix, wherein L_{max} of 7,464 cd m^{-2} is achieved, while luminance starts to drop with higher doping concentration (12.5 and 100 wt%). Figure 3.24b displays the effect of doping concentration on the current density-voltage characteristics of the OLEDs.

The current density shows an increment trend on increasing applied voltage from 0-9 V and then starts dropping. Meanwhile, the increasing doping concentration influences the current densities in the devices, indicating that **PQC-12b** contributes to enabling effective charge-carrier transport, charge carrier balance, the effective crystallinity of compounds, and smooth thin-film morphology hence improving the device performance. Figure 3.24c-d displays the effects of doping concentration on power efficacy and the current efficacy of the OLEDs, respectively. The power efficacies and current efficacies are initially improved as the doping concentration increases from 0 to 10 wt% and then decreases when doping concentration ranges up to 12.5 wt%. Consequently, OLED with 10 wt% **PQC-12b** doped in CBP exhibits the best performance, including a PE_{max} of 14.1 lm W^{-1}, a CE_{max} of 26.8 cd A^{-1}, an EQE_{max} of 8.0%, and L_{max} of 7,454 cd m^{-2}. As previously reported, OLEDs are having problems with high-efficiency roll-off. Remarkably, **PQC-12b** based OLED features low power efficacy roll-off and roll-up character in current efficacy and EQE. For example, the power efficacy is maintained at 13.2 lm W^{-1} at a luminance of 1,000 cd m^{-2}, indicating a 3.6% decrement of the power efficacy. EQE and current efficacy are increased from 23.6 to 25.8 cd A^{-1} and 6 to 8%, indicating an increment of 9 and 33% in CE and EQE. The suppressed efficiency roll-off and improved roll-up might be due to the exciton utilization efficiency (EUE), enhancing the reverse intersystem crossing (RISC) process.[62–64] CBP, α-NPD, TCTA, mCBP, and BCzPh exhibit EUE of 42.5, 10.7, 21.8, 19.1, and 29.7, respectively. A high EUE of 42.5, which is beyond the theoretical spin-statistics limit of 25%, is attained in the CBP-based device, which may be

TH-2983_156122010

attributed to the participation of triplet excitons in the radiative transition process through triplet-triplet annihilation or hot exciton channel.

3.2.5.4. Optimizing host

To select the suitable host, the four other host materials, *i.e.*, α-NPD, TCTA, mCBP, and BCzPh were employed. Figure 3.25 demonstrates the effect of host materials on the EL properties of solution-processed **PQC-12b** containing green OLEDs. Thus, the employed host materials also showed a strong influence on the device performance. Figure 3.25a displays the effect of hosts on luminance-voltage curves. As seen, the luminance of all hosts employed OLED is increased exponentially as the applied voltage changes up to 10 V and drops after reaching maximum luminance. The same trend is shown in the current density-voltage curves for all the devices, as shown in Figure 3.25b. Moreover, the CBP host employed OLED displayed low turn-on voltage compared to other hosts, which may be attributed to effective energy levels, facilitating balanced and efficient charge-injection in the emissive layer. Figure 3.25c exhibits the effects of hosts on the power efficacy of OLEDs. As seen, for example, α-NPD host employed OLED exhibited a PE_{max} of 5.3 lm $W^{-1,}$ and it was increased to 6.2, 11.6, and 18.5 lm W^{-1} as the host was changed to mCBP, TCTA, and BCzPh, respectively.

Moreover, for the same doping concentration, *i.e.*, 10 wt%, α-NPD host employed OLED displayed an EQE_{max} of 1.8%, and increases to 3.4, 3.8, and 5.4% as the host is changed to mCBP, TCTA, and BCzPh. Figure 3.25(d) explains the effects of hosts on the current efficacy of green OLEDs. As seen, CE_{max} is increased from 5.1 to 12.2, 13.0, and 17.8 cd A^{-1} as the host changes from α-NPD to mCBP, TCTA, and BCzPh, respectively. This improvement in efficiency by incorporating bipolar CBP host may be attributed to the following key factors: efficient energy transfer from host-to-guest, efficient exciton generation capability on host and guest, low electron trap between the emissive layer and ETL, effective electron-injection and hole-blocking property of employed ETL, and surface morphologies of the emissive layer.[65–70] Moreover, the performance of devices can be influenced by absolute photoluminescence quantum yield (PLQY).[71,72] In photoluminescence, a host can have a significant impact on emitters PLQY, resulting from the polarity effect of host materials and the energy-transfer process from host to guest. Hence, PLQY of thin-film emissive layers was measured using an integrating sphere in a nitrogen atmosphere. The **PQC-12b** exhibits a PLQY of 83±2% as neat film, and it is

TH-2983_156122010

changed to 94±2%, 91±2%, 87±2%, 89±2%, and 84±2% as the 10 wt% **PQC-12b** doped in CBP, BCzPh, TCTA, mCBP, and α-NPD, respectively.

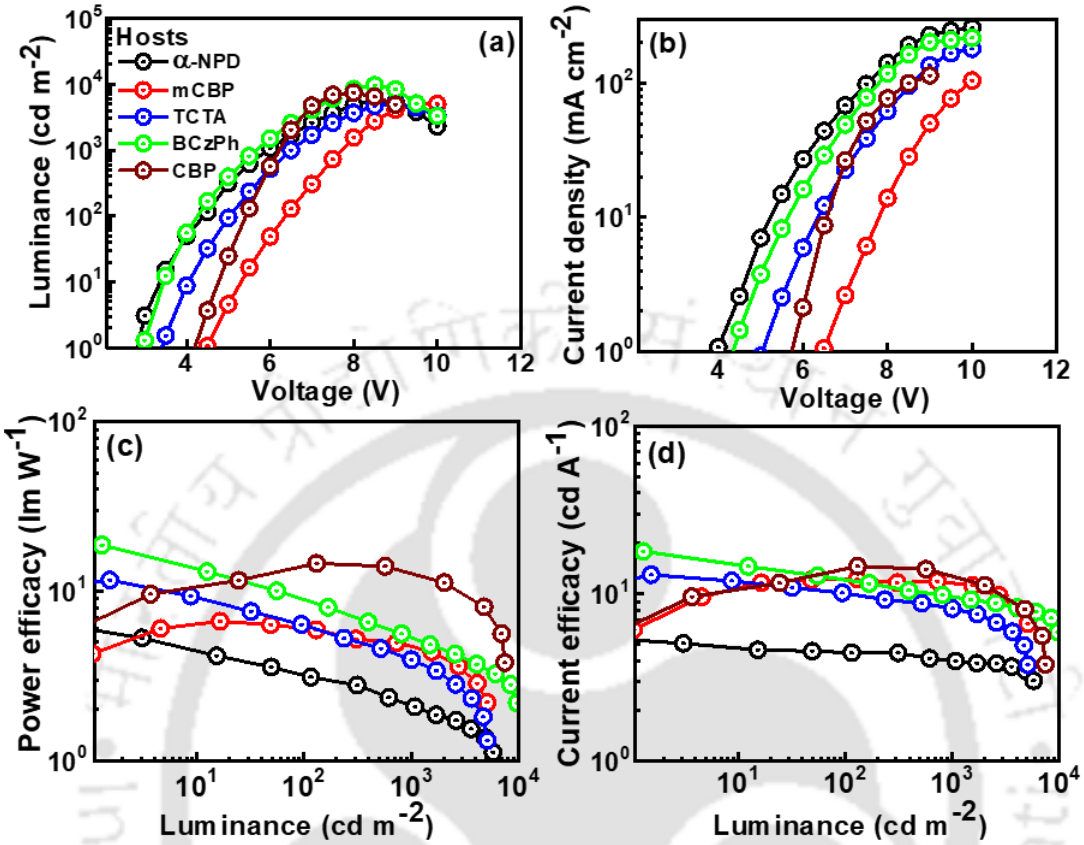

Figure 3.25. Effects of hosts on the (a) luminance, (b) current density, (c) power efficacy, and (d) current efficacy results of the solution-processed **PQC-12b** containing green organic LEDs.

3.2.5.5. Triplet exciton harvesting

In order to further improve the **PQC-12b** emitter-based device performance, a triplet harvesting approach were employed by using thermally activated delayed fluorescence (TADF) green emitter, *i.e.,* 1,2,3,5-tetrakis(carbazol-9-yl)-4,6-dicyanobenzene (4CzIPN). Energy-level diagram of studied OLED and schematic illustration of energy-transfer routes from host to guest is shown in Figure 3.26a-b respectively. The device energy-level diagram of studied OLED having device configuration of ITO (125 nm)/PEDOT:PSS (35 nm)/TAPC (10 nm)/ CBP: X wt% 4CzIPN and 10 wt% **PQC-12b** (20 nm)/TPBi (35 nm)/LiF (1 nm)/Al (100 nm), is shown in Figure 3.26a. In the emissive layer, the doping concentration of **PQC-12b** was fixed at 10% in the CBP host, and the doping concentration of the co-doped 4CzIPN device was X = 3, 6, 9, 12.5, and 15%. In the emitting layer, the singlet (25%) and triplet excitons (75%) were

TH-2983_156122010

generated on the singlet and triplet energy levels of host CBP under electrical excitation, as shown in Figure 3.26b. After that, singlet excitons were transferred from the singlet state of the host to singlet state of TADF emitter 4CzIPN by Förster resonance energy transfer (FRET) process, while triplet excitons were transferred from triplet state of host CBP to triplet state of 4CzIPN by dexter energy transfer (DET) process. After that, triplet excitons of 4CzIPN were harvested by reverse intersystem crossing (RISC) process from its triplet state to singlet state. Then, all the singlet excitons were transferred from their singlet state to the singlet state of emitter **PQC-12b** by FRET. Here, DET was ignored from 4CzIPN to emitter **PQC-12b** because the increased distance between host and guest may decrease its probability and outperformance of the efficiency of FRET for singlet excitons in comparison to DET. In order to understand the singlet (S_1) and triplet (T_1) energy levels of the compound **PQC-12b**, it was measured the emission spectra at room temperature (300K) and low temperature (77K) for solution state and thin-films (Figure 3.28).

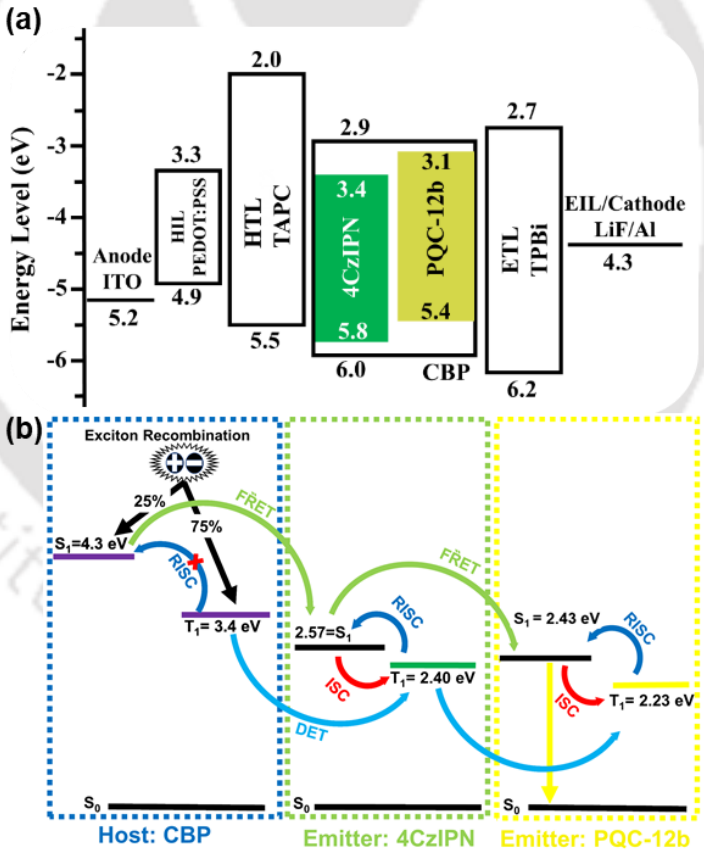

Figure 3.26. (a) Energy-level diagram of the solution-processed yellowish-green OLEDs. The green TADF emitter 4CzIPN is incorporated as a TADF sensitizer with the **PQC-12b** yellowish-green fluorescent emitter. (b) schematic illustration of energy-transfer routes from host to guest, which indicates the energy transfer through Dexter energy transfer (DET), Forster resonance energy transfer (FRET), intersystem crossing (ISC), and reverses intersystem crossing (RISC) pathways. TADF emitter was used to convert complete triplet excitons into singlet exciton and transfer them through FRET on yellowish-green emitter **PQC-12b**.

TH-2983_156122010

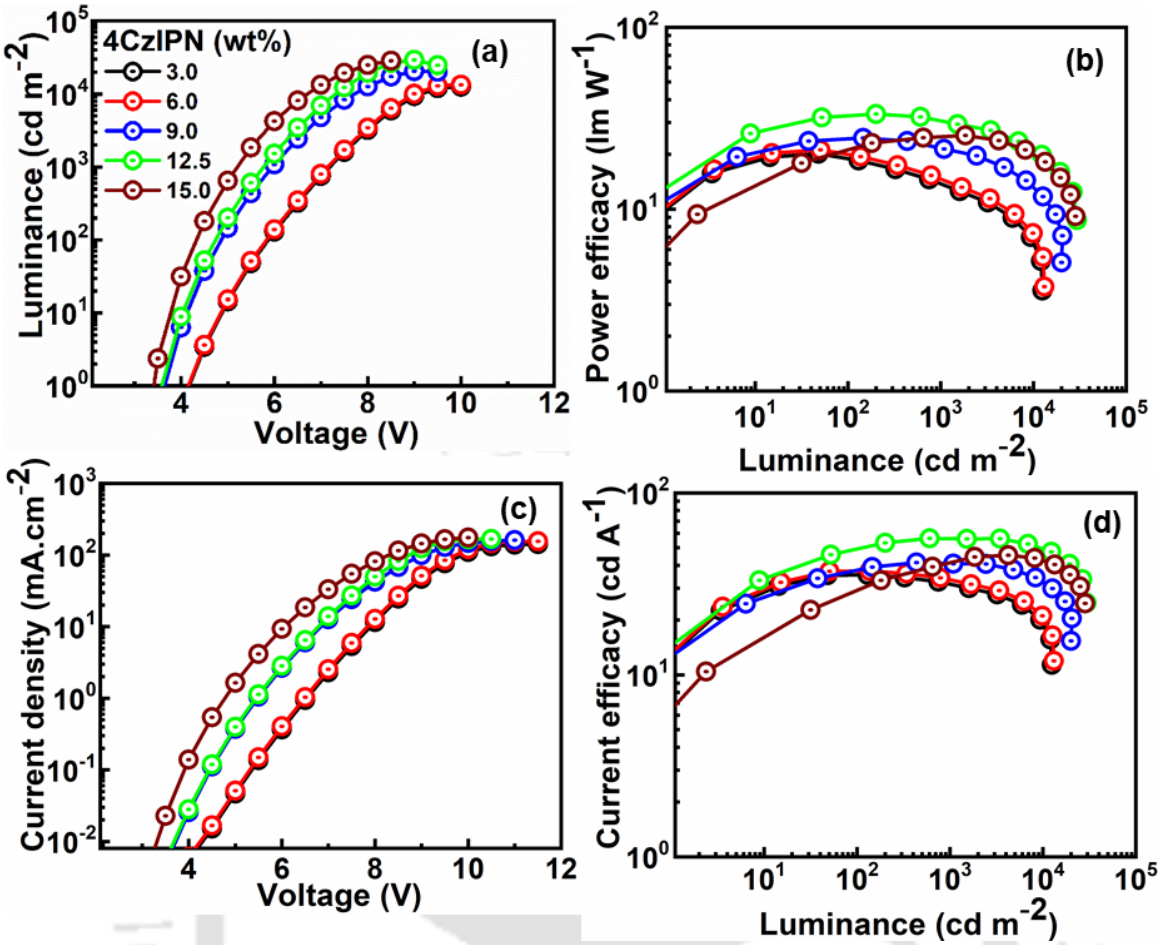

Figure 3.27. Effects of TADF emitter concentration on EL properties such as (a) luminance, (b) current density, (c) power efficacy, and (d) current efficacy results of the solution-processed **PQC-12b** containing yellowish-green OLEDs.

At room temperature, majority of the emission is observed from S_1 state. On freezing the sample at 77K in liquid nitrogen intramolecular rotations around the D-A bond gets restricted which is due to the enhanced rigidity of the molecular environment. However, this inhibits the non-radiative decay from T_1 state and thermally activated non-radiative decay channels and results in considerable phosphorescence emission from T_1. The prompt fluorescence spectra and phosphorescence spectrum in solution and thin films are shown in Figure 3.28a-b. The singlet and triplet energy levels were determined from the onset wavelengths of room temperature fluorescence and low temperature (77K) phosphorescence. In the solution state, **PQC-12b** possesses singlet and triplet energy of 2.39 and 2.24 eV. Thus, **PQC-12b** exhibited a ΔE_{ST} = 0.15 eV in solution phase, which is well within the limits of TADF materials.

In thin film state, **PQC-12b** at room temperature displays singlet and triplet energy of 2.43 and 2.23 eV. Thus the calculated value of ΔE_{ST} = 0.20 eV, which is smaller than the requirement of TADF materials (ΔE_{ST} = 0.30 eV) and ensures a facile photon conversion

TH-2983_156122010

from T_1 to S_1 by reverse intersystem crossing (RISC) process leading to TADF behavior. Further, it was also measured the prompt and delay decay time for the thin film of 10 wt% **PQC-12b** in CBP. This host-guest complex exhibited 3.67 ns prompt decay time (τ_p) and 4.66 µs delay decay time (τ_d). The lifetime of delayed fluorescence for **PQC-12b** is short enough in the microsecond scale, which specifies that an efficient exciton energy-transfer from triplet to singlet energy-level can be anticipated mostly due to smaller ΔE_{ST} (Figure 3.29).[73,74]

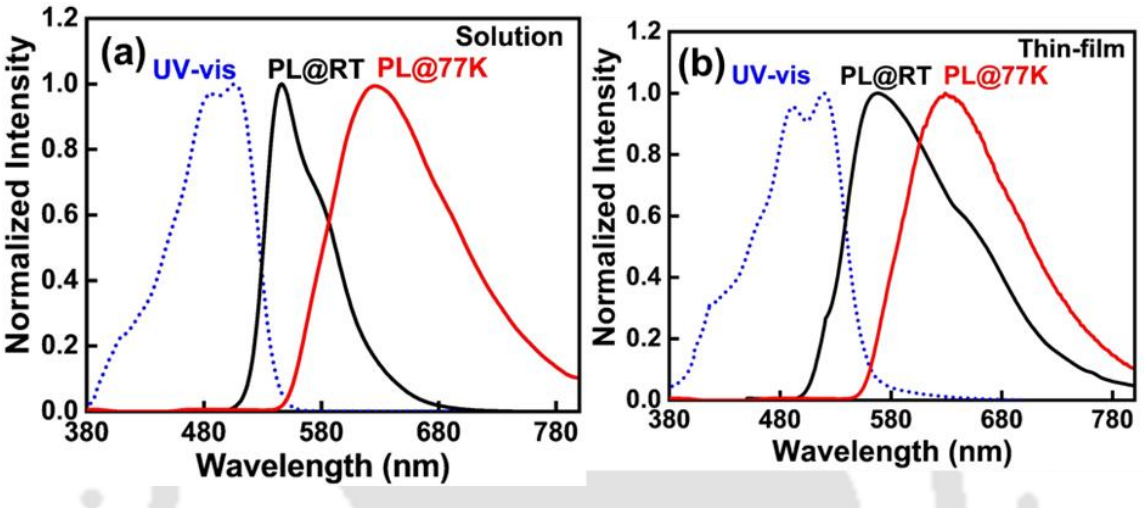

Figure 3.28. UV-vis absorbance and PL emission of compound **PQC-12b** at 300K and 77K in solution (a), the singlet and triplet energy was found 2.39 and 2.24 eV. The calculated ΔE_{ST} is 0.15 eV and in thin film (b) the singlet and triplet energy was found 2.43 and 2.23 eV. The calculated ΔE_{ST} is 0.20 eV.

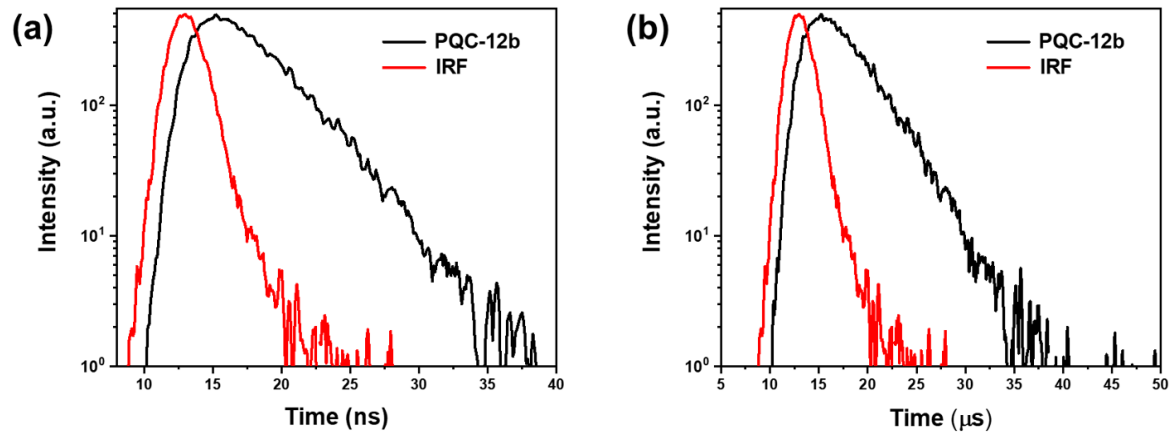

Figure 3.29. Transient PL decay curves (a) prompt (τ_p = 3.67 ns) and (b) delay (τ_d = 4.66 µs) of 10 wt% **PQC-12b** CBP doped films.

Figure 3.27a-d displays the effect of TADF emitter 4CzIPN concentration on EL properties of the solution-processed **PQC-12b** containing yellowish-green OLEDs and summarized in Table 3.11. Figure 3.27a displays the effect of 4CzIPN concentration on luminance-voltage curves. As the concentration of 4CzIPN increased from 3 to 12.5 wt%, the maximum luminance changed from 12,516 to 29,400 cd m^{-2} and decreased to 28,485

TH-2983_156122010

cd m^{-2} while concentration changed from 12.5 to 15 wt%. It was also observed that the luminance-voltages curves showed the highest luminance at the same voltage as the concentration increased from 3 to 15 wt%. Figure 3.27b shows the effects of 4CzIPN concentration on current density-voltage curves of fabricated OLED. It was observed that the current density increases as the applied voltage increases. All the devices showed diode characteristics. It was also observed that turn-on voltages of devices decrease as the concentration of 4CzIPN increases from 3 to 12.5 wt% and increases for 15 wt%. The effects of variation in concentration of 4CzIPN doping can be observed in the power efficacy-luminance curves, as shown in Figure 3.27c. The power efficacy of the devices shows an increasing trend when the concentration increases from 3 to 12.5%, with the 12.5% doping showing the best performance. However, when doping increases to 15.0%, the power efficacy of the device decreases, which can be attributed to concentration quenching.

Table 3.11. Effects of the doping concentration of TADF 4CzIPN on **el**ectroluminescent properties, *i.e.*, turn-on voltage, power efficacy, current efficacy, external quantum efficiency (EQE), CIE, and maximum luminance (L_{max}) of OLEDs.

PQC-12b Conc. (wt%)	4CzIPN Conc. (wt%)	Turn-on Voltage (V)	Power efficacy (lm W^{-1})	Current efficacy (cd A^{-1})	EQE (%)	CIE @100, 1,000 cd m^{-2}	L_{max} (cd m^{-2})
			@ 100 cd m^{-2}/ 1,000 cd m^{-2}/ 10,000 cd m^{-2}/ maximum values				
10	3	3.6	19.1/ 14.0/ 6.6/ 20.1	35.4/ 31.8/ 19.1/ 35.4	9.7/ 8.8/ 5.4/ 9.7	(0.43, 0.55)/ (0.43, 0.55)	12,516
	6	3.6	20.2/ 14.8/ 7.3/ 20.3	37.1/ 33.5/ 20.9/ 37.1	10.2/ 9.3/ 5.9/ 10.2	(0.43, 0.55)/ (0.43, 0.55)	13,142
	9	3.4	24.2/ 21.7/ 13.4/ 24.6	36.9/ 40.9/ 32.6/ 41.3	10.0/ 11.1/ 9.0/ 11.2	(0.40, 0.57)/ (0.40, 0.57)	20,505
	12.5	3.1	32.4/ 30.9/ 21.4/ 33.4	48.2/ 56.2/ 49.6/ 56.3	13.1/15.3/13.6/ 15.3	(0.39, 0.57)/ (0.39, 0.57)	29,400
	15	3.2	20.3/ 24.9/ 20.1/ 25.4	27.5/ 40.8/ 42.7/ 44.5	7.6/ 11.2/ 11.8/ 12.2	(0.37, 0.59)/ (0.37, 0.59)	28,485

The current efficacy-luminance curves followed the same trend, as shown in Figure 3.27f. The current efficacy rises with an increase in the doping concentration from initially 3% to obtain the best performance at 12.5%. The current efficacy, however, decreased by 15% due to the concentration quenching. The device performance, PE_{max}/CE_{max} of 3 wt%

TH-2983_156122010

based device increased from 20.1 lm W^{-1}/35.4 cd A^{-1} to 33.4 lm W^{-1}/56.3 cd A^{-1} for 12.5% doping. The EL spectra for the 4CzIPN cohost-based device show a narrower spectrum as compared with the EL spectra of the **PQC-12b** device, as shown in Figure 3.30. The incorporation of a TADF emitter as an assistant dopant or sensitizer helped to harvest all the triplet excitons helping in increasing the efficiency and reducing energy losses.[75-77] The device exhibited high color purity, paving the way for application in high-efficiency display/lighting systems without the need of employing color filters due to its narrow EL spectra (full width half maximum = 70 nm).

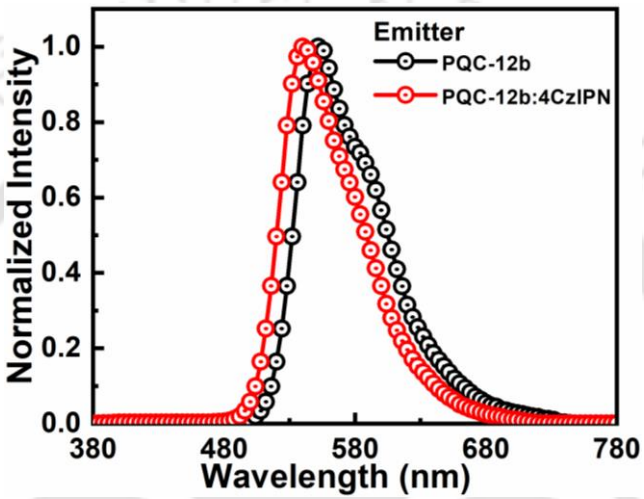

Figure 3.30. The comparison of EL spectra for **PQC-12b** alone and along with 4CzIPN co-host device.

3.2.5.6. White OLED device

To further evaluate the **PQC-12b** emitter performance, its application was explored in hybrid white OLED. It was fabricated by employing **PQC-12b** as a yellowish-green fluorescent emitter and typical phosphorescent blue emitter, *i.e.*, FIrpic. Figure 3.31a displays the device energy-level diagram of two-color hybrid OLED having device configuration of ITO (125 nm)/PEDOT: PSS (35 nm)/TAPC (10 nm)/CBP:20 wt% FIrpic and x wt% **PQC-12b** (20 nm)/TPBi (35 nm)/LiF (1 nm)/Al (100 nm), where x is 3, 5, 7.5, and 10 wt%. Their corresponding EL properties are shown in Figure 3.31a and summarized in Table 3.11. Figure 3.32a demonstrates the effect of **PQC-12b** concentration on luminance-voltages curves. In 3 wt% **PQC-12b** doped device displays the maximum luminance of 25,056 cd m^{-2} as compared to other devices at higher voltages. Figure 3.32b illustrates the effect of **PQC-12b** concentration on current density-voltage curves of hybrid white OLED. It is observed that the 5 wt% **PQC-12b** doped device exhibits higher current

TH-2983_156122010

density as compared to devices having 3, 7.5, and 10 wt% doping concentration. Figure 3.32c, d exhibits the effect of concentration on power efficacy-luminance and current efficacy-luminance curves. As seen, for example, PE_{max}/CE_{max} of 3 wt% **PQC-12b** based device changed from 36.2 lm W^{-1}/34.6 cd A^{-1} to 39.8 lm W^{-1}/38.1 cd A^{-1}, 40.5 lm W^{-1}/38.7 cd A^{-1} and 42.2 lm W^{-1}/40.3 cd A^{-1} as the concentration changes to 5, 7.5 and 10 wt% respectively. Figure 3.31b displays the effects of concentration on EL spectra of fabricated hybrid white OLED. All the EL spectra exhibit emission peaks of **PQC-12b** and FIrpic at 560 and 490 nm, respectively. As a result of strong yellowish-green emission, the device displays warm white-light emission with CIE coordinates of (0.37, 0.43). Figure 3.31c shows the EL spectra of the best performing white OLED at 100 cd m^{-2} with the device image (inset). All three best performing devices with their CIE coordinates are shown in the chromaticity diagram (Figure 3.33).

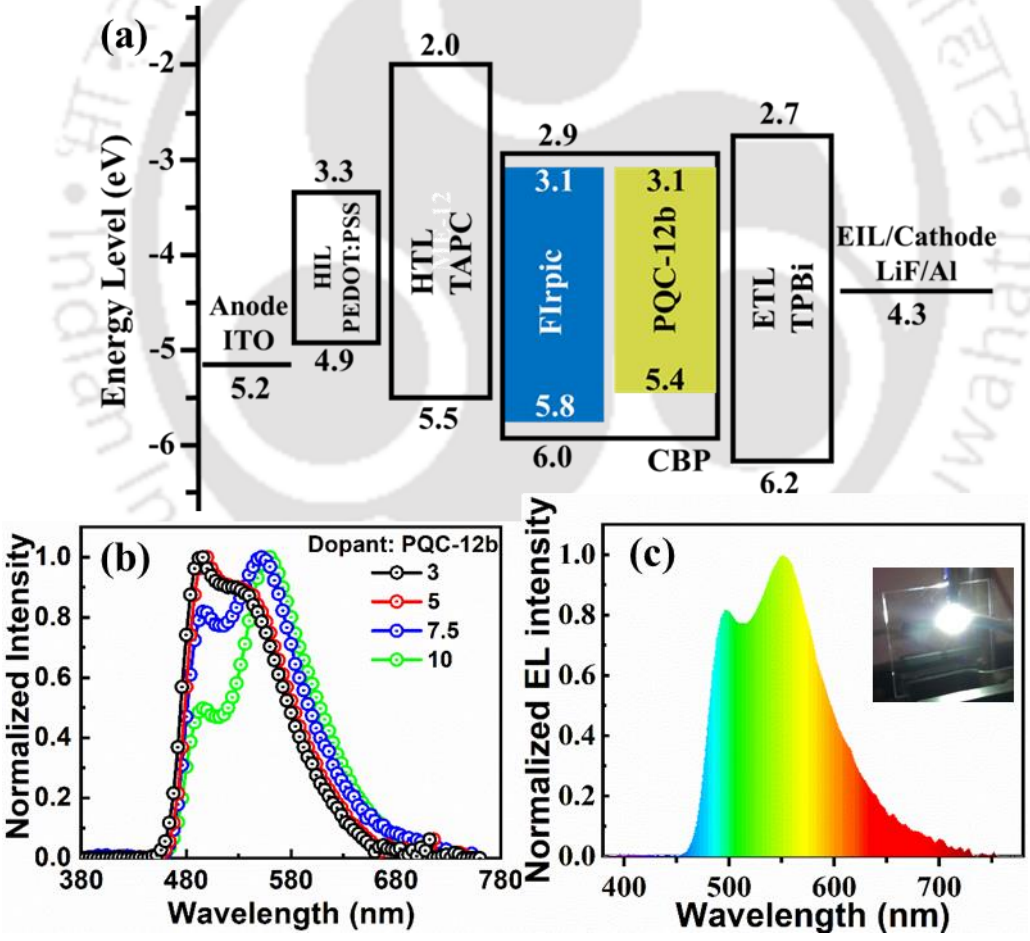

Figure 3.31. (a) Energy-level diagram of solution-processed white light by incorporating FIrpic as blue emitter and **PQC-12b** as yellowish-green emitter into CBP host. (b) EL spectra of the solution-processed hybrid white OLEDs (c) EL spectra of the best performing white OLED at a 100 cd m^{-2} with the device image (10 wt%). (inset).

TH-2983_156122010

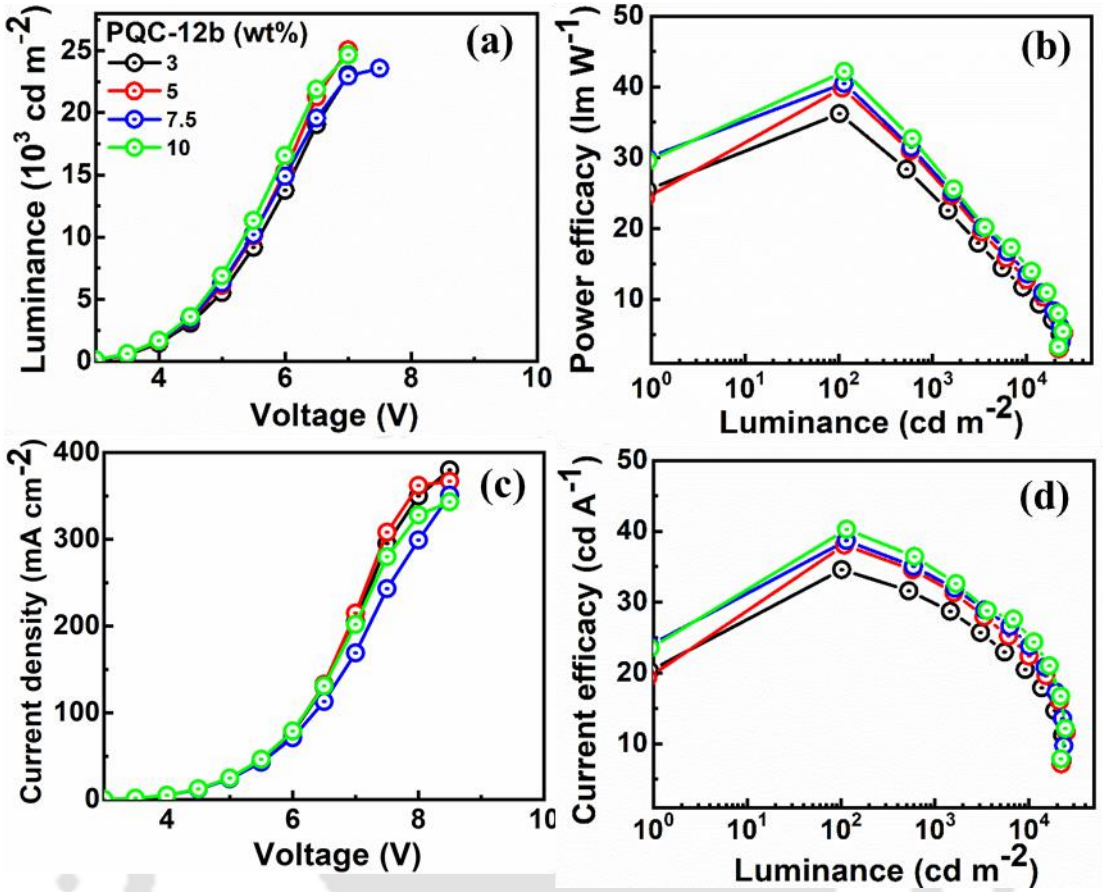

Figure 3.32. Dopant **PQC-12b** concentration effect on the (a) luminance, (b) current density, (c) power efficacy and (d) current efficacy.

Table 3.11. Dopant concentration effect on key electroluminescent properties of hybrid white OLEDs consisting of **PQC-12b** as a yellowish-green emitter and FIrpic as a blue emitter.

Hosts	Dopant Conc. (wt%)	Turn-on Voltage (V)	Power efficacy (lm W^{-1})	Current efficacy (cd A^{-1})	EQE (%)	CIE @100/1,000/10,000 cd m^{-2}	L_{max} (cd m^{-2})
			@ 100 cd m^{-2} /1,000 cd m^{-2}/ 10,000 cd m^{-2}/ maximum values				
CBP	3	3.0	36.0/ 25.4/ 11.3/ 36.2	34.4/ 30.1/ 20.0/ 34.6	11.8/ 10.3/ 6.8/ 11.9	(0.30, 0.42)/ (0.32, 0.43)/ (0.33, 0.43)	23056
	5	3.1	38.6/ 28.3/ 12.9/ 39.8	36.5/ 33.2/ 22.5/ 38.1	11.7/ 10.4/ 7.0/ 12.2	(0.35, 0.42)/ (0.36, 0.43)/ (0.37, 0.44)	25056
	7.5	3.2	39.2/ 29.0/ 13.7/ 40.5	36.8/ 33.8/ 23.9/ 38.7	11.0/ 10.6/ 7.0/ 11.5	(0.36, 0.43)/ (0.37, 0.44)/ (0.38, 0.44)	23579
	10	3.1	40.6/ 30.1/ 15.0/ 42.2	38.1/ 35.0/ 25.4/ 40.3	11.3/ 11.0/ 7.4/ 12.0	(0.37, 0.43)/ (0.38, 0.44)/ (0.38, 0.44)	24667

TH-2983_156122010

The achieved power efficacy for the fabricated solution-processed yellowish-green and warm white OLEDs in this work is either comparable or higher than that of the recently reported OLEDs in the recent literature. The best-performing yellowish-green OLED device exhibits power efficacies of 32.4 and 30.9 lm W^{-1} at 100 and 1,000 cd m^{-2}, respectively, the highest among all the reported yellowish-green fluorescent OLED devices. In addition, the best performing hybrid warm white OLED shows power efficacies of 40.6 and 30.1 lm W^{-1} at 100 and 1,000 cd m^{-2}, respectively. Our results indicate that the present study will motivate field scientists to design and synthesize the most promising materials for the fabrication of efficient monochromatic and hybrid warm white low cost and energy-saving solid-state lighting applications.

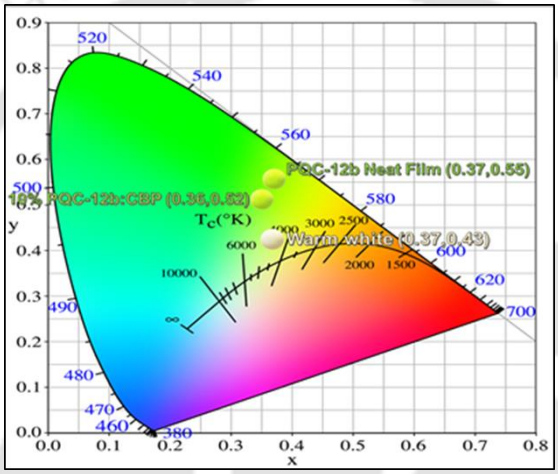

Figure 3.33. Chromaticity diagram of the best performing devices with their CIE coordinates.

3.2.5.7. Device lifetime

With the impressive performance of the **PQC-12b** emitter, the lifetime of studied OLEDs device was also measured. It was investigated the lifetime of different hosts employed with **PQC-12b** and hybrid white OLEDs. The operational device lifetimes of the 10 wt% **PQC-12b** doped in CBP, α-NPD, TCTA, mCBP, and BCzPh based devices were measured at an initial brightness of 5,000 cd m^{-2} and converted to 1,000 cd m^{-2}. Figure 3.34a illustrates the effect of hosts on device operational lifetime. The lifetimes up to 50% of initial luminance were 5.1, 4.2, 3.8, 2.4, and 1.5 h for CBP, mCBP, TCTA, BCzPh, and α-NPD, respectively, at initial brightness of 5,000 cd m^{-2}. The CBP-based device displayed 3.4 folds longer device operating lifetime than that of α-NPD, at 1,000 cd m^{-2}. This longer lifetime of the CBP-based device may be attributed to the high current efficacy of CBP-based devices relative to that of other hosts-based devices. The high current-efficacy

TH-2983_156122010

counteracts the device stress due to the low current-density at the same luminance.[78,79] Figure 3.34b displays the operational lifetime of hybrid white OLED with the best concentration of **PQC-12b**. The lifetime up to 50% of initial luminance was measured 15.5 h, at initial brightness of 10,000 cd m^{-2} and estimated 776 h at 1,000 cd m^{-2}. This indicates that the **PQC-12b** is considerably stable while applying external voltages. Thus, due to impressive efficiencies and device lifetime, **PQC-12b** can be used as an efficient material to fabricate highly efficient and stable cost-effective displays and lighting applications.

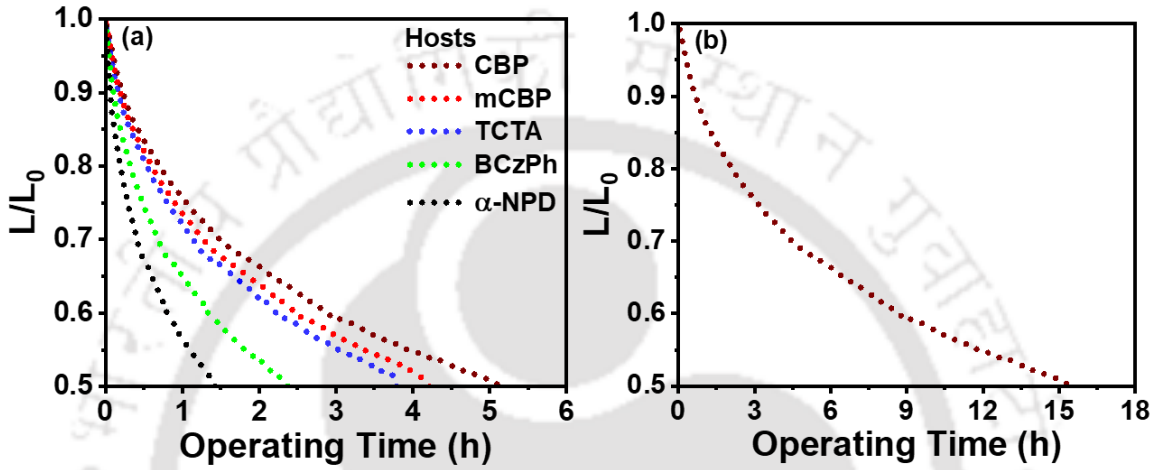

Figure 3.34. (a) Effects of the hosts on device operational lifetime employing **PQC-12b** as an emitter and different small molecules as hosts, i.e., CBP, mCBP, TCTA, BCzPh, and α-NPD. The half lifetime was measured at initial brightness of 5,000 cd m^{-2}. The CBP-based device showed a better device operating lifetime as compared to its counterparts. (b) Device operational lifetime of hybrid white organic LED with the best concentration of **PQC-12b** measured at 10,000 cd m^{-2}. Hybrid white organic LED displayed a half lifetime of 15.5 hr.

3.3. Conclusion

A new class of pyrazino[2,3-g]quinoxaline carbazole derivatives (**PQC-12n** and **PQC-12b**) were successfully synthesized and characterized and showing low band-gap, high molar extinction coefficients, bright fluorescence, and solvatochromism behavior. Such materials have good potential for application in chemical and biological sensing. The compound **PQC-12b** has shown excellent potential as a highly efficient yellow-green emitter in OLEDs. First, suitable hosts were screened with drift-diffusion simulation via software SETFOS 4.6. Then, **PQC-12b** was doped into different screened host materials, i.e., CBP, α-NPD, TCTA, mCBP, and BCzPh for fabricating solution-processable OLEDs. The CBP-based device exhibited maximum radiation exciton generation rate, maximum efficiencies, efficiency roll-up nature, and lowest turn-on voltage. To further improve the efficiencies of

TH-2983_156122010

CBP-based devices, the triplet exciton harvesting approach has been used by incorporating TADF emitter 4CzIPN into the emissive layer. The best optimized solution-processed yellowish-green OLED displayed a maximum power efficacy (PE_{max}) of 33.4 lm W^{-1}, a current efficacy (CE_{max}) of 56.3 cd A^{-1}, an external quantum efficiency (EQE_{max}) of 15.3%, and a maximum luminance (L_{max}) of 29,400 cd m^{-2}. The utility of the material was further explored by its application in the fabrication of solution-processable white OLED, which showed a PE_{max} of 42.2 lm W^{-1}, a CE_{max} of 40.3 cd A^{-1}, an EQE_{max} of 12.0%, and L_{max} of 24,667 cd m^{-2}. The material design with D-A-D architecture and device fabrication approach could show a promising potential to achieve a highly efficient, stable, solution-processable, environment-friendly display, which is also essential from the viewpoint of lighting applications.

3.4. Experimental section

In this section the detailed synthesis procedure and the molecular structural characterization data have been presented for the intermediates and target compounds mentioned in the scheme.

Synthesis of 9-alkyl-9*H*-carbazole (1n and 1b)[80]

9*H*-carbazole (5.0 g, 29.9 mmol) and KOH (5.0 g, 89.7 mmol) in DMSO (80 mL) were stirred at room temperature for 30 minutes. 1-dodecyl-bromide or 2-butyloctyl-bromide (7.8 g, 31.4 mmol) was added in the reaction mixture, the color was changed from brown to light brown and the reaction mixture was further stirred for 24 h. The reaction mixture was quenched by dilute HCl and extracted with chloroform. The organic layers were combined and dried with anhydrous sodium sulfate, filtered and concentrated. The crude product was purified by silica column chromatography using hexane as an eluent to give compounds **1n** and **1b** respectively.

1n: R_f = 0.43 (100% Hexane); White solid, 9.0 g, yield: 89.7%; FT-IR ν_{max} (in cm^{-1}): 3053, 2954, 2925, 2855, 1628, 1598, 1484, 1462, 1451, 1324; ^{1}H NMR (600 MHz, $CDCl_3$, 299 K): δ 8.18-8.17 (d, J = 7.8 Hz, 2H, H_{Ar}), 7.54-7.51 (m, 2H, H_{Ar}), 7.47-7.45 (d, J = 7.8 Hz, 2H, H_{Ar}), 7.31-7.28 (m, 2H, H_{Ar}), 4.34-4.32 (t, J = 7.2 Hz, 2H, 1× -N-CH_2-), 1.93-1.90 (m, 2H, 1× -CH_2-), 1.43-1.31 (m, 18H, 9× -CH_2-), 0.98-0.95 (t, J = 6.6 Hz, 3H, 1× -CH_3); ^{13}C NMR (150 MHz, $CDCl_3$, 298.1K): δ 140.40, 125.53, 122.79, 120.31, 118.66, 108.63, 43.03, 31.93, 29.62, 29.59, 29.52, 29.43, 29.35, 28.96, 27.32, 22.71, 14.15; MALDI-TOF exact mass calculated for $C_{24}H_{33}N$ (M^+): 335.2613, found: 335.002.

TH-2983_156122010

1b: R_f = 0.46 (100% Hexane); Colorless liquid, 8.6 g, yield: 85.7%; FT-IR ν_{max} (in cm^{-1}): 3053, 2954, 2924, 2855, 1655, 1623, 1589, 1494, 1466, 1326; ^{1}H NMR (600 MHz, $CDCl_3$, 299 K): δ 8.13-8.12 (d, *J* = 7.2 Hz, 2H, H_{Ar}), 7.49-7.46 (m, 2H, H_{Ar}), 7.42-7.40 (d, *J* = 7.8 Hz, 2H, H_{Ar}), 7.25-7.23 (m, 2H, H_{Ar}), 4.18-4.17 (d, *J* = 7.8 Hz, 2H, 1× -N-CH_2-), 2.15 (m, 1H, 1 × -CH-), 1.39-1.22 (m, 16H, 8 × -CH_2-), 0.87-0.86 (m, 6H, 2 × -CH_3); ^{13}C NMR (150 MHz, $CDCl_3$, 298.1K): δ 140.92, 125.50, 122.75, 120.23, 118.63, 108.94, 47.72, 37.97, 31.90, 31.80, 31.61, 29.63, 28.82, 26.58, 23.05, 22.61, 14.09, 14.05; MALDI-TOF exact mass calculated for $C_{24}H_{33}N$ (M^+): 335.2613, found: 335.087.

Synthesis of 1,2-bis(9-alkyl-9H-carbazol-3-yl)ethane-1,2-dione (2n & 2b)[81]

To a 250 ml two neck dried round-bottom flask (RB) under argon atmosphere containing solution of 9-alkyl-9*H*-carbazole (18.11 mmol, 1.0 equiv.) in 1,2-dichloroethane (80 mL), was added oxalyl chloride (10.87 mmol, 0.6 equiv.) by syringe at 0 °C. The reaction mixture was kept at 0 °C for 10 min, and then anhyd. $AlCl_3$ (9.05 mmol, 0.5 equiv.) was added. After 30 min at 0 °C, the reaction mixture was allowed to reach room temperature and stayed for overnight. The reaction mixture was then poured into 100 mL HCl (1M) solution. The organic layer was then extracted twice with dichloromethane (DCM) and dried with anhydrous sodium sulfate and concentrated. This crude product was purified in column chromatography with silica gel and eluted with 50% DCM-hexane to get the pure product. Removal of solvent yielded (40-45%) the product **2n** and **2b**.

2n: R_f = 0.41 (10% EtOAc-Hexane); White solid, 2.9 g, yield: 44.7%; FT-IR ν_{max} (in cm^{-1}): 3052, 2957, 2919, 2850, 1655, 1624, 1591, 1494, 1480, 1467, 1437, 1386, 1347, 1328, 1229; ^{1}H NMR (400 MHz, $CDCl_3$, 299 K): δ 8.80 (s, 2H, H_{Ar}), 8.22-8.20 (d, *J* = 8.4 Hz, 2H, H_{Ar}), 8.12-8.10 (d, *J* = 7.6 Hz, 2H, H_{Ar}), 7.53-7.43 (m, 6H, H_{Ar}), 7.30-7.26 (t, *J* = 7.2, 2H, H_{Ar}), 4.34-4.31 (t, *J* = 7.2 Hz, 4H, 2× -N-CH_2-), 1.92-1.84 (m, 4H, 2× -CH_2-), 1.38-1.27 (m, 12 H, 6× -CH_2-), 1.23 (m, 24H, 12× -CH_2-), 0.89-0.85 (t, *J* = 6.4 Hz, 6H, 2 × -CH_3); ^{13}C NMR (100 MHz, $CDCl_3$, 298.1K): δ 195.17, 144.15, 141.23, 127.29, 126.72, 124.95, 124.10, 123.15, 123.10, 120.94, 120.38, 109.38, 108.93, 43.46, 31.90, 29.58, 29.54, 29.46, 29.35, 29.31, 28.93, 27.25, 22.68, 14.10; MALDI-TOF exact mass calculated for $C_{50}H_{66}N_2O_2$ (M^+): 724.4968, found: 724.050.

2b: R_f = 0.48 (10% EtOAc-Hexane); Pale yellow liquid, 2.6 g, yield: 40.0%; FT-IR ν_{max} (in cm^{-1}): 3053, 2954, 2925, 2855, 1655, 1623, 1588, 1565, 1494, 1466, 1439, 1388, 1326, 1230; ^{1}H NMR (600 MHz, $CDCl_3$, 299 K): δ 8.84 (s, 2H, H_{Ar}), 8.25-8.24 (d, *J* = 8.4 Hz,

TH-2983_156122010

2H, H_{Ar}), 8.11-8.10 (d, J = 7.8 Hz, 2H, H_{Ar}), 7.52-7.50 (t, J = 7.8 Hz, 2H, H_{Ar}), 7.44-7.41 (dd, J_1= 4.8 Hz, J_2 = 8.4 Hz, 4H, H_{Ar}), 7.30-7.28 (t, J = 7.8 Hz, 4H, H_{Ar}), 4.14-4.13 (m, 4H, 2× -CH_2-), 2.12-2.10 (m, 2H, 2× -CH-), 1.38-1.33 (m, 8H, 4× -CH_2-), 1.32-1.23 (m, 18H, 9× -CH_2-), 1.21 (m, 8H, 4× -CH_2-), 0.87-0.85 (t, J = 6.6 Hz, 12H, 4× -CH_3); ^{13}C NMR (150 MHz, $CDCl_3$, 298.1K): δ 195.25, 144.66, 141.71, 127.82, 126.78, 124.94, 124.11, 123.14, 123.10, 120.90, 120.45, 109.80, 109.32, 48.04, 38.04, 31.95, 31.87, 31.67, 29.67, 28.88, 26.65, 23.11, 22.71, 14.20, 14.15; MALDI-TOF exact mass calculated for $C_{50}H_{65}N_2O_2$ (M^+): 724.4968, ($M+Na^+$): 747.4860, found: 747.680.

Synthesis of 2,3,7,8-tetrakis(9-alkyl-9H-carbazol-3-yl)pyrazino[2,3-g]quinoxaline (PQC-12n & PQC-12b)[25,82]

Compounds **2n** or **2b** (2.1 equiv.) and benzene-1,2,3,4-tetraamine tetrahydrochloride (1.0 equiv.) were transferred into a 50 mL two neck RB flask with 4 mL methanol and 12 mL acetic acid (1:3) under argon atmosphere, which was heated to 100 ^{o}C. After addition of 1.0 mL of triethylamine further refluxed at 130 ^{o}C for 12 h. and concentrated the reaction mixture. The crude product was purified by column chromatography on neutral alumina with 5-10% ethyl acetate-hexane, to yield (75-80%) solid orange product.

PQC-12n: R_f = 0.36 (10% EtOAc-Hexane); Orange solid, yield: 79.7%; FT-IR ν_{max} (in cm^{-1}): 3054, 2920, 2850, 1738, 1625, 1596, 1489, 1466, 1349, 1285, 1234, 1146; ^{1}H NMR (600 MHz, $CDCl_3$, 299 K): δ 9.07 (s, 2H, H_{Ar}), 8.61 (s, 4H, H_{Ar}), 8.06-8.05 (d, J = 7.2 Hz, 4H, H_{Ar}), 7.68-7.66 (dd, J_1 = 1.2 Hz, J_2 = 8.4 Hz, 4H, H_{Ar}), 7.49-7.46 (t, J = 7.2 Hz, 4H, H_{Ar}), 7.42-7.41 (d, J = 8.4 Hz, 4H, H_{Ar}), 7.27-7.26 (d, J = 7.8 Hz, 4H, H_{Ar}), 7.23-7.21 (t, J = 7.8 Hz, 4H, H_{Ar}), 4.28-4.26 (t, J = 7.2 Hz, 8H, 4× -CH_2-), 1.85-1.80 (m, 8H, 4× -CH_2-), 1.34-1.20 (m, 72H, 36× -CH_2-), 0.88-0.85 (t, J = 6.6 Hz 12H, 4× -CH_3); ^{13}C NMR (150 MHz, $CDCl_3$, 298.1K): δ 156.20, 141.25, 141.07, 140.73, 130.35, 128.26, 128.02, 126.06, 123.37, 123.24, 122.76, 120.99, 119.43, 109.09, 108.48, 43.42, 32.13, 29.82, 29.81, 29.79, 29.70, 29.59, 29.56, 29.13, 27.46, 22.91, 14.35; MALDI-TOF exact mass calculated for $C_{106}H_{131}N_8$ ($M+H^+$): 1516.0491, found: 1516.440.

PQC-12b: R_f = 0.53 (10% EtOAc-Hexane); Orange solid: yield: 75.0%; FT-IR ν_{max} (in cm^{-1}): 3052, 2955, 2924, 2854, 1853, 1737, 1626, 1596, 1548, 1491, 1466, 1408, 1378, 1339, 1282, 1249, 1202, 1146, 1124; ^{1}H NMR (600 MHz, $CDCl_3$, 299 K): δ 9.11 (s, 2H, H_{Ar}), 8.69 (s, 4H, H_{Ar}), 8.11-8.10 (d, J = 7.2 Hz, 4H, H_{Ar}), 7.66-7.64 (dd, J_1= 1.2 Hz, J_2= 8.4 Hz, 4H, H_{Ar}), 7.50-7.47 (t, J = 7.8 Hz, 4H, H_{Ar}), 7.42-7.40 (d, J = 8.4 Hz, 4H, , H_{Ar}), 7.25-

TH-2983_156122010

7.24 (m, 8H, H_{Ar}), 4.15-4.14 (d, *J* = 7.2 Hz, 8H, 4× -CH_2-), 2.12-2.10 (m, 4H, 4× -CH-), 1.34-1.19 (m, 64H, 32× -CH_2-), 0.87-0.82 (m, 24H, 8× -CH_3); ^{13}C NMR (150 MHz, $CDCl_3$, 298.1K): δ 155.98, 141.48, 141.27, 140.48, 130.06, 128.00, 127.75, 125.81, 123.07, 123.02, 122.41, 120.70, 119.19, 109.13, 108.43, 47.74, 37.88, 31.75, 31.46, 29.69, 29.58, 28.71, 26.48, 22.97, 22.56, 14.07, 14.02; MALDI-TOF exact mass calculated for $C_{106}H_{131}N_8$ ($M+H^+$): 1516.0491, found: 1516.605.

3.5. References

1. P. Rajamalli, N. Senthilkumar, P. Gandeepan, P. Y. Huang, M. J. Huang, C. Z. Ren-Wu, C. Y. Yang, M. J. Chiu, L. K. Chu, H. W. Lin, C. H. Cheng, *J. Am. Chem. Soc.*, 2016, **138**, 628.
2. J. Li, D. Liu, Y. Li, C. S. Lee, H. L. Kwong, S. Lee, *Chem. Mater.*, 2005, **17**, 1208.
3. Y. Im, S. H. Han, J. Y. Lee, *J. Ind. Eng. Chem.*, 2018, **66**, 381.
4. J. Li, A. C. Grimsdale, *Chem. Soc. Rev.*, 2010, **39**, 2399.
5. G. Sathiyan, E. K. T. Sivakumar, R. Ganesamoorthy, R. Thangamuthu, P. Sakthivel, *Tetrahedron Lett.*, 2016, **57**, 243.
6. Y. Wu, Y. Li, S. Gardner, B. S. Ong, *J. Am. Chem. Soc.* 2005, **127**, 614.
7. M. Reig, J. Puigdollers, D. Velasco, *J. Mater. Chem. C*, 2015, **3**, 506.
8. P. Monk, R. Mortimer, D. Rosseinsky, *Cambridge University Press: Cambridge* 2007, 1.
9. B. Lim, S. Y. Han, S. H. Jung, Y. J. Jung, J. M. Park, W. Lee, H. S. Shim, Y. C. Nah, *J. Ind. Eng. Chem.*, 2019, **80**, 93.
10. H. Uoyama, K. Goushi, K. Shizu, H. Nomura, C. Adachi, *Nature*, 2012, **492**, 234.
11. C. Adachi, *Jpn. J. Appl. Phys.*, 2014, **53**, 060101.
12. H. Jiang, J. Sun, J. Zhang, *Curr. Org. Chem.*, 2012, **16**, 2014.
13. P. Ledwon, *Org. Electron.*, 2019, **75**, 105422.
14. J. V. Grazulevicius, P. Strohriegl, J. Pielichowski, K. Pielichowski, *Prog. Polym. Sci.*, 2003, **28**, 1297.
15. B. Wex, B. R. Kaafarani, *J. Mater. Chem. C*, 2017, **5**, 8622.
16. X. Yang, X. Xu, G. Zhou, *J. Mater. Chem. C*, 2015, **3**, 913.
17. R. K. Gupta, D. Das, M. Gupta, S. K. Pal, P. K. Iyer, A. S. Achalkumar, *J. Mater. Chem. C*, 2017, **5**, 1767.
18. A. K. Yadav, B. Pradhan, H. Ulla, S. Nath, J. De, S. K. Pal, M. N. Satyanarayan, A. S. Achalkumar, *J. Mater. Chem. C*, 2017, **5**, 9345.
19. R. K. Gupta, H. Ulla, M. N. Satyanarayan, A. A. Sudhakar, *European J. Org. Chem.*, 2018, **13**, 1608.
20. R. K. Gupta, D. Das, P. K. Iyer, A. S. Achalkumar, *ChemistrySelect*, 2018, **3**, 5123.
21. A. Arai, H. Sasabe, K. Nakao, Y. Masuda, J. Kido, *Chem. Eur. J.*, 2021, **27**, 4971.
22. N. Blouin, M. Leclerc, *Acc. Chem. Res.*, 2008, **41**, 1110.
23. X. Liu, T. Liu, C. Duan, J. Wang, S. Pang, W. Xiong, Y. Sun, F. Huang, Y. Cao, *J. Mater. Chem. A*, 2017, **5**, 1713.
24. G. L. Schulz, M. Mastalerz, C. Q. Ma, M. Wienk, R. Janssen, P. Bäuerle,

TH-2983_156122010

Macromolecules, 2013, **46**, 2141.
25. T. Huang, D. Liu, J. Jiang, W. Jiang, *Chem. Eur. J.*, 2019, **25**, 10926.
26. M. Velusamy, J.-H. Huang, Y.-C. Hsu, H.-H. Chou, K.-C. Ho, P.-L. Wu, W.-H. Chang, J. T. Lin, C.-W. Chu, *Org. Lett.*, 2009, **11**, 4898.
27. M. Basak, G. Das, *Analyst*, 2021, **146**, 6239.
28. S. Gupta, M. D. Milton, *Dyes Pigm.* 2019, **165**, 474.
29. E. K. Unver, S. Tarkuc, D. Baran, C. Tanyeli, L. Toppare, *Tetrahedron Lett.*, 2011, **52**, 2725.
30. X. Wang, Y. Zhou, T. Lei, N. Hu, E.-Q. Chen, J. Pei, *Chem. Mater.*, 2010, **22**, 3735.
31. T. L. Tam, F. Zhou, H. Li, J. C. Y. Pang, Y. M. Lam, S. G. Mhaisalkar, H. Su, A. C. Grimsdale, *J. Mater. Chem.*, 2011, **21**, 17798.
32. L. P. Zhang, X. Li, T. Liu, L. Kang, X. Huang, Y. Zhao, *Chem. Commun.*, 2020, **56**, 5544.
33. I. Hisaki, N. Q. E. Affendy, N. Tohnai, *CrystEngComm.*, 2017, **19**, 4892.
34. F. Moreau, D. I. Kolokolov, A. G. Stepanov, T. L. Easun, A. Dailly, W. Lewis, A. J. Blake, H. Nowell, M. J. Lennox, E. Besley, S. Yang, M. Schröder, *Proc. Natl. Acad. Sci. U. S. A.*, 2017, **114**, 3056.
35. M. Mastalerz, V. Fischer, C. Q. Ma, R. A. J. Janssen, P. Bauerle, *Org. Lett.*, 2009, **11**, 4500.
36. P. Rybak, A. Krowczynski, J. Szydlowska, D. Pociecha, E. Gorecka, *Soft Matter*, 2022, **18**, 2006.
37. B. Sk, S. Khodia, A. Patra, *Chem. Commun.*, 2018, **54**, 1786.
38. R. Ishimatsu, S. Matsunami, K. Shizu, C. Adachi, K. Nakano, T. Imato, *J. Phys. Chem. A,* 2013, **117**, 5607.
39. S. Haseyama, A. Niwa, T. Kobayashi, *Nanoscale Res Lett,* 2017, **12**, 268.
40. V. Jankus, C. Winscom, A. P. Monkman, *J. Chem. Phys.*, 2009, **130**, 074501.
41. S. C. Dong, L. Zhang, J. Liang, L. S. Cui, Q. Li, Z. Q. Jiang, L. S. Liao, *J. Phys. Chem. C*, 2014, **118**, 2375.
42. R. Srivastava, L. R. Joshi, *Phys. Chem. Chem. Phys.*, 2014, **16**, 17284.
43. L. S. Cui, Y. Liu, X. D. Yuan, Q. Li, Z. Q. Jiang, L. S. Liao, *J. Mater. Chem. C*, 2013, **1**, 8177.
44. J. Lee, N. Chopra, S. H. Eom, Y. Zheng, J. Xue, F. So, J. Shi, *Appl. Phys. Lett.*, 2008, **93**, 123306.
45. F. Zhao, Y. Wei, H. Xu, D. Chen, T. Ahamad, S. Alshehri, Q. Pei, D. Ma, *Mater. Horizons*, 2017, **4**, 641.
46. P. Yuan, X. Qiao, D. Yan, D. Ma, *J. Mater. Chem. C*, 2018, **6**, 5721.
47. F.-C. Chen, S.-C. Chang, G. He, S. Pyo, Y. Yang, M. Kurotaki, J. Kido, *J. Polym. Sci., Part B: Polym. Phys*., 2003, **41**, 2681.
48. B. Ruhstaller, T. Flatz, D. Rezzonico, M. Moos, N. Reinke, E. Huber, R. Haeusermann, B. Perucco, *Proc., SPIE* 2008, **7051**, 70510J.
49. S. Shi, D. Ma, *Phys. Status Solidi A*, 2009, **206**, 2641.
50. S. J. Martin, G. L. B. Verschoor, M. A. Webster, A. B. Walker, *Org. Electron.*, 2002, **3**, 129.
51. T. Kim, K. H. Lee, J. Y. Lee, *J. Mater. Chem. C*, 2018, **6**, 8472.

TH-2983_156122010

52. A. Ainsebaa, J. L. Fave, M. Schott, *J. Appl. Phys.*, 2011, **110**, 104505.
53. M. Fröbel, S. Hofmann, K. Leo, M. C. Gather, *Appl. Phys. Lett.*, 2014, **104**, 071105.
54. E. Tutiš, D. Berner, L. Zuppiroli, *J. Appl. Phys.*, 2003, **93**, 4594.
55. J. Chan, A. D. Rakić, Y. T. Yeow, A. B. Djurišić, *Conf. Optoelectron. Microelectron. Mater. Devices, Proceedings*, 2004, 53.
56. A. Sharma, K. R. J. Thomas, M. R. Nagar, J. H. Jou, *Mater. Adv.*, 2021, **2**, 6326.
57. J. D. Girase, J. Tagare, Shahnawaz, M. R. Nagar, I. Siddiqui, J. H. Jou, S. Patel, S. Vaidyanathan, *Dyes Pigm.* 2021, **196**, 109791.
58. D. Thakur, M. R. Nagar, A. Tomar, D. K. Dubey, S. Kumar, S. S. Swayamprabha, S. Banik, J. H. Jou, S. Ghosh, *ACS Appl. Electron. Mater.*, 2021, **3**, 2317.
59. Anupriya, K. R. J. Thomas, M. R. Nagar, Shahnawaz, J.-H. Jou, *J. Photochem. Photobiol. A Chem.*, 2022, **423**, 113600.
60. Anupriya, K. R. J. Thomas, M. R. Nagar, Shahnawaz, J. H. Jou, *J. Mater. Sci. Mater. Electron.*, 2021, **32**, 26838.
61. J. H. Jou, S. Kumar, P. H. Fang, A. Venkateswararao, K. R. J. Thomas, J. J. Shyue, Y. C. Wang, T. H. Li, H. H. Yu, *J. Mater. Chem. C*, 2015, **3**, 2182.
62. J. D. Girase, S. R. Nayak, J. Tagare, Shahnawaz, M. R. Nagar, J. H. Jou, S. Vaidyanathan, *J. Inf. Disp.*, 2021.
63. C. Kaiyasuan, P. Chasing, P. Nalaoh, P. Wongkaew, T. Sudyoadsuk, K. Kongpatpanich, V. Promarak, *Chem. Asian J.*, 2021, **16**, 2328.
64. L. Wang, Z. Zhao, G. Zhan, H. Fang, H. Yang, T. Huang, Y. Zhang, N. Jiang, L. Duan, Z. Liu, Z. Bian, Z. Lu, C. Huang, *Light Sci. Appl.*, 2020, **9**, 157.
65. D. Y. Zhou, H. Z. Siboni, Q. Wang, L. S. Liao, H. Aziz, *J. Phys. Chem. C*, 2014, **118**, 24006.
66. J. Yang, X. Wu, J. Shi, B. Tong, Y. Lei, Z. Cai, Y. Dong, *Adv. Funct. Mater.*, 2021, **31**, 2108072.
67. B. Liu, D. Luo, J. Zou, D. Gao, H. Ning, L. Wang, J. Peng, Y. Cao, *J. Mater. Chem. C*, 2015, **3**, 6359.
68. B. S. B. Karunathilaka, U. Balijapalli, C. A. M. Senevirathne, S. Yoshida, Y. Esaki, K. Goushi, T. Matsushima, A. S. D. Sandanayaka, C. Adachi, *Nat. Commun.*, 2020, **11**, 4926.
69. T. Y. Cheng, J. H. Lee, C. H. Chen, P. H. Chen, P. S. Wang, C. E. Lin, B. Y. Lin, Y. H. Lan, Y. H. Hsieh, J. J. Huang, H. F. Lu, I. Chao, M. K. Leung, T. L. Chiu, C. F. Lin, *Sci. Rep.*, 2019, **9**, 3654.
70. E. Y. Park, D. H. Lee, T. N. Le, C. M. Shin, J. Lee, M. C. Suh, *RSC Adv.*, 2021, **11**, 29115.
71. Y. L. Zhang, Q. Ran, Q. Wang, Y. Liu, C. Hänisch, S. Reineke, J. Fan, L. S. Liao, *Adv. Mater.*, 2019, **31**, 1902368.
72. Z. Cai, X. Wu, H. Liu, J. Guo, D. Yang, D. Ma, Z. Zhao, B. Z. Tang, *Angew. Chemie - Int. Ed.*, 2021, **60**, 23635.
73. W. Li, M. Li, W. Li, Z. Xu, L. Gan, K. Liu, N. Zheng, C. Ning, D. Chen, Y.-C. Wu, S.-J. Su, *ACS Appl. Mater. Interfaces,* 2021, **13**, 5302.
74. L. Wang, X. Cai, B. Li, M. Li, Z. Wang, L. Gan, Z. Qiao, W. Xie, Q. Liang, N. Zheng, K. Liu, S.-J. Su, *ACS Appl. Mater. Interfaces,* 2019, **11**, 45999.

TH-2983_156122010

75. C.-Y. Chan, M. Tanaka, Y.-T. Lee, Y.-W. Wong, H. Nakanotani, T. Hatakeyama, C. Adachi, *Nat. Photonics*, 2021, **15,** 203.
76. A. Shahalizad, A. Malinge, L. Hu, G. Laflamme, L. Haeberlé, D. M. Myers, J. Mao, W. G. Skene, S. K. Cohen, *Adv. Funct. Mater.*, 2021, **31**, 2007119.
77. J. M. Ha, S. H. Hur, A. Pathak, J.-E. Jeong, H. Y. Woo, *NPG Asia Mater.* **2021**, *13***,** 53.
78. S. O. Jeon, K. H. Lee, J. S. Kim, S. G. Ihn, Y. S. Chung, J. W. Kim, H. Lee, S. Kim, H. Choi, J. Y. Lee, *Nat. Photonics*, 2021, **15**, 208.
79. V. V. Patil, K. H. Lee, J. Y. Lee, *J. Mater. Chem. C*, 2020, **8**, 3051.
80. C. J. Liu, C. C. Wang, D. L. Kuo, C. Y. Yu, *Polymer*, 2019, **181**, 121770.
81. D. Kiymaz, M. Sezgin, E. Sefer, C. Zafer, S. Koyuncu, *Int. J. Hydrogen Energy*, 2017, **42**, 8569.
82. W. Liu, X. Luo, Y. Bao, Y. P. Liu, G. H. Ning, I. Abdelwahab, L. Li, C. T. Nai, Z. G. Hu, D. Zhao, B. Liu, S. Y. Quek, K. P. Loh, *Nature Chemistry*, 2017, **9**, 563-570.

TH-2983_156122010

Chapter 4

Liquid Crystalline Naphthalene and Perylene Bisimide with $D_2\pi_2A$ Architecture and their Application in Organic Field Effect Transistors

TH-2983_156122010

4.1. Introduction

Rylenediimides are an emerging class of electron-deficient organic semiconductors with high thermal and photochemical stabilities.[1] These have been extensively used in the fabrication of organic electronic devices (i.e. field-effect transistors,)[2–6], perovskite solar cells,[4,7,8] exhibiting thermochromic,[9] photochromic,[10] electrochemical, electrochromic properties[11], nonlinear optical properties,[12] chemosensors,[13,14] as pigments, for bioimaging[15] and also in anticancer drugs.[16] This is due to their excellent redox activity, charge transport[17–19], photophysical and self-assembly[20] behaviors. These molecular platforms find application as the active component in several functional materials. Among the rylenediimides, naphthalene tetracarboxylic diimides (NDIs) and perylene tetracarboxylic diimides (PDIs) are a much-studied class of organic materials due to their large electron-deficient aromatic structure and their ability to form self-assembled structures by the structural modulation. They are also capable of reversible electrochemical reduction properties to form radical anion and radical dianions. NDIs and PBIs are also known for their intense visible light absorption, high stability, electron accepting ability, and high fluorescence quantum yields. Due to these properties, they are actively investigated by various research groups aiming at organic electronic devices, thermography, energy-transfer systems, and near-infrared-absorbing molecular systems.[21] Furthermore, the electronic properties can be modified by the substitution of electron-withdrawing or/and electron donating groups mainly at the core positions and to a smaller extent at the axial positions of the NDI/PBI scaffolds (Figure 4.1). The substitutions at the axial imide positions are mainly utilized to affect the solubility, aggregation and self-assembly properties while they have little effect on the electronic and optical properties.

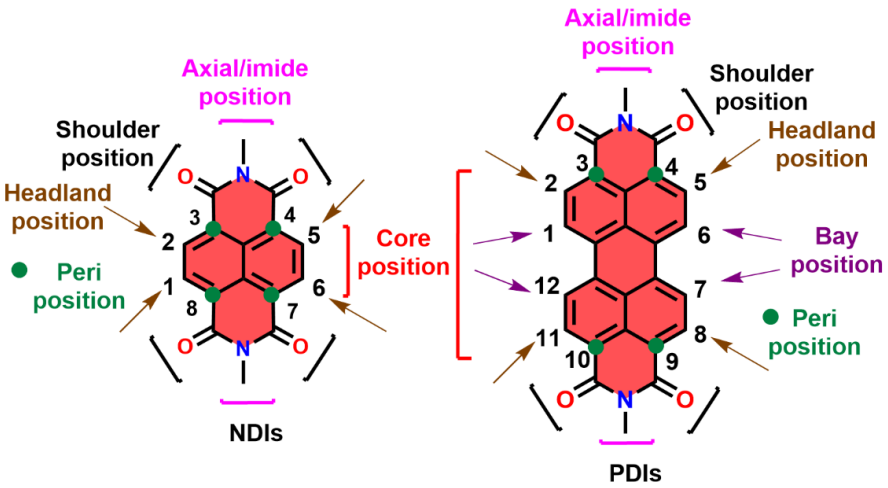

Figure 4.1. Molecular structures of naphthalene tetracarboxylic diimides (NDIs) and perylene tetracarboxylic diimides (PDIs) (Arrows and solid circles represent the substitution positions).

TH-2983_156122010

The various molecular structures (**4.1**-**4.22**) of imidazole, naphthalene and perylene derivatives are shown in the Figure 4.2, which were utilized in the OFETs studies.

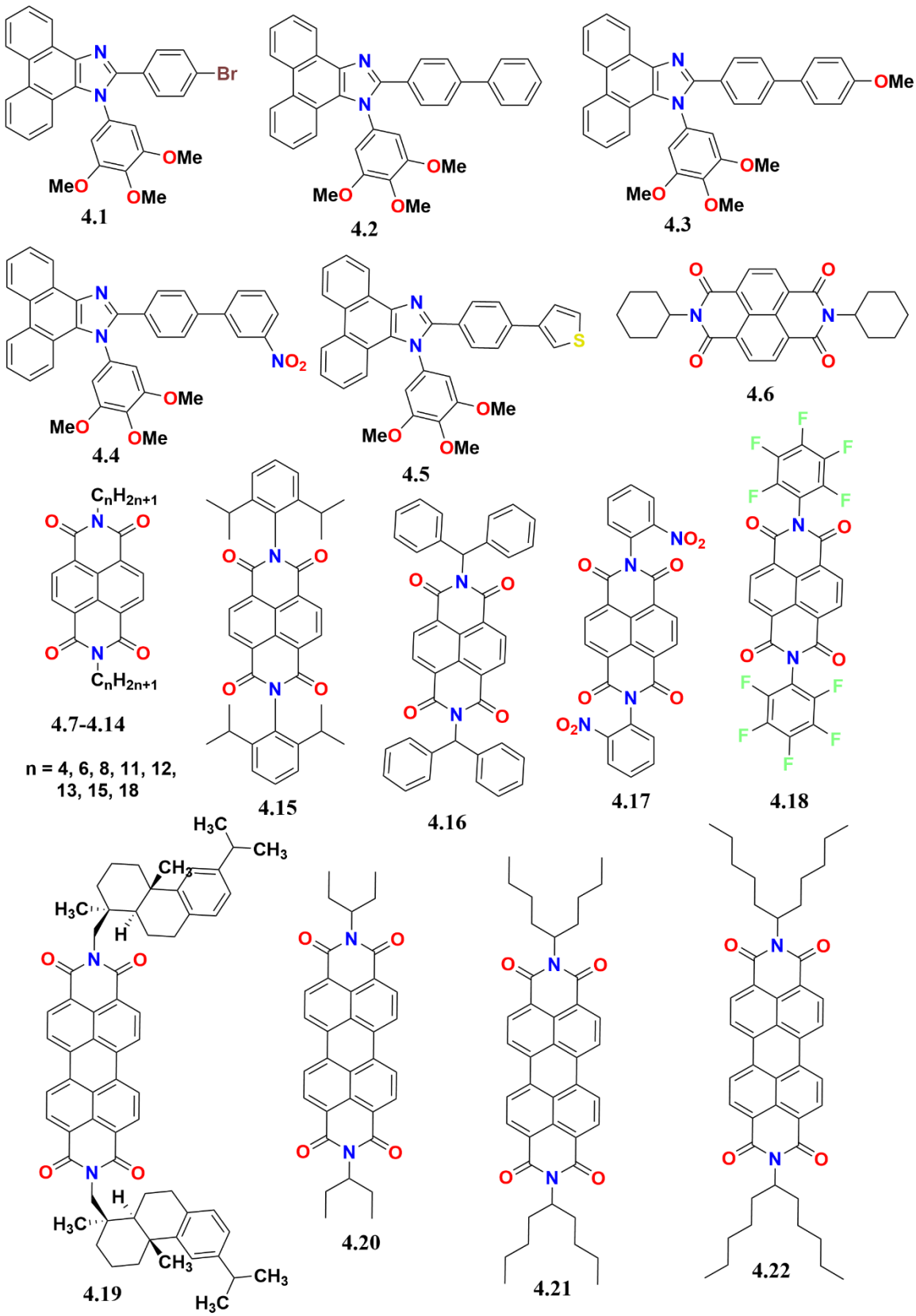

Figure 4.2. The various molecular structures of imidazole, naphthalene and perylene derivatives which were utilized in the OFETs studies.

TH-2983_156122010

Discotic molecules bearing a central aromatic core and peripheral flexible side-chains, can stabilize one dimensional (1D) columnar (Col) phases and thus rose to prominance due to their solution processability, self-assembly and their applicability in organic semiconductor devices. The columnar superstructures with a preferential conduction of charge carriers (holes and electrons) along the columnar axis than across the column, makes them 'molecular wires' in organic electronics. [22–24] However, it must be noted that most of the columnar semiconductors are good hole transport materials (p-type), and there is a dearth of good electron transport materials (n-type).[25–27] Col LCs derived NDI[28–32], PBI[33,34] and their derivatives bring together favourable absorption properties, electron transporting behavior and 1D columnar self-assembly, thus making them highly attractive for the application in organic electronics.[35,36] The imidazole moiety is an electron deficient moiety that can be used for hydrogen bond formation due to presence of free -NH, and thus can play an significant role in the creation of supramolecular aggregates. Further, this –NH can be subjected to *N*-alkylation to modify the self-assembly. S. Kumar *et. al*. has synthesized triphenylenoimidazole based Col LCs.[37] Sonalin *et al.* in 2020 reported phenanthro[9,10-d]imidazoles (PIs) with a D-A architecture to achieve a balanced transport of charge carriers. The solution processable bottom gate-top contact organic field-effect transistors (OFET) showed excellent hole mobility of 0.70 $cm^2 V^{-1} s^{-1}$ with an on/off ratio of 10^7.[38]

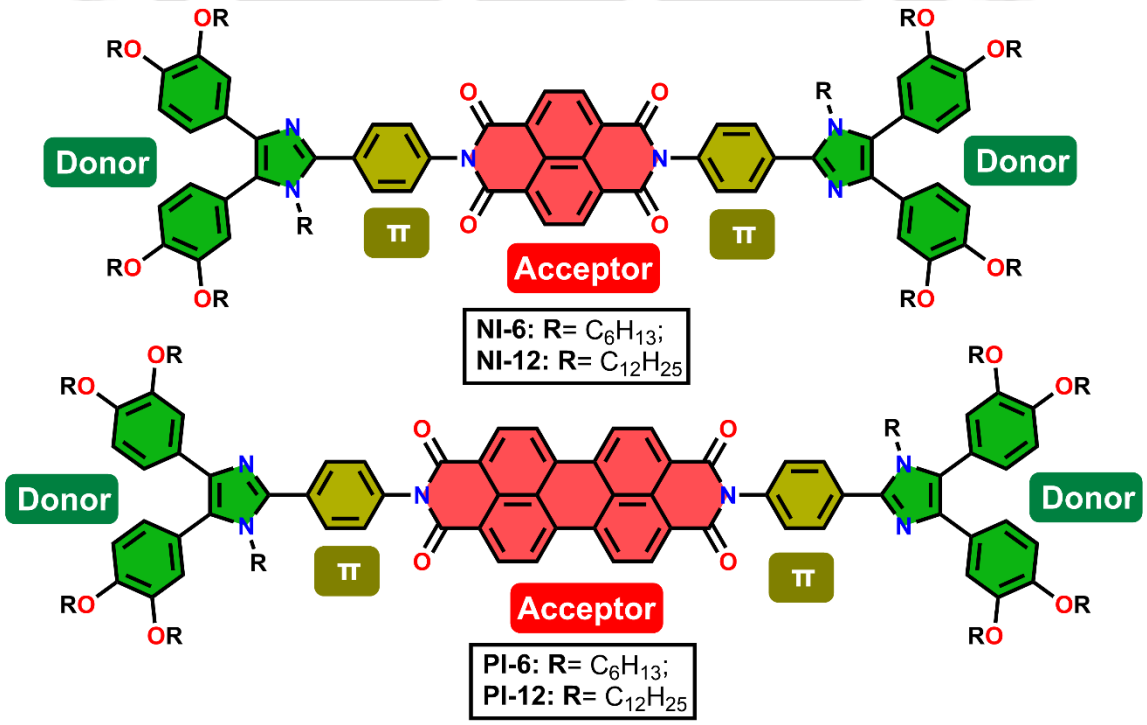

Figure 4.3. Schematic structural representation of the NI and PI derivatives with their donor-π-acceptor-π-donor (D_2-π_2-A) moieties along with flexible alkyl and alkoxy chains (R).

TH-2983_156122010

Considering all the above points, a new class of self-assembling organic semiconductors were synthesized in which comprising tetra-substituted imidazole moiety bearing two dialkoxy phenyl units as electron donors (D),[39–43] central naphthalene/perylene bisimide moieties act as acceptor (A) units and the phenyl moieties as π-bridges between the D and A units.[44] The structures of final target molecules based on the proposed donor-π-acceptor-π-donor (D_2-π_2-A) architecture are shown in Figure 4.3.

4.2. Results and discussion

4.2.1. Synthesis and molecular structure characterization

The synthetic scheme for the preparation of the target molecules are given in Scheme 4.1.

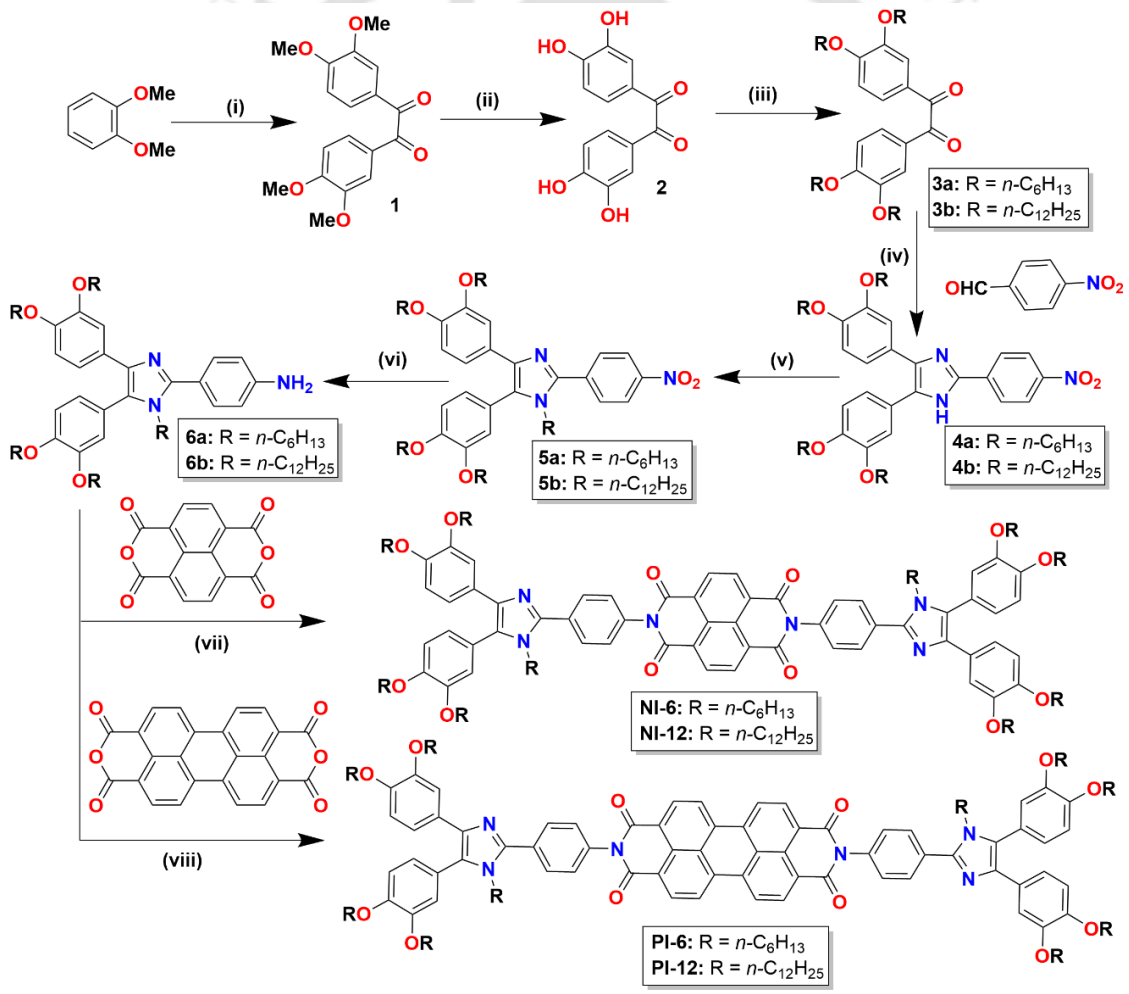

Scheme 4.1: Reagents and conditions: (i) 1,2-Dichloroethane, oxalyl chloride, anhydrous $AlCl_3$, 0 °C (30 min.), RT (17 h), 57%; (ii) 47% HBr, glacial acetic acid, reflux, 16 h, 80%; (iii) anhydrous K_2CO_3, 1-bromoalkane, anhydrous DMF, 80 °C, 17 h, 85-90%; (iv) NH_4OAc, CH_3COOH, 165 °C, MW, 5 min, 75-80%; (v) anhydrous K_2CO_3, 1-bromoalkane, DMF, 80 °C, 24 h, 85-88%; (vi) hydrazine hydrate/10% Pd-C, ethanol, reflux, 12h, 85-90%; (vii)/ (viii) zinc acetate, imidazole, 165 °C, microwave, 35 min. 65-85%.

TH-2983_156122010

The synthetic procedure of products **1**, **2, 3a** and **3b** were reported in chapter 2a. The nitro imidazole derivatives (**4a** and **4b**) were prepared by microwave-assisted coupling of diketones **3a** and **3b** with 4-nitrobenzaldehyde in the presence of ammonium acetate and acetic acid. The alkylation of **4a** and **4b** were carried out by heating with *n*-bromoalkanes and anhydrous potassium carbonate in DMF solvent to yield the product **5a** and **5b.** The reduction of *N*-alkylated nitro compounds with hydrazine hydrate and 10% Pd-C in ethanol solvent yielded corresponding amines (**6a** and **6b**). The final coupling of amines and rylenedianhydrides were carried out in microwave reactor in presence of zinc acetate, imidazole to yield the final **NI** and **PI** derivative's.

Structural characterization and purity of all the compounds **NI-6, NI-12, PI-6** and **PI-12** were investigated and confirmed by various analytical techniques such as ^{1}H, ^{13}C NMR, IR and MALDI-TOF/HRMS mass spectra, which were discussed in the experimental section of this chapter. One of the final NI and PI derivatives (**NI-12** and **PI-12**) were utilized in the OFETs device fabrication, ^{1}H and ^{13}C NMR spectra, which are shown in Figure 4.4 and Figure 4.5.

TH-2983_156122010

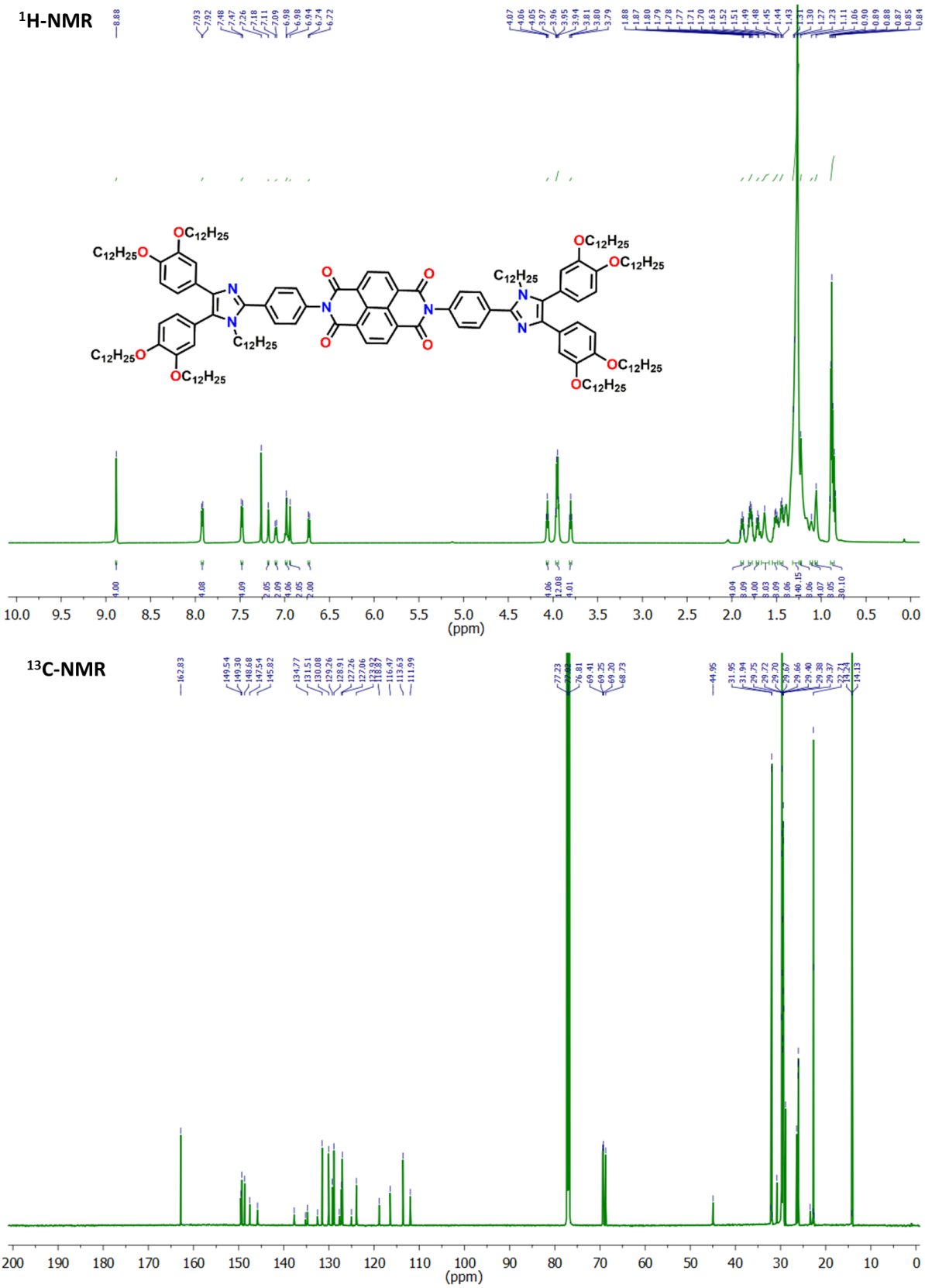

Figure 4.4. ^{1}H NMR (600 MHz) and ^{13}C NMR (150 MHz) spectra of compound **NI-12** in $CDCl_3$.

TH-2983_156122010

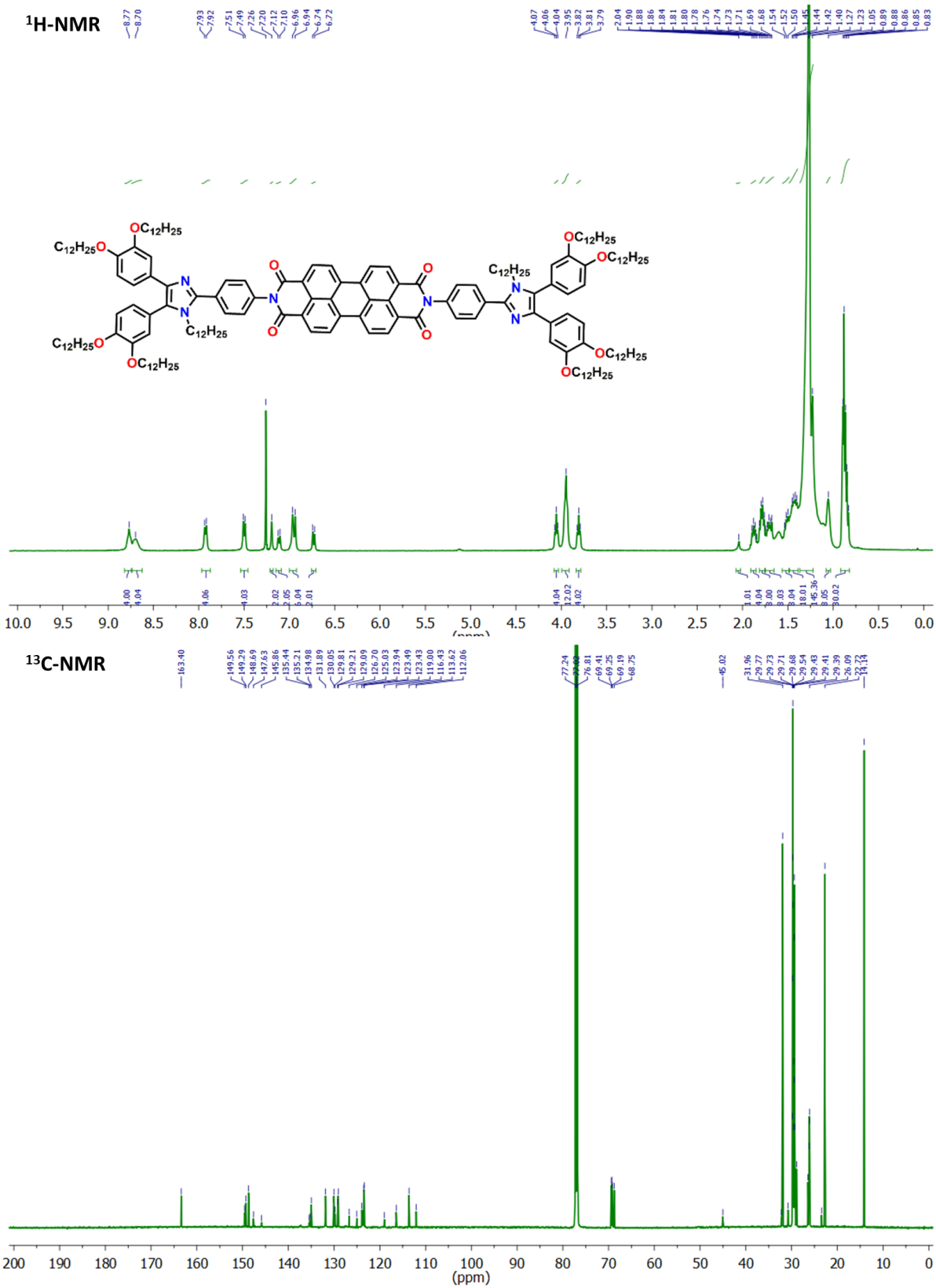

Figure 4.5. ^{1}H NMR (600 MHz) and ^{13}C NMR (150 MHz) spectra of compound **PI-12** in $CDCl_3$.

TH-2983_156122010

4.2.2. Thermal behavior

The thermal behavior of compounds NI-6, NI-12, PI-6 and PI-12 were studied with various techniques like polarizing optical microscopy (POM) along with a programmable hot stage, differential scanning calorimetry (DSC), thermogravimetric analysis (TGA) and X-ray diffraction (XRD) studies. The TGA analysis of these compounds showed that they got high thermal stability, with their 5% weight loss noticed in the range 315 to 400 ^{o}C as shown in Figure 4.6. With the combined analysis of the POM, DSC and XRD, it was confirmed that all NI and PI derivatives shown Col LC phases of different symmetry (Figure 4.7 and Table 4.1).

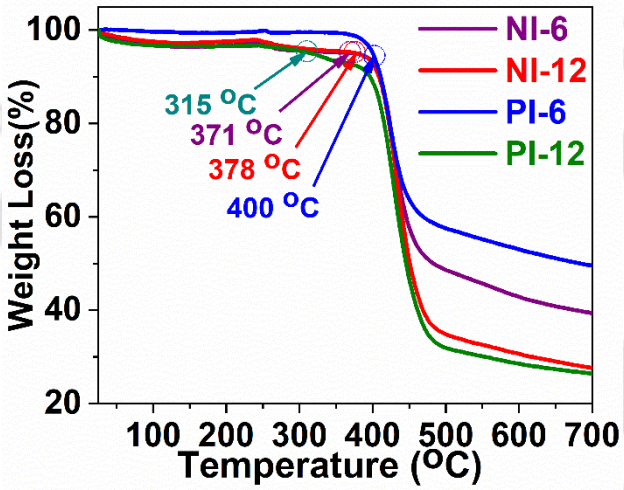

Figure 4.6. TGA thermograms of **NI-6, NI-12, PI-6** and **PI-12** at a scan rate of 10 °C min^{-1} under the Nitrogen gas atmosphere, which displays a thermal degradation at 5% weight loss.

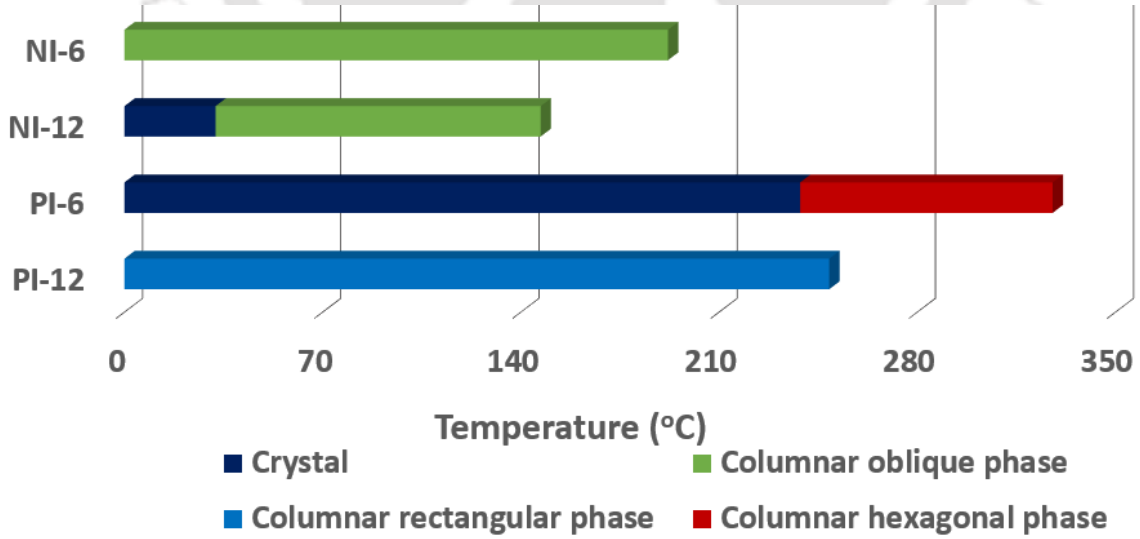

Figure 4.7. Bar graph representing the thermal behavior of **NI** and **PI** derivatives (based on second heating scan).

The sticky birefringent compound **NI-6** on heating under POM showed a phase transition to an isotropic liquid at around 192°C. This isotropic liquid later on cooling at a

TH-2983_156122010

rate of 5°C min^{-1} gave rise to the growth of a bright spherulitic texture around 180 °C, which was shearable on pressure (Figure 4.9a-c, Table 4.1).

Table 4.1 Phase transition temperatures[a] (°C) and corresponding enthalpies (kJ mol^{-1}) of the **NI** and **PI** derivatives

Entry	Phase sequence	
	Heating	**Cooling**
NI-6	Col_{ob} 191.97 (45.23) I	I 175.77 (42.82) Col_{ob}
NI-12	Cr 32.21 (32.84) Col_{ob} 147.02 (48.89) I	I 130.66 (21.14) Col_{ob} 24.77 (39.93) Cr
PI-6	Cr 238.67 (4.7) Col_h 327.83 (2.65) I	I 325.11 (2.80) Col_h 229.65 (2.65) Cr
PI-12	Col_r 248.92 (0.92) I	I 233.02 (0.06) Col_r[b]

[a]Peak temperatures in the DSC thermograms obtained during the first cooling and second heating cycles at 5 °C min^{-1}; [b]mesophase freezes in glassy state (Cr = crystal; Col_h = columnar hexagonnal; Col_{ob} = columnar oblique; Col_r = columnar rectangular; I = isotropic liquid.)

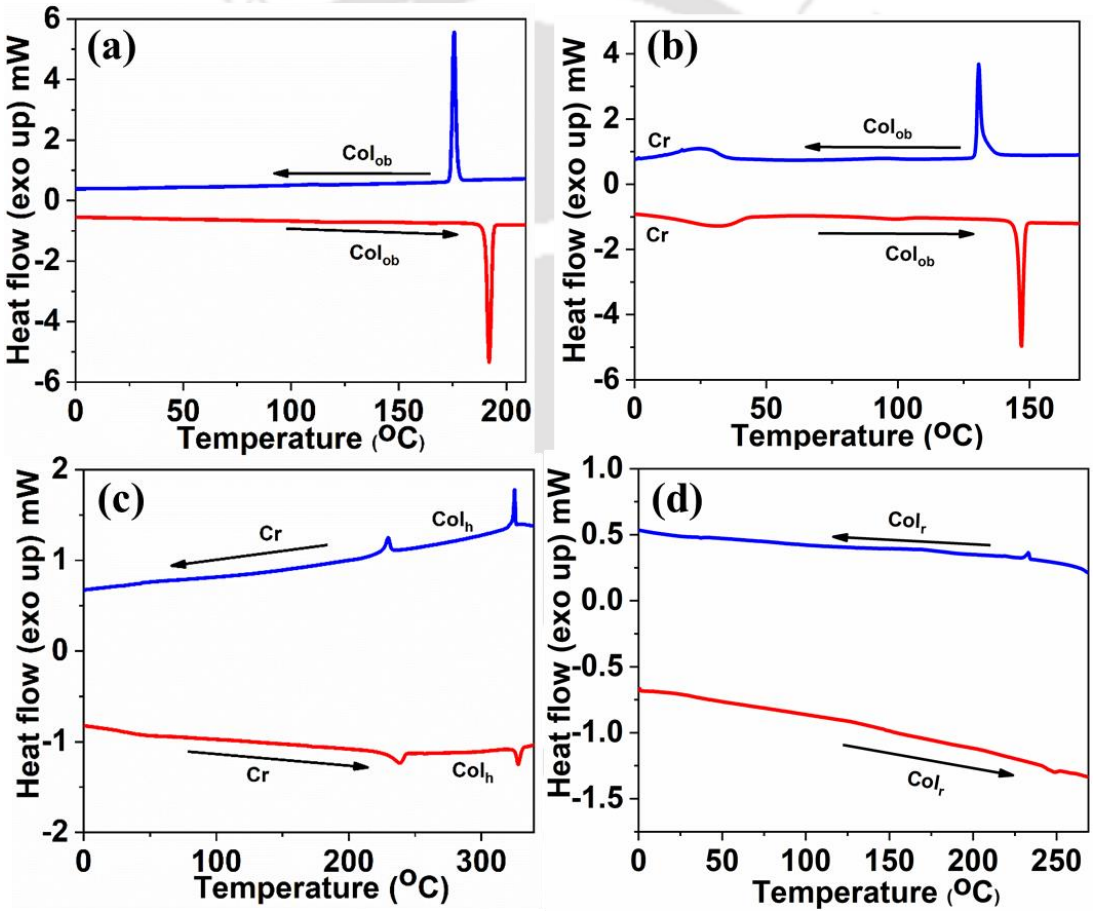

Figure 4.8 (a) DSC traces obtained for compound **NI-6, NI-12, PI-6** and **PI-12** in the second heating and cooling scans at a rate of 5 °C min^{-1} under the nitrogen gas atmosphere.

The texture remained stable down to room temperature without any crystallization peak noticed in DSC (Figure 4.8a). The phase transition was confirmed as columnar oblique (Col_{ob}) phase from high temperature and low temperature XRD studies (Table 4.2). For example, the XRD scans carried out at 170 °C and 100 °C exhibited many peaks at low and mid angle region along with broad diffused peaks in the wide angle region. The peaks in

TH-2983_156122010

the low and mid angle region can be indexed to the Col phase with oblique symmetry, while the diffused broad peak in the wide angle corresponds to the packing of flexible chains. The XRD pattern obtained at room temperature was similar to the higher temperature diffraction patterns as explained below. The plot of intensity *vs* 2θ profile obtained from the powder XRD 2-D pattern at 29 ^{o}C showed peaks with *d*-spacings of 39.96, 21.34, 19.40, 16.95 and 13.04 Å, which can be indexed to Miller indices 10, 01, 20, -11 and 30 of a parallelogram lattice (Figure 4.10c). The wide angle showed a diffused peak with a *d*-spacing of 4.28 Å corresponding to the packing of alkyl chains. This confirms the stabilization of Col_{ob} phase, where unit cell had the lattice parameters a = 44.0 Å, b = 23.5 Å, while the angle between the 2D lattice directions, *i.e.* $\gamma = 63.8^{o}$. Further, in the absence of a core-core peak in the wide angle the diffused peak with a *d*-spacing of 4.28 Å was considered as the height of the unit cell. The area S was found to be 928.1 Å^2 and the cell volume V as 3969.7 Å^3 leading to the number of molecules in a unit cell, *i.e.* $Z \approx 1$ (Figure 4.10d, Table 4.2).

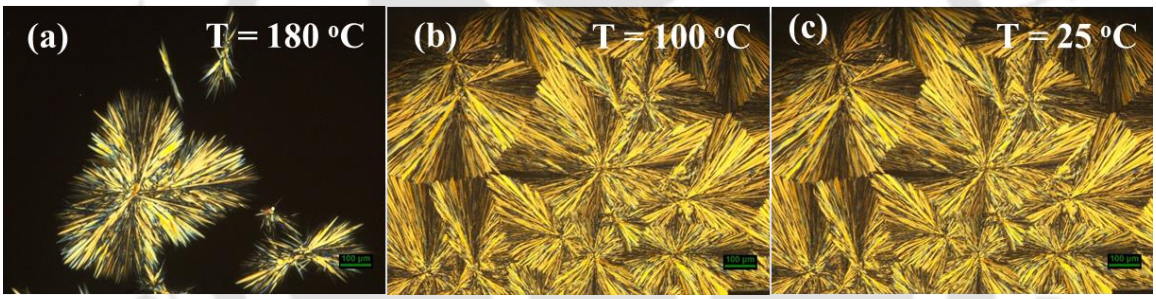

Figure 4.9. POM images of Col_{ob} phase for compound **NI-6** at 180 ^{o}C (a)100 ^{o}C (b) and 25 ^{o}C (c).

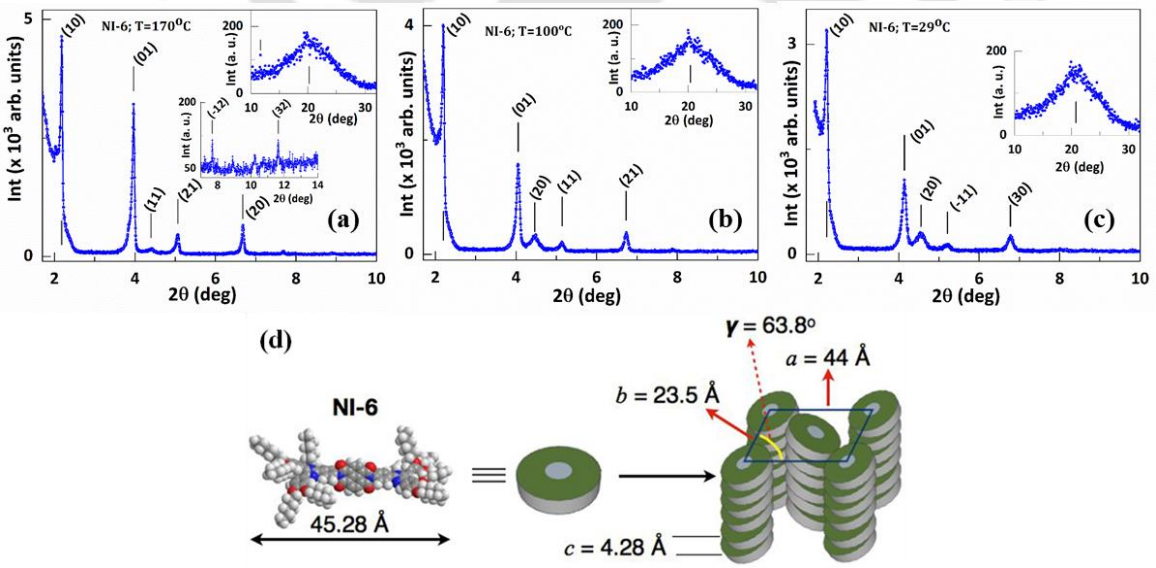

Figure 4.10 Intensity *vs* 2θ profile obtained from the XRD pattern at 170 ^{o}C (a) 100 ^{o}C (b) and 29 ^{o}C (c); schematic representation showing the self-assembly of **NI-6** to form Col_{ob} phase considered at 29 ^{o}C (d) (note that one molecule self-assemble to form a disc).

TH-2983_156122010

The compound **NI-12**, with longer peripheral chains melted into a birefringent mass on heating at 32 °C with ΔH = 32.8 kJ/mol. This on further heating turned into an isotropic liquid at 147 °C with an enthalpy change of 48.9 kJ mol^{-1}. Cooling of the isotropic liquid at a rate of 5 °C min^{-1} led to the formation of grain like pattern as shown in Figure 4.11a-c, which was shearable. The crystallization was seen at around 24.8 °C (ΔH = 39.9 kJ mol^{-1}) (Figure 4.8b).

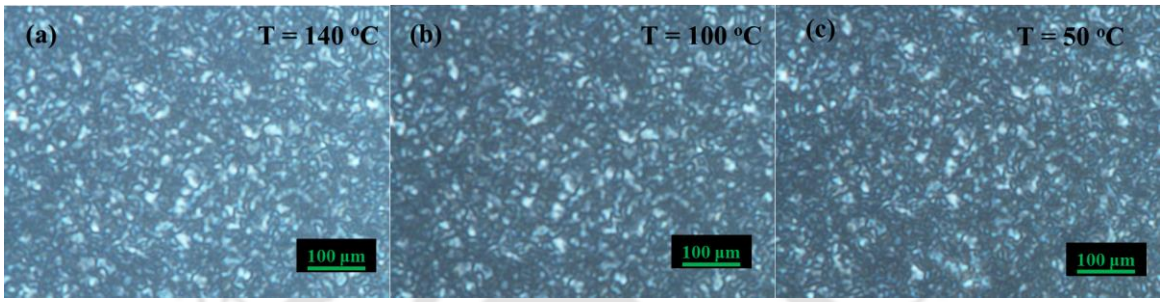

Figure 4.11. POM images of Col_{ob} phase for compound **NI-12** at 140 °C, 100 °C and 50 °C

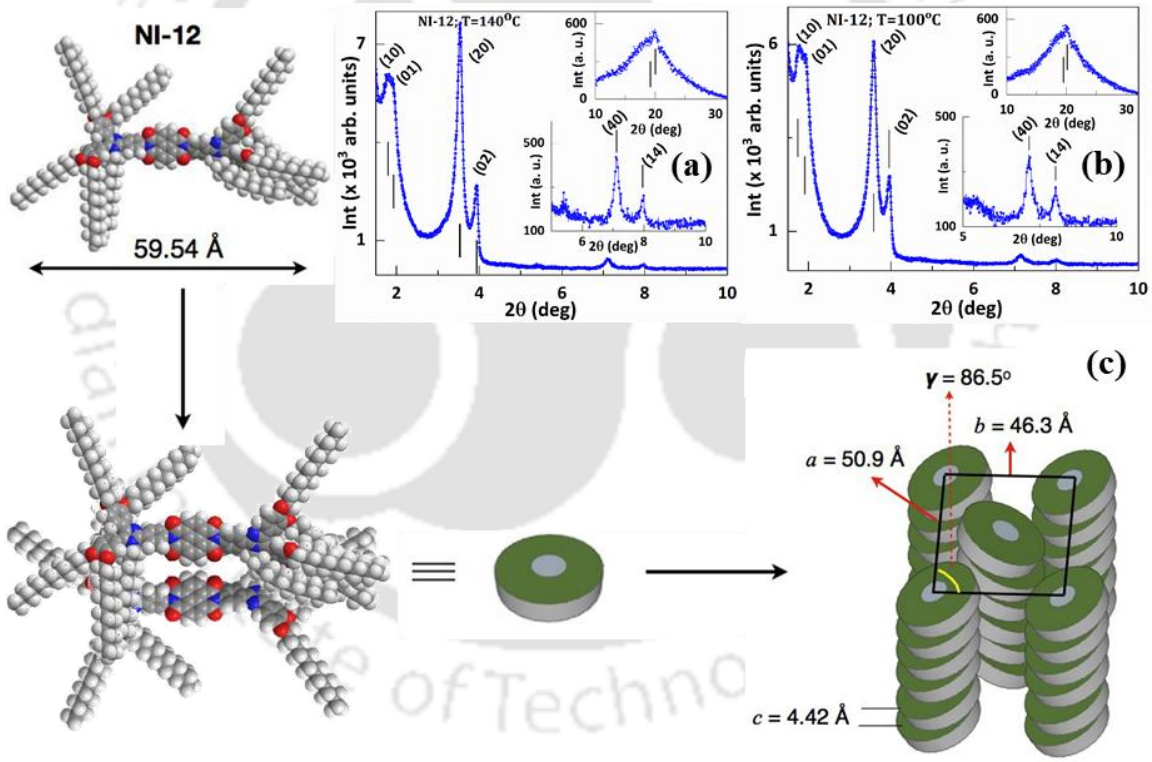

Figure 4.12 Intensity *vs* 2θ profile obtained from the XRD pattern at 140 °C (a) and 100 °C (b); schematic representation showing the self-assembly of **NI-12** to form Col_{ob} phase considered at 100 °C (c) (note that two molecules self-assemble to form a disc).

The XRD patterns obtained for the unaligned sample cooled from the isotropic liquid at 140 °C and 100 °C were similar (Figure 4.12 a-b). As an example, the diffraction pattern obtained at 100 °C, showed spacings of 50.87, 46.32, 24.68, 22.33, 12.36 and 11.03 Å at the low angle region ($0 < 2\theta < 10^o$), which could be assigned to the 10, 01, 20, 02, 40 and 14 reflections from a Col_{ob} lattice. In the wide angle region two diffused peaks were

TH-2983_156122010

found with a *d*-spacings of 4.56 Å and 4.42 Å, which are corresponding to the packing of alkyl tails and the stacking of the cores (Figure 4.12b). From the lattice parameters a = 50.9 Å and b = 46.3 Å, leading to a lattice area (S) of 2352.3 $Å^2$ and lattice volume (V) of 10394.0 $Å^3$. From this value, the number of molecules forming a disc (Z) was found to be around 2 (Figure 4.12c). The POM images up to crystallization temperature did not show any change in th optical texture confirming the presence of same mesophase.

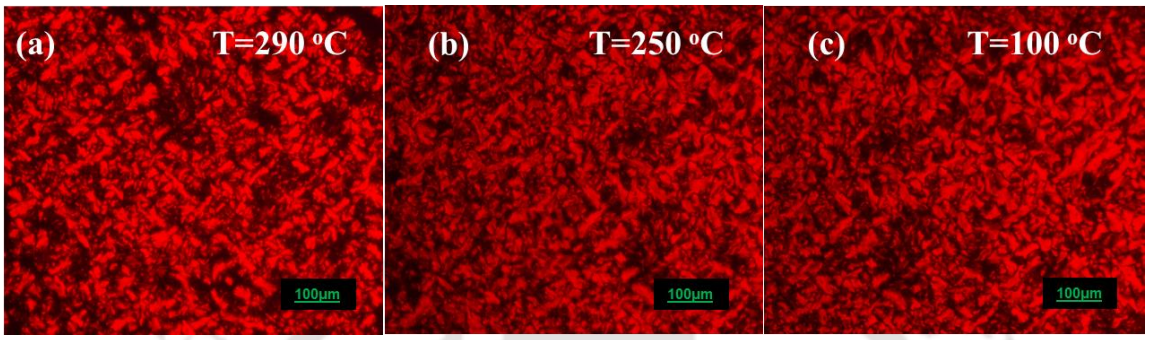

Figure 4.13 (a) POM images of Col_h phase for compound **PI-6** at 290 °C, Cr phase 250 °C and 100 °C.

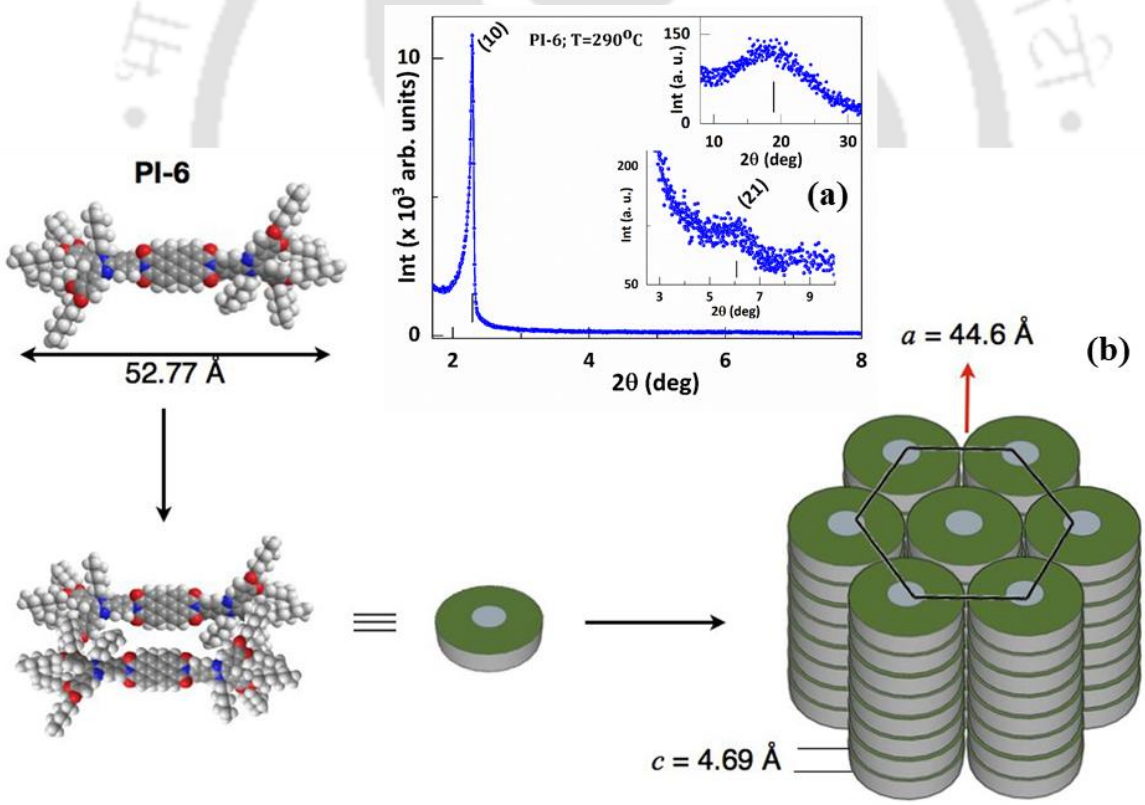

Figure 4.14 Intensity *vs* 2θ profile obtained from the XRD pattern at 290 °C (a); schematic representation showing the self-assembly of **PI-6** to form Col_h phase considered at 290 °C (b) (note that two molecules self-assemble to form a disc).

Compound **PI-6**, which is the higher rylene counterpart of **NI-6**, was a crystalline solid due to the enhanced π-π interactions, thus exhibiting higher melting and clearing points at 239 °C (ΔH = 4.7 kJ mol^{-1}) and 328 °C (ΔH = 2.7 kJ mol^{-1}) respectively (Figure

TH-2983_156122010

4.8c). Cooling of the isotropic melt led to the formation of a leaf like birefringent texture, characteristic of Col_h phase, finally crystallizing at 230 °C (Figure 4.13a-c). The X-ray diffraction pattern obtained at 290 °C was simpler in comparison to the naphthalene derivatives, where two *d*-spacings centered at 38.62 Å and 14.43 Å, which can be indexed to 10 and 21 reflections of a hexagonal lattice with the reciprocal ratio of 1:0.58. A diffused peak in the wide angle (4.69 Å) corresponds to the packing of alkyl chains and hence confirms the liquid crystalline nature (Figure 4.14a). The hexagonal lattice parameter a was found to be 44.6 Å, which is 15% lesser than the calculated molecular diameter of **PI-6**, thus pointing to the interdigitation of alkyl tails with the neighbouring columns. The number of molecules present in the unit hexagonal cell (Z) was found to be ≈ 2, which probably lie side by side to form a disc (Figure 4.14b).

Compound **PI-12**, with longer dodecyl flexible chains exhibited reduced melting and clearing points in comparison to **PI-6**. The sticky gummy mass did not show any characteristic texture. The birefringent mass on cooling from the isotropic liquid did not show any signs of crystallization both in POM and in DSC (Figure 4.8d and Figure 4.15a). The X-ray diffraction pattern obtained at 230 °C and 180 °C (Figure 4.15b-c) were found to be similar and confirmed the stabilization of Col_r phase, where a unit rectangular cell was composed of one molecule (Figure 4.15d). This is in contrast to **NI-12**, where a unit rectangular cell was formed by two molecules.

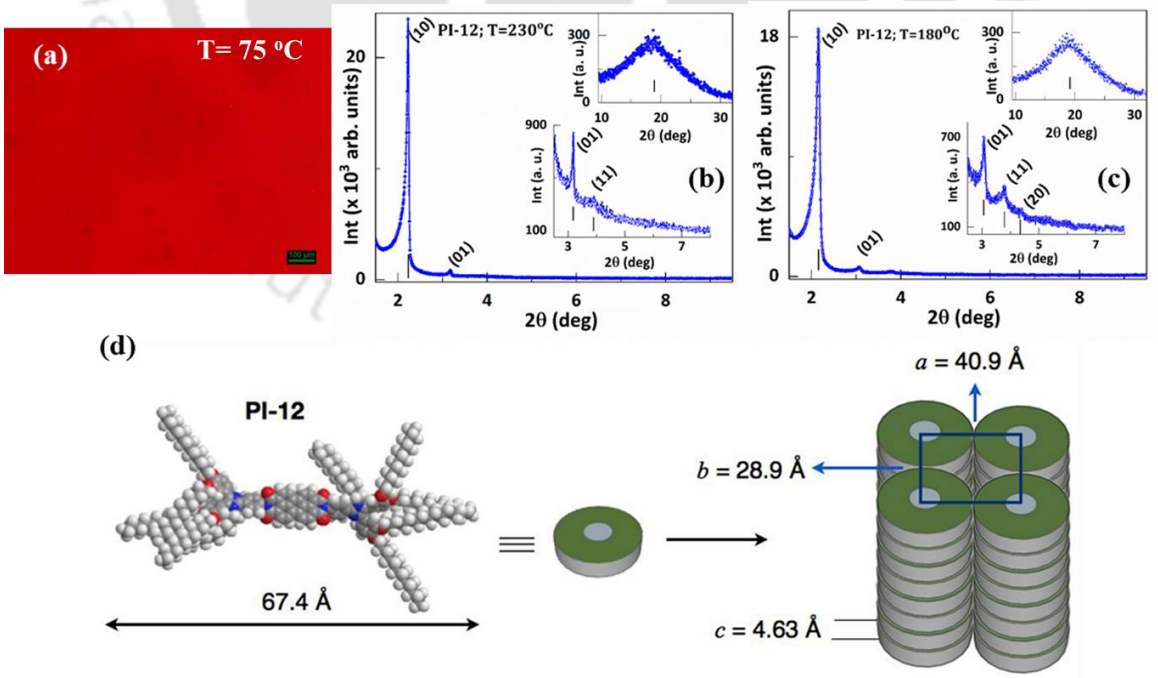

Figure 4.15 (a) POM image of Col_r phase for compound **PI-12** at 75 °C; Intensity *vs* 2θ profile obtained from the XRD pattern at 230 °C (b) and 180 °C (c); schematic representation showing the self-assembly of **PI-12** to form Col_r phase considered at 180 °C (d).

TH-2983_156122010

Table 4.2. Results of (*hk*) indexation of XRD profiles of the NI and PI compounds at a given temperature (T) of mesophases.

Compounds (D\ Å)	**Phase (T\ºC)**	**$d_{(obs)}$ (Å)**	**$d_{(cal)}$ (Å)**	**Miller indices hk**	**Lattice parameter (Å); lattice area S (Å^2); molecular volume V (Å^3)**
NI-6 (45.28) (MW:1824.54)	Col_{ob} (170)	40.52 22.27 20.10 17.45 13.23 11.50 7.60 4.40 (h_a=c)	40.52 22.27 20.26 17.45 13.17 11.66 7.56	10 01 11 21 20 -12 32	a = 42.4 b = 23.3 γ = 72.7º S = 944.9 V = 4157.4 Z = 1.4
	Col_{ob} (100)	40.17 21.79 19.77 17.19 13.13 4.36 (h_a=c)	40.17 21.79 20.09 17.19 13.01	10 01 20 11 21	a = 42.0 b = 22.8 γ = 73.2 º S = 914.8 V = 3988.6 Z = 1.3
	Col_{ob} (29)	39.96 21.34 19.40 16.95 13.04 4.28 (h_a=c)	39.49 21.09 19.75 15.92 13.16	10 01 20 -11 30	a = 44.0 b = 23.5 γ = 63.8 º S = 928.1 V = 3969.7 Z = 1.3
NI-12 (59.54) (MW: 2666.16)	Col_{ob} (140)	49.15 45.86 24.99 22.44 12.42 11.11 7.61 4.63 (h_a) 4.44 (h_c=c)	49.15 45.80 24.57 22.90 12.28 11.27 7.60	10 01 20 02 40 14	a = 49.2 b = 45.9 γ = 87.4 º S = 2253.5 V = 10427.4 Z = 2.3
	Col_{ob} (100)	50.87 46.32 24.68 22.33 12.36 11.03 4.56 (h_a) 4.42 (h_c=c)	50.78 46.23 25.39 23.11 12.69 11.42	10 01 20 02 40 14	a = 50.9 b = 46.3 γ = 86.5 º S = 2352.2 V = 10393.5 Z = 2.3
PI-6 (52.77) (MW:1948.19)	Col_h (290)	38.62 14.53 4.69 (h_a=c)	38.62 14.60	10 21	a = 44.6 S = 1722.7 V = 8079.3 Z = 2.5
PI-12 (67.37) (MW: 2790.3)	Col_r (230)	39.59 27.81 22.66 4.71 (h_a=c)	39.60 27.81 22.76	10 01 11	a = 39.6 b = 27.8 S = 1101.3 V = 5187 Z = 1.1
	Col_r (180)	40.89 28.88 23.35 20.35 4.63 (h_a=c)	40.89 28.88 23.59 20.45	10 01 11 20	a =40.9 b =28.9 S = 1180.9 V =5467.6 Z =1.2

TH-2983_156122010

[a]The diameter (D) of the disk (estimated from Chem 3D Pro 8.0 molecular model software from Cambridge Soft). d_{obs}: spacing observed; d_{cal}: spacing calculated (deduced from the lattice parameters; a for Col_h phase; a, b for Col_{ob} and Col_r phase; γ is the tilt angle for Col_{ob} phase). The spacings marked h_a and h_c correspond to diffuse reflections in the wide-angle region arising from correlations between the alkoxy chains and core regions, respectively. Z indicates the number of molecules per columnar slice of thickness h_c estimated from the lattice area S and the volume V. Whenever $h_c=c$ is not found h_a is considered for the calculation of Z, in such cases the value of Z shows an increase.

4.2.3. Photophysical properties

Photophysical properties of all four compounds (**NI-6**, **NI-12**, **PI-6** and **PI-12**) were investigated in chloroform solution (Table 4.3 and Figure 4.16). The absorption spectra of both **NI-6** and **NI-12** derivatives in micromolar solution showed two bands at 360 and 380 nm. While both **PI-6** and **PI-12** showed a red shifted absorption bands centered at 432, 461, 493 and 529 nm, the PL emission spectra of both **NI-6** and **NI-12** compounds showed an emission maximum at 407/408 and 431/433 nm with large Stokes shifts (1746-1806 cm^{-1}). The PL emission spectra of both **PI-6** and **PI-12** compounds showed an emission maximum at 544 and 577/578 nm with small Stoke shift (521 cm^{-1}). Both the series of compounds exhibited high molar extinction coefficients. Optical band gap found 3.17 and 2.26 eV for both **NI** and **PI** derivatives

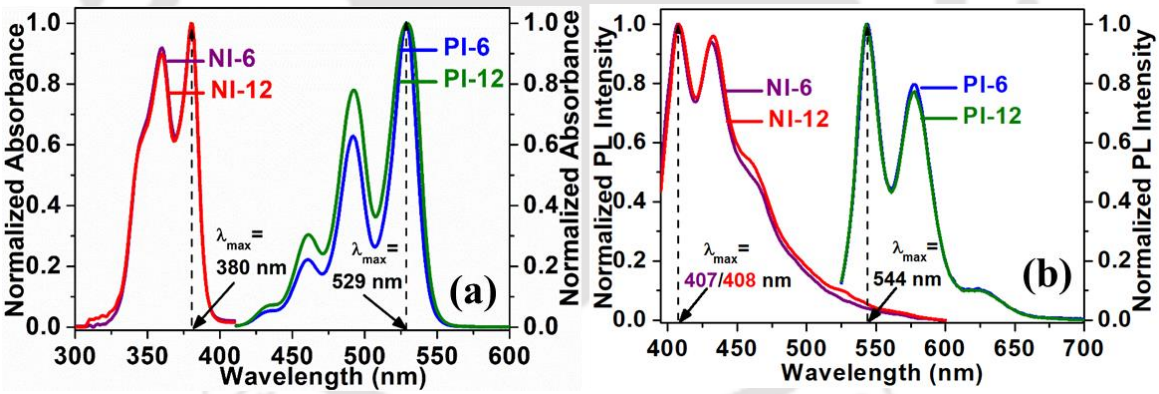

Figure 4.16. An overlay of the absorption (a) and emission spectra (b) of compound **NI-6, NI-12, PI-6** and **PI-12** in chloroform solution.

Table 4.3. Photophysical properties of **NI** and **PI** derivatives in solution state[a]

Compounds	Absorption (nm)	ε ($Lmol^{-1}cm^{-1}$)	Emission[b] (nm)	Stokes shift (cm^{-1})	$\Delta E^c_{g,\,opt}$ (eV)
NI-6	360, 380	52048	407, 431	1746	3.17
NI-12	360, 380	42551	408, 433	1806	3.17
PI-6	432, 461, 493, 529	126763	544, 577	521	2.26
PI-12	432, 461, 493, 529	82748	544, 578	521	2.26

[a] micromolar solutions in chloroform; [b] λ_{ex} = 380 and 529 nm for NI and PI derivatives; [c]optical band gap determined from the red edge of the longest wavelength in the UV-visible absorption spectra [$E_{g(eV)}=1240/\lambda_{onset}(nm)$].

TH-2983_156122010

4.2.4. Electrochemical properties and DFT studies

Cyclic voltammetry (CV) studies of all four compounds were carried out in anhydrous dichloromethane solutions in millimolar concentration. Compounds **NI-6** and **NI-12** exhibited an irreversible oxidation potential at ~ 1.03 V and the compounds **PI-6** and **PI-12** exhibited an irreversible oxidation potential at ~ 1.04 V at a scanning rate of 100 mV s^{-1}. From these values, the HOMO levels of these compounds were found to be around -5.32 and -5.33 eV. The LUMO levels were found to be around -2.15 and -3.07 eV respectively (Table 4.4 and Fig. 4.17a-e).

Table 4.4. Electrochemical properties (CV) of NI and PI derivatives in solution[a,b]

Compounds	E_{1oxd}[c]	E_{HOMO}[d,e]	E_{LUMO}[d,f]	$\Delta E_{g,opt}$[d,g]
NI-6	1.03	-5.32	-2.15	3.17
NI-12	1.03	-5.32	-2.15	3.17
PI-6	1.04	-5.33	-3.07	2.26
PI-12	1.04	-5.33	-3.07	2.26

[a]Dichloromethane solution; [b]experimental conditions: $Ag/AgNO_3$ as reference electrode, glassy carbon working electrode, platinum wire counter electrode, TBAP (0.1 M) as a supporting electrolyte at a scanning rate 100 mV s^{-1}, room temperature; [c]in volts (V); [d]in eV; [e]estimated from the formula by using $E_{HOMO} = -(4.8-E_{1/2,Fc/Fc+}+E_{oxd,onset})$ eV; [f]estimated from the formula by using $E_{LUMO}=E_{g,opt}+E_{HOMO})$ eV; [g]calculated from the red edge of the absorption band; $E_{1/2,\ Fc/Fc+} = 0.51$.

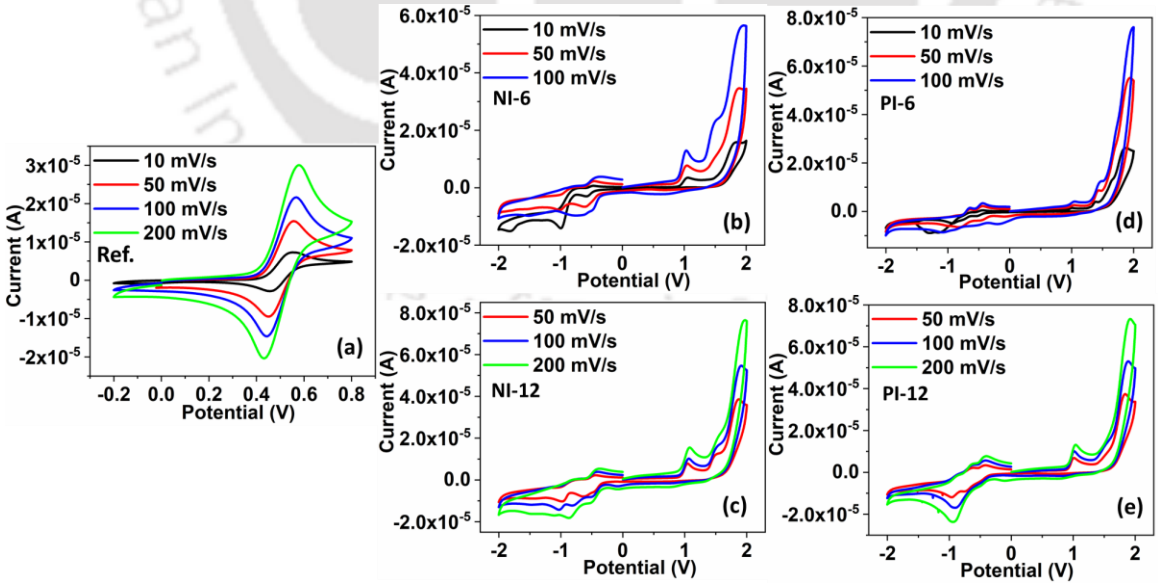

Figure 4.17. Cyclic voltammetry of (**Ref**.) ferrocene (a); cyclic voltammetry (CV) plots of compound **NI-6** (b) **NI-12** (c) **PI-6** (d) and **PI-12** (e) in DCM solution of tetra-*n*-butylammonium perchlorate (TBAP) (0.1 M) at a scanning rate 10, 50, 100 and 200 mV s^{-1}; the half wave potential of Fc/Fc+ was found to be 0.51 V relative to Ag/Ag+ reference electrode.

TH-2983_156122010

The DFT calculations of these rylene bisimides were carried out to obtain the energy-minimized structures, HOMO-LUMO levels (Figure. 4.18). The chain length was restricted to methyl to reduce the time taken for the calculation. In comparison to the energy levels obtained from electrochemistry, the DFT calculations showed an increased LUMO values (-3.39 and -3.46 eV for **NI** and **PI**) and increased HOMO value (-5.03 and -5.02 eV for **NI** and **PI**). The molecular diameter of optimized structure of **NI-6, NI-12, PI-6** and **PI-12** were found around 45.28, 59.54, 52.77, and 67.37 Å respectively.

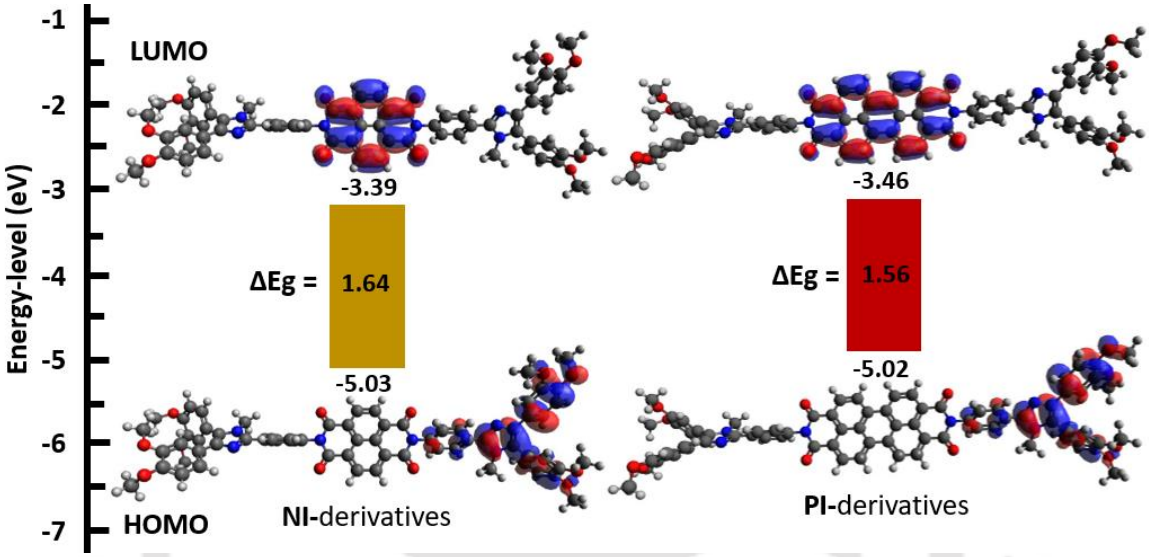

Figure. 4.18. HOMO and LUMO energy levels of **NI** and **PI** derivatives obtained from DFT. The calculations were performed at level (chain length is limited to methyl for clarity purpose).

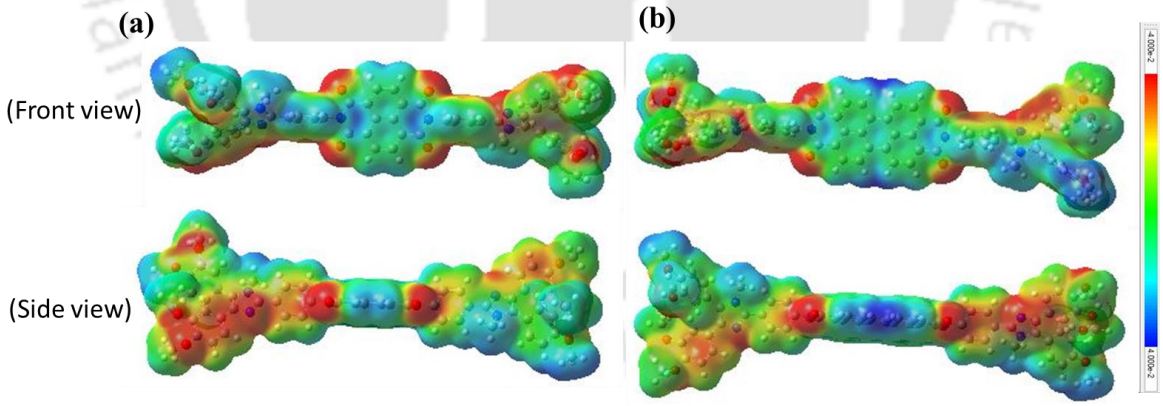

Figure. 4.19. 3D molecular electrostatic potential (MEP) contour map of **NI** and **PI** derivatives optimized structure (chain length is limited to methyl for clarity purpose).

The 3D molecular electrostatic potential (MEP) contour map of the optimized structure of these compounds are shown in Figure 4.19a-b. In the mapped electrostatic potential surface, the red and blue colors correspond to the negative and positive electrostatic potential respectively, whereas the green color corresponds to the zero

TH-2983_156122010

electrostatic potential. Thus the electron density is concentrated over oxygen atoms of the rylene bisimides while the central cores seems to be electron deficient.

4.2.5. Morphology studies

The morphology of compounds **NI-12** and **PI-12** was examined through field emission scanning electron microscopy (FESEM) and atomic force microscopy (AFM). In FESEM analyses, compound **NI-12** revealed a fibrous surface, while the compound **PI-12** showed the aggregated type of pattern. Also, in the magnified image (10 KX) of both compounds is also shown in Figure 4.20(a, b) and the same observation can be made. In the AFM studies, **NI-12** also observed the fibrous structure with RMS roughness around 6.75 nm Figure 4.20(c), whereas in the case of compound **PI-12** RMS roughness was found to be 3.27 nm Figure 4.20(d).

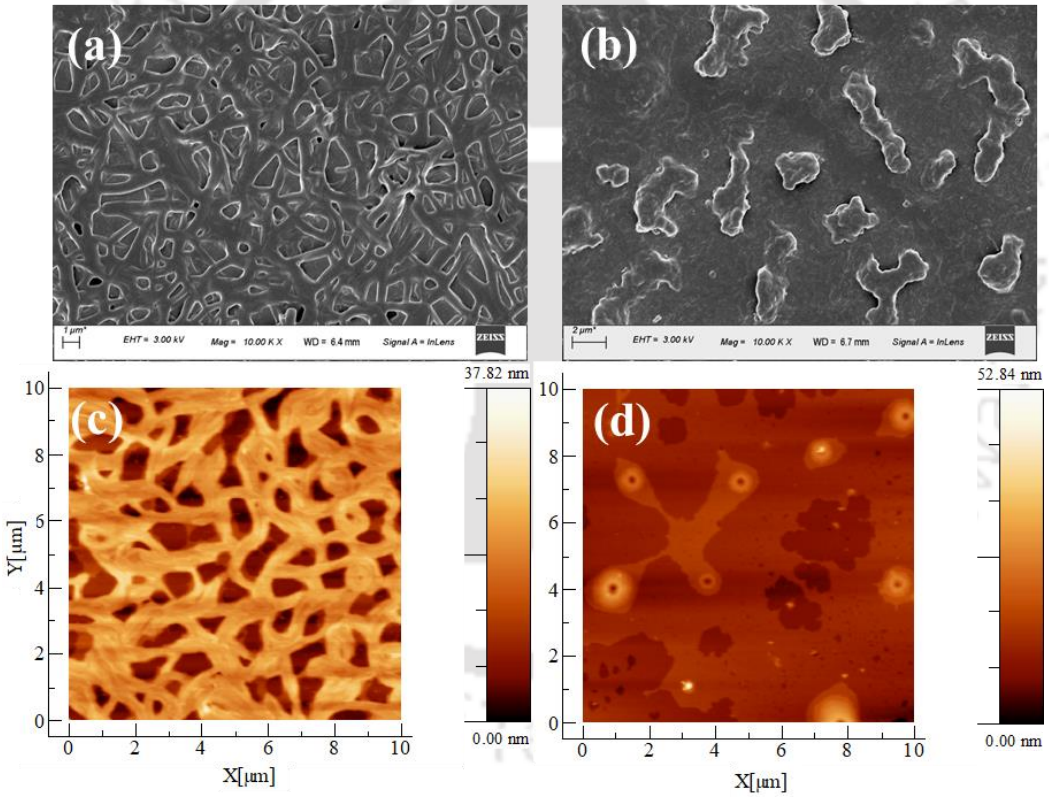

Figure 4.20. FESEM images were taken in thin films by drop-casting the solutions of **NI-12** (a) and **PI-12** (b) obtained from 5mg mL^{-1} concentration in THF solution. AFM images were obtained in thin films by drop-casting the solutions of **NI-12** (c) and **PI-12** (d) derivatives obtained from 1mg mL^{-1} concentration in THF solution.

4.2.6. Fabrication of the OFETs:

The fabrication of the OFETs was performed on silicon wafers with 300 nm of SiO_2 pre-grown over them. The wafers were thoroughly cleaned with sonication in acetone followed by isopropyl alcohol (IPA) for about 30 minutes; after that cleaned with deionized

TH-2983_156122010

(DI) water and dried. In order to remove organic impurities, the wafers were immersed in Piranha solution (3:1 H_2SO_4 and H_2O_2 mixture) for 30 minutes, rinsed with DI water, and the wafers were then dried under the N_2 stream and baked at 175 ^oC for 60 min. After the cleaning, the Aluminum was deposited with the thermal deposition technique. The contacts were patterned through optical lithography, and the process is described in Figure 4.21. The fabricated device parameters are mentioned in Figure 4.22.

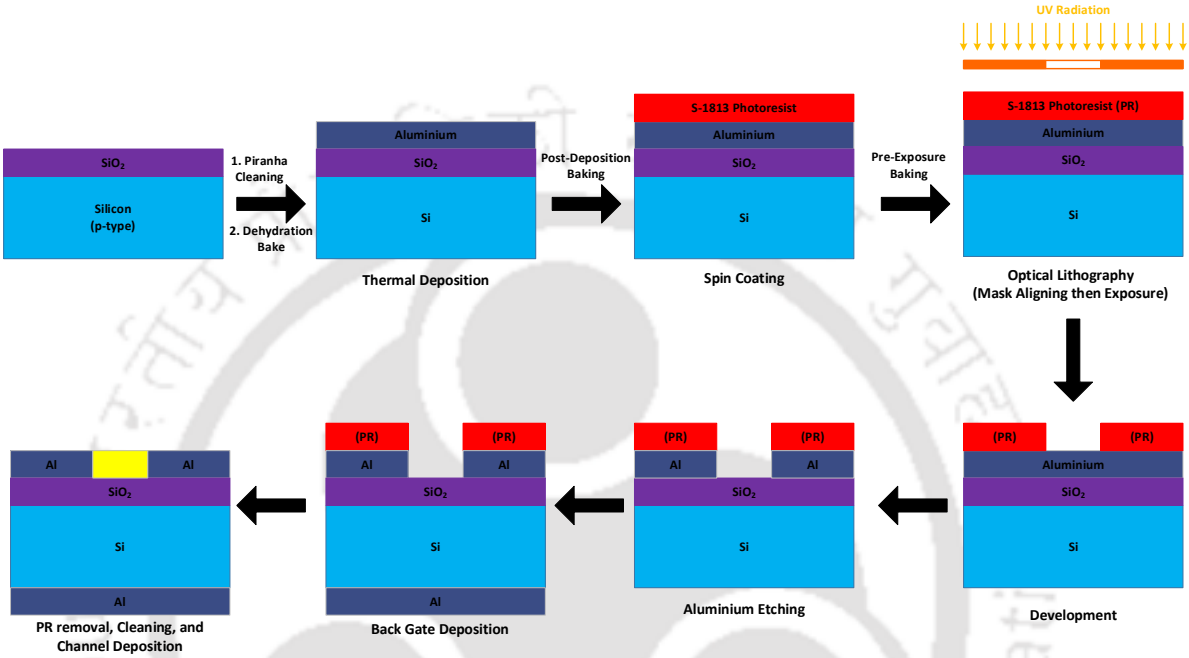

Figure 4.21. The schematic describing the fabrication steps for OFETs.

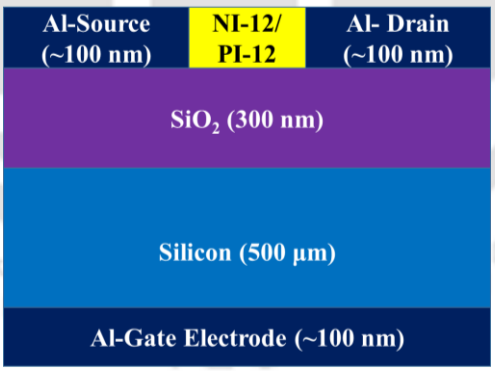

Figure 4.22. The schematic representation of OFET devices.

4.2.7. Electrical characterization:

The fabricated OFETs were subjected to electrical characterization through Keithley 2450 source meter. Two source meters were connected in Master-Slave fashion to get three-terminal measurements. The fabricated devices were probed with 10µm tungsten tips of the Evergreen BD-6 probe station. These probes were connected to the source meter through low-noise triaxial cables to ensure ultra-low leakage. The source

TH-2983_156122010

terminal was kept at ground potential, whereas drain and gate terminals were connected to the source meter unit and subjected to either constant potential or DC sweep (with a step of 0.05 V) as per the measurement requirements (I_D-V_G or I_D-V_D). During the I_D-V_G characterization, the drain terminal was kept at a low voltage of 0.5V. The threshold voltage of the OFETs was estimated from I_D-V_G characteristics through gate-voltage axis intercept.[45] The mobility of the carrier (presented in Table 4.5) was estimated with the help of the current equation of MOSFET given as follows:

$$I_D = \mu_n C_{ox} \frac{W}{2L} (V_G - V_{th})^2$$

Where I_D is the drain current, W/L is the ratio of width and length of the channel, C_{ox} is oxide capacitance, V_G is gate voltage, and Vth is the threshold voltage of the OFET. During the estimation of output characteristics, the gate was kept at a fixed potential, and the drain was swept from 0 to 1 volt with a step of 0.05 V. The output characteristics can be seen in Figure 4.23.

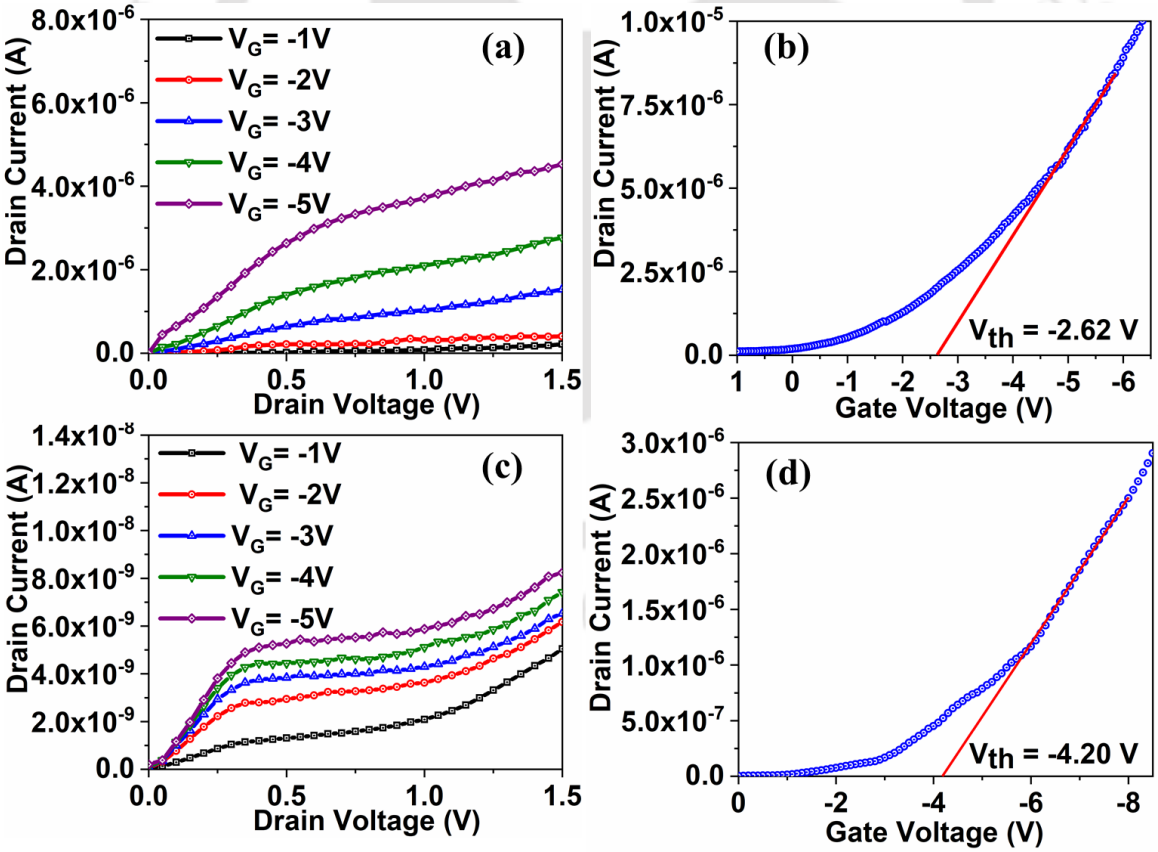

Figure 4.23. The output characteristic of I_D-V_D curves for **NI-12** OFET for various values of V_G (a); transfer characteristic of I_D-V_G curves for the same device at V_D = 2V (b); Output characteristic of I_D-V_D curves for **PI-12** OFET for various values of V_G (c) and transfer characteristic I_D–V_G curves for the same device at V_D = 2V (d).

TH-2983_156122010

It was observed that the threshold voltage for the NI-OFET is -2.62 Volt and the corresponding mobility and I_{on}/I_{off} were calculated 1.99 $cm^2\ V^{-1}\ s^{-1}$ and 1.22×10^2 respectively. However, for PI-OFET the threshold voltage is higher than that of NI-OFET, which is approx. -4.20 Volt, and the corresponding values for mobility and I_{on}/I_{off} were calculated 0.63 $cm^2\ V^{-1}\ s^{-1}$ and 10.02×10^2 respectively.

Table 4.5. Summary of the OFETs device data

Active layer	V_{th} (V)[a]	Hole mobility[b] $cm^2\ V^{-1}\ s^{-1}$	I_{on}/I_{off}[c]
NI-12	-2.62	1.99	1.22×10^2
PI-12	-4.20	0.63	1.00×10^3
[a] Threshold voltage. [b] Hole mobility. [c] Current on/off ratio of the OFETs.			

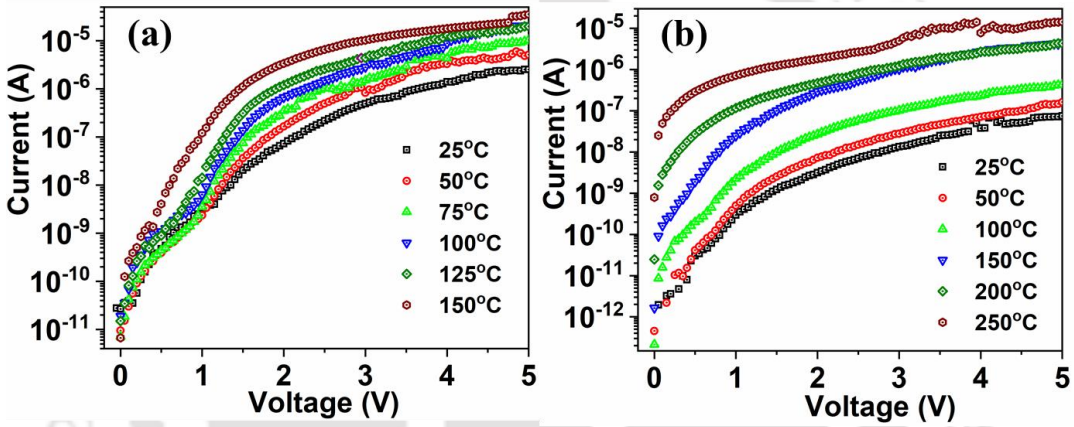

Figure 4.24. The temperature-dependent I-V characteristics for **NI-12** (a) and **PI-12** (b) derivatives on heating at a 5 $^oC\ min^{-1}$ rate.

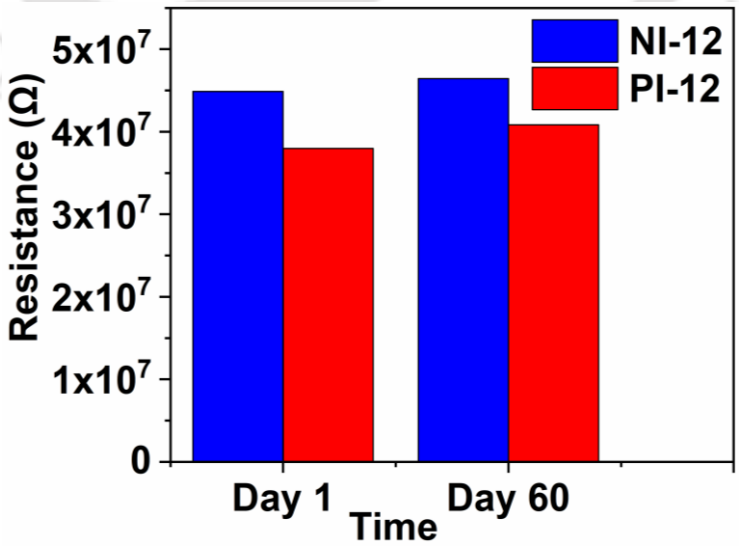

Figure 4.25 The stability of **NI-12** and **PI-12** OFET devices with respect to resistance vs time.

TH-2983_156122010

The thermal response on the current of the OFETs were plotted in Figure 4.24. It was observed that the current for both NI and PI-OFETs gets increased upon heating. The stability of both NI and PI OFETs devices measured in the gap of 60 days and found stable in term of resistance as shown in the Figure 4.25.

4.3. Conclusion:

A new donor-π-acceptor-π-donor (D_2-π_2-A) architecture of four new naphthalene and perylene bisimide-based imidazole liquid crystalline (NI and PI) derivatives were designed and synthesized which contains ten flexible chains for solution-processable organic semiconductors. All four compounds stabilized different liquid crystalline columnar phases. Higher thermal stability and lower band gaps were also observed in both NI and PI derivatives. NI derivatives showed larger Stokes shifts while PI derivatives exhibited very high molar extinction coefficients. We utilized two solution processable liquid crystalline compounds (**NI-12** and **PI-12**) for the fabrication in organic field-effect transistors and interestingly found the hole mobility to be 1.99 $cm^2\ V^{-1}\ s^{-1}$ for **NI-12** and 0.63 $cm^2\ V^{-1}\ s^{-1}$ for **PI-12** derivatives at room temperature in normal air condition.

4.4. Experimental section

In this section the detailed synthesis procedure and the molecular structural characterization data have been presented for the intermediates and target compounds mentioned in the scheme.

Synthesis of Compound 1, 2, 3a and 3b

The detailed synthetic procedure of products **1**, **2, 3a** and **3b** were reported previously in chapter 2a.

Synthesis of 4,5-bis(3,4-bis(alkyloxy)phenyl)-2-(4-nitrophenyl)-1H-imidazole (4a and 4b)[46]

Compounds **3a** or **3b** (1.0 equiv.), 4-Nitrobenzaldehyde (1.0 equiv.), and ammonium acetate (8.5 equiv.) were combined and dissolved in 3.0 mL of HOAc in a 10 mL reaction vial containing a magnetic stir bar. The reaction vessel was heated in the microwave reactor cavity for 5 min. at 155 °C, after which the vessel was cooled to room temperature. The reaction mixture was washed with distilled water, a yellow precipitate which was collected by filtration. The crude product was purified by column

TH-2983_156122010

chromatography on alumina and dried with a vacuum pump to afford the product **4a** or **4b** as a dark yellow solid.

4a: R_f = 0.33 (10% EtOAc-Hexane); Dark yellow solid, yield: 75%; FT-IR ν_{max} (in cm^{-1}) 3318, 2956, 2927, 2858, 1602, 1582, 1514, 1493, 1465, 1334, 1237, 1220, 1134, 852; ^1H NMR (600 MHz, $CDCl_3$, 299 K): 10.69 (s, 1H, >NH), 8.20-8.17 (d, J = 18 Hz, 2H, H_{Ar}), 8.07-8.05 (d, J = 12 Hz, 2H, H_{Ar}), 7.06-6.98 (bm,4H, H_{Ar}), 6.78-6.76 (d, J = 12Hz, 2H, H_{Ar}), 3.96-3.93 (t, J = 9 Hz, 4H, 2 × $–OCH_2$), 3.81 (s, 4H, 2 × $–OCH_2$), 1.77-1.66 (m, 8H, 4 × $–OCH_2$-CH_2), 1.44-1.26 (m, 24H, alkyl chain), 0.90-0.85 (m, 12H, 4 × $–CH_3$); ^{13}C NMR (150 MHz, $CDCl_3$, 298.1K): 148.84, 147.02, 142.83, 135.79, 125.47, 124.14, 113.54, 69.28, 69.20, 31.56, 31.52, 29.18, 29.14, 25.66, 25.63, 22.55, 13.96; MALDI-TOF exact mass calculated for $C_{45}H_{64}N_3O_6$ ($M+H^+$): 742.479, found: 742.720.

4b: R_f = 0.50 (10% EtOAc-Hexane); Dark yellow solid, yield: 80%; FT-IR ν_{max} (in cm^{-1}) 3311, 2955, 2918, 2850, 1602, 1587, 1517, 1497, 1466, 1339, 1242, 1136, 853; ^1H NMR (600 MHz, $CDCl_3$, 299 K): 10.64 (s, 1H, >NH), 8.24-8.20 (m, 2H, H_{Ar}), 8.09-8.08 (d, J = 6 Hz, 2H, H_{Ar}), 7.20-6.95 (m, 4H, H_{Ar}), 6.77-6.76 (d, J = 6 Hz, 2H, H_{Ar}), 3.95-3.93 (t, J = 6 Hz, 4H, 2 × $–OCH_2$), 3.81 (s, 4H, 2 × $–OCH_2$), 1.76 (bs, 4H, alkyl chain), 1.69 (bs, 4H, alkyl chain), 1.41 (s, 4H, alkyl chain), 1.35 (s, 4H, alkyl chain), 1.25 (bs, 64H, alkyl chain), 0.88-0.86 (m, 12H, 4 × $–CH_3$); ^{13}C NMR (150 MHz, $CDCl_3$, 298.1K): 148.64, 146.91, 142.74, 135.70, 125.41, 124.19, 113.18, 69.12, 31.92, 29.75, 29.71, 29.70, 29.67, 29.65, 29.46, 29.40, 29.38, 29.20, 29.16, 26.03, 26.02, 22.70, 14.14; MALDI-TOF exact mass calculated for $C_{69}H_{111}N_3O_6$ (M^+): 1077.847, found: 1077.614.

Synthesis of 4,5-bis(3,4-bis(alkyloxy)phenyl)-1-alkyl-2-(4-nitrophenyl)-1H-imidazole (5a and 5b)

Into a 100 mL RB flask, anhydrous K_2CO_3 (8.8 equiv.), compound **4a** or **4b** (1.0 equiv.), appropriate 1-bromoalkanes (4.4 equiv.), catalytic amount of KI and anhydrous *N*, *N*-dimethylformamide (40 mL) were placed and the reaction mixture was stirred at 80 ^oC under nitrogen atmosphere for 17 h. The reaction mixture was extracted with ethyl acetate and washed with water and dried over anhydrous sodium sulfate. Then solvent is evaporated. The crude product was purified by column chromatography on silica gel. Eluting with 2-5% ethyl acetate-hexane mixture and evaporation provided the product in 85-88% yield.

TH-2983_156122010

5a: R_f = 0.58 (10% EtOAc-Hexane); Bright yellow solid, yield: 85%; IR ν_{max} (in cm^{-1}) 2957, 2923, 2873, 2856, 1598, 1520, 1497, 1473, 1341, 1250, 1239, 1219, 1139, 853 ; ^{1}H NMR (600 MHz, $CDCl_3$, 299 K): 8.33-8.31 (d, *J* = 12 Hz, 2H, H_{Ar}), 7.92-7.90 (d, *J* = 12 Hz, 2H, H_{Ar}), 7.13 (s, 1H, H_{Ar}), 7.07-7.05 (d, *J* = 12Hz, 1H, H_{Ar}), 6.98-6.97 (d, *J* = 6 Hz, 1H, H_{Ar}), 6.93-6.91 (d, *J* = 12 Hz, 1H, H_{Ar}), 6.89 (s, 1H, H_{Ar}), 6.73-6.71 (d, *J* = 12 Hz, 1H, H_{Ar}), 4.06-4.04 (t, *J* = 6 Hz, 2H, 1 × -OCH_2), 3.94-3.90 (m, 6H, 3 × -OCH_2), 3.79-3.77 (t, *J* = 6 Hz, 2H, 1 × -NCH_2), 1.89-1.84 (m, 2H, alkyl chain), 1.81-1.74 (m, 4H, alkyl chain), 1.72-1.67 (m, 2H, alkyl chain), 1.54-1.49 (m, 2H, alkyl chain), 1.45-1.36 (m, 12H, alkyl chain), 1.32-1.30 (m, 12H, alkyl chain), 1.10-1.07 (m, 2H, alkyl chain), 0.98 (bs, 4H, alkyl chain), 0.93-0.87 (m, 12H, alkyl chain), 0.75-0.73 (t, *J* = 4 Hz, 3H, alkyl chain); ^{13}C NMR (150 MHz, $CDCl_3$, 298.1K): 149.58, 149.20, 148.54, 147.67, 147.28, 144.24, 138.45, 137.76, 130.48, 129.24, 127.07, 123.80, 123.68, 123.08, 118.85, 116.07, 113.39, 111.84, 69.22, 69.02, 68.98, 68.58, 44.99, 31.54, 31.52, 31.51, 31.48, 30.78, 30.52, 29.15, 29.07, 29.05, 25.86, 25.66, 25.59, 25.58, 25.55, 22.52, 22.51, 22.50, 22.15, 13.93, 13.90, 13.73; MALDI-TOF exact mass calculated for $C_{51}H_{76}N_3O_6$ ($M+H^+$): 826.573, found: 826.779.

5b: R_f = 0.78 (10% EtOAc-Hexane); Bright yellow solid, yield: 88%; IR ν_{max} (in cm^{-1}) 2957, 2918, 2873, 2850, 1597, 1520, 1498, 1471, 1341, 1251, 1219, 1139, 1024, 854; ^{1}H NMR (600 MHz, $CDCl_3$, 299 K): 8.35-8.33 (d, *J* = 12 Hz, 2H, H_{Ar}), 7.93-7.91 (d, *J* = 12 Hz, 2H, H_{Ar}), 7.12 (s, 1H, H_{Ar}), 7.05-7.04 (d, *J* = 6 Hz, 1H, H_{Ar}), 6.97-6.96 (d, *J* = 6 Hz, 1H, H_{Ar}), 6.93-6.91 (t, *J* = 6 Hz, H_{Ar}, 1H), 6.88 (s, 1H, H_{Ar}), 6.73-6.71 (d, *J* = 12 Hz, 1H, H_{Ar}), 4.05-4.03 (t, *J* = 6 Hz, 2H, 1 × -OCH_2), 3.95-3.90 (m, 6H, 3 × -OCH_2), 3.79-3.76 (t, *J* = 9 Hz, 2H, 1 × -NCH_2), 1.88-1.86 (t, *J* = 6 Hz, 2H, 1 × -OCH_2-CH_2), 1.80-1.76 (m, 4H, alkyl chain), 1.71-1.69 (t, *J* = 6 Hz, 2H, alkyl chain), 1.51-1.49 (t, *J* = 6 Hz, 2H, alkyl chain), 1.43-1.36 (m, 10H, alkyl chain), 1.25-1.22 (m, 72H, alkyl chain), 1.12-1.11 (bm, 2H, alkyl chain), 1.05 (bs, 2H, alkyl chain), 0.99 (bs, 4H, alkyl chain), 0.89-0.85 (m, 15H, 5 × -CH_3); ^{13}C NMR (150 MHz, $CDCl_3$, 298.1K): 149.69, 149.30, 148.63, 147.77, 147.34, 144.26, 138.52, 137.78, 130.50, 129.26, 127.14, 123.81, 123.76, 123.17, 118.93, 116.28, 113.53, 112.01, 69.35, 69.14, 69.09, 68.67, 45.03, 31.90, 31.89, 31.86, 30.60, 29.72, 29.69, 29.65, 29.63, 29.61, 29.59, 29.56, 29.53, 29.48, 29.44, 29.43, 29.41, 29.36, 29.34, 29.32, 29.28, 29.20, 28.71, 26.23, 26.08, 26.00, 25.99, 25.97, 22.64, 22.63, 14.05; MALDI-TOF exact mass calculated for $C_{81}H_{136}N_3O_6$ ($M+H^+$): 1247.042, found: 1247.666.

TH-2983_156122010

Synthesis of 4-(4,5-bis(3,4-bis(alkyloxy)phenyl)-1-alkyl-1H-imidazol-2-yl)aniline (6a and 6b)[47]

A mixture of compound **5a** and **5b** (1.0 equiv.), 10% Pd-C catalyst and hydrazine hydrate (3.0 equiv.) in ethanol (20 mL) were stirred at reflux for 12 h. after the disappearance of starting material, ethanol was removed under reduced pressure at 40 ^{o}C and the product were collected by filtration, recrystallized with ethanol and dried using vacuum pump. The product **6a** or **6b** were obtained as white sticky solids with yield up to 85-90%, which was used for next step without further purification.

Synthesis of NI-6, NI-12, PI-6 and PI-12[47]

A mixture of naphthalene or perylene bisanhydrides (1.0 equiv.), compound **6a** or **6b** (2.1 equiv.) and imidazole (1.0 g) were taken in a microwave vessel, flushed with nitrogen, and put in a microwave reactor. The mixture was heated to 165 °C for 35 min at 35 W. After cooling, the reaction mixture was poured in 2 N HCl and extracted with chloroform. The organic mixture was washed with water and a saturated sodium chloride solution. The crude compound was purified by neutral alumina column chromatography using the 50% chloroform–hexane system to yield 65-85% of the desired product.

NI-6: R_f = 0.50 (100% Chloroform); Gray solid, yield: 80%; IR ν_{max} (in cm^{-1}) 3079, 2957, 2927, 2857, 1716, 1671, 1515, 1502, 1468, 1343, 1241, 1193, 1138, 1017, 856, 769, 715; ^{1}H NMR (600 MHz, $CDCl_3$, 299 K): 8.87 (s, 4H, H_{Ar}), 7.92-7.91 (d, *J* = 6 Hz, 4H, H_{Ar}), 7.48-747 (d, *J* = 6 Hz, 4H, H_{Ar}), 7.18 (s, 2H, H_{Ar}), 7.09-7.08 (d, *J* = 6 Hz, 2H, H_{Ar}), 7.00-6.96 (m, 4H, H_{Ar}), 6.94 (s, 2H, H_{Ar}), 6.72-6.71 (d, *J* = 6 Hz, 2H, H_{Ar}), 4.08-4.06 (t, *J* = 6 Hz, 4H, 2 × -OCH_2**)** 3.97-3.93 (m, 12H, 6 × -OCH_2) 3.81-3.79 (t, *J* = 6 Hz, 4H, 2 × -NCH_2), 1.90-1.86 (m, 4H, alkyl chain), 1.82-1.75 (m, 8H, alkyl chain), 1.73-1.70 (m, 4H, alkyl chain), 1.67 (bs, 4H, alkyl chain), 1.54-1.51 (m, 4H, alkyl chain), 1.50-1.43 (m, 12H, alkyl chain), 1.41-1.38 (m, 12H, alkyl chain), 1.34-1.32 (m, 22H, alkyl chain), 1.16-1.12 (m, 4H, alkyl chain), 1.05 (bs, 6H, alkyl chain), 0.94-0.92 (t, *J* = 6 Hz, 6H, alkyl chain), 0.91-0.89 (m, 18H, alkyl chain), 0.80-0.78 (t, *J* = 6 Hz, 6H, 2 × –CH_3 group); ^{13}C NMR (150 MHz, $CDCl_3$, 298.1K): 162.85, 149.52, 149.29, 148.66, 147.52, 145.86, 137.69, 134.78, 132.55, 131.50, 130.08, 129.26, 128.91, 127.71, 127.26, 127.05, 123.90, 118.85, 116.44, 113.62, 111.97, 69.38, 69.23, 69.18, 68.72, 44.93, 31.66, 31.64, 31.61, 30.97, 30.73, 29.29, 29.21, 29.19, 26.05, 25.77, 25.69, 25.67, 22.63, 22.62, 22.61, 22.32, 14.06, 14.04, 14.01, 13.88; MALDI-TOF exact mass calculated for $C_{116}H_{155}N_6O_{12}$ ($M+H^+$): 1824.170, found: 1824.298.

TH-2983_156122010

NI-12: R_f = 0.67 (100% Chloroform); Gray solid, yield: 85%; IR ν_{max} (in cm^{-1}) 3079, 2957, 2919, 2850, 1716, 1671, 1516, 1502, 1467, 1343, 1241, 1193, 1138, 1018, 870, 770, 716; ^{1}H NMR (600 MHz, $CDCl_3$, 299 K): 8.88 (s, 4H, H_{Ar}), 7.93-7.92 (d, J = 6 Hz, 4H, H_{Ar}), 7.48-7.47 (d, J = 6 Hz, 4H, H_{Ar}), 7.18 (s, 2H, H_{Ar}), 7.11-7.09 (d, J = 12 Hz, 2H, H_{Ar}), 6.98 (s, 4H, H_{Ar}), 6.94 (s, 2H, H_{Ar}), 6.74-6.72 (d, J = 12 Hz, 2H, H_{Ar}), 4.07-4.05 (t, J = 6 Hz, 4H, 2 × -OCH_2), 3.97-3.94 (m, 12 H, 6 × -OCH_2), 3.81-3.79 (t, J = 6 Hz, 4H, 2 × -NCH_2), 1.91-1.86 (m, 4H, alkyl chain), 1.82-1.77 (m, 8H, alkyl chain), 1.72-1.70 (t, J = 6 Hz, 4H, alkyl chain), 1.63 (bs, 8H, alkyl chain), 1.52-1.48 (m, 8H, alkyl chain), 1.45-1.43 (m, 8H, alkyl chain), 1.31-1.27 (bm, 140H, alkyl chain), 1.23 (bs, 8H, alkyl chain), 1.11 (bs, 4H, alkyl chain), 1.06 (bs, 8H, alkyl chain), 0.90-0.84 (m, 30H, 10 × -CH_3); ^{13}C NMR (150 MHz, $CDCl_3$, 298.1K): 162.83, 149.54, 149.30, 148.68, 147.54, 145.82, 137.70, 135.21, 134.77, 132.56, 131.51, 130.08, 129.26, 128.91, 127.71, 127.26, 127.06, 125.03, 123.92, 118.87, 116.47, 113.63, 111.99, 69.41, 69.25, 69.20, 68.73, 44.95, 32.20, 31.95, 31.94, 31.83, 30.80, 29.78, 29.75, 29.72, 29.70, 29.67, 29.66, 29.64, 29.55, 29.52, 29.49, 29.41, 29.40, 29.38, 29.37, 29.28, 28.89, 26.42, 26.14, 26.08, 26.05, 26.04, 23.43, 22.81, 22.71, 22.69, 22.59, 14.24, 14.13; MALDI-TOF exact mass calculated for $C_{176}H_{275}N_6O_{12}$ ($M+H^+$): 2665.109, found: 2665.712.

PI-6: R_f = 0.27 (100% Chloroform); Dark red solid, yield: 65%; IR ν_{max} (in cm^{-1}) 2955, 2924, 2876, 2850, 1701, 1668, 1593, 1577, 1498, 1467, 1431, 1356, 1253, 1136, 1124, 809, 800, 746; ^{1}H NMR (600 MHz, $CDCl_3$, 299 K): 8.76-8.75 (d, J = 6 Hz, 4H, H_{Ar}), 8.66-8.65 (d, J = 6 Hz, 4H, H_{Ar}), 7.92-7.90 (d, J = 12 Hz, 4H, H_{Ar}), 7.51-7.49 (d, J = 12 Hz, 4H, H_{Ar}), 7.20 (s, 2H, H_{Ar}), 7.09-7.07 (d, J = 12 Hz, 2H, H_{Ar}), 6.98-6.95 (m, 4H, H_{Ar}), 6.93 (s, 2H, H_{Ar}), 6.73-6.72 (d, J = 6 Hz, 2H, H_{Ar}), 4.07-4.05 (t, J = 6 Hz, 4H, 2 × -OCH_2), 3.95-3.93 (t, J = 6 Hz, 12H, 6 × -OCH_2), 3.82-3.79 (t, J =6 Hz, 4H, 2 × -NCH_2), 1.90-1.85 (m, 4H, alkyl chain), 1.82-1.75 (m, 8H, alkyl chain), 1.71-1.67 (m, 8H, alkyl chain), 1.53-1.51 (t, J = 6 Hz, 4H, alkyl chain), 1.48-1.43 (m, 8H, alkyl chain), 1.39-1.37 (m, 12H, alkyl chain), 1.33-1.32 (m, 24H, alkyl chain), 1.25 (s, 2H, alkyl chain), 1.14-1.12 (t, J = 6 Hz, 4H, alkyl chain), 1.05 (bs, 6H, alkyl chain), 0.94-0.92 (t, J = 6 Hz, 6H, alkyl chain), 0.90-0.89 (m, 18H, alkyl chain), 0.80-0.78 (t, J = 6 Hz, 6H, 2 × -CH_3); ^{13}C NMR (150 MHz, $CDCl_3$, 298.1K): 163.16, 149.44, 149.20, 148.56, 147.90, 145.92, 139.25, 137.30, 135.32, 135.18, 135.40, 131.40, 129.93, 129.22, 129.15, 127.39, 126.05, 124.99, 123.83, 123.67, 123.25, 118.89, 116.29, 114.04, 113.50, 113.44, 111.88, 69.26, 69.12, 69.08, 68.63, 44.95, 33.80, 32.17, 31.90, 31.64, 31.62, 31.60, 31.58, 30.90, 30.59, 29.67, 29.60, 29.48, 29.33, 29.27,

TH-2983_156122010

29.26, 29.17, 29.13, 28.91, 26.36, 25.99, 25.75, 25.69, 25.66, 25.64, 23.41, 22.66, 22.60, 22.58, 22.28, 14.10, 14.03, 14.01, 13.99, 13.88; MALDI-TOF exact mass calculated for $C_{126}H_{159}N_6O_{12}$ ($M+H^+$): 1948.201, found: 1948.202.

PI-12: R_f = 0.40 (100% Chloroform); Dark red solid; yield: 70%; IR ν_{max} (in cm^{-1}) 2954, 2920, 2852, 1702, 1668, 1513, 1497, 1476, 1356, 1254, 1136, 1125, 809, 800, 746; ^1H NMR (600 MHz, $CDCl_3$, 299 K): 8.77 (bs, 4H, H_{Ar}), 8.70 (bs, 4H, H_{Ar}), 7.93-7.92 (d, *J* = 6 Hz, 4H, H_{Ar}), 7.51-7.49 (d, *J* = 12 Hz, 4H, H_{Ar}), 7.20 (s, 2H, H_{Ar}), 7.12-7.10 (d, *J* = 12 Hz, 2H, H_{Ar}), 6.96-6.94 (d, *J* = 12 Hz, 6H, H_{Ar}), 6.74-6.72 (d, *J* =12 Hz, 2H, H_{Ar}), 4.07-4.04 (t, *J* = 9 Hz, 4H, 2 × $-OCH_2$), 3.95 (bs, 12H, 6 × $-OCH_2$), 3.82-3.79 (t, *J* = 9 Hz, 4H, 2 × $-NCH_2$), 2.04 (s, 1H, alkyl chain), 1.90-1.84 (m, 4H, alkyl chain), 1.81-1.76 (m, 8H, alkyl chain), 1.74-1.68 (m, 8H, alkyl chain), 1.54-1.50 (m, 8H, alkyl chain), 1.45-1.40 (m, 18H, alkyl chain), 1.27-1.23 (bm, 145H, alkyl chain), 1.05 (bs, 8H, alkyl chain), 0.89-0.83 (m, 30H, 10 × $-CH_3$); ^{13}C NMR (150 MHz, $CDCl_3$, 298.1K): 162.13, 149.54, 149.30, 148.68, 147.54, 145.82, 137.70, 135.21, 134.77, 132.56, 131.51, 130.08, 129.26, 128.91, 127.71, 127.26, 127.06, 125.03, 123.92, 118.87, 116.47, 113.63, 111.99, 69.41, 69.25, 69.20, 68.73, 44.95, 32.20, 31.95, 31.94, 31.83, 30.80, 29.78, 29.75, 29.72, 29.70, 29.67, 29.66, 29.64, 29.55, 29.52, 29.49, 29.41, 29.40, 29.38, 29.37, 29.28, 28.89, 26.42, 26.14, 26.08, 26.05, 26.04, 23.43, 22.81, 22.71, 22.69, 22.59, 14.24, 14.13; MALDI-TOF exact mass calculated for $C_{186}H_{279}N_6O_{12}$ ($M+H^+$): 2789.140, found: 2789.910.

4.5. Appendix

In table 4.2 the $d_{(obs)}$ values were directly observed from XRD instruments. Using the LCDiXRD 1.0 software, indexing of XRD diffractions $d_{(cal)}$ values, Miller indices (*hkl*) and lattice parameters (*a, b, c, γ*) of columnar liquid crystals were obtained.

For Col_h phase, in Millar indices *hkl* the *l* value will be always 0;
So equation (1) [48-49] is

$$\frac{1}{d^2_{hk0}} = \frac{4}{3}\left(\frac{h^2+hk+k^2}{a^2}\right) \quad (1)$$

$a = d_{100} \times 2/\sqrt{3}$

$S = a^2 \times \text{Sin } 60^o$

$V = S \times h_c$

a is the hexagonal lattice constant, *S* = Lattice area, *V* = Volume, h_c corresponds to the thickness of a columnar slice. The ratio of the *d*-spacings indexed to Miller indices 10, 11, 20 of unit hexagonal cell is 1:0.57:0.5

TH-2983_156122010

For Col_r phase, equation (2) [48-49] is

$$\frac{1}{d^2_{hk0}} = \frac{h^2}{a^2} + \frac{k^2}{b^2} \qquad (2)$$

$S = a \times b$;

$V = S \times h_c$

a and b are the sides of the rectangular lattice.

For Col_{ob} phase, equation (3) [48-49] is

$$\frac{1}{d^2_{hk0}} = \frac{1}{(sin\gamma)^2}\left(\frac{h^2}{a^2} + \frac{k^2}{b^2} - \frac{2hkcos\gamma}{ab}\right) \quad (3)$$

$S = a \times b \times \sin\gamma$;

$V = S \times h_c$

a and b are the sides of the parallelogram lattice. γ is the angle between the sides a and b.

The number of molecules per unit cell (Z) are calculated using the standard formula

$$Z = \frac{\rho N_A V_{unit\ cell}}{M} \quad (4)$$

ρ = 1, the density of the liquid crystal phase; N_A = Avogadro's constant (6.022×10^{23});

M = Molecular weight. After simplifying equation (4)

The number of molecules in a unit cell (Z)= $0.6023 \times V$ / molecular weight.

4.6. References

1. J. Shukla and P. Mukhopadhyay, *European J. Org. Chem.*, 2019, **2019**, 7770–7786.
2. M. Ichikawa, Y. Yokota, H. G. Jeon, G. D. R. Banoukepa, N. Hirata and N. Oguma, *Org. Electron.*, 2013, **14**, 516–522.
3. G. E. Purdum, N. Yao, A. Woll, T. Gessner, R. T. Weitz, and Y. L. Loo, *Adv. Funct. Mater.*, 2016, **26**, 2357-2364.
4. D. B. Shaikh, A. Ali Said, Z. Wang, P. Srinivasa Rao, R. S. Bhosale, A. M. Mak, K. Zhao, Y. Zhou, W. Liu, W. Gao, J. Xie, S. V. Bhosale, S. V. Bhosale and Q. Zhang, *ACS Appl. Mater. Interfaces*, 2019, **11**, 44487–44500.
5. L. M. Kozycz, C. Guo, J. G. Manion, A. J. Tilley, A. J. Lough, Y. Li and D. S. Seferos, *J. Mater. Chem. C*, 2015, **3**, 11505–11511.
6. D. Shukla, S. F. Nelson, D. C. Freeman, M. Rajeswaran, W. G. Ahearn, D. M. Meyer and J. T. Carey, *Chem. Mater.*, 2008, **20**, 7486–7491.
7. K. Al Kurdi, D. P. McCarthy, D. P. McMeekin, S. O. Furer, M. H. Tremblay, S. Barlow, U. Bach and S. R. Marder, *Mater. Chem. Front.*, 2021, **5**, 450–457.
8. A. Nowak-Król, K. Shoyama, M. Stolte and F. Würthner, *Chem. Commun.*, 2018, **54**, 13763–13772.
9. M. Dharmarwardana, B. S. Arimilli, M. A. Luzuriaga, S. Kwon, H. Lee, G. A.

TH-2983_156122010

Appuhamillage, G. T. McCandless, R. A. Smaldone and J. J. Gassensmith, *CrystEngComm*, 2018, **20**, 6054–6060.
10. W. G. Chen, Z. J. Chen, L. Zhang, B. Wang, Z. Z. Lin, R. Cao, W. R. Wang, Y. Chen and Y. Wang, *Chem. Eng. J.*, 2022, **432**, 134411.
11. Y. R. Huang and S. H. Hsiao, *Dye. Pigment.*, 2022, **199**, 110056.
12. L. Wang, Y. L. Liu, Q. J. Li, S. H. Chen, D. He and M. S. Wang, *J. Phys. Chem. A*, 2022, **126**, 870–878.
13. S. Saha and P. Sahoo, *Bioorganic Med. Chem. Lett.*, 2021, **49**, 128287.
14. Q. H. Ling, J. L. Zhu, Y. Qin and L. Xu, *Mater. Chem. Front.*, 2020, **4**, 3176–3189.
15. J. A. Tyson, V. Mirabello, D. G. Calatayud, H. Ge, G. Kociok-Köhn, S. W. Botchway, G. Dan Pantoș and S. I. Pascu, *Adv. Funct. Mater.*, 2016, **26**, 5641–5657.
16. C. Platella, E. Napolitano, C. Riccardi, D. Musumeci and D. Montesarchio, *J. Med. Chem.*, 2021, **64**, 3578–3603.
17. N. Kumari, S. Naqvi, M. Ahuja, K. Bhardwaj and R. Kumar, *J. Mater. Sci. Mater. Electron.*, 2020, **31**, 4310–4322.
18. A. Luzio, L. Criante, V. D'Innocenzo and M. Caironi, *Sci. Rep.*, 2013, **3**, 1–6.
19. T. Mondal, T. Sakurai, S. Yoneda, S. Seki and S. Ghosh, *Macromolecules*, 2015, **48**, 879–888.
20. P. Rajdev, M. R., Molla and S. Ghosh, *Langmuir*, 2014, **30**, 1969-1976.
21. C. Huang, S. Barlow and S. R. Marder, *J. Org. Chem.*, 2011, **76**, 2386–2407.
22. W. Pisula, M. Zorn, J. Y. Chang, K. Müllen and R. Zentel, *Macromol. Rapid Commun.*, 2009, **30**, 1179–1202.
23. S. Sergeyev, W. Pisula and Y. H. Geerts, *Chem. Soc. Rev.*, 2007, **36**, 1902–1929.
24. D. Adam, P. Schuhmacher, J. Simmerer, L. Häussling, K. Siemensmeyer, K. H. Etzbachi, H. Ringsdorf and D. Haarer, *Nature*, 1994, **371**, 141–143.
25. J. M. Warman, M. P. De Haas, G. Dicker, F. C. Grozema, J. Piris and M. G. Debije, *Chem. Mater.*, 2004, **16**, 4600–4609.
26. B. A. Jones, M. J. Ahrens, M. H. Yoon, A. Facchetti, T. J. Marks, and M. R. Wasielewski, *Angew. Chem.*, 2004, **43**, 6363-6366.
27. M. Gsänger, J. H. Oh, M. Könemann, H. W. Höffken, A. M. Krause, Z. Bao, and F. Würthner, *Angew. Chem.*, 2010, **49**, 740-743.
28. K. D. Thériault, C. L. Radford, G. P. Nagabhushana, D. T. Hogan, V. E. Williams, T. L. Kelly and T. C. Sutherland, *Mater. Adv.*, 2022, **3**, 328–336.
29. M. R. Molla and S. Ghosh, *Chem. Mater.*, 2011, **23**, 95–105.
30. N. V. Ghule, R. S. Bhosale, S. V. Bhosale, T. Srikanth, N. V. S. Rao and S. V. Bhosale, *ChemistryOpen*, 2018, **7**, 61–67.
31. T. Sakurai, Y. Tsutsui, K. Kato, M. Takata and S. Seki, *J. Mater. Chem. C*, 2016, **4**, 1490–1496.
32. A. Takai, T. Kajitani, T. Fukushima, K. Kishikawa, T. Yasuda and M. Takeuchi, *J. Am. Chem. Soc.*, 2016, **138**, 11245–11253.
33. Y. D. Zhang, K. G. Jespersen, M. Kempe, J. A. Kornfield, S. Barlow, B. Kippelen and S. R. Marder, *Langmuir*, 2003, **19**, 6534–6536.
34. R. J. Chesterfield, J. C. McKeen, C. R. Newman, P. C. Ewbank, D. A. Da Silva Filho, J. L. Brédas, L. L. Miller, K. R. Mann and C. D. Frisbie, *J. Phys. Chem. B*,

TH-2983_156122010

2004, **108**, 19281–19292.
35. Y. Hu, Y. Qin, X. Gao, F. Zhang, C. A. Di, Z. Zhao, H. Li and D. Zhu, *Org. Lett.*, 2012, **14**, 292–295.
36. T. B. Singh, S. Erten, S. Günes, C. Zafer, G. Turkmen, B. Kuban, Y. Teoman, N. S. Sariciftci and S. Icli, *Org. Electron.*, 2006, **7**, 480–489.
37. S. Kumar and S. K. Gupta, *Tetrahedron Lett.*, 2011, **52**, 5363–5367.
38. S. Sonalin, A. Mishra, A. K. Sahu, A. K. Mishra, P. M. Imran, N. S. P. Bhuvanesh and S. Nagarajan, *J. Phys. Chem. C*, 2020, **124**, 13053–13062.
39. H. Shan, A. Liu, Y. Lv, X. Wu, Y. Ma, X. Jin and J. Guo, *Dye. Pigment.*, 2020, **180**, 108400.
40. D. Kathirvelan, S. Mayakrishnan, N. Uma Maheswari, C. Biswas, S. S. K. Raavi and T. K. Panda, *New J. Chem.*, 2020, 44, 1785–1794.
41. S. Takahashi, S. Nagai, M. Asami and S. Ito, *Mater. Adv.*, 2020, **1**, 708–719.
42. S. Bhattacharya, G. Reddy, S. Paul, S. S. Hossain, S. S. Kumar Raavi, L. Giribabu, A. Samanta and V. R. Soma, *Dye. Pigment.*, 2021, **184**, 108791.
43. J. Sivanadanam, I. S. Aidhen and K. Ramanujam, *New J. Chem.*, 2020, **44**, 10207–10219.
44. K. D. Thériault, C. L. Radford, G. P. Nagabhushana, D. T. Hogan, V. E. Williams, T. L. Kelly and T. C. Sutherland, *Mater. Adv.*, 2022, **3**, 328–336.
45. A. Ortiz-Conde, F. J. García Sánchez, J. J. Liou, A. Cerdeira, M. Estrada and Y. Yue, *Microelectron. Reliab.*, 2002, **42**, 583–596.
46. S. E. Wolkenberg, D. D. Wisnoski, W. H. Leister, Y. Wang, Z. Zhao and C. W. Lindsley, *Org. Lett.*, 2004, **6**, 1453–1456.
47. R. K. Gupta and A. S. Achalkumar, *J. Org. Chem.*, 2018, **83**, 6290–6300.
48. S. Laschat, A. Baro, N. Steinke, F. Giesselmann, C. Hägele, G. Scalia, R. Judele, E. Kapatsina, S. Sauer, A. Schreivogel, and M. Tosoni, *Angewandte Chemie International Edition*, 2007, **46**, 4832-4887.
49. K. Ohta, *Physics and chemistry of molecular assemblies*, 2020, World Scientific.

TH-2983_156122010